

Electronic Thesis and Dissertation Repository

3-3-2022 2:30 PM

Solid State NMR Spectroscopic Characterization of Metal Organic Frameworks


Vinicius Martins, *The University of Western Ontario*

Supervisor: Huang, Yining, *The University of Western Ontario*

A thesis submitted in partial fulfillment of the requirements for the Doctor of Philosophy degree in Chemistry

© Vinicius Martins 2022

Follow this and additional works at: <https://ir.lib.uwo.ca/etd>

 Part of the [Inorganic Chemistry Commons](#), [Materials Chemistry Commons](#), and the [Physical Chemistry Commons](#)

Recommended Citation

Martins, Vinicius, "Solid State NMR Spectroscopic Characterization of Metal Organic Frameworks" (2022). *Electronic Thesis and Dissertation Repository*. 8413.
<https://ir.lib.uwo.ca/etd/8413>

This Dissertation/Thesis is brought to you for free and open access by Scholarship@Western. It has been accepted for inclusion in Electronic Thesis and Dissertation Repository by an authorized administrator of Scholarship@Western. For more information, please contact wlsadmin@uwo.ca.

Abstract

Metal-organic frameworks are porous organic-inorganic materials that have attracted enormous attention due to their promising capabilities for several technologies, including carbon dioxide capture and storage, gas separation, and heterogeneous catalysis. The performance of MOFs for these applications is directly linked to their properties and, by extension, structures. Therefore, it is essential to understand the structure – property relationship. Solid-state NMR (SSNMR) spectroscopy is a technique that provides complementary information to X-ray diffraction-based techniques. SSNMR can provide short-range information around the NMR-active nucleus of interest. Furthermore, SSNMR can provide additional information regarding host-guest interactions and dynamics of adsorbed molecules, which play a crucial role in the adsorption capacity of materials.

Herein, we investigate the structure and properties of several representative MOFs via SSNMR. We demonstrate that ultra-high resolution ^{17}O SSNMR spectra can be acquired at an ultrahigh magnetic field of 35.2 T. This allowed us to obtain important information regarding the subtle changes in the structure of MOFs upon activation, phase transition, host-guest interactions, etc. We also investigate the structural changes of the flexible MIL-53(Al) MOF upon activation and hydration. ^{17}O SSNMR experiments carried out at 35.2 T provided further insights into the intermolecular interaction governing the crystal structure. We describe the ^{17}O NMR studies of MIL-121, a MOF with free carboxylic acid groups in the pores. The sensitivity of the ^{17}O NMR achieved at high magnetic fields allowed us to further investigate the MOFs exchanged with different metal ions. We demonstrate that the co-adsorption of water and CO_2 can be investigated using multinuclear SSNMR spectroscopy. The dynamics, adsorption sites, and intermolecular interaction were studied. Furthermore, this approach has also allowed to investigate the effect of water on the adsorption of carbon dioxide in ZnAtzOx.

Summary for Lay Audience

Metal-organic frameworks (MOFs) are porous materials that have found application in several technologies, including carbon capture and storage, catalysis, and gas separation. Understanding the structure and physicochemical properties of MOFs is crucial for development of new materials with real applications. Herein, we demonstrate how SSNRM spectroscopy can provide complementary information regarding the structure and properties of MOFs. Oxygen is a key element in the synthesis and properties of MOFs. We demonstrate that by performing ^{17}O SSNMR experiments at ultra-high field can provide unprecedented information that is complementary to X-ray crystallography. The ultra-high resolution allowed us to get information on the structure, host-guest interactions, activation process, phase transition, and structural flexibility. Furthermore, we show that SSNMR can be used to study the behavior of adsorbed CO_2 in an ultramicroporous MOF under humid conditions.

Keywords

Metal-organic frameworks, solid-state NMR spectroscopy, quadrupolar nucleus, CO₂ adsorption, water adsorption.

Co-Authorship Statement

This thesis contains materials from previously published manuscripts. Dr. Yining Huang was the corresponding author on all presented papers and was responsible for the supervision of Vinicius Martins. For copyright releases see the Appendix. Chapters 1 and 2 were written by Vinicius Martins and revised by Dr. Huang. Section 1.4.3 of Chapter 1 was based on the mini-review paper co-authored by Y. T. Angel Wong, Vinicius Martins, Bryan E.G. Lucier, and Yining Huang (Chem. Eur. J. 2018, 25, 1848.) Chapter 3 is based on the published article co-authored by Vinicius Martins, Jun Xu, Xiaoling Wang, Kuizhi Chen, Ivan Hung, Zhehong Gan, Christel Gervais, Christian Bonhomme, Shijia Jiang, Anmin Zheng, Bryan E. G. Lucier, and Yining Huang (J. Am. Chem. Soc. 2020, 142, 14877.) The samples were prepared and characterized by Vinicius Martins. ^{17}O SSNMR experiments at high field were performed by Xiaoling Wang, Kuizhi Chen, and Ivan Hung. Computational calculations were performed by Christel Gervais, Christian Bonhomme, Shijia Jiang, and Anmin Zheng. Vinicius Martins wrote the first draft of the manuscript which was revised by Bryan E.G Lucier, Jun Xu, and Yining Huang. Chapter 4 is based on the published paper co-authored by Vinicius Martins, Jun Xu, Ivan Hung, Zhehong Gan, Christel Gervais, Christian Bonhomme, and Yining Huang (Magn. Reson. Chem. 2021, 59, 940) Vinicius Martins prepared and characterized the samples. Kuizhi Chen and Ivan Hung performed the ^{17}O SSNMR experiments at high field. Christel Gervais and Christian Bonhomme performed the computational calculations. Vinicius Martins wrote the first draft of the manuscript. The manuscript was revised by Jun Xu and Yining Huang.

Acknowledgments

I thank Prof. Huang for his supervision and mentorship. Prof. Huang has been more than a supervisor. During these years of study, Prof. Huang has been a source of support, inspiration, and knowledge. I would like to thank the members of my thesis examination board for their important input towards the completion of my degree: Dr. Zhifeng Ding, Dr. François Lagugné-Labarhet, Dr. Kim Baines, and Dr. Michael Kerr. I would also like to include Dr. James A. Wisner for participating in my first-year report presentation. I am grateful to have had the opportunity to learn from the most inspiring and motivating professors during my graduate studies: Prof. John F. Corrigan, Prof. Yining Huang, Prof. Tsun-Kong Sham, Prof. Lijia Liu, Prof. Yang Song, and Prof. Mark S. Workentin. I extend my gratitude to all staff at the Chemistry Department. Specially, Dr. Mathew Willans and Dr. Bryan E. G. Lucier for training me and for all their patience. Many thanks to Dr. Paul Boyle, Aneta Borecki, and Dr. Kim Law for their help at the X-ray facility. I thank Ms. Darlene McDonald for all assistance. I would like to thank Mr. Barakat Misk for his technical supports. I thank my TA supervisors and technicians for the great experience I had contributing to the first and second-year laboratory: Sandra Zakaria Holtslag, M. Naeem Shahid, Robert Harbottle, Susan England, Mike Brandt, and Chris Levy. I would like to acknowledge and thank the help of Xiaoling Wang, Kuizhi Chen, Ivan Hung and Zhehong Gan for performing the experiments at the National High Magnetic Field Laboratory. Many thanks to Christel Gervais, Christian Bonhomme, Shijia Jiang and Anmin Zheng for the help with computational calculations. I cannot forget to thank my coworkers who helped me in the laboratory and for their helpful discussions: Zitong Wang, Shoushun Chen, Shan Jiang, Bligh Desveaux, Angela Li, Boqing Li, Angel Wong, Natalia Marins, Yihao Shen, Wanli Zhang, Jiabin Xu, and in special Sandamini Alahakoon for all the good conversations. I want to thank all my friends who supported me and helped me navigate through difficult times: Thiago, Felipe, Rafa, Evelyn, Carol, Vanessa, Olivia, Glenn, and Scott. Finally, I would like to thank my family who made this dream possible. It is impossible to describe my gratitude to my mother, Eliane, and my grandmother, Maria, for have unconditionally supported me in pursuit of my dreams and aspirations. I thank them for raising me to become who I am and for always encourage me to what is best. Last but not least, I would like to thank my brother, Elimar, my father, Mario, and my aunt Mariazinha for their support.

Table of Contents

Abstract.....	ii
Summary for Lay Audience.....	iii
Keywords	iv
Co-Authorship Statement.....	v
Acknowledgments.....	vi
Table of Contents.....	vii
List of Tables	xi
List of Figures.....	xii
List of Abbreviations	xix
List of Appendices	xx
Chapter 1	1
1 Metal-organic frameworks.....	1
1.1 The reticular chemistry and rational design of MOFs	2
1.2 Synthetic approaches of MOFs.....	6
1.2.1 Activation of MOFs	7
1.2.2 Post-synthetic modification (PSM) of MOFs	9
1.3 Characterization of MOFs.....	10
1.3.1 Nitrogen adsorption and desorption isotherms	11
1.3.2 Thermogravimetric analyses (TGA).....	11
1.3.3 X-ray crystallography	11
1.4 Characterization of MOFs via Solid-state NMR Spectroscopy	12
1.4.1 Probing the local structure of MOFs via ^1H , ^{13}C , and ^{17}O SSNMR	13
1.4.2 Probing CO_2 adsorption in MOFs via SSNMR	18
1.4.3 Probing water adsorption in MOFs.....	21

1.5	Outline of the thesis	23
1.6	References.....	23
Chapter 2.....		36
2	Basics of solid-state NMR spectroscopy	36
2.1	Physical background.....	36
2.2	Zeeman interaction.....	37
2.2.1	Chemical shielding (CS) interaction.....	38
2.2.2	Dipole coupling interaction.....	40
2.2.3	Quadrupolar interaction	41
2.3	SSNMR spectroscopic methods in chemistry.....	45
2.3.1	Magic Angle spinning (MAS)	46
2.3.2	Cross-polarization (CP)	47
2.3.3	Heteronuclear chemical shift correlation (HETCOR)	48
2.3.4	Rotational echo double resonance (REDOR).	49
2.3.5	Triple-Quantum MAS (3QMAS).....	50
2.3.6	¹³ C powder line-shape analysis.....	53
2.3.7	² H powder line-shape analysis.....	54
2.4	References.....	57
Chapter 3.....		60
3	Higher Magnetic Fields, Finer MOF Structural Information: ¹⁷ O Solid-State NMR at 35.2 T	60
3.1	Introduction.....	60
3.2	Experimental details.....	63
3.2.1	Synthesis and characterization of MOF samples	63
3.2.2	¹⁷ O solid-state NMR measurements.....	64
3.2.3	Spectral simulations	66

3.2.4	Theoretical calculations	66
3.3	Results and discussion	67
3.4	Conclusions and future work	80
3.5	References.....	81
Chapter 4.....		89
4	¹⁷ O solid-state NMR at ultrahigh magnetic field of 35.2 T: Resolution of inequivalent oxygen sites in different phases of MOF MIL-53(Al).....	89
4.1	Introduction.....	89
4.2	Experimental details.....	92
4.2.1	Sample preparation	92
4.2.2	SSNMR spectroscopy	93
4.2.3	Spectral simulations	94
4.2.4	Theoretical calculations	95
4.3	Results and discussion	95
4.4	Conclusions.....	105
4.5	References.....	106
Chapter 5.....		110
5	Characterization of oxygen sites in MOF MIL-121 and related materials via ¹⁷ O SSNMR spectroscopy	110
5.1	Introduction.....	110
5.2	Experimental details.....	113
5.2.1	Sample preparation and characterization.....	113
5.2.2	Solid-state NMR measurements	115
5.2.3	Spectral simulations	116
5.3	Results and discussion	117
5.4	Conclusions.....	136
5.5	References.....	137

Chapter 6.....	141
6 Probing the behavior of CO ₂ adsorbed in an ultramicroporous MOF under humid conditions using multinuclear solid-state NMR spectroscopy.....	141
6.1 Introduction.....	141
6.2 Experimental details.....	144
6.2.1 Sample preparation and characterization.....	144
6.2.2 Solid-state NMR.....	145
6.2.3 Spectral simulations.....	146
6.3 Results and discussion.....	146
6.4 Conclusions.....	171
6.5 References.....	172
Chapter 7.....	178
7 Summary, perspectives, and future work.....	178
7.1 Summary.....	178
7.2 Perspectives.....	180
7.3 Future work.....	181
Appendices.....	183
Copyright permissions.....	183
Appendix A3.....	192
Appendix A4.....	205
Appendix A5.....	211
Appendix A6.....	226

List of Tables

Table 3.1. Experimental ^{17}O NMR parameters, Calculated ^a δ_{iso} values, and peak assignments of $\alpha\text{-Mg}_3(\text{HCOO})_6$ ^b	72
Table 4.1. Refined experimental ^{17}O NMR parameters of three MIL-53(Al) phases.	101
Table 5.1. Experimental ^{17}O NMR parameters and peak assignments of MIL-121-as and MIL-121-ac.	125
Table 5.2. Refined ^{17}O EFG and CSA parameters of the MIL-121-as and MIL-121-ac.....	128
Table 5.3. Comparison between the experimental ^{17}O NMR parameters upon activation of MIL-121-as at 19.6 T.....	130
Table 5.4. Difference in the intensities in the oxygen signals upon metal-exchange.	134
Table 6.1. Experimental ^{13}C CSA parameters of $^{13}\text{CO}_2$ adsorbed within ZnAtzOx at 0.5 equivalent loading (or 5 atm). Parameters were obtained from analytical simulations of static ^{13}C SSNMR spectra.	149
Table 6.2. Experimental ^{13}C CSA parameters of $^{13}\text{CO}_2$ adsorbed within ZnAtzOx at 0.2 (2 atm) and 0.1 equivalent (1.5 atm) loading in Site 1. Parameters were obtained from analytical simulations of static ^{13}C SSNMR spectra. Site 2 was simulated using a gaussian curve with $\delta_{\text{iso}} = 150$ ppm and FWHM 100 ppm.....	151
Table 6.3. Librational angles (γ) of the water molecules loaded in ZnAtzOx at different levels.	162

List of Figures

Figure 1.1. Schematic representation of the assembly of MOFs and examples of SBUs and organic linkers.....	1
Figure 1.2. (left) The number of published papers on MOFs. Search was carried out on Scopus using the terms "metal-organic framework", "MOF", "porous coordination polymer", and "PCP". (right) The number of new MOF structures reported in the Cambridge Structural Database.....	2
Figure 1.3. Illustration of the two main approaches utilized in the design and synthesis of MOFs.	3
Figure 1.4. Deconstruction of the MOF-5 framework into the underlying 6-connected pcu topology. Caption: Zn, blue; O, red; C, grey. Adapted from reference 16 with permission. ...	4
Figure 1.5. a) Representation of the 12-connected Zr SBU and its shape; b) Representation of the UiO-66 fcu framework and its c) tetrahedral and octahedral cages. Adapted from references 35 and 37 with permission.....	5
Figure 1.6. Representation of the solvent exchange process in MOFs from high boiling point to low boiling point solvent followed by conventional thermal activation to remove solvent from MOFs by vacuum. Adapted from reference 43 with permission.	8
Figure 1.7. Representation of the structure of MOF-808 and the functionalization via post-synthetic modification using sulfuric acid. Adapted from reference 56 with permission.	10
Figure 1.8. ^1H - ^{13}C CP/MAS of the three phases of MIL-53 and their respective structures (11.7 T, spinning rate of 12.5 kHz). Adapted from reference 42 with permission.	14
Figure 1.9. Schematic illustration of the reaction vessel used in the dry gel conversion method.....	16
Figure 1.10. a) Simulated (red line) and experimental (black line) ^{13}C CSA powder patterns of ^{13}C -enriched CO_2 in $\text{Mg}_2(\text{DOBDC})$ at various temperatures. b) Illustration of CO_2 uniaxial	

rotation at the open Mg^{2+} site. Gray, red, and green spheres represent C, O, and Mg atoms, respectively. Adapted from reference 146 with permission.	19
Figure 1.11. Experimental and simulated 2H static spectra as a function of temperature of the 0.6 D_2O/Mg and D_2O/Zn samples. Figure adapted from reference 131 with permission.	22
Figure 2.1. Representation of the Zeeman interaction for a spin-1/2 nucleus.	37
Figure 2.2. Analytical simulations of theoretical ^{13}C CSA powder patterns depicting the effect of Ω and κ ($\delta_{iso} = 0$ ppm) at a magnetic field of 9.4 T. In a) the span is varied from 0 to 300 ppm while the δ_{iso} and skew are kept constant at 0 ppm and +1 respectively. In b) the skew is varied from +1 to -1 while δ_{iso} and span are kept constant at 0 and 300 ppm respectively. Spectra were simulated using the Dmfit software. ¹⁴	40
Figure 2.3. Representation of the nuclear charge distribution for spin-1/2 nuclei and quadrupolar nuclei (spin > 1/2).	42
Figure 2.4. a) Representation of the energy level diagram of a spin-3/2 nucleus, showing the perturbation of the first- and second-order quadrupolar interactions; b) Typical quadrupolar line-shape of a spin-3/2 nucleus showing the satellite and central transitions.	43
Figure 2.5. Illustration of the effects of a) the quadrupolar constant C_Q ($\delta_{iso} = 0$ ppm, $\eta_Q = 1$) and b) the asymmetry parameter η_Q ($\delta_{iso} = 0$ ppm, $C_Q = 8$ MHz) on the central transition of a spin-5/2 nuclei at 9.4 T. Spectra were simulated using the Dmfit software. ¹⁴	44
Figure 2.6. Illustration of the effects of the magnetic field on the central transition of a spin-5/2 nuclei with a C_Q of 8 MHz and η_Q of 0. Spectra were simulated using the Dmfit software. ¹⁴	45
Figure 2.7. Illustration of the 1-pulse NMR sequence.	46
Figure 2.8. Effect of MAS on a) ^{13}C at 9.4 T ($\delta_{iso} = 150$ ppm, $\Omega = 225$ ppm, and $\kappa = 1$); and b) ^{17}O at 9.4 T ($C_Q = 8$ MHz and $\eta_Q = 0$). Spectra were simulated using the Dmfit software. ¹⁴	47
Figure 2.9. Illustration of pulse sequence for cross-polarization from abundant spin I to dilute spin S with detection of the S magnetization.	48

Figure 2.10. Pulse sequence for ^1H - ^{13}C FSLG-HETCOR experiments.....	49
Figure 2.11. General REDOR pulse sequence. a) the control experiment providing the echo spectrum, S_0 , and b) the pulse sequence of the dephased spectrum S	50
Figure 2.12. a) Schematics of the basic two-pulse sequence used for 3QMAS experiments; b) ^{23}Na data in time domain obtained from 3QMAS of sodium oxalate; and c) ^{23}Na data in frequency domain obtained from 3QMAS of sodium oxalate. Adapted from reference 15 with permission.	51
Figure 2.13. ^{17}O 3QMAS NMR spectra of activated MIL-53 synthesized with pure Al (left), 50/50 Al/Ga (middle), and pure Ga (right). Adapted from reference 34 with permission.	52
Figure 2.14. Representation of the two polar angles θ and φ with respect to the external magnetic field B_0	53
Figure 2.15. Representation of the effect of a) the localized C_6 wobbling, b) the delocalized C_2 hopping, and the combined wobbling and hopping motions on the ^{13}C line-shape of CO_2 . d) Representation of the effect of the rate of motion on the ^{13}C CSA line-shape of CO_2 . The spectra were simulated with the Express ³⁵ software and using $\delta_{\text{iso}} = 125$ ppm, $\Omega = 335$ ppm, and $\kappa = 1$	55
Figure 2.16. a) Energy level diagram of ^2H ($I = 1$); b) illustration of the Pake doublet; c) simulations of the effect of different motion on the ^2H powder pattern; and d) the effect of the jump rate on the ^2H line-shape.....	56
Figure 3.1. (top, left to right) Representations of the framework of activated $\alpha\text{-Mg}_3(\text{HCOO})_6$, 12 framework oxygen sites, and 2 different oxygen bonding modes. Color coding: Mg, green; C, gray; H, white; O, red; $\mu_1\text{-O}$, orange; $\mu_2\text{-O}$, pink. (bottom) ^{17}O 1D MAS NMR spectra of ^{17}O -enriched $\alpha\text{-Mg}_3(\text{HCOO})_6$ at fields of 35.2 T (red) and 21.1 T (black) acquired at a spinning frequency of 18 kHz. The asterisk (*) denotes spinning sidebands (SSBs).....	68
Figure 3.2. ^{17}O 2D 3QMAS NMR spectra of ^{17}O -enriched $\alpha\text{-Mg}_3(\text{HCOO})_6$ at 35.2 T. Black dashed lines correspond to the slices examined. Blue and red solid lines denote experimental	

and simulated spectra, respectively. Asterisks (*) denote the SSBs. The 3QMAS spectra without markups are shown in Figure A3.8 for clarity. 71

Figure 3.3. Experimental and simulated ^{17}O 1D MAS NMR spectra of ^{17}O -enriched α - $\text{Mg}_3(\text{HCOO})_6$ at 35.2 T. The quadrupolar and CSA effects are both considered in these simulations, using the parameters shown in Table A3.3. In each phase, the signal intensity of each individual oxygen in the μ_1 -O sites is approximately equal, and the same is true for signals arising from the μ_2 -O sites. Asterisks (*) denote SSBs. 75

Figure 3.4. Schematic illustrations of DMF guest molecules within the zigzag channels of as-made α - $\text{Mg}_3(\text{HCOO})_6$. Only the Mg nodes are shown for clarity in the bottom diagram. The top inset shows a DMF molecule and two adjacent formate anions. The distances given were extracted from the DFT-optimized structures. Color coding: Mg, turquoise; N, blue; C, gray; H, white; O1S of DMF, red; μ_1 -O, orange; μ_2 -O, pink. 77

Figure 3.5. ^{17}O 1D MAS NMR spectra of ^{17}O -enriched fully (sample A) and partially activated (sample B) MIL-53(Al) samples at 35.2 T. The blue and red solid lines denote experimental and simulated spectra, respectively. Only the carboxylate oxygen regions are shown for clarity. The full spectra are shown in Figure A3.10. Asterisks (*) and dollar signs (\$) denote the SSBs of $-\text{COO}^-$ and μ_2 -OH, respectively. The structures of as-made and activated MIL-53(Al) phases are shown at the top. (b) ^{17}O 2D 3QMAS NMR spectrum of partially activated (sample B) ^{17}O -enriched MIL-53(Al) at 35.2 T. Black dashed lines correspond to the slices examined for analyses. 79

Figure 4.1. Schematic illustrations of the transformation between three MIL-53(Al) phases. Color coding: Al, green; O, red; C, grey; H_2BDC , turquoise. The hydrogen atoms are omitted for clarity. 90

Figure 4.2. Left: The inequivalent $-\text{COO}^-$ oxygen sites in different phases. Color coding: O, red; C, grey; H, blue. Right: ^{17}O 1D MAS NMR spectra of ^{17}O -enriched MIL-53(Al) samples at 35.2 T (red) and 21.1 T (black). MIL-53(Al)-as: the top two spectra; MIL-53(Al)-lp: the middle spectrum; MIL-53(Al)-np: the bottom two spectra. The asterisk (*) denotes spinning sidebands (SSBs). Note: the numbers of transients accumulated for each spectrum at 35.2 T

were only 1/4 and 1/8 of those at 21.1 T for MIL-53(Al)-as and MIL-53(Al)-np, respectively. The sample volume (~36 μL) at 35.2 T was less than half of that (~80 μL) at 21.1 T. 96

Figure 4.3. (a) ^{17}O 2D 3QMAS NMR spectra of ^{17}O -enriched MIL-53(Al)-as and MIL-53(Al)-np at 35.2 T. Blue and red solid lines denote experimental and simulated spectra, respectively. Only the regions corresponding to $-\text{COO}^-$ oxygen sites are shown. The total experimental times are 1.3 and 3.4 h for MIL-53(Al)-as and MIL-53(Al)-np, respectively. (b) Experimental and simulated ^{17}O 1D MAS NMR spectra of three MIL-53(Al) phases at 35.2 T. Both the quadrupolar and CSA effects are considered in simulation by using the parameters shown in Table 4.1. Asterisks (*) denote SSBs. The two oxygen species in MIL-53(Al) were shown on the top. 98

Figure 4.4. ^{17}O 1D experimental (black) and simulated (red) MAS NMR spectra of ^{17}O -enriched MIL-53(Al) samples at 35.2 T. blue dashed lines denote the isotropic chemical shift δ_{iso} . Only the regions corresponding to $\mu_2\text{-OH}$ oxygen sites are shown for clarity. Asterisks (*) denote SSBs. 103

Figure 5.1. a) Building blocks describing the structure of MIL-121; b) The structure of MIL-121-as contains unreacted pyromellitic acid ligands inside of the pores, which are then removed by activation. 111

Figure 5.2. Crystallographically non-equivalent oxygen atoms in the crystal structure of MIL-121-as and MIL-121-ac. 118

Figure 5.3. ^{17}O 1D MAS SSNMR spectra of MIL-121-as and MIL-121-ac acquired at 19.6 T and 35.2 T with spinning rate of 16 and 18 kHz, respectively. The spinning sidebands are labelled as * 120

Figure 5.4. $^{17}\text{O}\{^1\text{H}\}$ REDOR spectra of a) MIL-121-as and b) MIL-121-ac acquired at 19.6 T with a spinning frequency of 16 kHz. S_0 , ^{17}O spin-echo; S, REDOR experiment with a dephasing time of 0.062 ms; ΔS , REDOR difference. 121

Figure 5.5. a) Representation of the different hydrogen species in the MIL-121-ac; b) $^1\text{H}\text{-}^{17}\text{O}$ HETCOR spectrum of MIL-121-ac acquired at 19.6 T with a spinning frequency of 16 kHz; d) slices of the ^{17}O dimension at the ^1H signals. The label # denotes the signal of adsorbed

water inside of the pores. Water can be adsorbed during the packing of the sample into the rotor prior to the NMR measurements.	123
Figure 5.6. ^{17}O 2D 3QMAS NMR spectra of MIL-121-as and MIL-121-ac acquired at 19.6 T with a spinning rate of 16 kHz. The spinning sidebands are denoted as asterisks.	124
Figure 5.7. Experimental and simulated ^{17}O 1D MAS spectra of MIL-121-ac and MIL-121-as acquired at 19.2 T and 35.2 T with spinning rate of 16 and 18 kHz, respectively. Spinning sidebands are denoted by asterisk.	129
Figure 5.8. a) Representation of the main hydrogen bonding interactions taking place in the crystal structure of the MIL-121-as. b) Hydrogen bonding.	130
Figure 5.9. Representation of possible intramolecular hydrogen bonding before and after activating MIL-121.	131
Figure 5.10. Experimental ^{17}O 1D MAS spectra of MIL-121-ac and $\text{Na}^+/\text{Ag}^+@$ MIL-121 acquired at different magnetic fields with spinning rate of 16 kHz (19.6 T) and 18 kHz (35.2T). Spinning sidebands are denoted by asterisk.	133
Figure 5.11. Representation of possible interactions between the loaded metal cations and the MOF framework.	135
Figure 6.1. a) Asymmetric unit of the crystal structure of ZnAtzOx-as; b) ZnAtz layers pillared by oxalate ligands; c) coordination environment of Zn metal centers; d) cross-sections of the channels in ZnAtzOx. CCDC 1428296.	142
Figure 6.2. Experimental and simulated VT static ^{13}C NMR spectra of $^{13}\text{CO}_2$ -loaded ZnAtzOx at selected temperatures and gas loadings.	148
Figure 6.3. a) Experimental and simulated static ^{13}C SSNMR spectra of ZnAtzOx-as and ZnAtzOx-ac; b) ^1H - ^{13}C CP MAS spectra of ZnAtzOx loaded with different loadings of CO_2 (spinning rate of 10 kHz and contact time of 8 ms); c) Zoomed in region of adsorbed CO_2 ; and d) ^1H - ^{13}C CP MAS spectra of ZnAtzOx loaded 0.5 equivalent of CO_2 acquired with a spinning rate of 10 kHz and different contact times; e) Asymmetric unit of ZnAtzOx.	153

Figure 6.4. Representation of the a) wobbling, b) hopping and c) combined wobbling and hopping motions of a CO₂ molecule. The motions are described by the angles α and β respectively. Wobbling motions are modelled by a six-fold rotation, while hopping motions are modelled by a two-fold rotation..... 154

Figure 6.5. a) ¹H MAS spectra of ZnAtzOx-as and ZnAtzOx-ac acquired at 9.4 T with a spinning rate of 10 kHz; b) F2 cross-sections; c) F1 cross-sections; d) HETCOR Spectrum of ZnAtzOx loaded with 0.5 equivalent of CO₂. Spectra were acquired with spinning rate of 8 kHz and contact time of 8 ms. 156

Figure 6.6. Representation of CO₂ sites in ZnAtzOx. a) model of low CO₂ loading viewed from a-axis; b) model of low CO₂ loading viewed from b-axis; c) model of high CO₂ loading viewed from a-axis; d) model of high CO₂ loading viewed from b-axis..... 158

Figure 6.7. Experimental and simulated ²H static VT NMR spectra of D₂O-loaded ZnAtzOx at selected temperatures and loading. Static pattern of solid D₂O was simulated using C_Q = 225 kHz and $\eta_Q = 0$.^{24,25} R.T. stands for room temperature..... 160

Figure 6.8. a) ²H MAS spectra of ZnAtzOx loaded with 4 and 8% D₂O acquired at 21.1 T with a spinning rate of 30 kHz; b) Experimental and simulated ²H static VT NMR spectra of D₂O-loaded ZnAtzOx. 164

Figure 6.9. a) Experimental and simulated ⁶⁷Zn static spectra of activated and D₂O-loaded (8%) ZnAtzOx; b) Illustration of the coordination environment around the zinc centers in the crystal structure of ZnAtzOx. 166

Figure 6.10. Representation of the π -flips and librational motion of D₂O groups inside of the framework of ZnAtzOx for two crystallographic non-equivalent water sites. 167

Figure 6.11. Experimental and simulated static ¹³C NMR spectra of ZnAtzOx loaded with different concentrations of ¹³CO₂ and D₂O at 298 K..... 169

Figure 6.12. Representation of behavior of CO₂ and water inside of the pores of ZnAtzOx. 170

List of Abbreviations

3QMAS	Triple-quantum magic-angle spinning
BTC	1,3,5-benzenetricarboxylate
BTEC	Benzenetetracarboxylate
CSA	Chemical shift anisotropy
CP	Cross-polarization
DFT	Density functional theory
DMF	Dimethylformamide
DNP	Dynamic nuclear polarization
DOBDC	2,5-dioxo-1,4-benzenedicarboxylate
DUT	Dresden University of Technology
EFG	Electric field gradient
GIPAW	Gauge-including projector augmented wave
HKUST	Hong Kong University of Science and Technology
MAS	Magic-angle spinning
MD	Molecular dynamics
MIP	Materials of the Institute of Porous Materials of Paris
NHMFL	National High Magnetic Field Laboratory
OMS	Open metal site
PBE	Perdew, Burke, and Ernzerhof
SCH	Series-connected hybrid
SSNMR	Solid-state NMR spectroscopy
TGA	Thermogravimetric analyses
VASP	Vienna Ab initio simulation package
VT	Variable-temperature

List of Appendices

- Figure A3.1. Experimental (Exp) and simulated (Sim) PXRD patterns of α -Mg₃(HCO₂)₆. The ~ symbol denotes an intense reflection truncated for clarity. The simulated patterns were calculated based on the reported single crystal XRD structures. 192
- Figure A3.2. Le Bail refinement of unit cell parameters for the as-made (top) and the activated (bottom) α -Mg₃(HCOO)₆. 193
- Figure A3.3. TGA profiles for the as-made and activated α -Mg₃(HCOO)₆. 194
- Figure A3.4. ¹³C CP MAS NMR spectra of the as-made and activated α -Mg₃(HCOO)₆. The “DMF” label highlights resonances arising from guest DMF molecules, while the asterisk (*) denotes spinning sidebands (SSBs). 195
- Figure A3.5. Schematic illustration of the reaction vessel used in the dry gel conversion method. 196
- Figure A3.6. Experimental (Exp) and simulated (Sim) PXRD patterns of ¹⁷O-enriched MIL-53(Al). The simulated patterns were calculated based on the reported PXRD structures.⁵ The asterisk denotes a very small amount of the H₂O-adsorbed MIL-53(Al) phase. 197
- Figure A3.7. Experimental and simulated ¹⁷O 1D MAS NMR spectra of ¹⁷O-enriched as-made α -Mg₃(HCOO)₆ at 21.1 T, acquired at a spinning frequency of 18 kHz. Only the quadrupolar interaction is considered in the simulations. The asterisk (*) denotes SSBs. .. 198
- Figure A3.8. ¹⁷O 2D 3QMAS NMR spectra of ¹⁷O-enriched α -Mg₃(HCOO)₆ at 35.2 T without the markups present in Figure 3.2 of the main text. The asterisk (*) denotes spinning sidebands (SSBs). 198
- Figure A3.9. Experimental and simulated ¹⁷O 1D MAS NMR spectra of ¹⁷O-enriched α -Mg₃(HCOO)₆ at 35.2 T acquired at a spinning frequency of 18 kHz. The spectra were simulated by considering only the quadrupolar effect. The asterisk (*) denotes SSBs. Note: the intensities of the spinning sidebands in simulated spectra are very weak if only the quadrupolar interaction is considered. 199

Figure A3.10. The ^{17}O 1D MAS NMR spectra of (A) fully- and (B) partially-activated ^{17}O -enriched MIL-53(Al) at 35.2 T. The asterisk (*) denotes SSBs.	200
Table A3.1. Comparison between unit cell parameters of $\alpha\text{-Mg}_3(\text{HCOO})_6$ determined in this work and those previously reported.	201
Table A3.2. Calculated ^{17}O NMR parameters of $\alpha\text{-Mg}_3(\text{HCOO})_6$	202
Table A3.3. ^{17}O NMR parameters used in the simulation of 1D ^{17}O MAS spectra of ^{17}O -enriched $\alpha\text{-Mg}_3(\text{HCOO})_6$	203
Table A3.4. Experimental ^{17}O NMR parameters and tentative resonance assignments of carboxylate oxygen sites in two different MIL-53(Al) samples.	204
Figure A4.1. Illustration of the reaction vessel for the dry gel conversion method.	205
Figure A4.2. Powder XRD patterns of the MIL-53(Al)-as and MIL-53(Al)-np.	205
Figure A4.3. ^{17}O 2D 3QMAS NMR spectrum of ^{17}O -enriched MIL-53(Al)-as at 21.1 T. Only the regions corresponding to $-\text{COO}^-$ oxygen sites are shown for clarity.	206
Figure A4.4. Experimental and simulated ^{17}O 1D MAS NMR spectra of three ^{17}O -enriched MIL-53(Al) phases at 35.2 T. Only the quadrupolar effects are considered in simulation by using the parameters shown in Table 4.1. The asterisk (*) denotes SSBs. The satellite transitions were also observed in the spectrum of MIL-53(Al)-lp due to the use of a one-pulse sequence with a hard 90° excitation pulse.	207
Figure A4.5. Experimental and simulated ^{17}O 1D MAS NMR spectrum of ^{17}O -enriched MIL-53(Al)-lp in isotropic region at 35.2 T. Only the quadrupolar effect is considered in simulation and no line broadening is applied. The regions of two oxygen sites are expanded to compare the linewidth. The simulations were constructed using calculated C_Q and η_Q values with experimentally determined δ_{iso} values. Note the striking similarity in resonance widths between experimental and DFT-calculated spectra, suggesting that the main source of experimental resonance broadening in isotropic region is the second-order quadrupolar interaction.	208

Table A4.1. Additional details for ^{17}O 1D MAS NMR experiments.	209
Table A4.2. Additional details for ^{17}O 3QMAS NMR experiments.	209
Table A4.3. Experimental ^{17}O NMR parameters, calculated ^a δ_{iso} values, and assignments of $-\text{COO}^-$ oxygen sites for MIL-53(Al)-as and MIL-53(Al)-np.	209
Table A4.4. Calculated ^{17}O NMR parameters of three MIL-53(Al) phases.	210
Table A5.1. ^{17}O -enrichment details of the MIL-121 materials ^a	211
Table A5.2. Additional details for ^{17}O 1D MAS experiments at 19.6 T.	211
Table A5.3. Additional details for ^1H 1D MAS experiments at 19.6 T.	212
Table A5.4. Additional details for ^{17}O 1D MAS experiments at 21.1 T.	212
Table A5.5. Additional details for ^{17}O 1D MAS experiments at 35.2 T.	212
Table A5.6. Additional details for ^{17}O 3QMAS experiments at 19.6 T.	212
Table A5.7. Additional details for ^{17}O 3QMAS experiments at 19.6 T.	213
Table A5.8. Additional details for ^{17}O 3QMAS experiments at 35.2 T.	213
Table A5.9. Experimental ^{17}O EFG of MIL-121-as and MIL-121-ac obtained from 3QMAS spectra acquired at 19.6 T. ^a Obtained from simulation of F1 cross-sections of 3QMAS. ...	214
Table A5.10. ^{17}O EFG and CSA parameters of MIL-121-as and MIL-121-ac used as input for refinement of spectral parameters.	215
Table A5.11. ^{17}O EFG parameters of Na@MIL-121 and Ag@MIL-121.	216
Table A5.12. Metal exchange percentage of the metal-loaded MIL-121 samples.	216
Figure A5.1. Powder X-ray diffraction pattern of MIL-121 samples synthesized with varied amounts of water. Cu-K α ($\lambda = 1.541 \text{ \AA}$). The water volume was varied from 10 mL (original method) to 2 mL, while keeping the volume of 4.0 M HNO $_3$ at a 10/1.6 (H $_2$ O/HNO $_3$ v/v).241	

Figure A5.2. Thermogravimetric weight loss profiles for MIL-121 samples. As-made sample shows a constant weight loss rate up to around 300 °C.	217
Figure A5.3. Powder X-ray diffraction pattern of ¹⁷ O-labelled MIL-121 samples. Cu-Kα (λ = 1.540 Å).	218
Figure A5.4. ¹ H MAS SSNMR spectra of MIL-121 samples acquired at 19.5 T using a spinning speed of 16.0 kHz. The * label denotes spinning sidebands. The # label denotes adsorbed water within the pores. The \$ label denotes water adsorbed on the surface of the sample. Adsorption of water might occur during the packing of samples in the rotor.	119
Figure A5.5. ¹⁷ O 3QMAS spectrum of MIL-121-as acquired at 35.2 T using a spinning speed of 16.0 kHz. The * label denotes spinning sidebands.	220
Figure A5.6. Representation of the main hydrogen bonding interactions taking place in the crystal structure of the MIL-121-as.	220
Figure A5.7. ¹⁷ O parameters for a) MIL-121-as and b) MIL-121-ac at different magnetic fields. Blue lines represent experimental and red lines represent simulated.	221
Figure A5.8. Experimental and simulated ¹⁷ O 1D MAS spectra of metal-loaded acquired at 19.2 T with spinning rate of 16 kHz and at 35.2 and spinning rate of 18 kHz. Spinning sidebands are denoted by asterisk.	222
Figure A5.9. ¹⁷ O 3QMAS spectra of Ag@MIL-121 and In@MIL-121 acquired at 19.6 T with a spinning rate of 16 kHz.	223
Figure A5.10. ¹⁷ O 3QMAS spectra of Na@MIL-121 and Ca@MIL-121 acquired at 19.6 T with a spinning rate of 16 kHz.	224
Figure A6.1. Powder XRD diffractograms of ZnAtzOx samples.	224
Figure A6.2. CO ₂ adsorption isotherm of ZnAtzOx measured at 77 K.	226
Figure A6.3. Experimental and simulated VT static ¹³ C NMR spectra of ZnAtzOx loaded with 0.1, and 0.2 equivalent of ¹³ CO ₂	227

Figure A6.4 Experimental and simulated VT static ^{13}C NMR spectra of ZnAtzOx loaded with 0.5 equivalent $^{13}\text{CO}_2$.	228
Figure A6.5. a) ^1H MAS spectra of ZnAtzOx-ac and ^2H -exchanged ZnAtzOx-ac (spinning rate of 8 kHz); b) Experimental and simulated ^2H static VT spectra of ^2H -exchanged ZnAtzOx-ac.	229
Figure A6.6. Experimental and simulated VT static ^2H NMR spectra of ZnAtzOx loaded with 2% D_2O .	230
Figure A6.7. Experimental and simulated VT static ^2H NMR spectra of ZnAtzOx loaded with 4% D_2O .	231
Figure A6.8. Experimental and simulated VT static ^2H NMR spectra of ZnAtzOx loaded with 8% D_2O .	232
Figure A6.9. Experimental ^{67}Zn static spectra of ZnAtzOx samples.	233
Figure A6.10. Experimental and simulated VT static ^{13}C NMR spectra of ZnAtzOx loaded with 0.2 equivalent $^{13}\text{CO}_2$ and different amount of D_2O .	234
Figure A6.11. Experimental and simulated VT static ^{13}C NMR spectra of ZnAtzOx loaded with 0.2 equivalent $^{13}\text{CO}_2$ and different amount of D_2O .	235
Figure A6.12. Experimental and simulated VT static ^2H NMR spectra of ZnAtzOx co-loaded with 4% D_2O and 0.2 equivalent of CO_2 .	236
Figure A6.13. Experimental and simulated VT static ^2H NMR spectra of ZnAtzOx co-loaded with 4% D_2O and 0.2 equivalent of CO_2 .	237
Figure A6.14. Experimental and simulated VT static ^2H NMR spectra of ZnAtzOx co-loaded with 8% D_2O and 0.2 equivalent of CO_2 .	239
Table A6.1. Bond lengths around the Zn metal centers.	239
Table A6.2. Bond angles around the Zn metal centers.	239

Table A6.3. Details of guest loading in the ZnAtzOx. The molecular formula of ZnAtzOx is $Zn_2C_6H_6N_8O_4$, and the molecular weight is 384.9 g mol^{-1} . Moles of CO_2 were estimated by considering the ideal gas law. Density of D_2O is 1.107 g mL^{-1} . ^a The maximum CO_2 is the maximum theoretical CO_2 capacity based on the mass of the ZnAtzOx samples.	240
Table A6.4. Experimental 2H quadrupolar parameters of signal from D_2O adsorbed within ZnAtzOx at a loading level of 2%.	241
Table A6.5. Experimental 2H quadrupolar parameters of signal from D_2O adsorbed within ZnAtzOx at a loading level of 4%.	242
Table A6.6. Experimental 2H quadrupolar parameters of signal from D_2O adsorbed within ZnAtzOx at a loading level of 8%.	243
Table A6.7. Experimental ^{13}C CSA parameters of ZnAtzOx loaded with 0.2 equivalent of $^{13}CO_2$ and 4% D_2O	244
Table A6.8. Experimental ^{13}C CSA parameters of ZnAtzOx loaded with 0.2 equivalent of $^{13}CO_2$ and 8% D_2O	244
Table A6.9. Experimental ^{13}C CSA parameters of ZnAtzOx loaded with 0.5 equivalent of $^{13}CO_2$ and 4% D_2O	245
Table A6.10. Experimental ^{13}C CSA parameters of ZnAtzOx loaded with 0.5 equivalent of $^{13}CO_2$ and 8% D_2O	246

Chapter 1

1 Metal-organic frameworks

Metal-organic frameworks (MOFs), or porous coordination polymers (PCPs), are a class of porous hybrid materials comprised of multitopic organic ligands and inorganic units such as, metal ions or clusters, that are assembled into porous three-dimensional coordination networks (Figure 1.1). The organic polytopic linkers are usually carboxylates and azolates due to their tailorable geometry and topicity. The inorganic units are predominantly metal-oxo clusters (also called secondary building units, SBUs) with pendant carboxylate-terminated capping ligands.¹

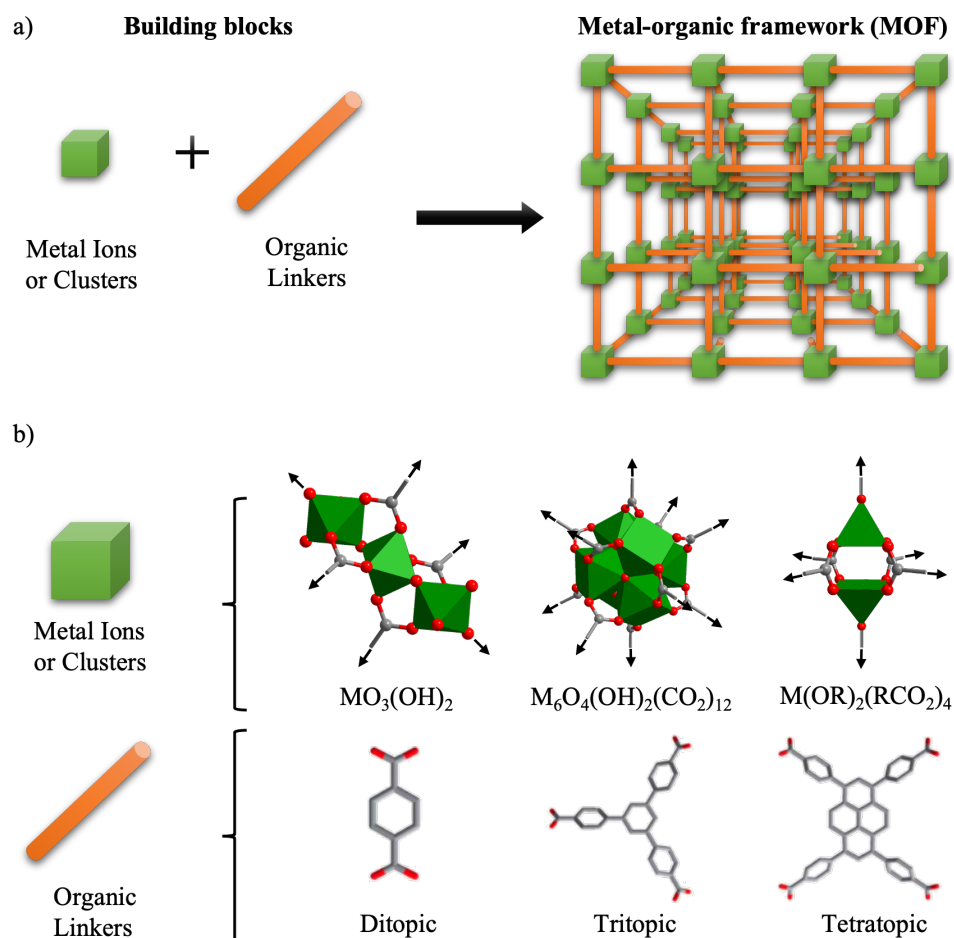


Figure 1.1. Schematic representation of the assembly of MOFs and examples of SBUs and organic linkers.

One of the hallmarks of MOFs is their tunable nature that allows for the designing of targeted structures with specific properties and functions. Because of that, MOFs are known for their extraordinarily high surface area, tunable pore size, and adjustable internal surface properties.² Ultimately, MOFs have been found to be promising candidates in several applications including heterogeneous catalysis,^{3,4} water harvesting⁵⁻⁸ and purification,^{9,10} and gas storage and separation,¹¹⁻¹⁴ among many other applications.¹⁵ Unsurprisingly, MOFs have seen an exponential growth as exemplified by Figure 1.2. In the last year, for example, the number of new MOF structures has reached about 8000. This shows the importance of characterizing MOFs.

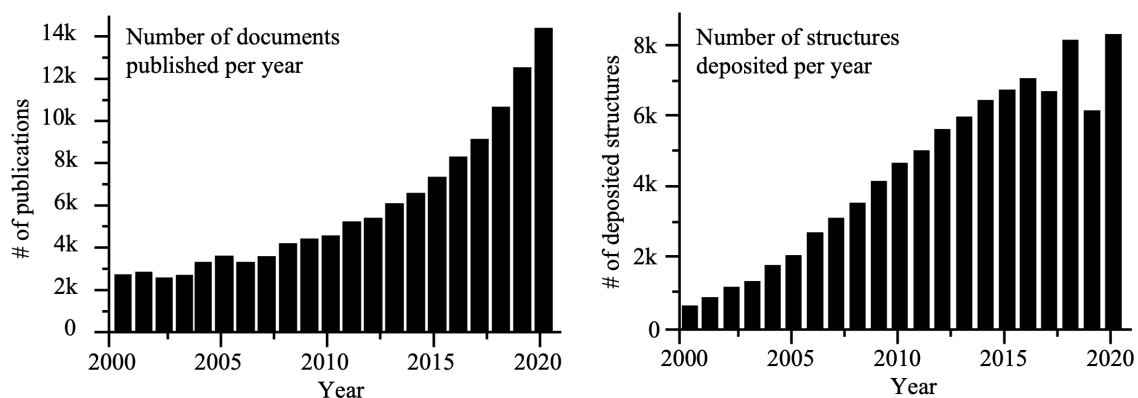


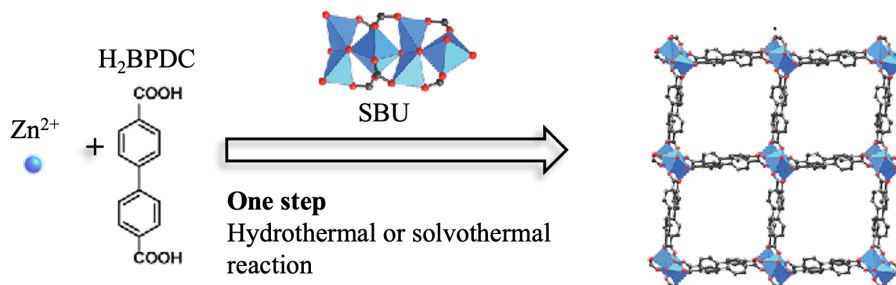
Figure 1.2. (left) The number of published papers on MOFs. Search was carried out on Scopus using the terms "metal-organic framework", "MOF", "porous coordination polymer", and "PCP". (right) The number of new MOF structures reported in the Cambridge Structural Database.

1.1 The reticular chemistry and rational design of MOFs

Throughout the maturation of the MOF field, several synthetic approaches to designing MOF structures have been developed. One approach is the reticular synthesis pioneered by Yaghi and coworkers.¹⁶⁻²¹ In essence, reticular synthesis can be described as the

process of assembling rigid molecular building blocks through strong bonding into predetermined networks (Figure 1.3).

Reticular chemistry approach



Two-step crystal engineering approach

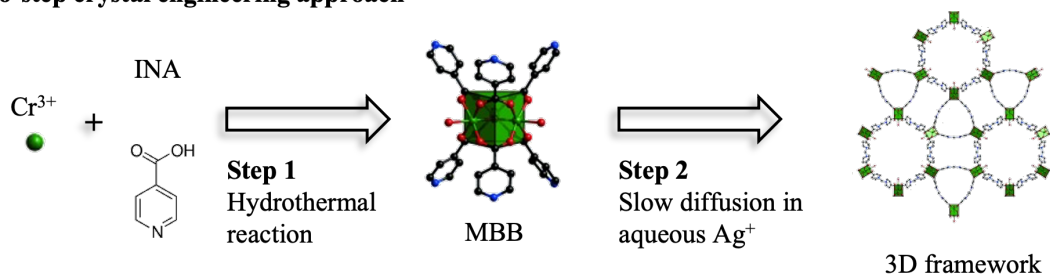


Figure 1.3. Illustration of the two main approaches utilized in the design and synthesis of MOFs.

Another example is the two-step crystal engineering approach introduced by Zaworotko and coworkers, which relies first on the preparation of molecular building blocks (MBBs) such as metal–oxo clusters with well-defined geometries. These MBBs are then connected together in a two-step synthetic process (Figure 1.3).^{22–25}

Typically, the design of MOFs using reticular synthesis involves the targeting of a specific network or topology tailored for a chosen application. In this sense, the structure of MOFs can be regarded as three-dimensional nets in which the SBUs and linkers represent the vertices and edges of the net (Figure 1.4).^{16–20,26} The topology of the

framework is described by three bold letters, which are abbreviations of the names of structures with the same connectivity (**dia** for diamond; **qtz** for quartz; **sod** for sodalite).^{27–29} For example, the well-known MOF-5 synthesized by combining the ditopic 1,4-benzenedicarboxylate (BDC) ligand and zinc (II) nitrate displays a 6-connected primitive cubic (**pcu**) net.

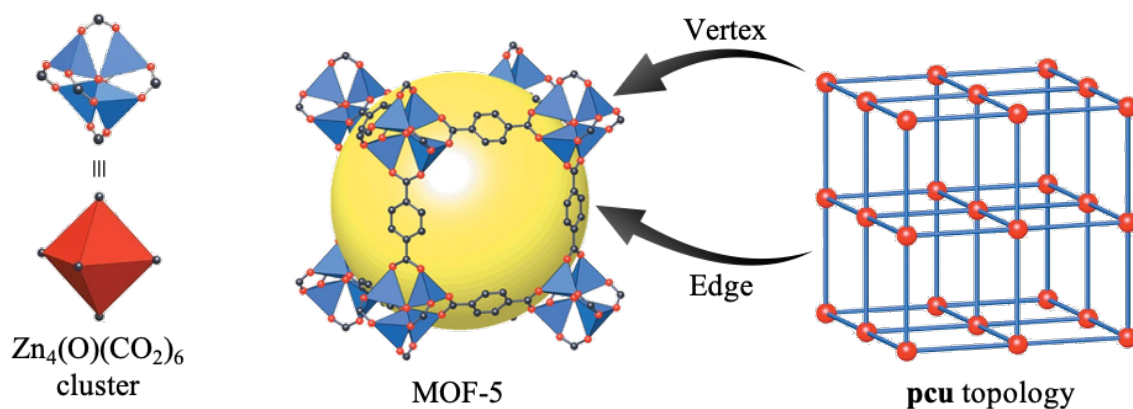


Figure 1.4. Deconstruction of the MOF-5 framework into the underlying 6-connected **pcu** topology. Caption: Zn, blue; O, red; C, grey. Adapted from reference 16 with permission.

The coordination of the carboxylate groups of the BDC ligands forms $\text{Zn}_4(\text{O})(\text{CO}_2)_6$ clusters with octahedral geometry, which are joined together by benzene linkers to form the **pcu** net.^{16,30} In this case, the $\text{Zn}_4(\text{O})(\text{CO}_2)_6$ clusters are regarded as the vertices and the benzene links, as the edges (Figure 1.4).

The reticular chemistry allows for the fine tuning of pore size and geometry via isorecticular contraction or expansion. One could employ building blocks with the same geometry but varying the length to fine-tune the size of the pores. Furthermore, the pore chemistry can be manipulated by using building blocks with the same geometry but with functional groups appended. An example of isorecticular pore functionalization and expansion can be illustrated by the UiO-66 MOF family. UiO stands for University of

Oslo, where it was first synthesized in 2008 by Lillerud and collaborators.³¹ The UiO-66 framework is comprised of 12-connected cuboctahedra $[\text{Zr}_6(\mu^3\text{-O})_4(\mu^3\text{-OH})_4(\text{CO}_2)_{12}]$ clusters (Figure 1.5a), which are extended by linking of the linear BDC ligands into a face-centered **fcu** network (Figure 1.5b). The structure of UiO-66 contains tetrahedral and octahedral microporous cages with dimensions of 7.5 to 12 Å (Figure 1.5c). The BET surface area was measured to be 1525 m² g⁻¹ and the CO₂ uptake to be 1.70 mmol g⁻¹.^{11,31}

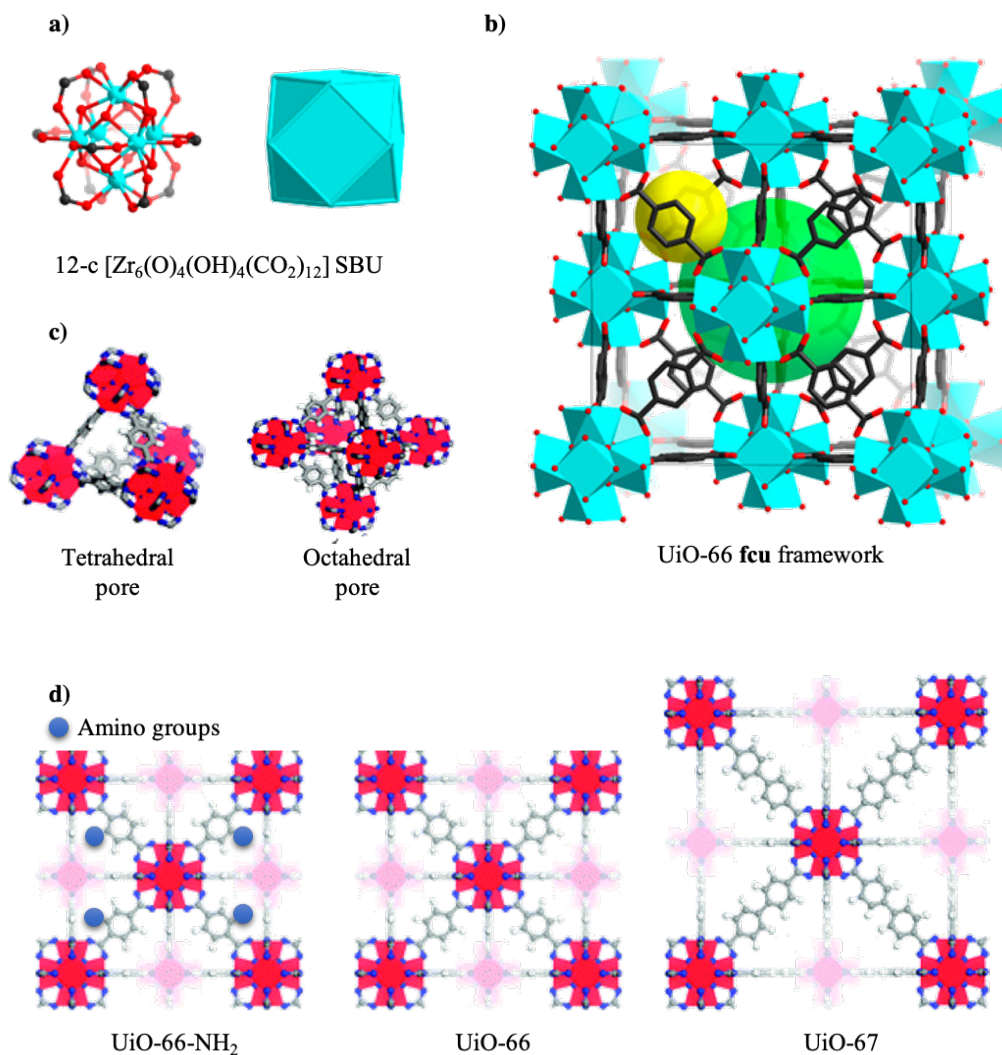


Figure 1.5. a) Representation of the 12-connected Zr SBU and its shape; b) Representation of the UiO-66 fcu framework and its c) tetrahedral and octahedral cages.

Adapted from references 35 and 37 with permission.

By replacing the BDC ligand with 2-aminobenzenedicarboxylic acid (BDC-NH₂), it was found that despite the BET surface area and pore volume have decreased, the CO₂ adsorption capacity of UiO-66-NH₂ (Figure 1.5) was increased by 64%. In addition, the isosteric heat of adsorption of CO₂ was increased by 47% with the presence of amino groups. This was attributed to the strong interaction between the NH₂ groups and CO₂ molecules. Therefore, by functionalizing the pore surface of the UiO-66 framework with amino groups through isoreticular chemistry, it was possible to fine-tune the CO₂ adsorption capacity of the material.^{32–34}

The expansion of the UiO-66 framework was successfully accomplished by replacing the BDC linker with 4,4' biphenyl-dicarboxylate (BPDC).³¹ The longer linker increased the size of the tetrahedral and octahedral cages in the isoreticular UiO-67 to 12 and 16 Å, respectively (Figure 1.5). As expected, UiO-67 displayed a larger BET surface area than that of UiO-66. H₂ adsorption studies have shown that the increase of the surface area greatly enhances the H₂ uptake capacity of the material. The H₂ uptake at 38 bar and 77 K increased from 2.4 mass% for UiO-66 up to 4.6 mass% for UiO-67.³⁵

As seen by the examples above, the exceptional tunability of MOFs achieved by reticular chemistry allows for the design of materials with specific structural and chemical properties for target applications. Perhaps that is the reason why MOFs have attracted such enormous attention in the last decades.

1.2 Synthetic approaches of MOFs

The reticular synthesis approach has allowed the idealisation of MOF frameworks by combining the building blocks together. However, achieving the optimal conditions to crystallize the building units is oftentimes very challenging. This problem gets even worse when the main goal of MOF chemists is to obtain large single crystals for the complete structural characterization via XRD.³⁶ Usually, the first step in the synthesis of MOFs involves the mixing of well-soluble metal salts (such as metal nitrates, sulfates, or acetates) with the precursors of organic linkers, in a polar organic solvent, typically an amine (triethylamine) or amide (diethylformamide, dimethylformamide).

Then, the metal–organic structures are formed by self-assembly at temperatures ranging from room temperature up to 200 °C under solvothermal conditions for several hours or days.³⁷ Example of room temperature synthesis is the crystallization or slow evaporation of the solvent to yield single crystals of the MOFs, such as in the case of the synthesis of the well-known MOF-5, MOF-74, and ZIF-8.^{38,39}

The most common synthetic approach of MOFs, however, is the solvothermal reaction. Solvothermal reactions are carried out in closed vessels under autogenous pressure above that of the boiling point of the solvent. This method allows for the tuning of the reaction conditions, such as the rate of nucleation and crystal growth by adjusting the temperature and time of the reaction. Variation of the reaction temperature has a strong influence on the product formation and often yields more condensed structures at higher temperatures.³⁷

1.2.1 Activation of MOFs

The final key step in producing MOFs with permanent porosity involves the activation of the material by removing pore blocking ligands used during the synthesis from the framework such as solvent, modulators, and unreacted linker precursors. Often, surface areas and pore volumes observed experimentally are lower than those predicted by simulations. This is usually attributed to incomplete activation or framework collapse, which limits their applications.^{40,41} The activation process can be quite challenging because the removal of adsorbed molecules is associated with significant capillary forces, and thus, surface tension, which can lead to complete activation or partial collapse of frameworks.⁴⁰

The traditional strategy for activating MOFs is thermal activation. This process, also called calcination, involves the heating of the material under vacuum for a few hours. For example, the synthesis of MIL-53(Al) MOF under solvothermal conditions leads to unreacted BDC ligands occluded inside of the pores. These ligands can be successfully removed from the 1D rhombic-shaped channels of MIL-53(Al) by heating the sample at 330 °C for three days, leading to a surface area of 1140 m²g⁻¹.⁴² It was later shown that a higher BET surface area of 1203 m²g⁻¹ could be achieved by calcinating the sample at

400 °C.⁴¹ The high energy costs and long timescales make calcination an undesirable technique for the activation of MOFs.⁴¹ One alternative approach is to exchange the high-boiling molecules in the pores (such as solvents or unreacted ligands) for a lower boiling point solvent (such as methanol and acetone) followed by activation at lower temperatures. Solvents with low boiling points and/or low surface tension have lower capillary forces during MOF activation, limiting the chance of material decomposition.⁴³ An illustration of the solvent exchange followed by thermal evacuation is given in Figure 1.6.

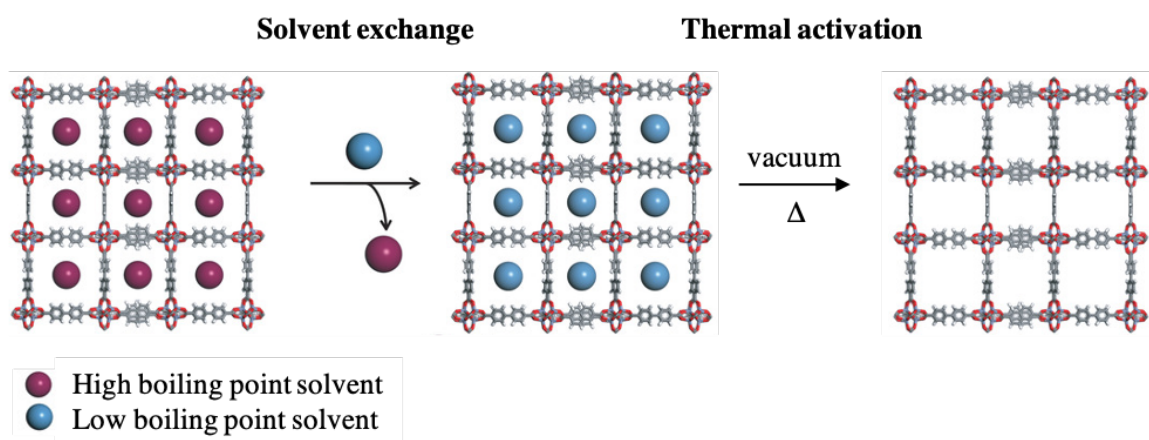


Figure 1.6. Representation of the solvent exchange process in MOFs from high boiling point to low boiling point solvent followed by conventional thermal activation to remove solvent from MOFs by vacuum. Adapted from reference 43 with permission.

Alongside efforts to avoid structural collapse of low-stability MOFs by solvent exchange, alternative approaches have been developed to activate MOFs. These approaches include supercritical CO₂ activation, freeze drying, and chemical treatment.^{40,41,44} More recent approaches include microwave-assisted activation,⁴⁵ which was first studied in MOFs in 2017, and photothermal activation process using UV-Vis light, which causes heat to be generated locally within the material and evaporates the solvent molecules.⁴⁶

1.2.2 Post-synthetic modification (PSM) of MOFs

Another approach for the synthesis and functionalization of MOFs is the post-synthetic modification (PSM). PSM has emerged as a powerful tool for introducing different functionalities into the MOF framework and to modify the physical and chemical environment of the pores and cavities within the frameworks. In this regard, PSM can be advantageous compared to the pre-functionalization approach because of the greater control over the functional groups that can be incorporated into the framework.^{47,48}

The two major PSM strategies for functionalizing involve (i) the covalent chemical modification of the linker component of the MOF, and (ii) the changes in the coordination environment of the SBUs without affecting the overall topology of the SBUs or the framework.^{49,50} Several pathways of PSM of MOFs have been developed such as metal exchange, ligand exchange and chemical functionalization, and guest incorporation.^{48,51}

An important example of PSM is the incorporation of metal cations in the pores of MIL-121 for sensing applications.⁵² MIL-121 is synthesized by combining 1,2,4,5-benzenetetracarboxylic acid (BTEC) with aluminum nitrate to form a three-dimensional framework with free, uncoordinated CO₂H groups protruding in the pores.⁵³ The uncoordinated CO₂H groups of MIL-121(Al) enabled the post-synthetic incorporation of Eu³⁺ cations with luminescent properties. The resulting Eu@MIL-121 material was used to detect Ag⁺, a heavy metal ion, in aqueous solutions and displayed high sensitivity and selectivity towards the ions. Another example of PSM is the sulfation of MOF-808 to produce a superacid MOF with enhanced catalytic properties of the material.⁴ MOF-808 is comprised of Zr₆O₄(OH)₄(CO₂)₆ SBUs connected to six 1,3,5-benzenetricarboxylate ligands (BTC) to form a 3D framework with **spn** topology containing tetrahedral and octahedral cages with internal pore diameters of 4.8 and 18.4 Å, respectively (Figure 1.7).⁵⁴ The SBUs also contained capping formate ligands, which can be replaced by other chemical groups. Indeed, upon sulfation carried out by submerging the samples in different concentrations of aqueous sulfuric acid solutions, these formate ligands are replaced by sulfate groups leading to the functionalized MOF-808. The inclusion the SO₄ groups led to catalytically active MOFs for various acid-catalyzed reactions including

Friedel–Crafts acylation, esterification, and isomerization. The PSM of MOFs provides another pathway for the functionalization of MOFs and can therefore be used for improving specific structural characteristics of MOFs for several applications, including catalysis and gas adsorption.

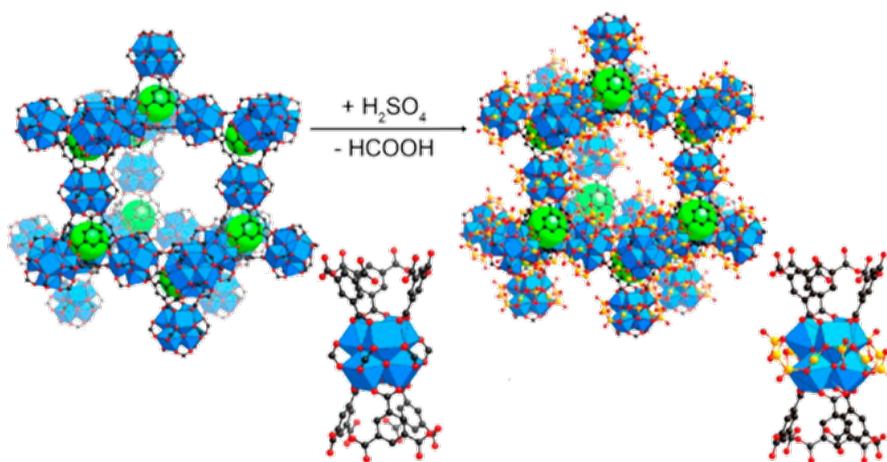


Figure 1.7. Representation of the structure of MOF-808 and the functionalization via post-synthetic modification using sulfuric acid. Adapted from reference 56 with permission.

1.3 Characterization of MOFs

A key challenge of MOF chemistry is the complete structural characterization. The main characterization techniques include X-ray diffraction and surface area analyses. These techniques can be used to determine the topology, crystal structure, phase purity, surface area and porosity of MOFs. Another important characterization technique that has been widely used in the characterization of MOFs is solid-state NMR (SSNMR) spectroscopy, which will be discussed later.^{44,55}

1.3.1 Nitrogen adsorption and desorption isotherms

Permanent porosity is an intrinsic property of MOFs. Therefore, determining surface area, pore volumes and pore size distribution is critical for characterizing MOFs. Usually, nitrogen (N₂) gas adsorption at 77 K is most commonly employed for this purpose. The surface area is usually derived using the Brunauer–Emmett–Teller (BET) theory of adsorption.^{56–61} The data collected are displayed in the form of a BET isotherm, which plots the amount of gas adsorbed as a function of the relative pressure. By plotting $[(p/p_0)/n(1 - p/p_0)]$ vs p/p_0 (where n is the amount of gas adsorbed, p is pressure, and p_0 is saturation pressure of N₂) the apparent surface area of the MOF can be calculated. The results obtained from the experimental N₂ adsorption/desorption measurements are then compared with the theoretical values. Pore volume and pore size distributions can be derived from X-ray crystal structures, while the surface area and adsorption of gases can be compared with the values calculated using density functional theory (DFT).^{56–60}

1.3.2 Thermogravimetric analyses (TGA)

TGA is commonly used to study the thermal stability and confirm the activation of MOFs. TGA measures the mass loss in a sample over time as a result of temperature changes in a controlled and stable atmosphere. This method provides information in several processes in MOFs, including the loss of water or solvent, decarboxylation, pyrolysis, oxidation, or other types of decomposition.⁶²

1.3.3 X-ray crystallography

Single-crystal X-ray diffraction is rightly considered to be the ultimate technique for the structural determination of crystalline materials. The crystal structures of MOFs are, in general, determined using crystallographic techniques such as single-crystal and powder X-ray diffraction. These techniques are widely employed. However, the structure solution of porous materials is not always straightforward. Factors preventing structural elucidation include the presence of disordered solvent molecules occupying the pores and difficulties associated with the growing of good diffraction-quality crystals.^{63–68} When the obtention of suitable single crystals for SCXRD is not possible, the structure solution from PXRD data can still be accomplished. However, this is usually a more challenging

process and requires information from other characterization techniques such as DFT calculations and synchrotron-based X-ray techniques.^{69–71}

A complementary technique to XRD is solid-state NMR (SSNMR) spectroscopy. SSNMR can probe short-range ordering and local structure around the nucleus of interest in polycrystalline materials. In fact, SSNMR has been used to provide key structural information on the framework structure which helps de refinement of crystal structures and can also furnish dynamic information.

1.4 Characterization of MOFs via Solid-state NMR Spectroscopy

In the past decades, solid-state NMR (SSNMR) spectroscopy has been extensively employed to characterize the framework structure of porous materials, including MOFs, and explore their interaction with guest molecules and their dynamics.^{72–81}

Most organic linkers are composed of hydrogen, carbon, and oxygen. Given the critical role of these atoms play in MOF structure, properties, and applications, ^1H , ^{13}C , and ^{17}O are ideal targets for SSNMR studies.^{74,77,80–85} Additionally, metal atoms play key roles in the MOF structures and applications. ^{25}Mg , ^{27}Al , ^{67}Zn , ^{71}Ga , ^{91}Zr , and ^{115}In SSNMR spectroscopies have provided important information regarding the local structure of these metal ions and, thus regarding the framework and host-guest interactions.^{74,77,80–85}

Molecular motion in MOFs is another important phenomenon that is important in processes that involves adsorption of gases, the rotation of linkers, the diffusion of ions, and the catalytical reactions of chemicals. SSNMR can capture dynamic processes across a large range of time scale and determine the mode and rate of motion for selected molecular components either of the host framework or of the guest molecules.⁷⁶

Combining the dynamic information available from SSNMR with complementary data from techniques such computational chemistry or X-ray diffraction yields a comprehensive range of structural and dynamic information.

1.4.1 Probing the local structure of MOFs via ^1H , ^{13}C , and ^{17}O SSNMR

^1H and ^{13}C SSNMR

^1H MAS NMR plays a key role in establishing or confirming the proposed MOF structures. For example, the structure of several important MOFs containing bridging/capping hydroxyl groups, such as MIL-53,⁴² MIL-121,⁵³ and UiO-66(Zr)³¹ were refined from powder XRD data. However, locating and identifying hydrogen can be quite challenging. In these cases, ^1H SSNMR experiments were used to unambiguously identify the bridging/capping hydroxyl groups.⁸⁶

By using high-resolution ^1H SSNMR techniques at high magnetic field with fast spinning, it is possible to obtain ultrahigh-resolution spectra which allows for the identification of hydrogens with very similar chemical environment.^{87–89} This, in turn, facilitates the observation of subtle changes in the local environment of hydrogen atoms and can reveal important information regarding host-guest interactions. In addition, it can provide qualitative information regarding the loading level of the adsorbates.

^{13}C SSNMR spectroscopy is also routinely used to characterize the MOF framework. However, the natural abundance of ^{13}C makes it a less sensitive probe. Regardless, high-resolution ^{13}C SSNMR can still be easily acquired, thanks to the advance of spectroscopic technique such as, ^1H to ^{13}C cross polarization experiments (CP). CP experiments involve the transfer in magnetization from abundant spins (e.g., ^1H) to insensitive nuclei (e.g., ^{13}C) through the heteronuclear dipolar interaction. In addition to the sensitivity enhancement, it also provides the information on distance, by extension, connectivity between two spins involved. For example, ^{13}C SSNMR has provided crucial information on the phase transition in MIL-53 due to the breathing effect by probing the ^{13}C signals from the framework.^{42,90} The ^{13}C CPMAS spectra of the three phases of MIL-53, namely MIL-53-as, MIL-53-lp, and MIL-53-np, displayed distinct characteristics in the region of the signals from the ligand (Figure 1.8).

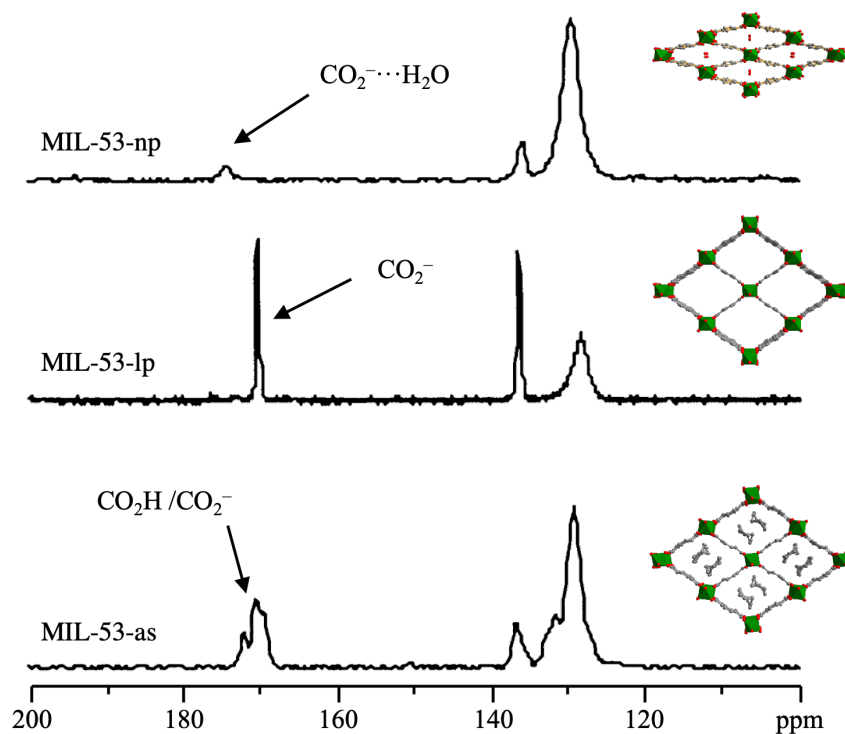


Figure 1.8. ^1H - ^{13}C CP/MAS of the three phases of MIL-53 and their respective structures (11.7 T, spinning rate of 12.5 kHz). Adapted from reference 42 with permission.

On one hand, the spectrum of MIL-53-as contains two signals at around 170 ppm attributed to the coordinated and unreacted ligand. On the other hand, the spectrum of MIL-53-ac only displayed one signal attributed to the coordinated ligand. Upon hydration, the signal attributed to the carbon atoms from the carboxylate groups was shifted to larger chemical shifts and displayed lower intensity. The authors attributed this fact to the presence of water in the pores interacting with these groups and causing the phase change.⁴²

^{17}O SSNMR

Oxygen is present in most of the linkers in the framework and plays important role in hydrogen bond interactions taking place between host-guest.^{18,91,92} Furthermore, certain

MOFs have framework hydroxyl species and oxygen anions (O^{2-}) controlling the formation of metal clusters, or SBUs. The framework oxygens directly affect the MOF topology and play key roles in MOF applications such as carbon capture,^{93–95} sensing^{15,96,97} and catalysis.^{36,98,99}

Ideally, ^{17}O SSNMR can be utilized for characterization of different oxygen species.^{77,100–108} However, unlike for 1H and ^{13}C SSNMR spectroscopy, ^{17}O SSNMR studies in MOFs are still scarce.^{100,109–115} This fact has been attributed to the nature of oxygen's only NMR-active isotope, ^{17}O .^{116,117} ^{17}O has a quadrupolar nucleus, meaning that the nuclear charge distribution is anisotropic, resulting in a nuclear quadrupole moment that can interact with the electric field gradient around the nucleus caused by the surrounding electronic environment. The second-order quadrupolar interaction leads to severe spectral broadening that cannot be completely removed by conventional magic-angle spinning (MAS) techniques. The extremely low natural abundance of the ^{17}O isotope (0.038%) severely limits its intrinsic sensitivity.^{116,117} Nevertheless, the development of pulse sequences in the recent years and the advances in the magnet and rf techniques, along with the development of new ^{17}O enrichment approaches, ^{17}O SSNMR spectroscopy has shown great potential for the characterization of MOFs.^{100,109–115} Furthermore, techniques such as dynamic nuclear polarization (DNP) can enhance the sensitivity associated with the low natural abundance of the ^{17}O isotope by transferring magnetization from abundant 1H nuclei to ^{17}O nuclei.

Due to the low natural abundance, ^{17}O enrichment of MOFs is necessary for ^{17}O SSNMR experiments. Several approaches have been developed for the synthesis of ^{17}O -enriched MOFs.^{100,109–115} For example, ^{17}O -enriched MIL-53(Sc) was prepared via post-synthetic ^{17}O enrichment, which involves the heating of the MOF material immersed in ^{17}O -enriched water under hydrothermal conditions.¹¹¹ A more cost-effective approach is the dry gel conversion (DGC),¹¹⁸ which involves the heating of the solid reagents in the presence of water vapor under autogenous conditions, as described in Figure 1.9.

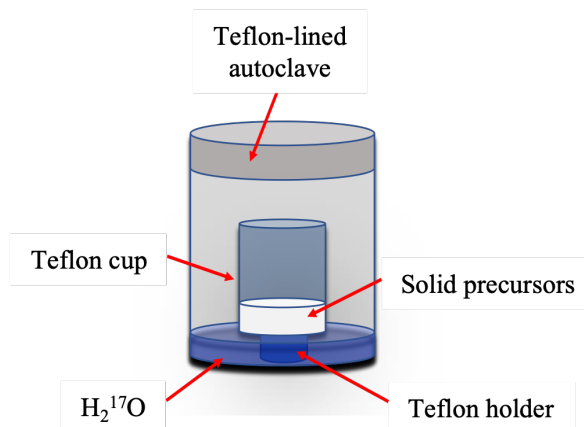


Figure 1.9. Schematic illustration of the reaction vessel used in the dry gel conversion method.

DGC reduces the amount of H₂¹⁷O used, which is more cost effective. This method has been successfully used for the preparation of ¹⁷O-enriched MIL-53(Al).^{100,109,111} Alternatively, ¹⁷O-enriched MOFs can be synthesized by adding a small amount of H₂¹⁷O in the synthesis of the MOF where the bulk solvent is non-aqueous. Examples of MOFs synthesized by this approach are ¹⁷O-enriched α-Mg₃(HCO₂)₆ and UiO-66 MOFs.¹⁰⁰ ¹⁷O enrichment can also be achieved by the direct ¹⁷O-exchange of the oxygen atoms of the linker precursor, which is subsequently employed in the synthesis. MOF-74(Mg) and MOF-5 have been synthesized using the latter approach.¹¹³

The first report of ¹⁷O SSNMR study of MOFs was reported in 2008 by Fischer et al. In this work, the authors demonstrated that ¹⁷O MAS NMR can be used to probe the local environment around oxygen species in the framework as well as the incorporation of ZnO₂ nanoparticles into the framework of the MOF-5. The ¹⁷O MAS spectra of the pure MOF-5 displayed one signal at ca. -50 ppm, which was attributed to the oxygen involved in the ZnO₄ cluster. Upon loading of ZnO nanoparticles, an extra signal attributed to ZnO species appeared in the -20 ppm region of the spectra, demonstrating that ¹⁷O can be used to track the presence of guest species in the framework. Furthermore, this work demonstrated for the first time that ¹⁷O can be used to characterize MOFs.¹¹³

MIL-53, an important MOF prototypical with flexible nature, was studied via ^{17}O SSNMR spectroscopy. In this case, the ability to separate signals from different types of oxygen in the framework allowed the detection of the phase transition and the breathing effect associated with activation.^{100,109,111,114} Bignami and coworkers demonstrated wide applicability of ^{17}O SSNMR to investigate cation disorder and its effect on the physical and chemical properties of MOFs.¹¹¹ The authors obtained high-resolution ^{17}O SSNMR spectra of several mixed-metal MIL-53(Al/Ga) samples.¹¹¹ The samples were prepared by using different stoichiometric ratios (Al/Ga of 50/50 and 80/20) of the two metal nitrate sources in the synthesis.

The ^{17}O MAS NMR spectra revealed significant differences in the hydroxyl region for the different samples. High-resolution ^{17}O 3QMAS spectra were then acquired to extract the average quadrupolar parameters from each resonance. By fitting the ^{17}O MAS spectra using these parameters, the authors were able to extract the relative intensities of each signal, and therefore determine the mixture composition of the sample.¹¹¹ More recently, Rice and collaborators utilized ^{17}O SSNMR spectroscopy to study the breathing behavior of these MIL-53(Al/Ga) samples.¹¹⁴ The authors have obtained high resolution ^{17}O 3QMAS and MAS SSNMR spectra of the mixed-metal MIL-53 materials. By comparing the changes in the spectral parameters, the authors found an increased preference for clustering of like cations as the Ga content increases in the frameworks.¹¹⁴

To circumvent the problem of insensitivity associated with the low natural abundance of the ^{17}O isotope, ^{17}O SSNMR experiments can be performed in combination with dynamic nuclear polarization (DNP) techniques.^{119–121} ^1H nuclei are hyperpolarized (meaning a large population difference between the nuclear spin energy levels) by DNP and then magnetization is transferred to ^{17}O nuclei by means of $^1\text{H}\rightarrow^{17}\text{O}$ cross-polarization. As a result, the gain in sensitivity allows for the acquisition of ^{17}O spectra without isotopic enrichment.^{122,123} Carnevale and coworkers recently reported for the first time the ^{17}O SSNMR study of MIP-206 MOF without isotopic enrichment.¹¹⁰ MIP-206 is a porous Zr-oxo-cluster carboxylate-based MOF containing 4 distinct oxygen sites. DNP-enhanced $^1\text{H}\rightarrow^{17}\text{O}$ CP MAS spectrum acquired at field of 18.6 T shows a set of four well resolved signals, agreeing with the crystal structure. Furthermore, the spectral parameters obtained

from the ^{17}O 1D MAS spectrum were in remarkable agreement with those obtained from DFT calculations. This facilitated the spectral assignment of each four oxygen sites present in the framework of the MIP-206 MOF. Another approach to enhance the sensitivity is to carry out ^{17}O SSNMR experiments at high magnetic fields, which will be discussed in Chapter 3.

1.4.2 Probing CO_2 adsorption in MOFs via SSNMR

The storage and separation of CO_2 using porous materials is a technology that has attracted enormous attention due to climate change. MOFs have shown promising properties for gas capture and storage due to their high surface areas and tunable structure and properties.^{81,124} A complete characterization of the dynamics and properties of adsorbed CO_2 is, therefore, crucial.^{11,125,126} SSNMR spectroscopy is a powerful technique for studying gas adsorption in MOFs because it can probe the long- and short-range dynamics of CO_2 .^{75,76,79,124,127–134} Therefore, it can provide important information on diffusivity^{135–139} and local dynamics of chemically¹⁴⁰ and physically^{112,127,131,135,139,141–148} adsorbed CO_2 in MOFs.

Static in situ variable-temperature (VT) ^{13}C experiments are the most commonly employed methods to probe the motions of CO_2 . The static SSNMR spectra of ^{13}C isotope is dominated by the chemical shift anisotropy (CSA) interaction.¹⁴⁹ This interaction is anisotropic, meaning that the C-13 line-shape is determined by the orientation of the CO_2 molecules. Therefore, molecular motions such as rotation, wobbling, or hopping between adsorption sites may affect the observed spectra.¹⁵⁰ By comparing simulated spectra as a function of temperature with the experimental spectra, it is possible to assess these types of molecular motion and its energetics, as well as the preferred adsorbed molecular orientation.^{79,151}

This approach was employed by Reimer and coworkers in the first comprehensive SSNMR studies of CO_2 dynamics in the MOF-74(Mg).^{146,147} MOF-74 consists of an array of hexagonal channels containing Mg^{2+} cations with open metal sites (OMSs) at the vertices.¹⁵² The open metal sites in the framework act as preferential adsorption sites for

CO₂. In this work, the authors acquired variable temperature ¹³C NMR spectra ranging from 12 K to 400 K (Figure 1.10).

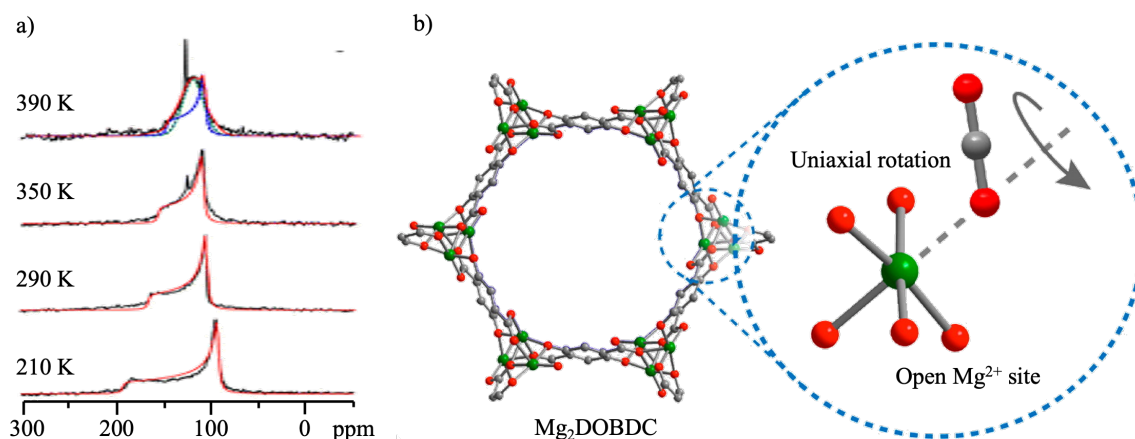


Figure 1.10. a) Simulated (red line) and experimental (black line) ¹³C CSA powder patterns of ¹³C-enriched CO₂ in Mg₂(DOBDC) at various temperatures. b) Illustration of CO₂ uniaxial rotation at the open Mg²⁺ site. Gray, red, and green spheres represent C, O, and Mg atoms, respectively. Adapted from reference 146 with permission.

The ¹³C line-shapes exhibited distinct and broad chemical shift anisotropy (CSA) powder pattern, which suggested a strong physical interaction between CO₂ molecules and the MOF framework. Simulation of the motionally averaged NMR line-shapes were carried out and revealed that the CO₂ molecules undergo a fast uniaxial rotation at the open Mg²⁺ site (Figure 1.10). The CO₂ dynamics in Mg-MOF-74 was further investigated by Hayes and co-workers using various CO₂ loading levels. The static ¹³C SSNMR spectrum obtained at the lowest loading agreed with that recorded by Reimer and co-workers. However, at higher loadings, the powder patterns were different. As shown by density functional theory (DFT) calculations, the spectral changes were due to CO₂ going from sampling primarily the OMSs at lower loadings, to spending more time at additional binding sites at higher loadings.¹⁴⁸ This demonstrates that SSNMR spectroscopy, when used together with computational methods, can reveal the existence of additional binding sites.

More recently, Inukai and coworkers studied the adsorption of CO₂ in the MOF-74(Mg) under high pressure.¹³⁰ The authors employed ¹³C static experiments to investigate the dynamics of adsorbed CO₂ and found good agreement with previous results.^{146–148} In addition to the results of the CSA analyses, high-resolution MAS NMR spectra provided information on the position and the dynamics of the CO₂ molecules. The results suggested that the mobility of the CO₂ molecules decreased with increasing pressure due to the presence of extensive CO₂–CO₂ interactions. Furthermore, T₁ relaxation experiments revealed the occurrence of unusually slow localized wobbling and hopping motions at a rate of 10⁻⁸ s.¹³⁰

CO₂ dynamics in MOFs without OMSs, such as MIL-53(Al, Ga)-np and MIL-53-NH₂(Al, Ga)-np, have also been investigated.¹²⁷ In these two cases, static VT ¹³C experiments revealed that CO₂ undergoes a localized wobbling about the hydroxyl groups on the linker and a two-fold hopping between adjacent hydroxyl sites. As compared to MIL-53, smaller wobbling angles, α , were observed for MIL-53-NH₂. This indicates a decrease in dynamics and thus an increase in CO₂-MOF interaction, consistent with previous observations that amine functionalization can enhance CO₂ capture ability.¹⁵³ This shows that static VT ¹³C SSNMR spectroscopy can be used to evaluate host-guest interaction strength.

The lack of OMSs in some MOFs can make the CO₂ binding sites less than trivial to determine. Nevertheless, the CO₂ binding sites in these MOFs can be identified via cross polarization (CP) NMR experiments.^{127,131} Under favorable conditions, CP will transfer magnetization from abundant spins (e.g., ¹H) to nearby dilute spins (e.g., ¹³C), enhancing the signal of the dilute spins.¹⁴⁹ Using ¹H→¹³C CP experiments, the CO₂ binding sites in α -Mg₃(COOH)₆ were found to be the formate hydrogens that extends into the MOF channels.¹³¹ A long CP contact time (ca. 10 ms) was required to efficiently detect the adsorbed ¹³CO₂ signal since the ¹H_{formate} and ¹³C atoms are relatively distant ($d(^1\text{H}\cdots^{13}\text{C}) = 3.9 \text{ \AA}$ for the closest hydrogen, as obtained from molecular dynamics (MD) simulations) and the adsorbed CO₂ is quite mobile. Nonetheless, the presence of a signal shows that the hydrogens must be close to CO₂ and must serve as CO₂ binding sites. This conclusion was supported by MD simulations.

The separation of CO₂ from other gases, including methane, is of industrial significance.^{154,155} The selectivity of adsorption from ¹³CO₂/¹³CH₄ gas mixtures in the flexible SNU-9 and DUT-8 MOFs was studied by high-pressure in situ NMR spectroscopy.¹³⁷ The selectivity of adsorption from ¹³CO₂/¹³CH₄ gas mixtures was studied via ¹³C SSNMR experiments. The authors were able to get qualitative information regarding selectivity factor in the ¹³CO₂/¹³CH₄ mixture from the intensity of the signals in the spectra.

1.4.3 Probing water adsorption in MOFs

The sensitivity of MOF structure to water is a major issue when considering these materials for adsorption applications.^{5,156,157} It is well known that water can affect the structural stability as well as the adsorption performance of MOFs.^{7,156,158–161} Therefore, a better understanding of the effect of water on MOF stability and adsorption properties is crucial to the development of new water-stable adsorbents.¹²⁹ However, although SNMR is a powerful technique for such characterization, only a few studies have been reported so far on the stability^{162–164} and water adsorption in MOFs.^{162,165}

Bertmer and collaborators used ¹H and ¹³C NMR spectroscopic experiments to investigate the structural changes due to water adsorption within the Cu₃(BTC)₂ MOF.¹⁶³ The authors measured ¹H MAS spectra of Cu₃(BTC)₂ samples with different water content, alongside with analysis of the intensities of ¹H NMR spinning sidebands. The experiments revealed a strong hyperfine coupling between the ¹H and ¹³C nuclei suggesting a proximity between the water molecules and the open Cu²⁺. These results were later confirmed by the same authors.¹⁶⁴ In this case, they employed deuterated Cu₃(BTC)₂ samples in order to remove the NMR signal from protons of the framework and enhance the resolution in the ¹H MAS spectra. The high-resolution spectra provided additional insight into the hydration process and the authors were able to identify the different adsorption sites in the framework. These works demonstrate that ¹H and ¹³C SSNMR spectroscopy can be employed to study the stability of MOFs upon contact with water.

Understanding the dynamics of adsorbed water inside of MOFs is important because it provides further insights into the mechanisms of adsorption of water in MOFs.^{7,157,160} Ćelic et al. reported the study of water removal from the pores of zinc trimesate MOF, $[\text{Zn}_2(\text{BTC})(\text{OH})-(\text{H}_2\text{O})]$, and the dynamics of adsorbed water molecules inside of the pores. ^1H MAS experiments were used to demonstrate the removal of water species at different temperatures. VT ^2H MAS SSNMR experiments of the MOF loaded with $^2\text{H}_2\text{O}$ instead of H_2O elucidated the sequence of removal of coordinated and adsorbed water. The use of ^2H MAS SSNMR provided additional information that could not be obtained by TGA. This work demonstrates that SSNMR can be employed to study the mechanisms of adsorption of water in MOFs.¹⁶²

Xu et al. employed VT ^2H static SSNMR experiments to probe the dynamics of heavy water ($^2\text{H}_2\text{O}$) in the MOF-74(M) family (Figure 1.11).¹³³

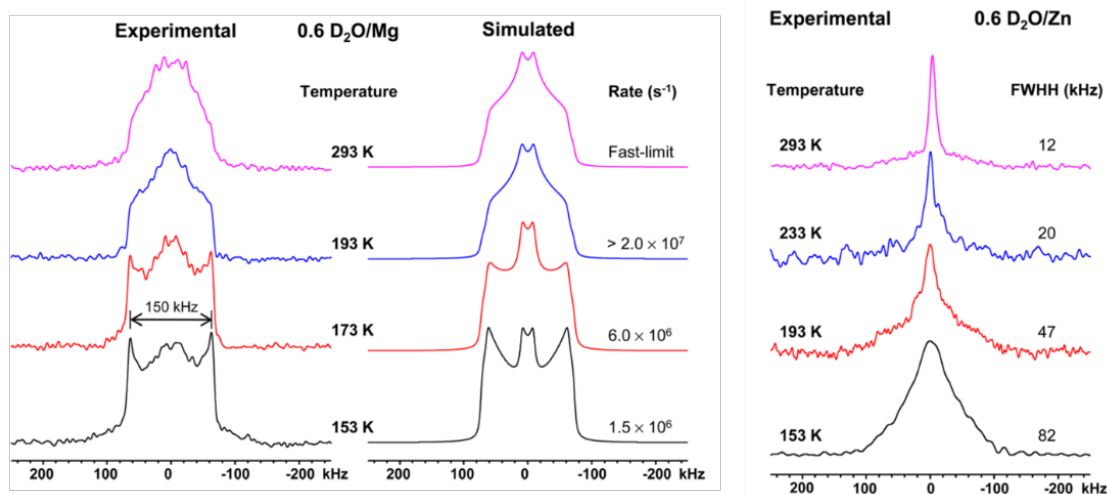


Figure 1.11. Experimental and simulated ^2H static spectra as a function of temperature of the $0.6 \text{ D}_2\text{O}/\text{Mg}$ and $\text{D}_2\text{O}/\text{Zn}$ samples. Figure adapted from reference 131 with permission.

The ^2H static spectra of the samples at different temperatures displayed a single, broad pattern with a quadrupolar coupling constant, C_Q , of 97.5 kHz and an asymmetric parameter, η_Q , of 0.75. Spectral simulations allowed the authors to identify π flip-flop motions around the molecular axis of adsorbed water. Moreover, these experiments revealed that the water molecules display a higher affinity to Zn^{2+} centers in MOF-74(Zn) than to Mg^{2+} in MOF-74(Mg).

1.5 Outline of the thesis

In this thesis, we discuss the application of solid-state NMR in the characterization of MOFs. In chapter 1, an introduction to metal-organic frameworks is given and a review on the SSNMR characterization of MOFs is provided. In chapter 2, the fundamentals of SSNMR and experiments are highlighted. Chapters 3–5 deal with the characterization of MOFs via ^{17}O SSNMR. Chapter 3 describes the use of ^{17}O SSNMR at ultra-high field of 35.2 T in the characterization of the challenging $\alpha\text{-Mg}_3(\text{HCO}_2)_6$. The next chapter describes how ^{17}O SSNMR can be used to probe the phase transformations of the MIL-53(Al) MOF. Chapter 5 demonstrates that ^{17}O SSNMR can also be used to probe the post-synthetic modification of MOFs. In chapter 6, the adsorption of CO_2 and water in the ultramicroporous ZnAtzOx MOF is studied via ^{13}C and ^2H SSNMR and the effect of co-adsorption is discussed. Finally, chapter 7 lays out the summary and the future outlook.

1.6 References

- (1) Chen, Z.; Wasson, M. C.; Drout, R. J.; Robison, L.; Idrees, K. B.; Knapp, J. G.; Son, F. A.; Zhang, X.; Hierse, W.; Kühn, C.; Marx, S.; Hernandez, B.; Farha, O. K. *Faraday Discuss.* **2021**, 225, 9.
- (2) Hong-Cai, Z.; Long, J. R.; Yaghi, O. M. *Chem. Rev.* **2012**, 112, 673–674.
- (3) Bavykina, A.; Kolobov, N.; Khan, I. S.; Bau, J. A.; Ramirez, A.; Gascon, J. *Chem. Rev.* **2020**, 120, 8468.

- (4) Jiang, J.; Gándara, F.; Zhang, Y. B.; Na, K.; Yaghi, O. M.; Klemperer, W. G. J. *Am. Chem. Soc.* **2014**, 136, 12844.
- (5) Kalmutzki, M. J.; Diercks, C. S.; Yaghi, O. M. *Adv. Mater.* **2018**, 30, 1.
- (6) Canivet, J.; Fateeva, A.; Guo, Y.; Coasne, B.; Farrusseng, D. *Chem. Soc. Rev.* **2014**, 43, 5594.
- (7) Burtch, N. C.; Jasuja, H.; Walton, K. S. *Chem. Rev.* **2014**, 114, 10575.
- (8) Hanikel, N.; Prévot, M. S.; Yaghi, O. M. *Nat. Nanotechnol.* **2020**, 15, 348.
- (9) Wang, C.; Kim, J.; Malgras, V.; Na, J.; Lin, J.; You, J.; Zhang, M.; Li, J.; Yamauchi, Y. *Small* **2019**, 15, 1.
- (10) Dhaka, S.; Kumar, R.; Deep, A.; Kurade, M. B.; Ji, S. W.; Jeon, B. H. *Coord. Chem. Rev.* **2019**, 380, 330.
- (11) Li, H.; Wang, K.; Sun, Y.; Lollar, C. T.; Li, J.; Zhou, H. C. *Mater. Today* **2018**, 21, 108.
- (12) Petit, C. *Curr. Opin. Chem. Eng.* **2018**, 20, 132.
- (13) Suh, M. P.; Park, H. J.; Prasad, T. K.; Lim, D.-W. *Chem. Rev.* **2010**, 100, 782.
- (14) Liu, Y.; Wang, Z. U.; Zhou, H.-C. *Greenh. Gases Sci. Technol.* **2012**, 2, 239.
- (15) Cui, Y.; Li, B.; He, H.; Zhou, W.; Chen, B.; Qian, G. *Acc. Chem. Res.* **2016**, 49, 483.
- (16) Yaghi, O. M.; O’Keeffe, M.; Ockwig, N. W.; Chae, H. K.; Eddaoudi, M.; Kim, J. *Nature* **2003**, 423, 705.
- (17) O’Keeffe, M.; Yaghi, O. M. *Chem. Rev.* **2012**, 112, 675.
- (18) Kalmutzki, M. J.; Hanikel, N.; Yaghi, O. M. *Sci. Adv.* **2018**, 4, 1.

- (19) Lyu, H.; Ji, Z.; Wuttke, S.; Yaghi, O. M. *Chem* **2020**, *6*, 2219.
- (20) Jiang, H.; Alezi, D.; Eddaoudi, M. *Nat. Rev. Mater.* **2021**, *6*, 466.
- (21) Freund, R.; Canossa, S.; Cohen, S. M.; Yan, W.; Deng, H.; Guillerm, V.; Eddaoudi, M.; Madden, D. G.; Fairen-Jimenez, D.; Lyu, H.; Macreadie, L. K.; Ji, Z.; Zhang, Y.; Wang, B.; Haase, F.; Wöll, C.; Zaremba, O.; Andreo, J.; Wuttke, S.; Diercks, C. S. *Angew. Chemie Int. Ed.* **2021**, *60*, 23946.
- (22) Schoedel, A.; Cairns, A. J.; Belmabkhout, Y.; Wojtas, L.; Mohamed, M.; Zhang, Z.; Proserpio, D. M.; Eddaoudi, M.; Zaworotko, M. J. *Angew. Chem. Int. Edit.* **2013**, *125*, 2974.
- (23) Mukherjee, S.; Zaworotko, M. J. *Trends Chem.* **2020**, *2*, 506.
- (24) Schoedel, A.; Wojtas, L.; Kelley, S. P.; Rogers, R. D.; Eddaoudi, M.; Zaworotko, M. J. *Angew. Chemie Int. Ed.* **2011**, *50*, 11421.
- (25) O'Hearn, D. J.; Bajpai, A.; Zaworotko, M. J. *Small* **2021**, *17*, 2006351.
- (26) Yuan, S.; Qin, J.-S.; Li, J.; Huang, L.; Feng, L.; Fang, Y.; Lollar, C.; Pang, J.; Zhang, L.; Sun, D.; Alsalme, A.; Cagin, T.; Zhou, H.-C. *Nat. Commun.* **2018**, *9*, 1.
- (27) Keeffe, M. O.; Peskov, M. a; Ramsden, S. J.; Yaghi, O. M. *Acc. Chem. Res.* **2008**, *41*, 1782.
- (28) Li, M.; Li, D.; O'Keeffe, M.; Yaghi, O. M. *Chem. Rev.* **2013**, *114*, 1343.
- (29) Alexandrov, E. V.; Shevchenko, A. P.; Blatov, V. A. *Cryst. Growth Des.* **2019**, *19*, 2604.
- (30) Li, H.; Eddaoudi, M.; O'Keeffe, M.; Yaghi, O. M. *Nature* **1999**, *402*, 276.
- (31) Cavka, J. H.; Jakobsen, S.; Olsbye, U.; Guillou, N.; Lamberti, C.; Bordiga, S.; Lillerud, K. P. *J. Am. Chem. Soc.* **2008**, *130*, 13850.
- (32) Garibay, S. J.; Cohen, S. M. *Chem. Commun.* **2010**, *46*, 7700.

- (33) Silva, C. G.; Luz, I.; Llabrés I Xamena, F. X.; Corma, A.; García, H. *Chem. Eur. J.* **2010**, *16*, 11133.
- (34) Kandiah, M.; Nilsen, M. H.; Usseglio, S.; Jakobsen, S.; Olsbye, U.; Tilset, M.; Larabi, C.; Quadrelli, E. A.; Bonino, F.; Lillerud, K. P. *Chem. Mater.* **2010**, *22*, 6632.
- (35) Chavan, S.; Vitillo, J. G.; Gianolio, D.; Zavorotynska, O.; Civalieri, B.; Jakobsen, S.; Nilsen, M. H.; Valenzano, L.; Lamberti, C.; Lillerud, K. P.; Bordiga, S. *Phys. Chem. Chem. Phys.* **2012**, *14*, 1614.
- (36) Silva, P.; Vilela, S. M. F.; Tomé, J. P. C.; Almeida Paz, F. *Chem. Soc. Rev.* **2015**, *44*, 6774.
- (37) Stock, N.; Biswas, S. *Chem. Rev.* **2012**, *112*, 933.
- (38) Tranchemontagne, D. J.; Hunt, J. R.; Yaghi, O. M. *Tetrahedron* **2008**, *64*, 8553.
- (39) Cravillon, J.; Münzer, S.; Lohmeier, S. J.; Feldhoff, A.; Huber, K.; Wiebcke, M. *Chem. Mater.* **2009**, *21*, 1410.
- (40) Farha, O. K.; Hupp, J. T. *CrystEngComm.* **2013**, *15*, 9258.
- (41) Woodliffe, J. L.; Ferrari, R. S.; Ahmed, I.; Laybourn, A. *Coord. Chem. Rev.* **2021**, *428*, 213578.
- (42) Loiseau, T.; Serre, C.; Huguenard, C.; Fink, G.; Taulelle, F.; Henry, M.; Bataille, T.; Férey, G. *Chem. Eur. J.* **2004**, *10*, 1373.
- (43) Ma, J.; Kalenak, A. P.; Wong-Foy, A. G.; Matzger, A. J. *Angew. Chem. Int. Edit.* **2017**, *56*, 14810.
- (44) Howarth, A. J.; Peters, A. W.; Vermeulen, N. A.; Wang, T. C.; Hupp, J. T.; Farha, O. K. *Chem. Mater.* **2017**, *29*, 26.
- (45) Kalinovsky, Y.; Cooper, N. J.; Main, M. J.; Holder, S. J.; Blight, B. A. *Dalt. Trans.* **2017**, *46*, 15704.

- (46) Espín, J.; Garzón-Tovar, L.; Carné-Sánchez, A.; Imaz, I.; Maspoch, D. *ACS Appl. Mater. Interfaces* **2018**, 10, 9555.
- (47) Wang, Z.; Cohen, S. M. *Chem. Soc. Rev.* **2009**, 38, 1315.
- (48) Mandal, S.; Natarajan, S.; Mani, P.; Pankajakshan, A. *Adv. Funct. Mater.* **2021**, 31, 1.
- (49) Tanabe, K. K.; Cohen, S. M. *Chem. Soc. Rev.* **2011**, 40, 498.
- (50) Ali Akbar Razavi, S.; Morsali, A. *Linker Functionalized Metal-Organic Frameworks. Coord. Chem. Rev.* **2019**, 399, 213023.
- (51) Islamoglu, T.; Goswami, S.; Li, Z.; Howarth, A. J.; Farha, O. K.; Hupp, J. T. *Acc. Chem. Res.* **2017**, 50, 805.
- (52) Hao, J.-N.; Yan, B. J. *Mater. Chem. A* **2014**, 2, 18018.
- (53) Volkringer, C.; Loiseau, T.; Guillou, N.; Férey, G.; Haouas, M.; Taulelle, F.; Elkaim, E.; Stock, N. *Inorg. Chem.* **2010**, 49, 9852.
- (54) Furukawa, H.; Gándara, F.; Zhang, Y. B.; Jiang, J.; Queen, W. L.; Hudson, M. R.; Yaghi, O. M. J. *Am. Chem. Soc.* **2014**, 136, 4369.
- (55) Gropp, C.; Canossa, S.; Wuttke, S.; Gándara, F.; Li, Q.; Gagliardi, L.; Yaghi, O. M. *ACS Cent. Sci.* **2020**, 6, 1255.
- (56) Ambroz, F.; Macdonald, T. J.; Martis, V.; Parkin, I. P. *Small Methods* **2018**, 2, 1.
- (57) Walton, K. S. W.; Snurr, R. Q. *J. Am. Chem. Soc.* **2007**, 129, 8552.
- (58) McMillan, W. G.; Teller, E. J. *Phys. Colloid Chem.* **2002**, 55, 17.
- (59) Brunauer, S.; Emmett, P. H.; Teller, E. J. *Am. Chem. Soc.* **2002**, 60, 309.
- (60) Rouquerol, J.; Llewellyn, P.; Rouquerol, F. *Stud. Surf. Sci. Catal.* **2007**, 160, 49.

- (61) Osterrieth J, Rampersad J, Madden DG, Rampal N, Skoric L, Connolly B, et al. How Reproducible Are Surface Areas Calculated from the BET Equation? ChemRxiv. Cambridge: Cambridge Open Engage; **2021**; This content is a preprint and has not been peer-reviewed.
- (62) Healy, C.; Patil, K. M.; Wilson, B. H.; Hermanspahn, L.; Harvey-Reid, N. C.; Howard, B. I.; Kleinjan, C.; Koliën, J.; Payet, F.; Telfer, S. G.; Kruger, P. E.; Bennett, T. D. *Coord. Chem. Rev.* **2020**, 419, 213388.
- (63) Zhang, J. P.; Liao, P. Q.; Zhou, H. L.; Lin, R. B.; Chen, X. M. *Chem. Soc. Rev.* **2014**, 43, 5789.
- (64) Gándara, F.; Bennett, T. D. *IUCrJ* **2014**, 1, 563.
- (65) Øien-Ødegaard, S.; Shearer, G. C.; Wragg, D. S.; Lillerud, K. P. *Chem. Soc. Rev.* **2017**, 46, 4867.
- (66) Albalad, J.; Sumby, C. J.; MasPOCH, D.; Doonan, C. J. *CrystEngComm* **2021**, 23, 2185.
- (67) Bloch, W. M.; Champness, N. R.; Doonan, C. J. *Angew. Chemie Int. Ed.* **2015**, 54, 12860.
- (68) Lee, S.; Bürgi, H.-B.; Alshimri, S. A.; Yaghi, O. M. *J. Am. Chem. Soc.* **2018**, 140, 8958.
- (69) Javier M.-R. *Dalt. Trans.* **2020**, 49, 13897.
- (70) Harris, K. D. M.; Tremayne, M.; Kariuki, B. M. *Angew. Chem. Int. Ed.* **2001**, 40, 1626.
- (71) Rahimabadi, P. S.; Khodaei, M.; Koswattage, K. R. *X-Ray Spectrom.* **2020**, 49, 348.
- (72) Li, S.; Lafon, O.; Wang, W.; Wang, Q.; Wang, X.; Li, Y.; Xu, J.; Deng, F. *Recent Adv. Mater.* **2020**, 32, 1.

- (73) Hoffmann, H. C.; Debowski, M.; Müller, P.; Paasch, S.; Senkovska, I.; Kaskel, S.; Brunner, E. *Materials (Basel)*. **2012**, *5*, 2537.
- (74) Brunner, E.; Rauche, M. *Chem. Sci.* **2020**, *11*, 4297.
- (75) Wong, Y. T. A.; Martins, V.; Lucier, B. E. G.; Huang, Y. *Chem. Eur. J.* **2019**, *25*, 1848.
- (76) Fu, Y.; Guan, H.; Yin, J.; Kong, X. *Coord. Chem. Rev.* **2021**, *427*, 213563.
- (77) Ashbrook, S. E.; Dawson, D. M.; Seymour, V. R. *Phys. Chem. Chem. Phys.* **2014**, *16*, 8223.
- (78) Lucier, B. E. G.; Chen, S.; Huang, Y. *Acc. Chem. Res.* **2018**, *51*, 319.
- (79) Witherspoon, V. J.; Xu, J.; Reimer, J. A. *Chem. Rev.* **2018**, *118*, 10033.
- (80) Martineau-Corcos, C. *Curr. Opin. Colloid Interface Sci.* **2018**, *33*, 35.
- (81) Hughes, A. R.; Blanc, F. *CrystEngComm* **2021**, *23*, 2491.
- (82) Lucier, B. E. G.; Zhang, Y.; Huang, Y. *Concepts Magn. Reson. Part A Bridg. Educ. Res.* **2016**, *45A*, 1.
- (83) Reif, B.; Ashbrook, S. E.; Emsley, L.; Hong, M. *Nat. Rev. Methods Prim.* **2021**, *1*, 2.
- (84) Moran, R. F.; Dawson, D. M.; Ashbrook, S. E. *Int. Rev. Phys. Chem.* **2017**, *36*, 39.
- (85) Bonhomme, C.; Gervais, C.; Laurencin, D. *Prog. Nucl. Magn. Reson. Spectrosc.* **2014**, *77*, 1.
- (86) Sutrisno, A.; Huang, Y. *Solid State Nucl. Magn. Reson.* **2013**, *49*, 1.
- (87) Xu, J.; Terskikh, V. V.; Chu, Y.; Zheng, A.; Huang, Y. *Chem. Mater.* **2015**, *27*, 3306.

- (88) Schnell, I.; Spiess, W. H. J. *Magn. Reson.* **2001**, 151, 153.
- (89) Hodgkinson, P. *Annu. Reports NMR Spectrosc.* **2011**, 72, 185.
- (90) Alhamami, M.; Doan, H.; Cheng, C. H. *Materials (Basel)*. **2014**, 7, 3198.
- (91) Ghasempour, H.; Wang, K. Y.; Powell, J. A.; ZareKarizi, F.; Lv, X. L.; Morsali, A.; Zhou, H. C. *Coord. Chem. Rev.* **2021**, 426, 213542.
- (92) Wu, G.; Hung, I.; Gan, Z.; Terskikh, V.; Kong, X. J. *Phys. Chem. A* **2019**, 123, 8243.
- (93) Li, J. R.; Ma, Y.; McCarthy, M. C.; Sculley, J.; Yu, J.; Jeong, H. K.; Balbuena, P. B.; Zhou, H. C. *Coord. Chem. Rev.* **2011**, 255, 1791.
- (94) Wang, T.; Lin, E.; Peng, Y. L.; Chen, Y.; Cheng, P.; Zhang, Z. *Coord. Chem. Rev.* **2020**, 423, 213485.
- (95) Ding, M.; Flaig, R. W.; Jiang, H.-L.; Yaghi, O. M. *Chem. Soc. Rev.* **2019**, 48, 2783.
- (96) Hu, M.-L.; Razavi, S. A. A.; Piroozzadeh, M.; Morsali, A. *Inorg. Chem. Front.* **2020**, 7, 1598.
- (97) Li, H.-Y.; Zhao, S.-N.; Zang, S.-Q.; Li, J. *Chem. Soc. Rev.* **2020**, 49, 6364.
- (98) Liu, J.; Liang, J.; Xue, J.; Liang, K. *Small* **2021**, 17, 2100300.
- (99) Dhakshinamoorthy, A.; Asiri, A. M.; Garcia, H. *ChemCatChem* **2020**, 12, 4732.
- (100) He, P.; Xu, J.; Terskikh, V. V.; Sutrisno, A.; Nie, H. Y.; Huang, Y. J. *Phys. Chem. C* **2013**, 117, 16953.
- (101) Ashbrook, S. E.; Davis, Z. H.; Morris, R. E.; Rice, C. M. *Chem. Sci.* **2021**, 12, 5016.
- (102) Wu, G. *Prog. Nucl. Magn. Reson. Spectrosc.* **2019**, 114, 135.

- (103) Shen, L.; Peng, L. *Chinese J. Catal.* **2015**, 36, 1494.
- (104) Lapina, O. B.; Shubin, A. A.; Terskikh, V. V. *Mod. Magn. Reson.* **2018**, 1125.
- (105) Yamada, K. *Recent Applications of Solid-State ¹⁷O NMR*, 1st ed.; Elsevier Ltd, **2010**; Vol. 70.
- (106) Ohlin, C. A.; Casey, W. H. *Annu. Reports NMR Spectrosc.* **2018**, 94, 187.
- (107) Kong, X.; Terskikh, V. V.; Khade, R. L.; Yang, L.; Rorick, A.; Zhang, Y.; He, P.; Huang, Y.; Wu, G. *Angew. Chemie Int. Ed.* **2015**, 54, 4753.
- (108) Palmer, J.; Wu, G. *Annu. Reports NMR Spectrosc.* **2021**, 94, 187.
- (109) Martins, V.; Xu, J.; Hung, I.; Gan, Z.; Gervais, C.; Bonhomme, C.; Huang, Y. *Magn. Reson. Chem.* **2020**, 53, 1.
- (110) Carnevale, D.; Mouchaham, G.; Wang, S.; Baudin, M.; Serre, C.; Bodenhausen, G.; Abergel, D. *Phys. Chem. Chem. Phys.* **2021**, 23, 2245.
- (111) Bignami, G. P. M.; Davis, Z. H.; Dawson, D. M.; Morris, S. A.; Russell, S. E.; McKay, D.; Parke, R. E.; Iuga, D.; Morris, R. E.; Ashbrook, S. E. *Chem. Sci.* **2018**, 9, 850.
- (112) Wang, W.; Waang, W. D.; Lucier, B. E. G.; Terskikh, V. V.; Huang, Y. *J. Phys. Chem. Lett.* **2014**, 5, 3360.
- (113) Mueller, M.; Hermes, S.; Kaehler, K.; Muhler, M.; Fischer, R. A. *ACS Natl. Meet. B. Abstr.* **2008**, 5, 4576.
- (114) Rice, C. M.; Davis, Z. H.; McKay, D.; Bignami, G. P. M.; Chitac, R. G.; Dawson, D. M.; Morris, R. E.; Ashbrook, S. E. *Phys. Chem. Chem. Phys.* **2020**, 22, 14514.
- (115) Martins, V. V. V.; Xu, J.; Wang, X.; Chen, K.; Hung, I.; Gan, Z.; Gervais, C.; Bonhomme, C.; Jiang, S.; Zheng, A.; Lucier, B. E. G.; Huang, Y.; Hung, I.; Gan, Z.;

- Gervais, C.; Bonhomme, C.; Jiang, S.; Zheng, A.; Lucier, B. E. G. G.; Huang, Y. J. *Am. Chem. Soc.* **2020**, 142, 14877.
- (116) Ashbrook, S. E.; Smith, M. E. *Chem. Soc. Rev.* **2006**, 35, 718.
- (117) Gerothanassis, I. P. *Prog. Nucl. Magn. Reson. Spectrosc.* **2010**, 57, 95.
- (118) Xu, W.; Dong, J.; Li, J.; Li, J.; Wu, F. J. *Chem. Soc. Chem. Commun.* **1990**, 10, 755.
- (119) Michaelis, V. K.; Markhasin, E.; Daviso, E.; Herzfeld, J.; Griffin, R. G. *J. Phys. Chem. Lett.* **2012**, 3, 2030.
- (120) Blanc, F.; Sperrin, L.; Jefferson, D. A.; Pawsey, S.; Rosay, M.; Grey, C. P. *J. Am. Chem. Soc.* **2013**, 135, 2975.
- (121) Brownbill, N. J.; Gajan, D.; Lesage, A.; Emsley, L.; Blanc, F. *Chem. Commun.* **2017**, 53, 2563.
- (122) Maly, T.; Debelouchina, G. T.; Bajaj, V. S.; Hu, K.-N.; Joo, C.-G.; Mak-Jurkauskas, M. L.; Sirigiri, J. R.; Wel, P. C. A. van der; Herzfeld, J.; Temkin, R. J.; Griffin, R. G. *J. Chem. Phys.* **2008**, 128, 052211.
- (123) Lilly Thankamony, A. S.; Wittmann, J. J.; Kaushik, M.; Corzilius, B. *Prog. Nucl. Magn. Reson. Spectrosc.* **2017**, 102, 120.
- (124) Bernin, D.; Hedin, N. *Curr. Opin. Colloid Interface Sci.* **2018**, 33, 53.
- (125) Younas, M.; Rezakazemi, M.; Daud, M.; Wazir, M. B.; Ahmad, S.; Ullah, N.; Inamuddin; Ramakrishna, S. *Prog. Energy Combust. Sci.* **2020**, 80.
- (126) Yu, J.; Xie, L. H.; Li, J. R.; Ma, Y.; Seminario, J. M.; Balbuena, P. B. *Chem. Rev.* **2017**, 117, 9674.
- (127) Zhang, Y.; Lucier, B. E. G. G.; Huang, Y. *Phys. Chem. Chem. Phys.* **2016**, 18, 8327.

- (128) Vieira, R.; Marin-Montesinos, I.; Pereira, J.; Fonseca, R.; Ilkaeva, M.; Sardo, M.; Mafra, L. J. *Phys. Chem. C* **2021**, 125, 14797.
- (129) Bertmer, M. *Annu. Reports NMR Spectrosc.* **2020**, 101, 1.
- (130) Inukai, M.; Kurihara, T.; Noda, Y.; Jiang, W.; Takegoshi, K.; Ogiwara, N.; Kitagawa, H.; Nakamura, K. *Phys. Chem. Chem. Phys.* **2020**, 22, 14465.
- (131) Lu, Y.; Lucier, B. E. G.; Zhang, Y.; Ren, P.; Zheng, A.; Huang, Y. *Phys. Chem. Chem. Phys.* **2017**, 19, 6130.
- (132) Chen, S.; Lucier, B. E. G.; Boyle, P. D.; Huang, Y. *Chem. Mater.* **2016**, 28, 5829.
- (133) Xu, J.; Sinelnikov, R.; Huang, Y. *Langmuir* **2016**, 32, 5468.
- (134) Lucier, B. E. G.; Chan, H.; Zhang, Y.; Huang, Y. *Eur. J. Inorg. Chem.* **2016**, 2016, 2017.
- (135) Forse, A. C.; Gonzalez, M. I.; Siegelman, R. L.; Witherspoon, V. J.; Jawahery, S.; Mercado, R.; Milner, P. J.; Martell, J. D.; Smit, B.; Blümich, B.; Long, J. R.; Reimer, J. *A. J. Am. Chem. Soc.* **2018**, 140, 1663;
- (136) Forse, A. C.; Colwell, K. A.; Gonzalez, M. I.; Benders, S.; Torres-Gavosto, R. M.; Blümich, B.; Reimer, J. A.; Long, J. R. *Chem. Mater.* **2020**, 32, 3570.
- (137) Sin, M.; Kavooosi, N.; Rauche, M.; Pallmann, J.; Paasch, S.; Senkovska, I.; Kaskel, S.; Brunner, E. *Langmuir* **2019**, 35, 3162–3170.
- (138) Forse, A. C.; Altobelli, S. A.; Benders, S.; Conradi, M. S.; Reimer, J. A. *J. Phys. Chem. C* **2018**, 122, 15344.
- (139) Peksa, M.; Lang, J.; Stallmach, F. *Microporous Mesoporous Mater.* **2015**, 205, 11.

- (140) Forse, A. C.; Milner, P. J.; Lee, J.-H.; Redfearn, H. N.; Oktawiec, J.; Siegelman, R. L.; Martell, J. D.; Dinakar, B.; Porter-Zasada, L. B.; Gonzalez, M. I.; Neaton, J. B.; Long, J. R.; Reimer, J. A. *J. Am. Chem. Soc.* **2018**, 140, 18016.
- (141) Bon, V.; Pallmann, J.; Eisbein, E.; Hoffmann, H. C.; Senkowska, I.; Schwedler, I.; Schneemann, A.; Henke, S.; Wallacher, D.; Fischer, R. A.; Seifert, G.; Brunner, E.; Kaskel, S. *Microporous Mesoporous Mater.* **2015**, 216, 64.
- (142) Gul-E-Noor, F.; Michel, D.; Krautscheid, H.; Haase, J.; Bertmer, M. *J. Chem. Phys.* **2013**, 139, 034202.
- (143) Wu, B.; Wong, Y. T. A.; Lucier, B. E. G.; Boyle, P. D.; Huang, Y. *ACS Omega* **2019**, 4, 4000.
- (144) Zhang, Y.; Lucier, B. E. G.; McKenzie, S. M.; Arhangelskis, M.; Morris, A. J.; Friščić, T.; Reid, J. W.; Terskikh, V. V.; Chen, M.; Huang, Y. *ACS Appl. Mater. Interfaces* **2018**, 10, 28582.
- (145) Peksa, M.; Burrekaew, S.; Schmid, R.; Lang, J.; Stallmach, F. *Microporous Mesoporous Mater.* **2015**, 216, 75.
- (146) Kong, X.; Scott, E.; Ding, W.; Mason, J. A.; Long, J. R.; Reimer, J. A. *J. Am. Chem. Soc.* **2012**, 134, 14341.
- (147) Lin, L.-C.; Kim, J.; Kong, X.; Scott, E.; McDonald, T. M.; Long, J. R.; Reimer, J. A.; Smit, B. *Angew. Chemie Int. Ed.* **2013**, 52, 4410.
- (148) Marti, R. M.; Howe, J. D.; Morelock, C. R.; Conradi, M. S.; Walton, K. S.; Sholl, D. S.; Hayes, S. E. *J. Phys. Chem. C* **2017**, 121, 25778.
- (149) Price, W. S. *Spin Dynamics: Basics of Nuclear Magnetic Resonance*, 2nd Ed.; **2009**; Vol. 34A.
- (150) Vold, R. L.; Hoatson, G. L. *J. Magn. Reson.* **2009**, 198, 57.
- (151) Melix, P.; Heine, T. *ChemPhysChem* **2021**, 22, 2336.

- (152) Dietzel, P. D. C.; Blom, R.; Fjellvåg, H. *Eur. J. Inorg. Chem.* **2008**, 23, 3624.
- (153) Arstad, B.; Fjellvåg, H.; Kongshaug, K. O.; Swang, O.; Blom, R. *Adsorpt.* **2008**, 14, 755.
- (154) Li, J.-R.; Sculley, J.; Zhou, H.-C. *Chem. Rev.* **2011**, 112, 869.
- (155) Keskin, S.; van Heest, T. M.; Sholl, D. S. *ChemSusChem* **2010**, 3, 879.
- (156) Kolle, J. M.; Fayaz, M.; Sayari, A. *Chem. Rev.* **2021**, 121, 7280.
- (157) Liu, X.; Wang, X.; Kapteijn, F. *Chem. Rev.* **2020**, 120, 8303.
- (158) Chanut, N.; Bourrelly, S.; Kuchta, B.; Serre, C.; Chang, J.-S.; Wright, P. A.; Llewellyn, P. L. *ChemSusChem* **2017**, 10, 1543.
- (159) Li, P.; Chen, J.; Zhang, J.; Wang, X. *Sep. Purif. Rev.* **2015**, 44, 19.
- (160) Liu, B.; Vikrant, K.; Kim, K.-H.; Kumar, V.; Kailasa, S. K. *Environ. Sci. Nano* **2020**, 7, 1319.
- (161) Chanut, N.; Bourrelly, S.; Kuchta, B.; Serre, C.; Chang, J.-S.; Wright, P. A.; Llewellyn, P. L. *ChemSusChem* **2017**, 10, 1543.
- (162) Birsa Čelič, T.; Mazaj, M.; Guillou, N.; Elkaïm, E.; El Roz, M.; Thibault-Starzyk, F.; Mali, G.; Ranguš, M.; Čendak, T.; Kaučič, V.; Zabukovec Logar, N. *J. Phys. Chem. C* **2013**, 117, 14608.
- (163) Gul-E-Noor, F.; Jee, B.; Pöpl, A.; Hartmann, M.; Himsl, D.; Bertmer, M. *Phys. Chem. Chem. Phys.* **2011**, 13, 7783.
- (164) Gul-E-Noor, F.; Michel, D.; Krautscheid, H.; Haase, J.; Bertmer, M. *Microporous Mesoporous Mater.* **2013**, 180, 8.
- (165) E. Khudozhitkov, A.; S. Arzumanov, S.; V. Toktarev, A.; V. Cherepanova, S.; A. Gabrienko, A.; I. Kolokolov, D.; G. Stepanov, A. *Phys. Chem. Chem. Phys.* **2021**, 23, 18925.

Chapter 2

2 Basics of solid-state NMR spectroscopy

Thorough structural characterization of MOFs is important because it allows the understanding of the relationship between the properties and structures of these materials. It facilitates the rational design of advanced materials with improved properties. Solid-state NMR (SSNMR) spectroscopy has emerged as a powerful spectroscopic technique complementary to XRD as it probes the short-range ordering and local structure around the nucleus of interest. SSNMR can provide information on the chemical composition, local environment, pore connectivity, and host-guest interactions of solid materials.¹⁻⁷

2.1 Physical background

Most atomic nuclei possess a type of angular momentum called spin (I). In general, (i) isotopes with even mass numbers have integer spin and isotopes with odd mass numbers have half-integer spin; (ii) when the number of proton and neutrons are both even, the nuclear spin is zero, $I = 0$, and (iii) when the number of protons and neutrons are both odd, the spin is an integer larger than zero. For example, the ^{12}C isotope has 6 neutrons and 6 protons, therefore it has a nuclear spin of zero and is not an NMR-active nucleus. On the other hand, the ^{13}C isotope has 6 protons and 7 neutrons and an odd atomic mass. Therefore, the ^{13}C isotope has a half-integer spin ($I = 1/2$).⁸⁻¹⁰

Another important intrinsic characteristic of nuclei is magnetism. The magnetic moment, μ , and the spin angular momentum of a nucleus are related to each other by:

$$\mu = \gamma I$$

where γ is the gyromagnetic ratio (also called magnetogyric ratio) of the nucleus and is normally specified in unit of $\text{rad s}^{-1} \text{T}^{-1}$.

In order to understand NMR, it is important to realize that the nucleus with its magnetic and electric properties can interact with magnetic and electric environments.⁸⁻¹⁰

2.2 Zeeman interaction

This interaction occurs between nuclear spins and the static external magnetic field applied, B_0 . A nucleus with nuclear spin I has $2I + 1$ possible energy levels. These energy levels are distinguished by the magnetic quantum numbers m_I , where $m_I = -I, -I + 1, \dots, I - 1, I$. In the absence of B_0 , these energy levels are degenerate. However, under the influence of an external magnetic field, the nuclear spin energies become different. The energies are given by:

$$E = -\gamma\hbar B_0 m_I \text{ (Equation 2.1)}$$

where γ is the gyromagnetic ratio, \hbar is the reduced Planck's constant ($h/2\pi$), B_0 is the external magnetic field, and m_I is the magnetic quantum number.⁸⁻¹⁰

For example, ^1H has a spin of $I = 1/2$. There are 2 possible energy levels ($2 \cdot 1/2 + 1 = 2$) specified by the magnetic quantum numbers $m_I = -1/2$ and $m_I = +1/2$ (Figure 2.1).

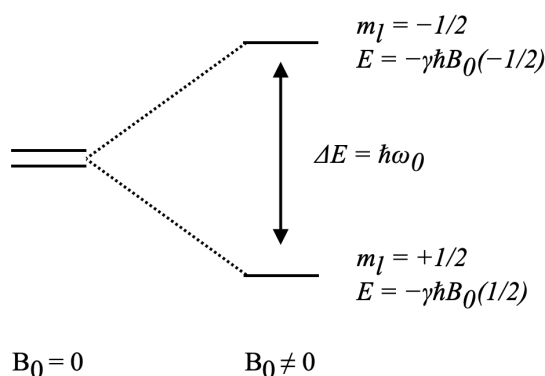


Figure 2.1. Representation of the Zeeman interaction for a spin-1/2 nucleus.

In the presence of B_0 , these two levels split by $\Delta E = -\gamma\hbar B_0$, and the energy difference is directly proportional to the frequency of precession, ω_0 , also called the Larmor frequency, given in unit of rad s^{-1} :

$$\Delta E = \hbar\omega_0 \text{ (Equation 2.2)}$$

$$\omega_0 = -\gamma B_0 \text{ (Equation 2.3)}$$

The relationship between ΔE and B_0 indicates that the increase in the magnetic field increases the energy difference, which in turn increases the population differences according to the Boltzmann distribution:

$$\frac{N_\beta}{N_\alpha} = e^{\frac{-\Delta E}{kT}} \text{ (Equation 2.4)}$$

where N_β and N_α are the populations of the higher and lower energy levels, respectively, k is the Boltzmann constant and T is temperature in K. Since a larger energy separation gap leads to a greater population difference, a subsequent increase in the signal to noise ratio within the measured spectrum is expected.⁸⁻¹⁰

2.2.1 Chemical shielding (CS) interaction

When an external magnetic field is applied to an atom in a molecule, it induces circulating currents of electrons that, in turn, produce a small magnetic field. This induced magnetic field can add to or subtract from the external field experienced by the nucleus, changing its resonance frequency. The degree to which the electron density is affected by applied field, B_0 , depends on the orientation of the molecule with respect to B_0 .⁸⁻¹⁰

The CS interaction is represented by the following Hamiltonian:

$$\hat{H}_{CS} = -\gamma\hbar\hat{I}\cdot\sigma\cdot B_0 \text{ (Equation 2.5)}$$

where \hat{I} is the spin operator and σ is the nuclear magnetic shielding tensor, or CS tensor.

The nuclear magnetic shielding can be represented by a second-rank tensor with three principal components σ_{11} , σ_{22} , σ_{33} . This tensor is described by a 3×3 matrix:

$$\sigma_{PAS} = \begin{bmatrix} \sigma_{11} & 0 & 0 \\ 0 & \sigma_{22} & 0 \\ 0 & 0 & \sigma_{33} \end{bmatrix}$$

The tensor components are defined so that σ_{11} corresponds to the least shielded component and σ_{33} to the most shielded component: $\sigma_{11} \leq \sigma_{22} \leq \sigma_{33}$. In powdered samples, the molecules have all possible orientations, which often results in a very broad NMR spectrum, called powder pattern. The broad pattern arises from the distribution of many signals with different frequencies depending on the molecular orientation with respect to B_0 .⁸⁻¹⁰ It is convenient to describe the tensor in terms of chemical shift, δ , which are reported relative to a reference sample:

$$\delta_{ii} = \frac{\sigma_{ii}^{\text{ref}} - \sigma_{ii}^{\text{obs}}}{1 - \sigma_{ii}^{\text{ref}}} \text{ (Equation 2.6)}$$

where σ_{ii}^{ref} is the component of the chemical shielding and the observed sample, respectively.⁸⁻¹⁰ The δ_{ii} being δ_{11} , δ_{22} , and δ_{33} represent the three directions of the CS tensor.

There are three major conventions used to describe the chemical shift anisotropy: (i) the IUPAC convention;¹¹ (ii) the Maryland convention;¹² and (iii) the Haeberlen convention.¹³ Herein, we will use the Maryland convention and therefore, only this convention will be described. The Maryland convention is derived from the three principle components δ_{11} , δ_{22} , and δ_{33} of the chemical shift tensor and defines three different parameters: (i) isotropic chemical shift, δ_{iso} ; (ii) span, Ω ; and (iii) skew, κ . These parameters are given by:

$$\delta_{\text{iso}} = \frac{\delta_{11} + \delta_{22} + \delta_{33}}{3} \text{ (Equation 2.7)}$$

$$\Omega = \delta_{11} - \delta_{33} \text{ (Equation 2.8)}$$

$$\kappa = \frac{3(\delta_{22} - \delta_{\text{iso}})}{\Omega} \text{ (Equation 2.9)}$$

The chemical shift anisotropy (CSA) of the powder pattern is given by the span. The value of δ_{iso} corresponds to that of observed in solution spectra. The Ω determines the width of the powder pattern. The skew describes the shape of the powder pattern. The effect of these parameters on the CSA pattern is depicted in Figure 2.2.⁸⁻¹⁰

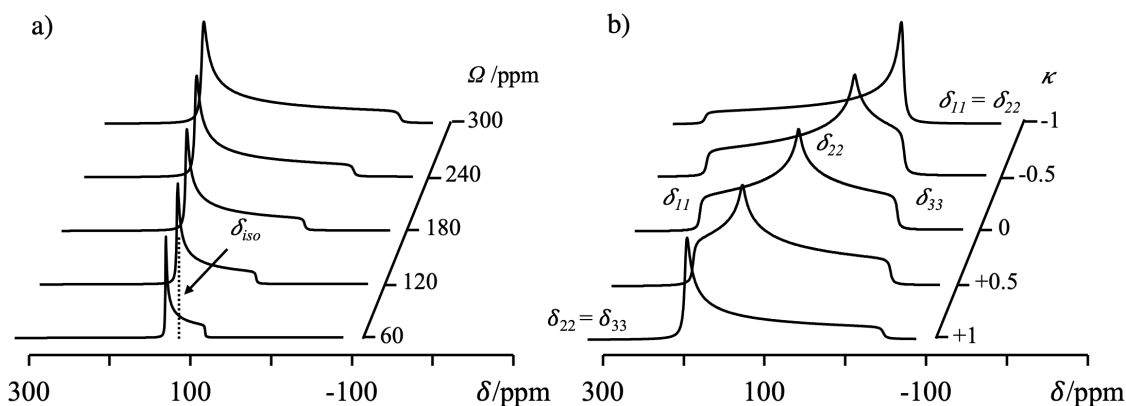


Figure 2.2. Analytical simulations of theoretical ^{13}C CSA powder patterns depicting the effect of Ω and κ ($\delta_{\text{iso}} = 0$ ppm) at a magnetic field of 9.4 T. In a) the span is varied from 0 to 300 ppm while the δ_{iso} and skew are kept constant at 0 ppm and +1 respectively. In b) the skew is varied from +1 to -1 while δ_{iso} and span are kept constant at 0 and 300 ppm respectively. Spectra were simulated using the Dmfit software.¹⁴

2.2.2 Dipole coupling interaction

The magnetic moments of the spins also interact through space with each other.

Therefore, the magnetic field produced by one spin will change the effective magnetic field experienced by another nucleus and vice versa. The degree to which the spin I affects the magnetic field experienced by spin S, or the strength of the dipolar coupling, is represented by the Hamiltonian:⁸⁻¹⁰

$$H_{\text{DD}} = -d(3 \cos^2 \theta - 1)[A + B + C + D + E + F] \quad (\text{Equation 2.10})$$

where θ is the orientation of the internuclear vector with respect to B_0 and d is the dipolar coupling constant, given by:

$$d = \left(\frac{\mu_0}{4\pi} \right) \frac{\hbar \gamma_I \gamma_S}{r_{\text{IS}}^3} \quad (\text{Equation 2.11})$$

The terms A, B, C, D, E, and F are known as the “dipolar alphabet”:⁸⁻¹⁰

$$A = \hat{I}_z \hat{S}_z (3 \cos^2 \theta - 1) \text{ (Equation 2.12)}$$

$$B = -\frac{1}{4} [\hat{I}_+ \hat{S}_- + \hat{I}_- \hat{S}_+] (3 \cos^2 \theta - 1) \text{ (Equation 2.13)}$$

$$C = -\frac{3}{2} [\hat{I}_z \hat{S}_+ + \hat{I}_+ \hat{S}_z] \sin \theta \cos \theta e^{+i\phi} \text{ (Equation 2.14)}$$

$$D = -\frac{3}{2} [\hat{I}_z \hat{S}_- + \hat{I}_- \hat{S}_z] \sin \theta \cos \theta e^{+i\phi} \text{ (Equation 2.15)}$$

$$E = -\frac{3}{4} [\hat{I}_+ \hat{S}_+] \sin^2 \theta e^{-2i\phi} \text{ (Equation 2.16)}$$

$$F = -\frac{3}{4} [\hat{I}_- \hat{S}_-] \sin^2 \theta e^{+2i\phi} \text{ (Equation 2.17)}$$

where θ and ϕ are polar angles and \hat{I}_+ , \hat{S}_+ and \hat{I}_- , \hat{S}_- are the raising and lowering operators respectively acting on spins I and S.

In solution, fast reorientation of molecules is isotropic, therefore the dipolar coupling is averaged to zero because of the $(3 \cos^2 \theta - 1)$ term. However, in the solid state, the presence of dipolar coupling produces a broad spectrum.⁸⁻¹⁰

The dipolar interaction between two different heteronuclei can be reduced by irradiating the sample at the resonant frequency of the nucleus to be decoupled, causing the net magnetization to flip rapidly compared to the interaction strength. This decoupling can enhance the resolution and sensitivity of the NMR spectra of samples containing heteronuclei.⁸⁻¹⁰

2.2.3 Quadrupolar interaction

In nuclei with spin greater than 1/2, the positive charge distribution of the nucleus is not spherical, generating an electric quadrupole moment, Figure 2.3.

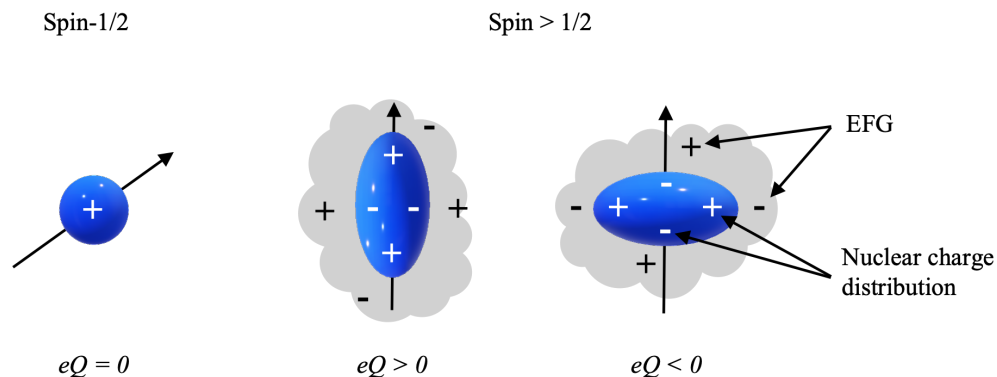


Figure 2.3. Representation of the nuclear charge distribution for spin-1/2 nuclei and quadrupolar nuclei (spin > 1/2).

The quadrupole moment is specific for each nucleus. The interaction of this quadrupole moment with the electric field gradient (EFG) surrounding the nucleus is called the quadrupolar interaction. Like the CS interaction, the EFG around the nucleus can be described by a tensor with three principal values which are associated with three principal axes. These values are related by:

$$V_{xx} + V_{yy} + V_{zz} = 0 \text{ (Equation 2.18)}$$

with V_{xx} , V_{yy} , and V_{zz} being the principal values in the x, y, and z directions.⁸⁻¹⁰

The magnitude of the quadrupolar interaction is defined by the quadrupolar coupling constant (C_Q) as the product of quadrupole moment and largest EFG tensor component, V_{zz} :

$$C_Q = \frac{e \cdot Q \cdot V_{zz}}{h} \text{ (Equation 2.19)}$$

where e is the elementary charge (1.602×10^{-19} C), Q is the constant that describes the nuclear electric quadrupole moment, V_{zz} is the z component of the EFG felt at the nucleus, and h is the Planck's constant.⁸⁻¹⁰

The "shape" or asymmetry of the EFG tensor is given by:

$$\eta_Q = \frac{V_{xx} - V_{yy}}{V_{zz}} \text{ (Equation 2.20)}$$

Generally, the quadrupolar interaction is treated as a perturbation to the Zeeman levels because it affects the energy of the levels. For example, for spin $I = 3/2$, there are four energy levels: $m_I = +3/2$, $m_I = +1/2$, $m_I = -1/2$, and $m_I = -3/2$. In the absence of an external magnetic field, these four energy levels are degenerated, that is, have the same energy. However, under the influence of an external magnetic field, these levels have different energies. This is illustrated in Figure 2.4.⁸⁻¹⁰

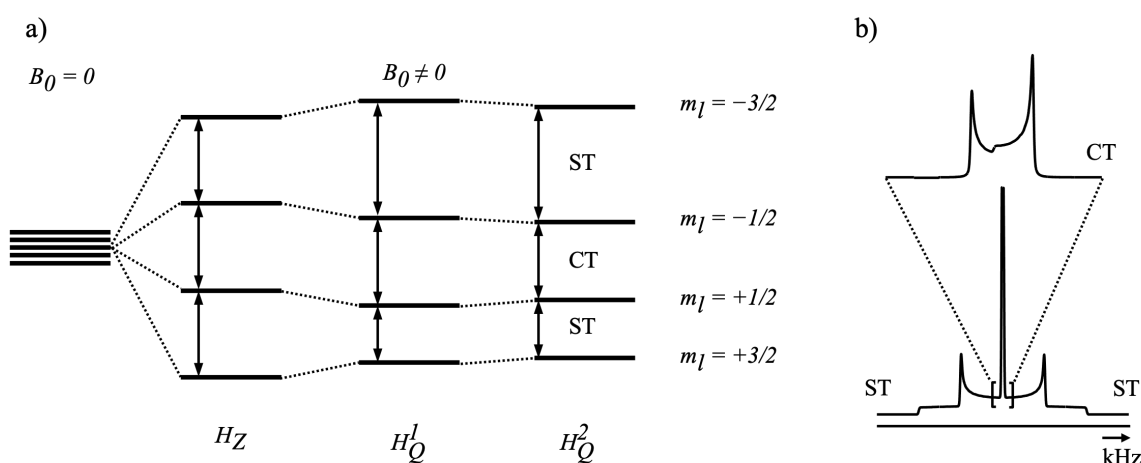


Figure 2.4. a) Representation of the energy level diagram of a spin-3/2 nucleus, showing the perturbation of the first- and second-order quadrupolar interactions; b) Typical quadrupolar line-shape of a spin-3/2 nucleus showing the satellite and central transitions.

The $m_I = +1/2 \leftrightarrow m_I = -1/2$ transition is called central transition (CT) and remains unaffected by the first-order interaction. The other two transitions are called satellite transitions (STs) and are affected by the first-order QI to a considerable extent. Hence, measurement of the CT transition is favored in SSNMR experiments because it has a narrower and more intense pattern than the ST signals. However, the CT can be affected by the second-order quadrupolar interaction.

When the second-order quadrupolar interaction is strong enough, the signal becomes broader and has a line-shape. The line-shape of the observed CT is described by the C_Q and the asymmetry parameter, η_Q . The effects of these parameters on the NMR powder pattern are depicted in Figure 2.5.

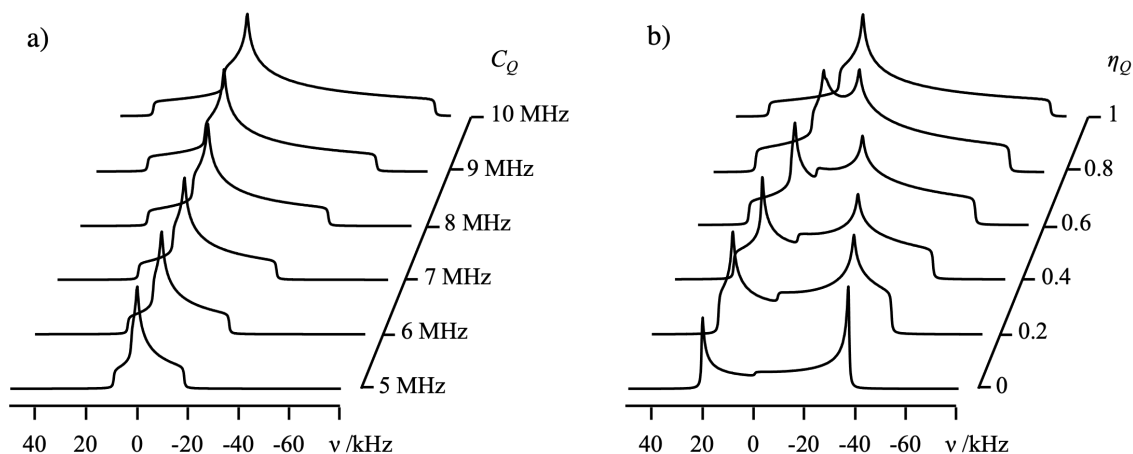


Figure 2.5. Illustration of the effects of a) the quadrupolar constant C_Q ($\delta_{\text{iso}} = 0$ ppm, $\eta_Q = 1$) and b) the asymmetry parameter η_Q ($\delta_{\text{iso}} = 0$ ppm, $C_Q = 8$ MHz) on the central transition of a spin-5/2 nuclei at 9.4 T. Spectra were simulated using the Dmfit software.¹⁴

The C_Q is related to the breadth of the powder pattern, while η_Q is related to the separation of the “horns” in the powder pattern. The breadth of the CT is inversely proportional to the Larmor frequency of the nucleus observed. Since the Larmor frequency is directly proportional to B_0 , the breadth of the CT is, therefore, inversely proportional to B_0 . Thus, the second-order quadrupolar interaction can be reduced by performing experiments at higher magnetic fields. The decrease in the breadth of the CT line-shape at higher magnetic fields is depicted in Figure 2.6.⁸⁻¹⁰

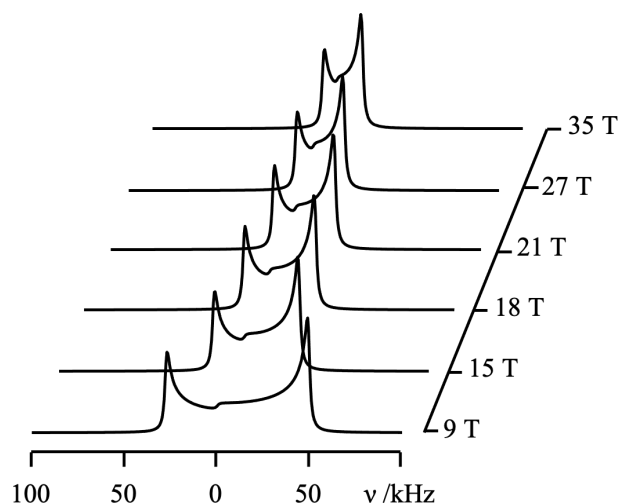


Figure 2.6. Illustration of the effects of the magnetic field on the central transition of a spin-5/2 nuclei with a C_Q of 8 MHz and η_Q of 0. Spectra were simulated using the Dmfit software.¹⁴

2.3 SSNMR spectroscopic methods in chemistry

In the most basic NMR experiment, called one pulse experiment (Figure 2.7), the sample is placed in a strong magnetic field which is aligned with the z-axis. After reaching thermal equilibrium, the produced magnetization is then rotated to the xy-plane by applying a radiofrequency (rf) field.

The rf field is then turned off and, as the magnetization precesses around the magnetic field, the signal is detected through their free induction decay (FID). The FID, given in time domain, is then processed through Fourier Transformation, yielding the NMR spectra in the frequency domain.⁸⁻¹⁰

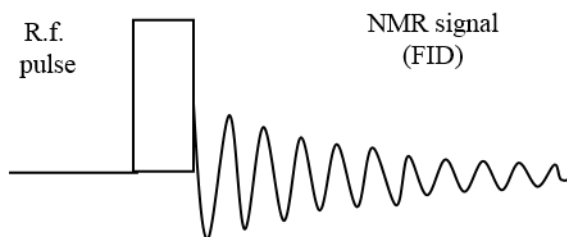


Figure 2.7. Illustration of the 1-pulse NMR sequence.

2.3.1 Magic Angle spinning (MAS)

In the solid-state, the anisotropic interactions described previously contain an angular dependent term ($3 \cos^2 \theta - 1$). Therefore, the effects of chemical shift anisotropy, dipolar interaction and the first-order quadrupolar interaction can be reduced or completely removed by spinning sample at the “magic-angle” 54.74° , when $(3 \cos^2 \theta - 1)$ is zero, ($\cos \theta = 1/\sqrt{3}$). Magic-angle spinning (MAS) is a technique in which the sample is packed into a rotor and spun at a rate in the order of kHz. The spinning axis is tilted at the magic angle with respect to B_0 . If the MAS frequency is larger than the respective anisotropic interaction strength, those interactions can be completely averaged to zero or to the δ_{iso} in the case of the CS interaction. If the averaging is incomplete, a manifold of spinning sidebands (SSBs) appears tracing out the shape of the static powder pattern.^{16,17} The SSBs are separated by the spinning frequency.

The effect of MAS on the CSA pattern of a spin $I = 1/2$ is depicted in Figure 2.8. MAS experiments greatly reduce the CS and dipolar interactions and allow for the acquisition of high-resolution spectra since the signals become very narrow.^{16,17} However, MAS techniques cannot completely average out the second-order quadrupolar interaction and therefore the central transition still has a line-shape and width (Figure 2.8). On one hand, this limits the acquisition of high-resolution spectra of samples containing quadrupolar nuclei. On the other hand, this allows for the extraction of the quadrupolar parameters, which provides important structural information as the line-shapes are highly affected by the EFG parameters.

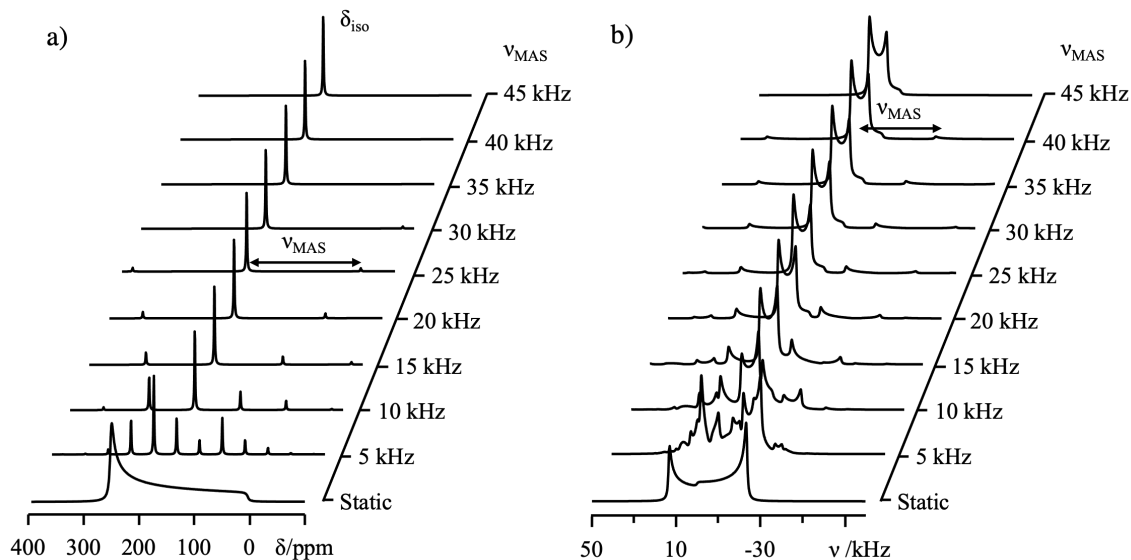


Figure 2.8. Effect of MAS on a) ^{13}C at 9.4 T ($\delta_{\text{iso}} = 150$ ppm, $\Omega = 225$ ppm, and $\kappa = 1$); and b) ^{17}O at 9.4 T ($C_Q = 8$ MHz and $\eta_Q = 0$). Spectra were simulated using the Dmfit software.¹⁴

2.3.2 Cross-polarization (CP)

CP involves the transfer of magnetization from abundant nuclei (I) such as ^1H to enhance the signal of rare nuclei (S) such as ^{13}C . The pulse sequence for a typical CP experiment (Figure 2.9) is based on the Hartmann-Hahn approach for establishing a dipolar contact between two different spin systems I and S.^{18,19} The Hartmann-Hahn condition is given by:

$$\gamma_I B_I = \gamma_S B_S \quad (\text{Equation 2.21})$$

where γ_D and γ_A are the gyromagnetic ratios of dilute spin S and abundant spin I, respectively, and B_S and B_I are the frequency fields that are applied for dilute spin S and abundant spin I.

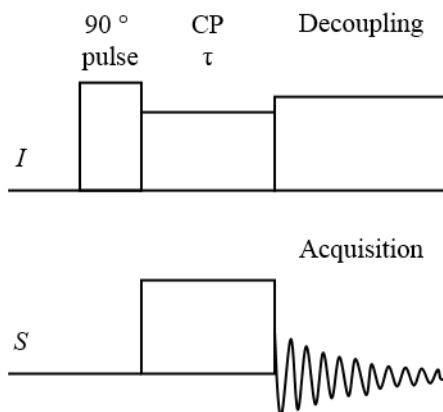


Figure 2.9. Illustration of pulse sequence for cross-polarization from abundant spin I to dilute spin S with detection of the S magnetization.

Initially, a 90° pulse is applied to the sensitive spin, I, to bring the net magnetization into the xy plane. Then, rf field is applied to spins I and S for a contact time, τ , promoting the transfer of magnetization from I to S. Finally, the S net magnetization is detected while the magnetization of nuclei I is decoupled.²⁰ When combined with MAS, CP can greatly enhance signal to noise ratio of the spectra of dilute spins. The maximum enhancement that can be expected by the cross-polarization is given by the ratio of gyromagnetic constants of spin I and spin S (γ_I/γ_S).^{18,19} For example, the maximum enhancement in signal to noise for the CP between ^1H and ^{13}C is 4:

$$\frac{\gamma_{^1\text{H}}}{\gamma_{^{13}\text{C}}} = \frac{26.8 \cdot 10^7 \text{ rad} \cdot \text{s}^{-1} \cdot \text{T}^{-1}}{6.72 \cdot 10^7 \text{ rad} \cdot \text{s}^{-1} \cdot \text{T}^{-1}} = 3.99 \text{ (Equation 2.22)}$$

2.3.3 Heteronuclear chemical shift correlation (HETCOR)

HETCOR is a two-dimensional (2D) experiment that allows for the correlation of ^1H chemical shifts with the chemical shifts of another nucleus, such as ^{13}C or ^{15}N . HETCOR is based on the heteronuclear dipolar interaction. A common example is the ^1H - ^{13}C frequency-switched Lee-Goldberg (FSLG) HETCOR experiment. The pulse sequence is depicted in Figure 2.10.^{21–23}

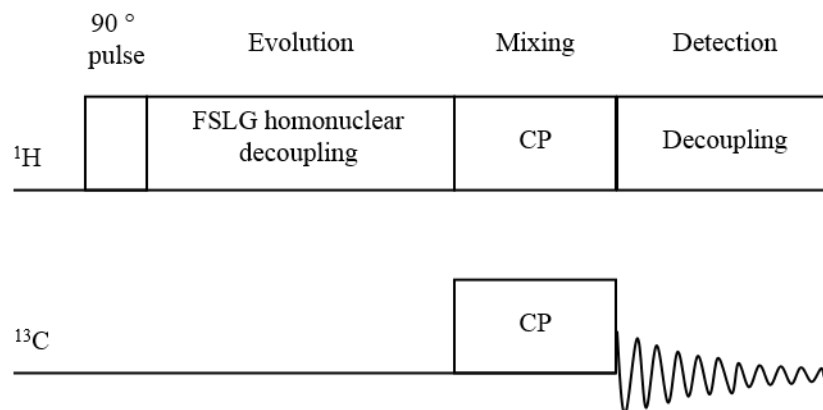


Figure 2.10. Pulse sequence for ^1H - ^{13}C FSLG-HETCOR experiments.

A 90° pulse is applied to the ^1H channel. During the evolution period, the ^1H chemical shifts evolve while the dipolar coupling is averaged by MAS and the FSLG pulse. Next, during the mixing period, a CP sequence is used to transfer the ^1H magnetization to ^{13}C . Finally, during the detection period, the ^{13}C FID is observed while the ^1H heteronuclear decoupling is applied. The resulting 2D spectrum displays the ^{13}C shifts in the direct dimension (F2) and the ^1H shifts in the indirect dimension (F1). FSLG is a homonuclear decoupling technique that consists of the application of the magic-angle pulse (θ_m) that produces an effective field in the rotating frame at the magic-angle with respect B_0 .^{24,25} This makes the spin precesses rapidly around the magic angle axis, which results in the averaging of ^1H - ^1H homonuclear dipolar coupling interaction. For heteronuclear decoupling, a two-pulse phase-modulation (TPPM) sequence is used.²²

2.3.4 Rotational echo double resonance (REDOR).

REDOR is a powerful experiment for determining the dipolar couplings between two unlike spins S and I.²⁶ A typical pulse sequence is depicted in Figure 2.11. Initially, a 90° pulse is applied to spin I channel, and then a series of rotor synchronized 180° pulses are applied to spin S, which recouples the dipolar interaction, resulting in a spectrum S with reduced signal for the observed nucleus I. The dephased spectrum S is compared to a control spectrum, S_0 , and the difference spectra, ΔS , provide correlation between nuclei I and S.²⁷

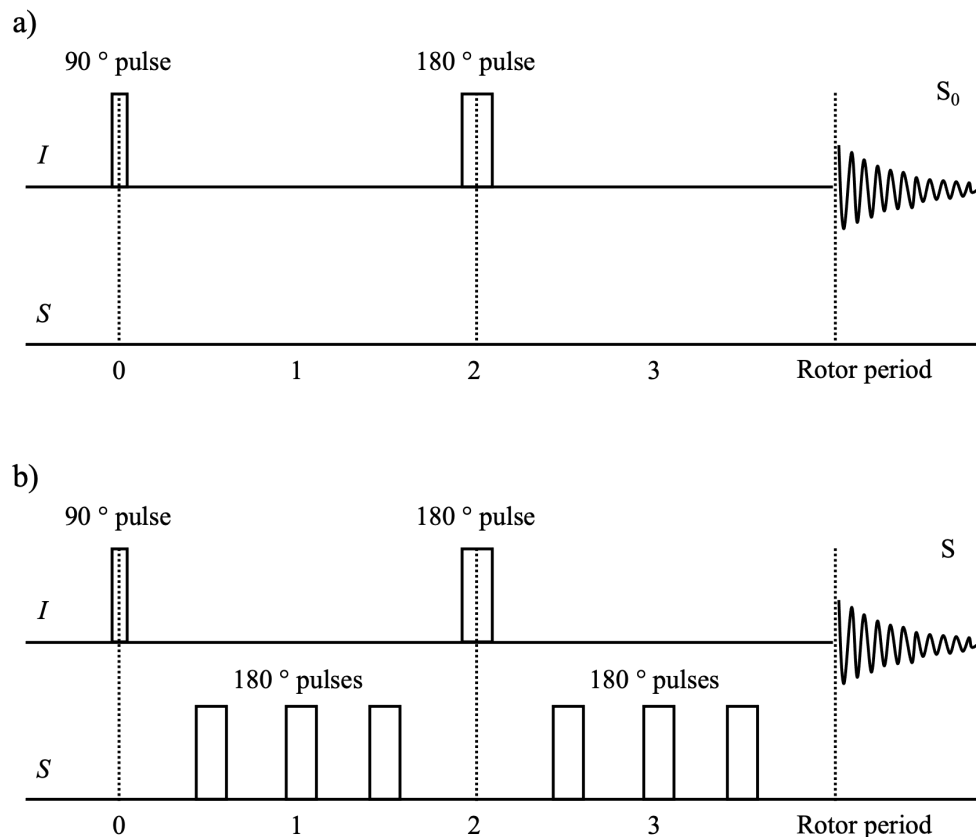


Figure 2.11. General REDOR pulse sequence. a) the control experiment providing the echo spectrum, S_0 , and b) the pulse sequence of the dephased spectrum S .

2.3.5 Triple-Quantum MAS (3QMAS)

As mentioned previously, the second-order quadrupolar interaction affects the central transition of quadrupolar nuclei, causing line broadening of the signal.

This broadening cannot be removed completely by MAS experiments.²⁸ 3QMAS is a 2D experiment that provides a high-resolution spectrum along the indirect dimension (F1) which correlates with the corresponding MAS spectrum in the direct dimension (F2).^{15,29,30} The spinning of the sample at the magic angle removes the CSA and the heteronuclear dipolar interactions while radiofrequency pulses are applied to manipulate the spins and remove the second-order quadrupolar interaction. The simplest version of

3QMAS experiments consists of two RF pulses with a delay between them. In the pulse sequence depicted in Figure 2.12, the first pulse excites all possible multiple quantum coherences and the desired one (i.e., $m_1 = 3/2 \leftrightarrow -3/2$) is selected by choosing an appropriate phase cycling (φ).²⁹

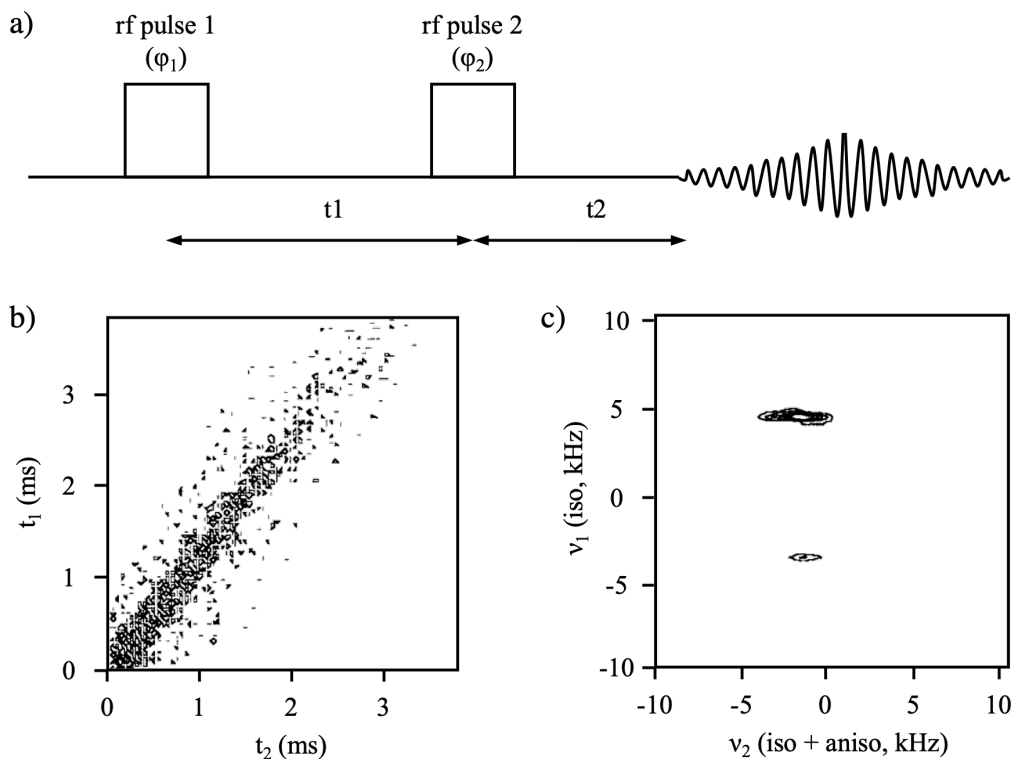


Figure 2.12. a) Schematics of the basic two-pulse sequence used for 3QMAS experiments; b) ^{23}Na data in time domain obtained from 3QMAS of sodium oxalate; and c) ^{23}Na data in frequency domain obtained from 3QMAS of sodium oxalate. Adapted from reference 15 with permission.

After the multiple quantum evolution time, t_1 , a second pulse is applied. This pulse converts the coherence back to single-quantum coherence and a purely isotropic second-order quadrupolar echo is formed at a time $t_2 = k \cdot t_1$. In the case of spin $3/2$, the constant k is equal to 3 and the dataset collected in the time domain is tilted, as shown in Figure

2.12. In order to process and get a 2D Fourier transformed spectrum in the frequency domain, a shear transformation by a factor equal to the coherence level ($k, 3/2$) must be applied.³¹ 3QMAS experiments often suffer from a low sensitivity. This is because the excitation of the 3Q coherences is not very efficient and requires strong rf pulses in the order of 100 kHz. For example, the maximum 3Q signal is approximately 55% of the CT signal for spin-3/2 nuclei.³² In order to improve the S/N ratio of 3QMAS spectra, rotor synchronized 3QMAS experiments can be performed. In this case, the spinning sidebands are folded back into the center band, increasing the S/N ratio.³³

Rice and coworkers have recently demonstrated the use of 3QMAS technique in characterization of the breathing behavior of the MIL-53 MOF synthesized with mixed metals (Al and Ga).³⁴ The authors collected ^{17}O 3QMAS spectra of ^{17}O -enriched MIL-53 samples and were able to identify and resolve the different oxygen species in the framework with similar chemical environments (Figure 2.13).

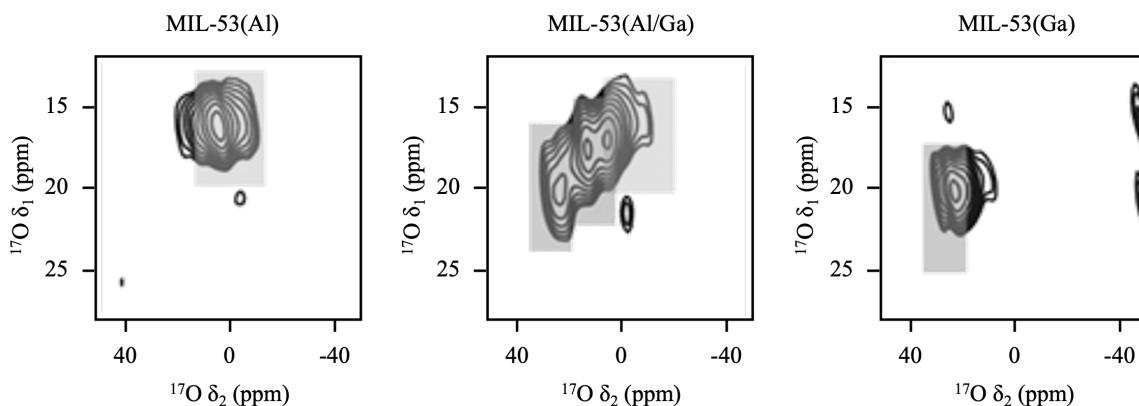


Figure 2.13. ^{17}O 3QMAS NMR spectra of activated MIL-53 synthesized with pure Al (left), 50/50 Al/Ga (middle), and pure Ga (right). Adapted from reference 34 with permission.

For example, the ^{17}O 3QMAS spectrum of the activated the pure MIL-53(Al) displayed only one signal in the hydroxyl region corresponding to a single Al-OH-Al species. Upon

increasing the concentration of Ga cations in the framework, additional signals at higher chemical shift appear, which were attributed to the Al-OH-Ga and Ga-OH-Ga. This additional signal is evident from the 3QMAS spectrum of the 50/50 mixture of Al/Ga. For the pure MIL-53(Ga), only the signal at high chemical shift attributed to the Ga-OH-Ga species is observed.

2.3.6 ^{13}C powder line-shape analysis

As mentioned previously, the CS interaction is anisotropic. This means that a change of molecular orientation causes a change in strength of the interaction. This in turn causes distinctive changes in the powder patterns, which depends on (i) the rate of the reorientation and (ii) the geometry of the molecular motion. The rate of reorientation is sometimes referred to as jump rate ($1/\tau$). In general, only motion in which τ is of the order of the nuclear spin interaction can be assessed via line-shape analysis. In the low ($\tau < 10^3$ Hz) and fast ($\tau > 10^7$ Hz) regimes, the line-shape remains constant.⁸⁻¹⁰

The geometry of the motion can be described by a change in the molecular orientation. Accordingly, the orientation of the molecule-fixed frame with respect to B_0 is defined by two polar angles θ and φ , as depicted in Figure 2.14.

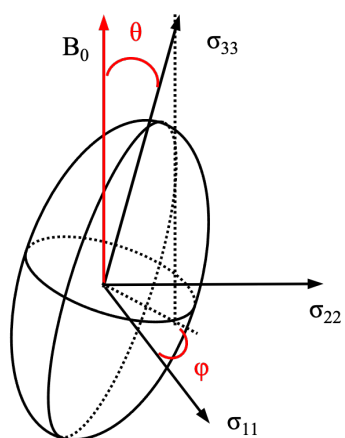


Figure 2.14. Representation of the two polar angles θ and φ with respect to the external magnetic field B_0 .

The rotation operator $R(\alpha, \beta, \gamma)$ rotates the Principal Axis System (PAS) of a particular Cartesian tensor into coincidence with a reference frame fixed in the laboratory.³⁵ This operator describes a rotation first through angle γ about the PAS z-axis, then through angle β about the original (PAS) y-axis and finally by angle α about the original (PAS) z-axis.³⁵ Each orientational site within a given jump frame is specified by Euler angles (α, β, γ) for the rotation that rotates the coordinate axes for this site into coincidence with the reference axes of the next frame. This process begins with the PAS for the EFG tensors (for experiments involving spin $I > 1/2$) or CSA tensors (for $I = 1/2$).³⁵

An example of the effect of the molecular motion on the ^{13}C powder pattern of CO_2 is depicted in Figure 2.15. The CO_2 molecules can undergo a motion called wobbling, in which it rotates around a C_6 axis. This motion can be described by an angle α (note that this is not a Euler angle). The increase of the wobbling angle causes a decrease in the breadth (or the span) of the line-shape. Another motion that CO_2 molecules can undergo is the hopping between two sites. This motion has an effect on the skew and span of the line-shape, as shown in Figure 2.15.

2.3.7 ^2H powder line-shape analysis

^2H solid-state NMR spectroscopy has been extensively used to probe molecular motion in solids.³⁶ The ^2H isotope is a quadrupolar nucleus with spin $I = 1$ and with a small quadrupole moment ($Q = 2.860 \text{ mb}$) compared to other quadrupolar nuclei in the periodic table.³⁷ In most compounds, the quadrupolar coupling constants of ^2H are small, ranging from 140 and 220 kHz. Despite small quadrupolar coupling constants, the ^2H powder pattern is broadened by the first-order quadrupolar interaction. This is because the ^2H has a spin $I = 1$ and therefore the CT is absent. Consequently, the CS interaction, dipolar coupling, and other interactions can be ignored since they are small compared to the QI.⁸ Under static conditions, when $\eta_Q = 0$ the typical ^2H line-shape has a symmetric doublet shape called “Pake” pattern, Figure 2.16.³⁸ A similar line-shape to that of water can be obtained for the π -flips around the benzene molecule. In this case, an angle of 120° yields a broader powder pattern compared to that of the π -flips of water.

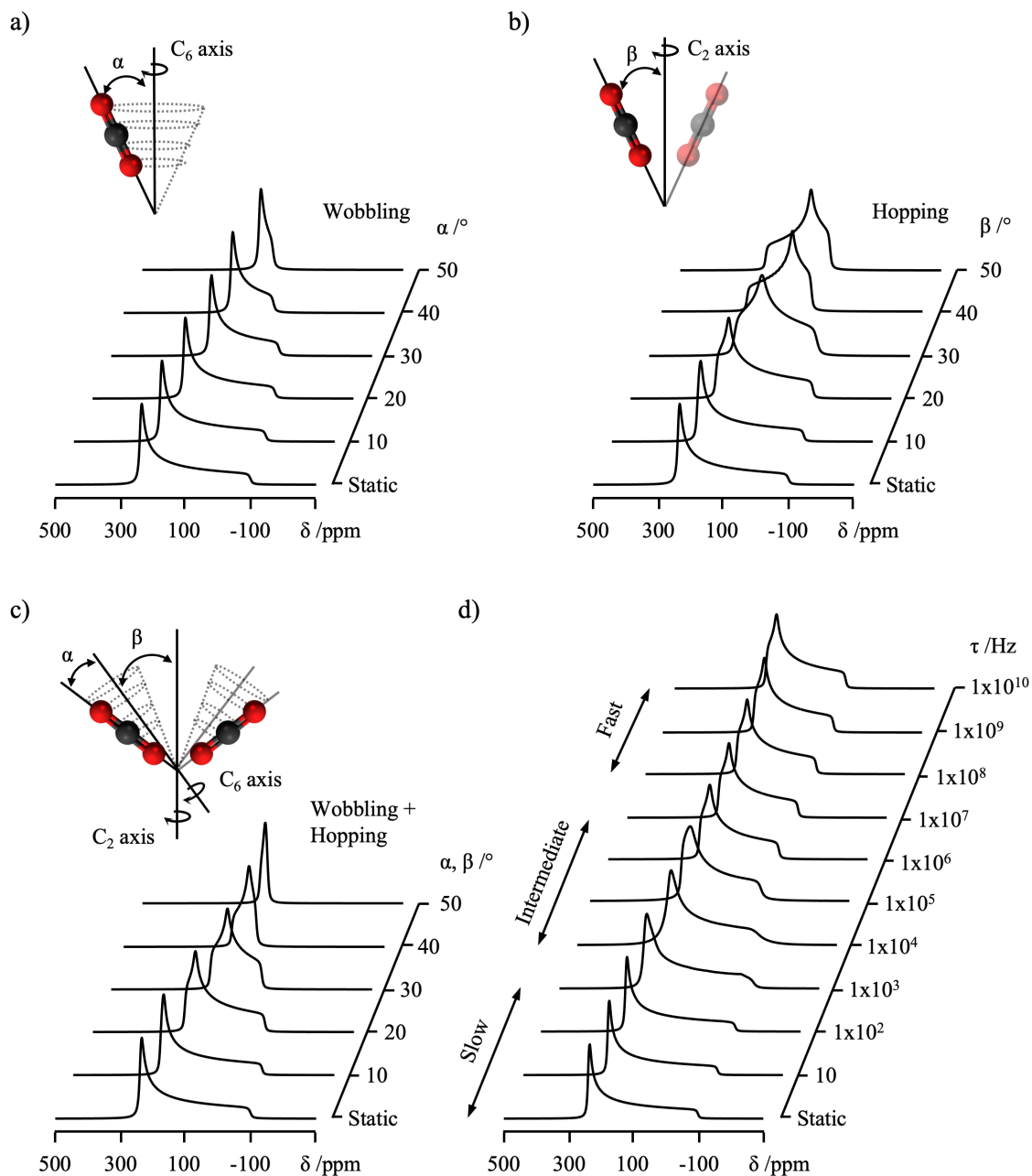


Figure 2.15. Representation of the effect of a) the localized C_6 wobbling, b) the delocalized C_2 hopping, and the combined wobbling and hopping motions on the ^{13}C line-shape of CO_2 . d) Representation of the effect of the rate of motion on the ^{13}C CSA line-shape of CO_2 . The spectra were simulated with the Express³⁵ software and using $\delta_{\text{iso}} = 125$ ppm, $\Omega = 335$ ppm, and $\kappa = 1$.

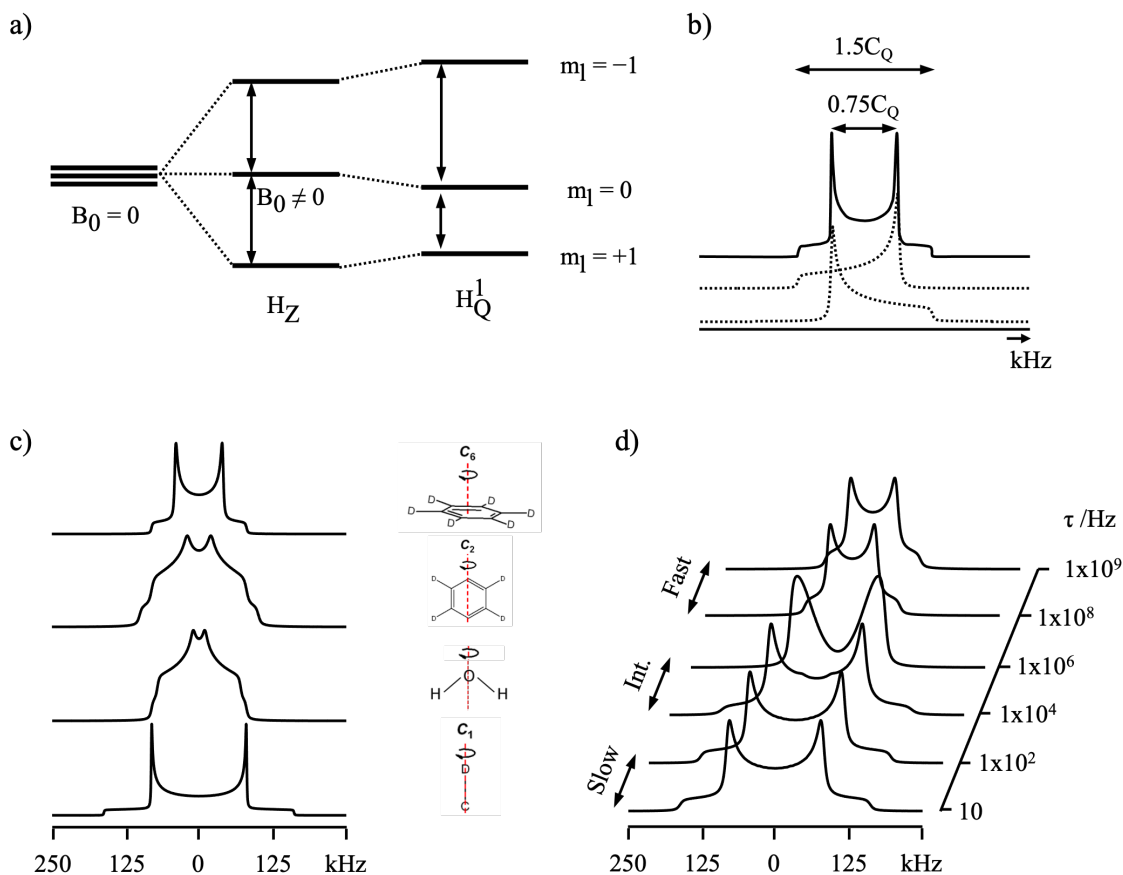


Figure 2.16. a) Energy level diagram of ^2H ($I = 1$); b) illustration of the Pake doublet; c) simulations of the effect of different motion on the ^2H powder pattern; and d) the effect of the jump rate on the ^2H line-shape.

Another example is the six-fold rotation of the benzene molecule. In this case, the “horns” are separated by $0.75C_Q$ and the breadth of the signal is given by $1.5C_Q$. Similar to the ^{13}C line-shapes, the ^2H Pake pattern is also sensitive to both the rate and reorientation geometry of the molecular motion. The difference is that in this case the EFG tensor principle axis frame is taken as the molecule-fixed frame.^{8–10} The effect of motions on the ^2H powder pattern is depicted in Figure 2.16. A static C– ^2H or O– ^2H bond always displays a Pake doublet-like NMR pattern. An important example of the ^2H line-shape is that of the π -flips of water with a H–O–H angle of 104.5° .

2.4 References

- (1) Reif, B.; Ashbrook, S. E.; Emsley, L.; Hong, M. *Nat. Rev. Methods Prim.* **2021**, 1, 1.
- (2) Ashbrook, S. E.; Smith, M. E. *Chem. Soc. Rev.* **2006**, 35, 718.
- (3) Li, S.; Lafon, O.; Wang, W.; Wang, Q.; Wang, X.; Li, Y.; Xu, J.; Deng, F. *Recent Adv. Mater.* **2020**, 32, 1.
- (4) Ashbrook, S. E.; Davis, Z. H.; Morris, R. E.; Rice, C. M. *Chem. Sci.* **2021**, 12, 5016.
- (5) Wu, G. *Prog. Nucl. Magn. Reson. Spectrosc.* **2008**, 52, 118.
- (6) Wu, G. *Prog. Nucl. Magn. Reson. Spectrosc.* **2019**, 114, 135.
- (7) Castiglione, F.; Mele, A.; Raos, G. *¹⁷O NMR: A “Rare and Sensitive” Probe of Molecular Interactions and Dynamics*, 1st Ed. Blackwell Science, **2002**.
- (8) Duer, M. J. *Solid State NMR Spectroscopy: Principles and Applications*, 2005.
- (9) Levitt, M. H. *Spin Dynamics: Basics of Nuclear Magnetic Resonance*, 2nd Ed. John Wiley and Sons, **2009**.
- (10) Fyfe, C. A. *Solid State NMR for Chemists*, 1st Ed. John Wiley and Sons, **1983**.
- (11) Harris, R. K., Becker, E. D., Menezes, S. M. C., Goodfellow, R., Granger, P. *Pure Appl. Chem.* **2001**, 73, 1795.
- (12) Mason, J. *Solid State Nucl. Magn. Reson.* **1993**, 2, 285.
- (13) Harris, R. K.; Becker, E. D.; Cabral De Menezes, S. M.; Granger, P.; Hoffman, R. E.; Zilm, K. W. *Pure Appl. Chem.* **2008**, 80, 59.
- (14) Massiot, D.; Fayon, F.; Capron, M.; King, I.; Le Calvé, S.; Alonso, B.; Durand, J. O.; Bujoli, B.; Gan, Z.; Hoatson, G. *Magn. Reson. Chem.* **2002**, 40, 70.

- (15) Medek, A.; Harwood, J. S.; Frydman, L. J. *Am. Chem. Soc* **1995**, 117, 12779.
- (16) Andrew, E. R.; Bradbury, A.; Eades, R. G. *Nature* **1958**, 182, 1659.
- (17) Lowe, I. J. *Phys. Rev. Lett.* **1959**, 2, 285.
- (18) Pines, A.; Gibby, M. G.; Waugh, J. S. *J. Chem. Phys.* **1972**, 56, 1776.
- (19) Pines, A.; Gibby, M. G.; Waugh, J. S. *J. Chem. Phys.* **2003**, 59, 569.
- (20) Fyfe, C. A.; Wong-Moon, K. C.; Huang, Y.; Grondey, H.; Mueller, K. T. *J. Phys. Chem.* **2002**, 99, 8707.
- (21) Caravatti, P.; Bodenhausen, G.; Ernst, R. R. *Chem. Phys. Lett.* **1982**, 89, 363.
- (22) Caravatti, P.; Braunschweiler, L.; Ernst, R. R. *Chem. Phys. Lett.* **1983**, 100, 305.
- (23) Van Rossum, B. J.; Schulten, E. A. M.; Raap, J.; Oschkinat, H.; De Groot, H. J. M. *J. Magn. Reson.* **2002**, 155, 1.
- (24) Lee, M.; Goldberg, W. I. *Phys. Rev.* **1965**, 140, A1261.
- (25) Bielecki, A.; Kolbert, A. C.; Levitt, M. H. *Chem. Phys. Lett.* **1989**, 155, 341.
- (26) Schnell, I. *Prog. Nucl. Magn. Reson. Spectrosc.* **2004**, 45, 145.
- (27) Gullion, T.; Schaefer, J. J. *Magn. Reson.* **1989**, 8, 196.
- (28) Wi, S.; Ashbrook, S. E.; Wimperis, S.; Frydman, L. J. *Chem. Phys.* **2003**, 118, 3131.
- (29) Vega, S.; Naor, Y. J. *Chem. Phys.* **1981**, 75, 75.
- (30) Goldbourt, A.; Madhu, P. K. *Curr. Dev. Solid State NMR Spectrosc.* 1st Ed. Springer, **2002**.
- (31) Hung, I.; Trébosc, J.; Hoatson, G. L.; Vold, R. L.; Amoureux, J. P.; Gan, Z. J. *Magn. Reson.* **2009**, 201, 81.

- (32) Amoureux, J. P.; Fernandez, C.; Frydman, L. *Chem. Phys. Lett.* **1996**, 259, 347.
- (33) Ashbrook, S. E.; Wimperis, S. J. *Magn. Reson.* **2005**, 177, 44.
- (34) Rice, C. M.; Davis, Z. H.; McKay, D.; Bignami, G. P. M.; Chitac, R. G.; Dawson, D. M.; Morris, R. E.; Ashbrook, S. E. *Phys. Chem. Chem. Phys.* **2020**, 22, 14514.
- (35) Vold, R. L.; Hoatson, G. L. *J. Magn. Reson.* **2009**, 198, 57.
- (36) Bräuniger, T.; Jansen, M. *Zeitschrift für Anorg. und Allg. Chemie* **2013**, 639, 857.
- (37) Harris, R. K.; Becker, E. D.; Menezes, S. M. C. de; Goodfellow, R.; Granger, P. *Pure Appl. Chem.* **2001**, 73, 1795.
- (38) Pake, G. E. *J. Chem. Phys.* **2004**, 16, 327.

Chapter 3

3 Higher Magnetic Fields, Finer MOF Structural Information: ^{17}O Solid-State NMR at 35.2 T

3.1 Introduction

The element of oxygen is ubiquitous across nearly all scientific fields. Therefore, the characterization of oxygen local electronic and geometric environments is very important. ^{17}O solid-state NMR (SSNMR) spectroscopy has become an ideal site-specific characterization tool for probing oxygen local environments, as ^{17}O is sensitive to the chemical shift and quadrupolar interactions,^{1,2,11,3-10} has a large diagnostic chemical shift range,^{12,13,22-25,14-21} and is influenced by coupling to neighboring NMR-active nuclei (e.g., ^1H , ^{13}C , and ^{15}N).²⁶⁻³¹ There has been tremendous progress made in NMR methodology and technology in recent years, yet the potential of ^{17}O SSNMR for uncovering detailed structural and bonding information in oxygen-containing compounds has been limited by the inherently low sensitivity and resolution resulting from the very low natural abundance (0.038%), relatively low gyromagnetic ratio ($\gamma = -5.774 \text{ MHz T}^{-1}$), and quadrupolar nature (spin $I = 5/2$) of ^{17}O .³²

The sensitivity problem associated with the low ^{17}O natural abundance can be mitigated by isotopic enrichment.¹⁶⁻²² To address the relatively low γ value and quadrupolar nature of ^{17}O , NMR measurements can be performed at high magnetic fields; this not only inherently enhances sensitivity but also reduces spectral line broadening associated with the second-order quadrupolar interaction. A new series-connected resistive/superconducting hybrid magnet operating at a record-high magnetic field strength of 35.2 T (^1H Larmor frequency of 1.5 GHz) has recently entered service,³³ which promises very high ^{17}O SSNMR resolution in biomolecules and minerals.³³⁻³⁵ In this work, taking advantage of the state of the art magnet and rf technology, we targeted microporous $\alpha\text{-Mg}_3(\text{HCOO})_6$ to demonstrate that a very high spectral resolution of ^{17}O SSNMR spectra can be achieved at 35.2 T, providing an excellent opportunity for characterizing promising materials such as metal-organic frameworks (MOFs).

MOFs are a fascinating family of hybrid organic–inorganic porous materials with many practical applications.^{36,37} SSNMR spectroscopy of MOFs has proven to be a powerful tool for characterizing the immediate environment about metal centers and probing the local structure of organic linkers.^{38–40} SSNMR can also provide information on the behavior of adsorbed guests, which is critically important for many applications.^{41,42} For example, MOFs are promising materials for the removal of greenhouse gases such as CO₂ and storage of fuels such as H₂ and CH₄. SSNMR can provide information on the location of guest species,^{10,43–47} which is critically important for practical applications, as the location of guest gas molecules can be directly linked to binding site positions and strength, respectively. Similarly, ascertaining the location of guest species in MOFs is key to understanding their applications in sensing and drug delivery.^{48–51} Oxygen present in various carboxylate ligands, which are the most extensively used organic linkers, is a key constituent of many important MOFs.^{52–56} Oxygen anions (O²⁻) are also associated with the metal clusters of the frameworks (e.g., MOF-5).⁵² Hydroxyl groups are common linkers bridging metal clusters (e.g., MIL-53)⁵³ and exist as part of the secondary building units (e.g., UiO-66).⁵⁴ Water molecules can directly bond to the metal center, with well-known examples including as-made MOF-74 and HKUST-1.^{55,56} These oxygen species play critical roles in applications such as guest adsorption/separation,⁵⁷ sensing,⁴⁸ catalysis,⁵⁸ solid-state conductors,⁵⁹ and biomedicine,^{49–51} rendering oxygen a key target for MOF characterization. Although ¹⁷O SSNMR has been utilized to examine some MOFs,^{10,15–17} potential successes in molecular-level characterization and site assignment have been limited by spectral resolution.

Microporous α -Mg₃(HCOO)₆ is an attractive target for ¹⁷O SSNMR characterization for several reasons.

- (i) Microporous α -Mg₃(HCOO)₆ is a commercially available and low-cost MOF with good molecular selectivity, such as a preference for C₂H₂ over CO₂.^{60,61} It is a representative small-pore MOF suitable for gas adsorption.
- (ii) This MOF presents a very challenging case for characterization by ¹⁷O SSNMR, as the crystal structure features 12 inequivalent carboxylate oxygen sites across

two bonding modes. Using our highest available field of 21.1 T at the time, only two ^{17}O NMR signals corresponding to the two different oxygen bonding modes of formate anions could be observed (vide infra).¹⁶ As increasing the magnetic field from 21.1 to 35.2 T leads to an improvement in resolution by a factor of 2.8 (the second-order quadrupolar broadening in ppm varies as the inverse ratio of the fields squared),¹ resolving many of these inequivalent oxygen sites at 35.2 T should be possible.

(iii) The applications of MOFs require the removal of the solvent molecules from inside the pores of as-made MOFs in a process known as “activation”. Activation often leads to changes in the framework structure. While significant changes can be detected by X-ray diffraction, activation-induced changes for MOFs, including $\alpha\text{-Mg}_3(\text{HCOO})_6$, can be subtle (i.e., small changes in unit cell parameters), and the specific molecular-level alterations cannot be detected by diffraction-based methods. Thus, it is important to develop SSNMR as a method complementary to XRD. The high spectral resolution that can be achieved at 35.2 T holds promise for providing fine details on oxygen local environments, reflecting the changes resulting from activation.

(iv) MOFs have many potential applications across fields such as biology and medicine.^{62,63} Thus, nonconventional $\text{O}\cdots\text{H}-\text{C}$ hydrogen bonding involving guest species and bioactive components in the framework can play important roles for host–guest interactions in BioMOFs, a new subclass of MOFs,^{49,50} or MOF-based drug delivery systems.⁵¹ Since nonconventional $\text{O}\cdots\text{H}-\text{C}$ hydrogen bonding has been observed in as-made $\alpha\text{-Mg}_3(\text{HCOO})_6$ ($\text{C}_6\text{H}_6\text{Mg}_3\text{O}_{12}\cdot\text{C}_3\text{H}_7\text{NO}$, where $\text{C}_3\text{H}_7\text{NO}$ is *N,N'*-dimethylformamide or DMF),⁶⁴ this system has been selected as a model compound to explore the possibility of using ^{17}O SSNMR at 35.2 T to directly probe this weak host–guest interaction in MOF systems.

Our results show that the ^{17}O SSNMR spectra of $\alpha\text{-Mg}_3(\text{HCOO})_6$ samples acquired at 35.2 T indeed exhibit very high resolution, allowing many inequivalent framework oxygen sites to be identified. The high resolution and sensitivity realized at 35.2 T not

only lead to ultrafine information on oxygen local environment and corresponding subtle changes upon activation but also make it possible to detect weak host–guest interactions such as nonconventional O···H–C hydrogen bonding. To further illustrate the benefits of performing ^{17}O SSNMR at an ultrahigh field of 35.2 T, we examined two activated MOF MIL-53(Al) samples; the high spectral resolution and sensitivity allowed us to unambiguously distinguish partially activated from fully activated MIL-53(Al) samples. The very high resolution and sensitivity of ^{17}O SSNMR achievable at 35.2 T detailed in this work illustrates the great potential of SSNMR for unlocking fine structural information in solids as higher magnetic fields become increasingly available.

3.2 Experimental details

3.2.1 Synthesis and characterization of MOF samples

As-made ^{17}O -enriched $\alpha\text{-Mg}_3(\text{HCOO})_6$ was synthesized according to the reported procedure.¹⁶ The starting materials were used as received without further purification. A mixture of $\text{Mg}(\text{NO}_3)_2 \cdot 6\text{H}_2\text{O}$ (3 mmol, Aldrich) and HCOOH (6 mmol, Aldrich) was dissolved in 10 mL of DMF and 0.25 mL of ^{17}O -enriched H_2O (6 mmol, CortecNet, 35 atom %) in a 23 mL Teflon-lined autoclave. The container was sealed and heated at 383 K for 2 days. After the autoclave was cooled to room temperature, the white powder product was collected, washed with DMF, and dried overnight at 363 K. Activated ^{17}O -enriched $\alpha\text{-Mg}_3(\text{HCOO})_6$ was obtained by heating as-made ^{17}O -enriched $\alpha\text{-Mg}_3(\text{HCOO})_6$ at 423 K overnight under dynamic vacuum. The PXRD patterns of ^{17}O -enriched $\alpha\text{-Mg}_3(\text{HCOO})_6$ samples are shown in Figure A3.1 in the Supporting Information.

In the experimental PXRD patterns of as-made and activated $\alpha\text{-Mg}_3(\text{HCOO})_6$, the two low-angle reflections at $2\theta = 9.7^\circ$ (-101) and 9.9° (101) are much weaker than the reflection at 10.7° (011), which strays from the comparable intensities apparent in the simulated PXRD spectra. A previous study demonstrated that the PXRD patterns of $\alpha\text{-Mg}_3(\text{HCOO})_6$ crystals prepared under different synthetic conditions may exhibit different intensity patterns.⁶⁵ In particular, the three low-angle reflections at 9.7° , 9.9° , and 10.7° have different relative intensities if water is involved. For $\alpha\text{-Mg}_3(\text{HCOO})_6$ samples prepared in the presence of water, the relative intensity pattern for the three

aforementioned low-angle diffractions looks very similar to that seen in Figure A3.1 but is distinct from the simulated PXRD pattern based on the structure determined from a single crystal prepared in nonaqueous DMF solvent.⁶⁰ In the present work, ¹⁷O-enriched α -Mg₃(HCOO)₆ was prepared in the presence of ¹⁷O-enriched H₂O. Although the synthesis of α -Mg₃(HCOO)₆ is very straightforward and highly reproducible, and we have made this MOF routinely in many studies with and without water,^{16,43–46,64,66–68} to unambiguously confirm the identity of the samples used in the present study, we repeated the sample preparation several times. These additional samples were prepared under the exact same conditions used for preparing ¹⁷O-enriched MOF, except that normal water was used rather than ¹⁷O-enriched water. Figure A3.1 indicates that when the samples were prepared in the presence of a small amount of water, the relative intensities of the first two low-angle reflections are significantly lower than that of the third reflection, which is consistent with the literature.⁶⁵ We performed a Le Bail fit of the PXRD data using the GSAS II package (Figure A3.2)⁶⁹ and obtained unit cell parameters of the samples prepared in the presence of water that are comparable to those reported in the literature (Table A3.1); these data indicate that, although the relative intensities of reflections may differ, the samples indeed share the same crystal structure.

The activation process for this MOF has been proven to be robust.^{60,64,66,70} To verify that the solvent DMF molecules occluded inside the channels are completely removed upon activation, TGA profiles and ¹H–¹³C CP/MAS SSNMR spectra were obtained (Figure A3.3 and Figure A3.4). The results unanimously agree that the activation process is very effective, and the solvent molecules are completely removed. The synthesis of ¹⁷O-enriched MIL-53(AI) samples and corresponding PXRD patterns can be found in Figure A3.5 and Figure A3.6.

3.2.2 ¹⁷O solid-state NMR measurements

The 1D rotor-synchronized spin–echo spectrum of activated α -Mg₃(HCOO)₆ was recorded at 21.1 T (¹⁷O Larmor frequency of 122.0 MHz) on a Bruker Avance II spectrometer at the National Ultrahigh-Field NMR Facility for Solids in Ottawa, Ontario, Canada. A 4 mm H/X MAS Bruker probe and a spinning frequency of 18 kHz were used. The recycle delay was 4 s. A $\pi/2$ pulse of 4 μ s was used.

1D and 2D ^{17}O SSNMR experiments at 35.2 T were performed on the series-connected hybrid (SCH) magnet (^{17}O Larmor frequency of 203.4 MHz) at the National High Magnetic Field Laboratory (NHMFL) in Tallahassee, FL, USA.³³ A Bruker Avance NEO console and a NHMFL home-built single-resonance 3.2 mm low- γ MAS probe were used, along with a spinning frequency of 18 kHz and a pulse delay of 0.1 s. The pulse delay was optimized to achieve the highest S/N, and no significant changes in NMR line-shapes were observed when different pulse delays were employed. A $\pi/2$ pulse of 5.0 μs was used in 1D rotor-synchronized spin echo experiments. All rotor-synchronized 3QMAS spectra were acquired using the shifted-echo pulse sequence.⁷¹ The 3Q excitation and conversion pulses were 3.0 and 1.0 μs , respectively. The number of t_1 increments was 34. Since the shifted echo is phase modulated, the number of time increments was also 34, corresponding to a maximum t_1 evolution time of ~ 1.9 ms. Note that, during spectral acquisition, the number of t_1 increments was carefully chosen to include a significant portion beyond the point where the signal dropped to the baseline noise level, ensuring that the shifted-echo 3QMAS spectra were acquired with the highest S/N during the limited SCH magnet time without compromising the resolution. The 3QMAS spectra were acquired using rotor-synchronized t_1 increments to avoid spinning sidebands, which are significant due to the chemical shift anisotropy (CSA) at the very high field and 3Q excitation/conversion modulation along the indirect F1 dimension. However, this restricts the F1 window to the spinning frequency (18 kHz), which is not wide enough to cover the spread of resonances and spinning side bands (SSBs). Fortunately, this problem can be solved by the Q-shearing method to the $k = 3$ Q representation.⁷² The F1 spectral window can then be zero-filled and expanded to whatever limits are needed for shearing back to the isotropic representation with a large and unfolded F1 window. In the present case, the F1 spectral window was zero-filled eight times and expanded to give an unfolded F1 window of 8×18 kHz after Q shearing. Consequently, the F1 digital resolution is equivalent to 8×34 t_1 increments with the final expanded F1 window. The ^{17}O spectra were referenced to 18 atom % ^{17}O -enriched $\text{H}_2^{17}\text{O}(\text{l})$ or distilled water at 0 ppm.

3.2.3 Spectral simulations

For quadrupolar nuclei such as ^{17}O (spin $I > 1/2$), their electric quadrupole moments interact with the surrounding EFG, resulting in broad powder patterns rather than sharper resonances. The interplay between the quadrupolar interaction and the CSA effect makes the shapes of powder patterns more complicated and difficult to simulate. The dmfit software package was used to simulate SSNMR spectra using the Int2QUAD mode, including both the quadrupolar and CSA effects.⁷³ In dmfit, the EFG tensor is described by three principal components in the following order: $|V_{YY}| \leq |V_{XX}| \leq |V_{ZZ}|$. The quadrupolar coupling constant (C_Q) and asymmetry parameter (η_Q) describe the spherical and cylindrical symmetry of the EFG tensor, respectively, and are defined as follows: $C_Q = (eQV_{ZZ}/h) \times 9.7177 \times 10^{21}$ (in Hz) and $\eta_Q = (V_{YY} - V_{XX})/V_{ZZ}$, where e is the electric charge, Q is the quadrupole moment ($-2.558 \times 10^{-30} \text{ m}^2$),³² and a conversion factor of $9.7177 \times 10^{21} \text{ V m}^{-2}$ is used during the calculation of C_Q to convert from atomic units to Hz. The chemical shift (CS) tensor is also described by three principal components such that $|\delta_{22} - \delta_{\text{iso}}| \leq |\delta_{11} - \delta_{\text{iso}}| \leq |\delta_{33} - \delta_{\text{iso}}|$, and the isotropic chemical shift $\delta_{\text{iso}} = (\delta_{11} + \delta_{22} + \delta_{33})/3$ is related to the bonding modes. The CSA parameters are defined by $\Delta_{\text{CS}} = \delta_{33} - \delta_{\text{iso}}$ and $\eta_{\text{CS}} = |(\delta_{22} - \delta_{11})/\Delta_{\text{CS}}|$. Three Euler angles (ϕ, χ, ψ) are employed to describe the orientations of the CS tensor with respect to the EFG principal (fixed) axis frame using the ZYZ convention: the corresponding transformation matrix was used to deduce the new directional characteristics of the CS tensor with respect to the EFG system. As a result, eight independent parameters, $C_Q, \eta_Q, \delta_{\text{iso}}, \Delta_{\text{CS}}, \eta_{\text{CS}}, \phi, \chi,$ and ψ , are required to characterize a single ^{17}O site when both the quadrupolar and the CSA effects are considered. All uncertainties in NMR parameters were estimated by bidirectional variation of the parameter of interest in both directions from the best-fit value while all other NMR parameters were held constant.

3.2.4 Theoretical calculations

The unit cell parameters were set to the single-crystal XRD parameters⁶⁰ and kept fixed during geometry optimizations to ensure consistency between experimental and optimized structures. Proton positions were then optimized using the VASP (Vienna Ab initio Simulation Package) code⁷⁴ based on the Kohn–Sham density functional theory

(DFT) and using a plane-wave pseudopotential approach. The NMR parameters were then calculated within the Kohn–Sham DFT using the QUANTUM-ESPRESSO code.⁷⁵ The PBE generalized gradient approximation⁷⁶ was used, and the valence electrons were described by norm-conserving pseudopotentials⁷⁷ in the Kleinman–Bylander form.⁷⁸ The wave functions were expanded on a plane wave basis set with a kinetic energy cutoff of 80 Ry. The integral over the first Brillouin zone was performed using a Monkhorst–Pack $2 \times 2 \times 2$ k-point grid for the charge density and chemical shift tensor calculation. The magnetic shielding tensor was computed using the gauge-including projector augmented wave (GIPAW) approach,^{79–81} which enables the reproduction of the results of a fully converged all-electron calculation. The isotropic chemical shift δ_{iso} is defined as $\delta_{\text{iso}} = \sigma_{\text{iso}} - \sigma_{\text{iso}}(\text{ref})$, where σ_{iso} is the isotropic magnetic shielding and $\sigma_{\text{iso}}(\text{ref})$ is the isotropic magnetic shielding of the same nucleus in a reference compound. In the present case, the fit of the linear correlation between the experimental δ_{iso} and the calculated σ_{iso} values of ^{17}O for Na_2SiO_3 , $\alpha\text{-Na}_2\text{Si}_2\text{O}_5$, α - and γ -glycine, and $\alpha\text{-SrSiO}_3$ enabled the determination of the relation between δ_{iso} and calculated σ_{iso} for the ^{17}O nucleus, as described previously.²¹ It is worth noting that, for most MOFs, the solvent molecules are disordered inside the framework. Very often, disordered solvent molecules have to be removed before calculation. In the present case, the DMF molecules are orderly distributed within the channels. This rare situation makes the calculation not only simpler but also more accurate.

3.3 Results and discussion

The three-dimensional framework of microporous $\alpha\text{-Mg}_3(\text{HCOO})_6$ is formed by corner- and edge-sharing MgO_6 octahedra interconnected by formate ligands (Figure 3.1) and features zigzag channels measuring $4.5 \times 5.5 \text{ \AA}$.⁶⁰ Among the 12 crystallographically distinct framework oxygen sites, 6 are associated with the carboxylate group and adopt a $\mu_2\text{-O}$ bonding mode (sites O1, O3, O5, O7, O9, and O11), and the other 6 are associated with the carboxylate group and are in a $\mu_1\text{-O}$ bonding mode (sites O2, O4, O6, O8, O10, and O12). The $\text{C}\text{-}\mu_1\text{-O}$ bonds have a shorter length and more double-bond character in comparison to the $\text{C}\text{-}\mu_2\text{-O}$ bonds. However, the local environments of all 6 $\mu_1\text{-O}$ sites are almost identical, while the 6 $\mu_2\text{-O}$ sites are also very similar.

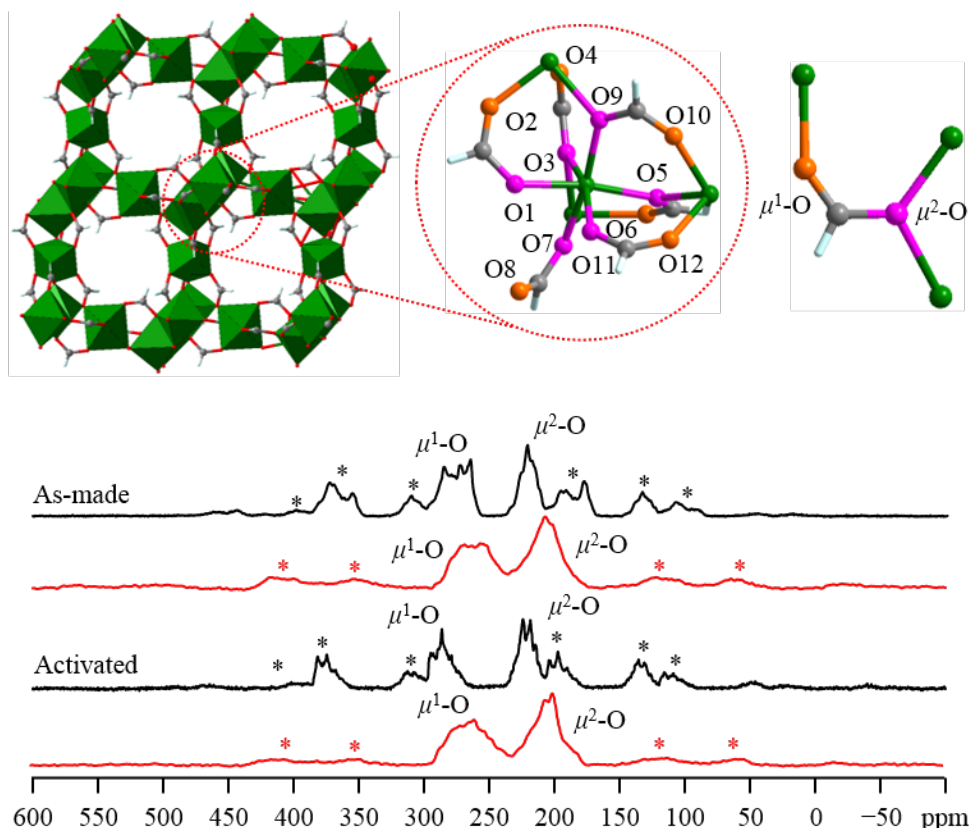


Figure 3.1. (top, left to right) Representations of the framework of activated α - $\text{Mg}_3(\text{HCOO})_6$, 12 framework oxygen sites, and 2 different oxygen bonding modes. Color coding: Mg, green; C, gray; H, white; O, red; μ_1 -O, orange; μ_2 -O, pink. (bottom) ^{17}O 1D MAS NMR spectra of ^{17}O -enriched α - $\text{Mg}_3(\text{HCOO})_6$ at fields of 35.2 T (red) and 21.1 T (black) acquired at a spinning frequency of 18 kHz. The asterisk (*) denotes spinning sidebands (SSBs).

As a result, only 2 signal groups were resolved in the previous ^{17}O 1D magic-angle spinning (MAS) spectrum of as-made α - $\text{Mg}_3(\text{HCOO})_6$ at 21.1 T (Figure 3.1).¹⁶ Those two ^{17}O signals were simulated reasonably well by two ^{17}O powder patterns at 21.1 T and were assigned to groups of μ_1 - and μ_2 -O sites, respectively (Figure A3.7).

As-made MOFs typically consist of solvent molecules occupying their pores and channels; thus, the creation of permeable spaces in MOFs by evacuating the solvent (i.e., the activation process) is a prerequisite for many applications. Therefore, it is of

fundamental importance to understand the effect of activation on the MOF structure, especially regarding the subtle local environment changes that are invisible in diffraction-based techniques but very important for applications. The single-crystal XRD data of as-made and activated α -Mg₃(HCOO)₆ phases indicate that the local oxygen environments only undergo very minor changes upon removal of DMF solvent during activation, as the Mg²⁺ ions are coordinatively saturated and this MOF framework is fairly rigid.⁶⁰ Consequently, detecting the very small activation-induced structural changes via ¹⁷O SSNMR is quite challenging, as evidenced by the nearly identical ¹⁷O 1D MAS spectra of the two phases at 21.1 T (Figure 3.1). It is apparent that higher spectral resolution is necessary to detect the subtle difference in oxygen local environment. The activation method employed in this work for DMF solvent removal from α -Mg₃(HCOO)₆ is well established.^{60,70} On the basis of our previous experience, we are certain that this activation process completely removes all residual DMF guests from the as-made MOF.^{64,66} To confirm, we carried out TGA alongside ¹H–¹³C CP/MAS experiments, and the results unambiguously prove that the activation is complete (Figure A3.3 and Figure A3.4).

The newly obtained ¹⁷O 1D MAS NMR spectra of as-made and activated α -Mg₃(HCOO)₆ phases at 35.2 T are shown in Figure 3.1 alongside the 21.1 T spectra. At 35.2 T, the resonances of both phases are considerably narrower, owing to the reduced second-order quadrupolar broadening. The spectral envelope containing all overlapping signals of the μ_1 -O group is now completely separated from that of the μ_2 -O group at 35.2 T, and several diagnostic spectral features including the “edges” and “horns” of individual ¹⁷O SSNMR resonances have emerged. Thus, this spectral envelope must consist of several overlapping powder patterns corresponding to multiple μ_1 -O sites. Similarly, the spectral envelope of the μ_2 -O group should also be simulated using multiple powder patterns. However, due to the severe overlap of powder patterns, it is very challenging to determine the number of oxygen sites and their corresponding NMR parameters using only a 1D MAS spectrum. Furthermore, the ¹⁷O 1D MAS spectra of as-made and activated α -Mg₃(HCOO)₆ phases are now distinctly different at 35.2 T, implying that the activation-induced structural changes not apparent at 21.1 T are now discernible, owing to the much higher spectral resolution achieved at 35.2 T. It is worth mentioning that the

changes in the μ_1 -O spectral envelope are also more significant than those in the μ_2 -O envelope, suggesting that the local environments of μ_1 -O sites are more influenced by activation in comparison to μ_2 -O sites. The spectra exhibit very intense spinning sidebands due to the chemical shift anisotropy (CSA) enhanced at 35.2 T.

As mentioned earlier, the ^{17}O 1D MAS spectra at 35.2 T feature overlapping resonances arising from multiple ^{17}O sites, indicating that the maximum achievable 1D spectral resolution is still not high enough to resolve fine features. This is because the conventional 1D MAS experiments only partially averages the ^{17}O second-order quadrupolar interaction. To further enhance spectral resolution, 2D 3QMAS experiments were performed:⁸² this technique can eliminate the ^{17}O second-order quadrupolar broadening along the indirect F1 dimension and thus separate the overlapping signals observed in 1D MAS spectra. The ^{17}O 2D 3QMAS spectra of as-made and activated α - $\text{Mg}_3(\text{HCOO})_6$ at 35.2 T are shown in Figure 3.2. There are a number of well-resolved signals along the F1 dimension in the spectra of the as-made and activated phases, respectively. Since the number of resolved signals in the isotropic dimension (7 for the as-made phase and 8 for the activated phase) is smaller than the 12 crystallographically distinct framework oxygen sites, some signals along the F1 dimension must correspond to very similar signals arising from multiple oxygen sites with almost identical NMR parameters. For each F2 cross-section extracted at δ_1 along the F1 dimension, the isotropic chemical shift, δ_{iso} (in ppm), and the quadrupolar product, $P_Q = C_Q(1 + \eta_Q/3)^{1/2}$ (in MHz), can be obtained directly from the spectral center of gravity (δ_2) along the F2 dimension¹⁷ using the equations⁸³

$$\delta_{\text{iso}} = \frac{17}{27}\delta_1 + \frac{10}{27}\delta_2 \text{ (Equation 3.1)}$$

$$P_Q = \left\{ \frac{170}{81} \frac{[4I(2I-1)^2]}{[4I(I+1)-3]} (\delta_1 - \delta_2) \right\}^{1/2} \nu_0 10^{-3} \text{ (Equation 3.2)}$$

where ν_0 is the Larmor frequency and I is the spin quantum number.

The δ_{iso} and P_Q values derived from each peak along the F1 dimension are given in Table 3.1. These two values are determined accurately from the resonance positions in the F1

and F2 dimensions, without the need of fitting the F2 cross-section, under the S/N obtained with the limited magnet time. For the peaks along the isotropic dimension corresponding to a single oxygen site, C_Q and η_Q values can be extracted by fitting the F2 cross-section. If a peak along the F1 dimension originates from multiple oxygen sites, δ_{iso} and P_Q represent average values.

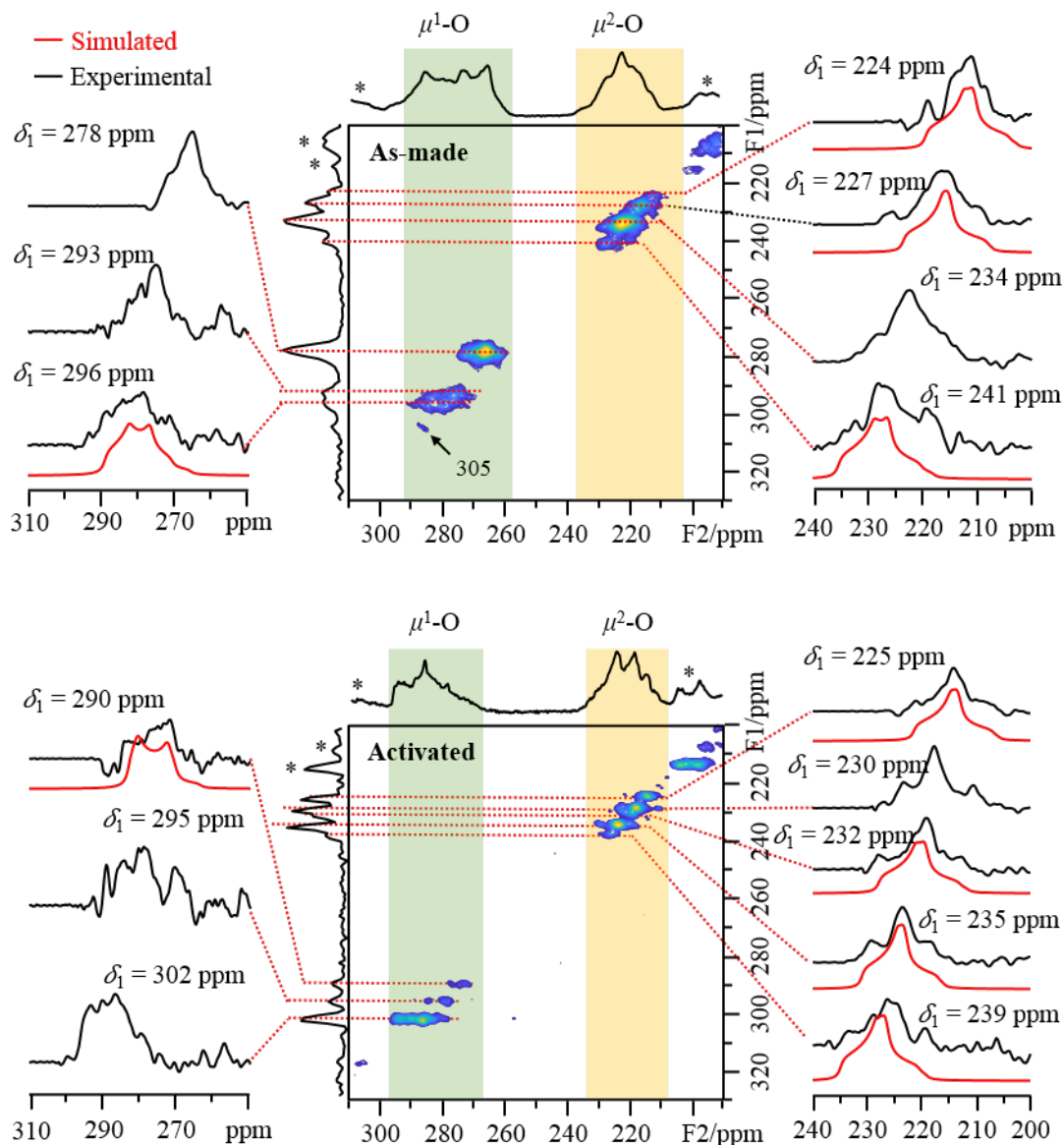


Figure 3.2. ^{17}O 2D 3QMAS NMR spectra of ^{17}O -enriched $\alpha\text{-Mg}_3(\text{HCOO})_6$ at 35.2 T. Black dashed lines correspond to the slices examined. Blue and red solid lines denote experimental and simulated spectra, respectively. Asterisks (*) denote the SSBs. The 3QMAS spectra without markups are shown in Figure A3.8 for clarity.

Table 3.1. Experimental ^{17}O NMR parameters, Calculated^a δ_{iso} values, and peak assignments of $\alpha\text{-Mg}_3(\text{HCOO})_6$ ^b

Sample	O Type	δ_1 (ppm)	P_Q (MHz)	δ_{iso} (ppm)	$\delta_{\text{iso,calc}}$ (ppm)	Ass.	C_Q (MHz)	η_Q
as-made	$\mu_2\text{-O}$	224(1)	7.2(5)	220(2)	227.1	O3	6.5(4)	0.8(1)
	$\mu_2\text{-O}$	227(1)	6.6(5)	223(2)	230.5	O9	6.0(4)	0.9(1)
	$\mu_2\text{-O}$	234(1)	6.6(5)	230(2)	236.1	O1		
					238.9	O11		
					239.4	O5		
	$\mu_2\text{-O}$	241(1)	7.8(5)	236(2)	256.4	O7	7.0(4)	0.7(1)
	$\mu_1\text{-O}$	278(1)	7.5(5)	273(2)	288.7	O10		
					291.2	O6		
					293.2	O4		
	$\mu_1\text{-O}$	293(1)	8.8(5)	286(2)	295.5	O12		
297.2					O8			
$\mu_1\text{-O}$	296(1)	8.3(5)	290(2)	306.5	O2	7.9(4)	0.5(1)	
				DMF	305(1)	9.1(5)	298(2)	308.3
activated	$\mu_2\text{-O}$	225(1)	6.6(5)	221(2)	227.7	O9	6.0(4)	0.8(1)
	$\mu_2\text{-O}$	230(1)	7.5(5)	225(2)	232	O3		
					232	O5		
	$\mu_2\text{-O}$	232(1)	7.2(5)	228(2)	234.7	O1	6.5(4)	0.8(1)
	$\mu_2\text{-O}$	235(1)	6.9(5)	231(2)	238.7	O11	6.1(4)	0.8(1)
	$\mu_2\text{-O}$	239(1)	7.2(5)	235(2)	243.5	O7	6.4(4)	0.8(1)
	$\mu_1\text{-O}$	290(1)	7.8(5)	285(2)	285.3	O6	7.7(4)	0.2(1)
	$\mu_1\text{-O}$	295(1)	8.1(5)	289(2)	288	O8		
					289.9	O10		
	$\mu_1\text{-O}$	302(1)	7.5(5)	297(2)	296.4	O12		
296.5					O4			
				298.5	O2			

To assign each resolved signal in the isotropic dimension to a single or multiple oxygen sites, gauge-including projector augmented wave (GIPAW) density functional theory

(DFT) calculations were carried out,^{79–81} as this approach has been proven to be very reliable for ^{17}O NMR spectral assignments in various systems.^{13–15,20,21,24} Although the calculated δ_{iso} value may not exactly match the experimental value, assignments of multiple signals on the basis of relative calculated δ_{iso} values are typically valid.^{13–15,20,21,24} Accordingly, calculated δ_{iso} values were used for the assignment of each signal in the F1 dimension (Table 3.1) to the framework oxygen site(s). For example, the order of calculated δ_{iso} values for μ_2 -O sites in as-made $\alpha\text{-Mg}_3(\text{HCOO})_6$ is $\text{O3} < \text{O9} < \text{O1} \approx \text{O11} \approx \text{O5} < \text{O7}$. The ^{17}O signal with the lowest measured δ_{iso} value of 220 ppm ($\delta_1 = 224$ ppm) is thus assigned to O3, the ^{17}O signal with the second-lowest δ_{iso} value of 223 ppm ($\delta_1 = 227$ ppm) is assigned to O9, the ^{17}O signal with the third-lowest δ_{iso} value of 230 ppm ($\delta_1 = 234$ ppm) and significantly higher intensity is assigned to O1, O5, and O11, and the ^{17}O signal with the highest δ_{iso} value of 236 ppm ($\delta_1 = 241$ ppm) is assigned to O7. The ^{17}O signals of μ_1 -O sites are assigned in a similar fashion. Since the ^{17}O signals at $\delta_1 = 224$, 227, and 241 ppm each correspond to a single oxygen site, their C_Q and η_Q values can be further extracted by fitting the F2 cross-sections (Table 3.1). The 2D 3QMAS spectrum of activated $\alpha\text{-Mg}_3(\text{HCOO})_6$ was analyzed with the same approach, and the results are also shown in Table 3.1.

The spinning sidebands in 1D spectra are particularly intense, suggesting that a very large chemical shift anisotropy (CSA) is present at the ultrahigh magnetic field of 35.2 T. Efforts were made to simulate ^{17}O 1D MAS spectra to estimate the ^{17}O CSA. Theoretically, fitting a 1D MAS spectrum with 12 sites requires 96 independent parameters if the EFG and CSA effects are both considered. Therefore, to practically simulate the spectrum, some approximations must be employed to reduce the number of fitting parameters. Thus, the experimental C_Q , η_Q , and δ_{iso} values of oxygen sites that were resolved in the F1 dimension (e.g., O2, O3, O7, and O9 sites of the as-made phase) were directly used in simulations without adjustment. For oxygen sites that are unresolved in the F1 dimension (e.g., O1, O5, and O11 sites of the as-made phase), P_Q and δ_{iso} are average values. However, it is evident from the line-shape of cross-sections that these sites give rise to very similar NMR parameters. For the 1D spectral simulations, the calculated η_Q values (Table A3.2) were used without further adjustment and the corresponding C_Q values were obtained from the known relationship between P_Q

and C_Q/η_Q . The δ_{iso} values were obtained by using the average δ_{iso} as a starting point and making slight adjustments. Keeping the C_Q and η_Q constant during the simulation is reasonable, as the anisotropy from the EFG is much smaller in comparison to the CSA at the ultrahigh magnetic field. The small variation of the EFG parameters among different sites contributes very little to the intensity of the SSBs (Figure A3.9).

To include the CSA effects, additional NMR parameters must be incorporated: two CSA parameters including the reduced anisotropy Δ_{CS} and the chemical shift asymmetry parameter η_{CS} , along with three Euler angles (ϕ , χ , ψ) describing the orientations of the chemical shift tensor with respect to the EFG tensor principal axis frame.⁷³ It is reasonable to assume that the six μ_1 -O sites have the same Δ_{CS} , since they reside in very similar chemical environments and the Δ_{CS} value for all six μ_2 -O sites have the same value yet are distinct from that of μ_1 -O sites. The Δ_{CS} values for μ_1 -O and μ_2 -O were modified during simulations, but the calculated η_{CS} values and Euler angles (Table A3.2) were kept constant.

The final simulated 1D MAS spectra are shown in Figure 3.3, illustrating that the isotropic regions and SSBs can be simulated reasonably well by considering both the quadrupolar and the CSA effects (Table A3.3). If only the second-order quadrupolar interaction is considered, the isotropic regions of ^{17}O signals can still be simulated accurately, but the simulated SSBs are far too low in intensity (Figure A3.9). It is also worth noting that there is a very weak ^{17}O signal at $\delta_1 = 305$ ppm ($P_Q = 9.1$ MHz, $\delta_{\text{iso}} = 298$ ppm) in the 3QMAS spectrum. The signal position suggests that it arises from DMF molecules within MOF channels.⁸⁴ Apparently, DMF oxygen atoms are also subject to ^{17}O exchange under the reaction conditions. The enhanced sensitivity and resolution of ^{17}O SSNMR at 35.2 T permit detection of the DMF signal; thus, it was included in the simulation of the 1D MAS spectrum of as-made $\alpha\text{-Mg}_3(\text{HCOO})_6$ (i.e., the O1S site). In general, the calculated δ_{iso} values are slightly overestimated in comparison to experimental values. Several factors can be responsible for these discrepancies, including (i) limitations of the GIPAW method, (ii) possible inaccuracy of the crystal structure, (iii) temperature effects on the crystal structure, and (iv) dynamics within the crystal structure.⁸⁵ In this case, the single-crystal structures are based on the XRD data obtained

at 100 K. In addition, our DFT calculations do not consider molecular motions such as the librational motions of formate anions reported for the related β -Ca(HCOO)₂ at room temperature,⁸⁶ while NMR experiments are subject to their influence.

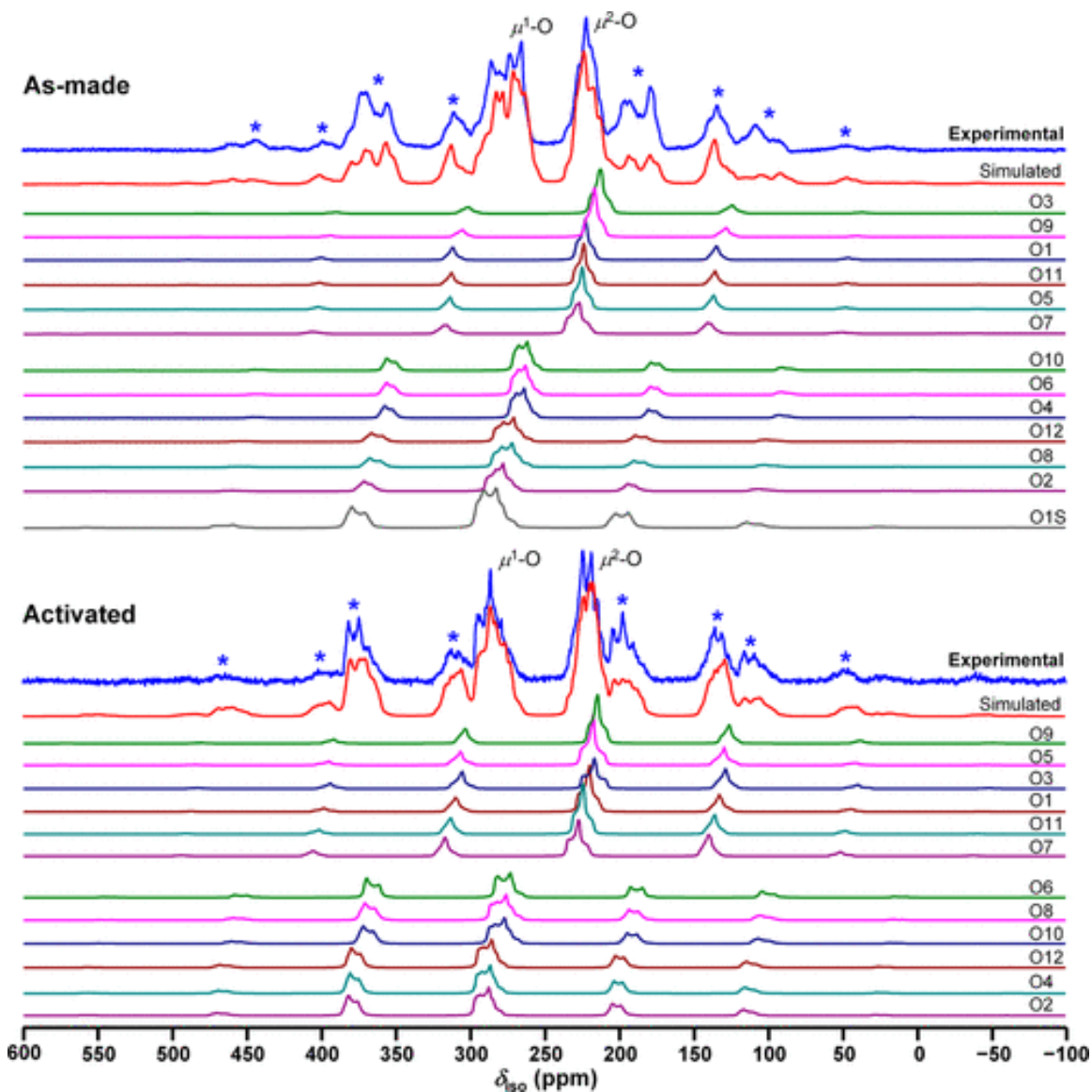


Figure 3.3. Experimental and simulated ^{17}O 1D MAS NMR spectra of ^{17}O -enriched α - $\text{Mg}_3(\text{HCOO})_6$ at 35.2 T. The quadrupolar and CSA effects are both considered in these simulations, using the parameters shown in Table A3.3. In each phase, the signal intensity of each individual oxygen in the μ_1 -O sites is approximately equal, and the same is true for signals arising from the μ_2 -O sites. Asterisks (*) denote SSBs.

^{17}O 2D 3QMAS experiments at an ultrahigh magnetic field strength of 35.2 T have unlocked the identification of 12 inequivalent framework oxygen sites in both the as-made and activated phases of $\alpha\text{-Mg}_3(\text{HCOO})_6$. The experimental P_Q and δ_{iso} values of μ_1 -O sites range from 7.5 to 8.8 MHz and from 273 to 297 ppm, respectively; these ranges are 6.6–7.8 MHz and 220–236 ppm for μ_2 -O sites. Both sets of these ranges are typical for C=O and C–O environments of carboxylates.^{3,8}

The very high resolution achieved at 35.2 T permits the observation of small changes in ^{17}O NMR parameters such as δ_{iso} at each oxygen site upon activation, which were not observable at a lower field of 21.1 T. Such changes reflect the influence and interaction of guest DMF solvent molecules with the MOF host. Activation of the as-made $\alpha\text{-Mg}_3(\text{HCOO})_6$ phase and the corresponding removal of DMF molecules from the pores only result in subtle changes in local bond angles and distances, while the long-range order is preserved.⁶⁰ A comparison between the experimental ^{17}O δ_{iso} values of as-made and activated $\alpha\text{-Mg}_3(\text{HCOO})_6$ phases reveals that more significant changes occur at μ_1 -O sites in comparison to μ_2 -O sites. This disparity in local structural changes is because each μ_2 -O site is firmly anchored to the framework by two Mg atoms and one C atom; thus, the degree of perturbation on their local oxygen coordination spheres by guest molecules is not as evident as for the coordination spheres of μ_1 -O sites, which are only bound to the framework via one Mg atom and one C atom. The most significant activation-induced changes are associated with the δ_{iso} values of O4 and O10 (>15 ppm). Figure 3.4 illustrates the orderly arrangement of DMF molecules along the zigzag channels of $\alpha\text{-Mg}_3(\text{HCOO})_6$. Each DMF molecule interacts with two adjacent framework formate anions containing O4 and O10 sites. According to the criteria for the formation of $\text{O}\cdots\text{H}-\text{C}$ nonconventional hydrogen bonds ($\text{O}\cdots\text{H}$ distance < 2.72 Å and $\text{O}\cdots\text{H}-\text{C}$ angle $> 130^\circ$),⁸⁷ both the $\text{O1S}\cdots\text{H5}$ distance of 2.38 Å and the $\text{O1S}\cdots\text{H5}-\text{C5}$ bond angle of 157° in as-made $\alpha\text{-Mg}_3(\text{HCOO})_6$ are in favor of weak hydrogen bonding. Thus, the significant change in the δ_{iso} value of O10, bound to C5 via a C– μ_1 -O bond, is due to an $\text{O1S}\cdots\text{H5}-\text{C5}$ hydrogen-bonding interaction.

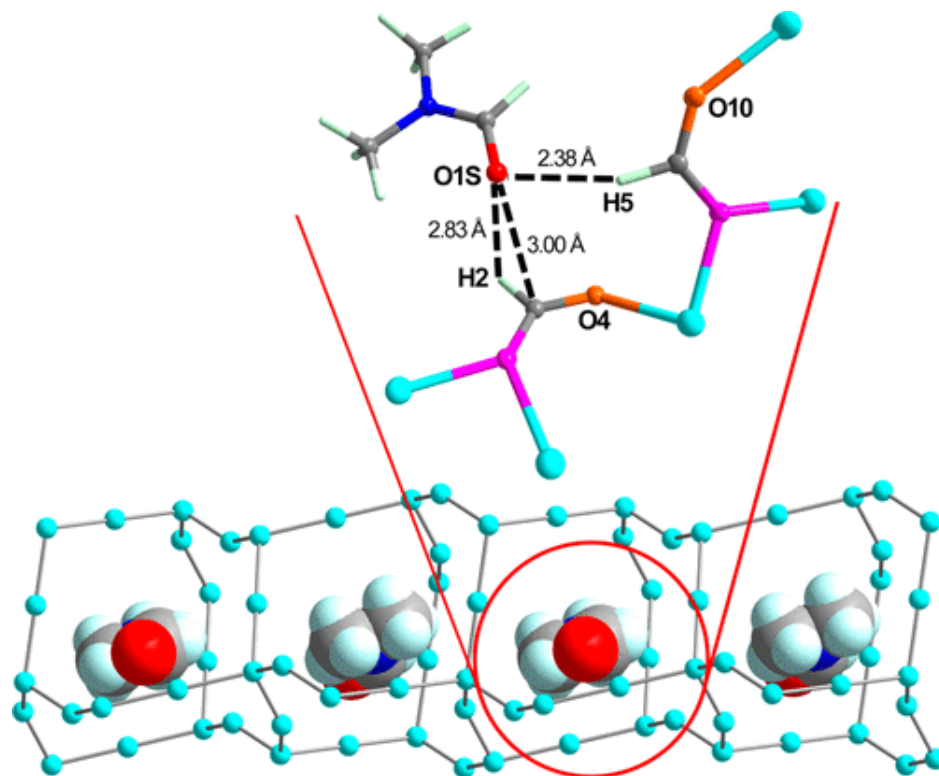


Figure 3.4. Schematic illustrations of DMF guest molecules within the zigzag channels of as-made α - $\text{Mg}_3(\text{HCOO})_6$. Only the Mg nodes are shown for clarity in the bottom diagram. The top inset shows a DMF molecule and two adjacent formate anions. The distances given were extracted from the DFT-optimized structures. Color coding: Mg, turquoise; N, blue; C, gray; H, white; O1S of DMF, red; μ_1 -O, orange; μ_2 -O, pink.

In the case of O4, although both the O1S \cdots H2 distance of 2.83 Å and the O1S \cdots H2–C2 bond angle of 88° are not very favorable for O1S \cdots H2–C2 hydrogen bond formation, the O1S \cdots C2 distance of 3.00 Å is considerably shorter than the summation of their van der Waals radii (3.22 Å),⁸⁸ pointing toward van der Waals forces between O1S and C2 as being responsible for the significant change in the δ_{iso} value of O4 upon activation. The formation of a O1S \cdots H5–C5 hydrogen bond is also evident from the δ_{iso} value of the DMF amide oxygen site (O1S) in as-made α - $\text{Mg}_3(\text{HCOO})_6$. As demonstrated in the literature,⁸⁴ the δ_{iso} value of the DMF amide oxygen in the absence of hydrogen bonding is 323 ppm, and this value decreases with increasing hydrogen-bonding strength. The δ_{iso}

value of 298 ppm for O1S corresponds to a hydrogen-bonding strength between those of infinitely diluted DMF in ethanol (299.3 ppm) and infinitely diluted DMF in methanol (292.5 ppm).⁸⁴ It is the high sensitivity and high resolution achieved at an ultrahigh field of 35.2 T that make it possible to detect the site-specific O \cdots H–C nonconventional hydrogen bonding involving O10 and O1S and estimate the strength of this interaction. As mentioned earlier, nonconventional O \cdots H–C hydrogen bonding can play important roles in the host–guest interactions in BioMOFs or MOF-based drug delivery systems.^{49–51} Thus, the ability to detect this type of weak interaction and estimate its strength by ¹⁷O SSNMR at ultrahigh field, as demonstrated in this study, provides researchers a useful tool for investigating this type of host–guest interaction in MOF systems.

To further demonstrate the power of an ultrahigh magnetic field on MOF characterization using ¹⁷O SSNMR, we examined two activated MOF MIL-53(Al) samples. MIL-53(Al) is a well-studied MOF with high thermal and chemical stability and is very promising in guest separation.⁸

As Figure 3.5a illustrates, the channels of as-made MIL-53(Al) are occupied by the unreacted linker precursor molecules, 1,4-benzenedicarboxylic acid (H₂BDC). After activation, the channel dimension increases from 7.3 \times 7.7 to 8.5 \times 8.5 Å² due to the removal of the hydrogen-bonding interaction between H₂BDC and the carboxylate of BDC²⁻ linkers in the framework. Upon activation, the framework topology is retained, but the crystal symmetry changes from Pnma in the as-made phase to Imma in the activated phase.⁴⁷ There have been two reports on ¹⁷O SSNMR studies of MIL-53 conducted at lower magnetic fields.^{16,17}

Activation of MIL-53 is not very straightforward. Early on, activation of as-made MIL-53(Al) was performed by direct calcination in air at 503 K for 3 days.⁴⁷ The conditions were harsh and led to reduced crystallinity. To avoid such harsh activation conditions, a milder alternate route was developed by first exchanging the trapped H₂BDC with DMF under solvothermal conditions (e.g., 423 K) for an extended period (e.g., 12 h or longer) and then heating the DMF-exchanged MOF at 473 K under dynamic vacuum (\leq 1 mbar) overnight.⁸⁹

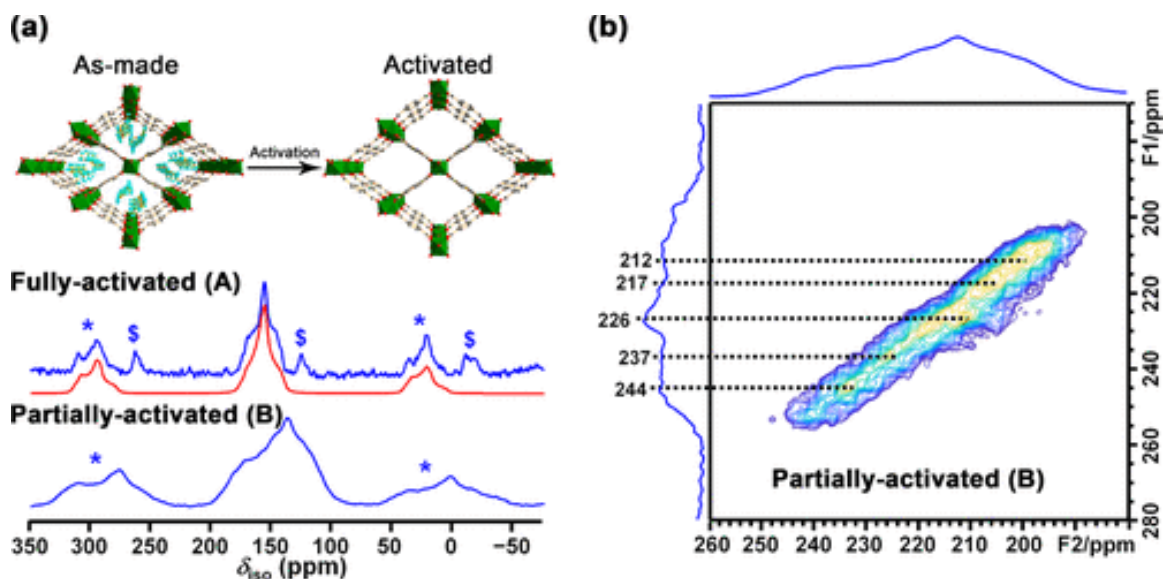


Figure 3.5. ^{17}O 1D MAS NMR spectra of ^{17}O -enriched fully (sample A) and partially activated (sample B) MIL-53(Al) samples at 35.2 T. The blue and red solid lines denote experimental and simulated spectra, respectively. Only the carboxylate oxygen regions are shown for clarity. The full spectra are shown in Figure A3.10. Asterisks (*) and dollar signs (\$) denote the SSBs of $-\text{COO}^-$ and $\mu_2\text{-OH}$, respectively. The structures of as-made and activated MIL-53(Al) phases are shown at the top. (b) ^{17}O 2D 3QMAS NMR spectrum of partially activated (sample B) ^{17}O -enriched MIL-53(Al) at 35.2 T. Black dashed lines correspond to the slices examined for analyses.

We prepared two ^{17}O -enriched MIL-53(Al) samples which were activated under identical conditions except for the DMF exchange time: 24 h for sample A and 12 h for sample B. According to the literature, an exchange time of 12 h should be sufficient for the activation of MIL-53(Al).⁹⁰ Although the PXRD patterns of samples A and B look very similar (Figure A3.6), the ^{17}O 1D MAS spectra at 35.2 T of samples A and B look distinctly different in the carboxylate region (Figure 3.5). The spectrum of sample A exhibits a relatively narrow pattern that can be well fitted with a single set of ^{17}O NMR parameters (Table A3.4), indicating that the signal corresponds to a single oxygen site.

This is consistent with the crystal structure of the activated phase, which only has one carboxylate oxygen site in the unit cell.⁴⁷ Thus, the ^{17}O MAS spectrum clearly indicates

that the sample exchanged with DMF for 24 h is fully activated. The spectrum of sample B displays a rather broad profile in the carboxylate region that cannot be simulated by a single oxygen site, implying the existence of multiple carboxylate oxygen environments in this sample. It appears that this MOF sample is only partially activated. The ^{17}O 3QMAS spectrum of sample B obtained at 35.2 T provides detailed information. A long spectral “ridge” is observed for the carboxylate oxygen sites, implying that the partial activation can contribute to the distributions of the quadrupolar coupling and chemical shift and consequently to line broadening. Such a situation is not unexpected, since MIL-53(Al) is a flexible MOF that undergoes a phase transition from Pnma in the as-made phase to Imma upon full activation without breaking any bonds. It appears that sample B represents an intermediate state between these two phases. Furthermore, the unreacted linker precursors in the channels are disordered and seem to be randomly removed. Nonetheless, five peaks are extracted above the “ridge” at $\delta_1 = 212, 217, 226, 237,$ and 244 ppm, respectively. The corresponding P_Q and δ_{iso} values are shown in Table A3.4. On the basis of the δ_{iso} values, the peaks at $\delta_1 = 212$ and 217 ppm are assigned to the $-\text{OH}$ and $\text{C}=\text{O}$ groups of H_2BDC molecules within the MOF channels, respectively.³³ The signal at $\delta_1 = 237$ ppm is attributed to the oxygen site in the empty channels because its δ_{iso} value (232 ppm) is similar to that of activated MIL-53(Al), while the resonances at $\delta_1 = 226$ and 244 ppm are tentatively assigned to the oxygen sites in the occupied channels with local environments similar to those in as-made MIL-53(Al).^{16,17} The high resolution and sensitivity of ^{17}O NMR gained at 35.2 T not only allow for unambiguously distinguishing partially activated from fully activated MIL-53(Al) samples but also permit observation of several oxygen sites in empty and occupied channels in partially activated MIL-53(Al).

3.4 Conclusions and future work

In summary, the very high spectral resolution and sensitivity achieved at an ultrahigh magnetic field of 35.2 T in this work represents an advance in ^{17}O SSNMR spectroscopy. At 35.2 T, many inequivalent carboxylate oxygen sites have been identified in ^{17}O SSNMR spectra of both the activated and as-made $\alpha\text{-Mg}_3(\text{HCOO})_6$ MOFs. The very high resolution achieved at 35.2 T enables the observation of subtle changes in ^{17}O SSNMR

spectra of as-made and activated α - $\text{Mg}_3(\text{HCOO})_6$ phases. These alterations arise from weak site-specific interactions between DMF guests and the MOF framework, such as hydrogen bonding and van der Waals forces. The investigation of these weak interactions is important for MOF applications in various fields, including gas adsorption and biomedical applications. The advantage of performing ^{17}O SSNMR experiments at 35.2 T for MOF characterization is further illustrated by the activation of MIL-53(Al). The partially and fully activated phases of MIL-53(Al) can be unambiguously distinguished. Several oxygen sites with different local environments in the partially activated phase are tentatively identified.

This work illustrates how a wide variety of organic and inorganic compounds are now viable targets for ^{17}O SSNMR at an ultrahigh magnetic field of 35.2 T. The sensitivity and resolution afforded at this field strength greatly extend the volume and quality of structural and chemical information available from ^{17}O SSNMR spectroscopy, as much of these data are unavailable at or below magnetic fields of 21.1 T.

3.5 References

- (1) Ashbrook, S. E.; Smith, M. E. *Chem. Soc. Rev.* **2006**, 35 (8), 718.
- (2) Brownbill, N. J.; Gajan, D.; Lesage, A.; Emsley, L.; Blanc, F. *Chem. Commun.* **2017**, 53, 2563.
- (3) Wu, G. *Prog. Nucl. Magn. Reson. Spectrosc.* **2008**, 52, 118.
- (4) Yamada, K. *Recent Applications of Solid-State ^{17}O NMR*, 1st Ed.; Elsevier, **2010**.
- (5) Gerothanassis, I. P. *Prog. Nucl. Magn. Reson. Spectrosc.* **2010**, 57, 95.
- (6) Castiglione, F.; Mele, A.; Raos, G. *^{17}O NMR: A “Rare and Sensitive” Probe of Molecular Interactions and Dynamics*, 1st ed.; Elsevier, **2015**.
- (7) Ohlin, C. A.; Casey, W. H. *Annu. Reports NMR Spectrosc.* **2018**, 94, 187.
- (8) Wu, G. *Prog. Nucl. Magn. Reson. Spectrosc.* **2019**, 114, 135.

- (9) Buannic, L.; Blanc, F.; Middlemiss, D. S.; Grey, C. P. *J. Am. Chem. Soc.* **2012**, 134, 14483.
- (10) Wang, W.; Waang, W. D.; Lucier, B. E. G.; Terskikh, V. V.; Huang, Y. *J. Phys. Chem. Lett.* **2014**, 5, 3360.
- (11) Holmes, S. T.; Schurko, R. W. *J. Phys. Chem. C* **2018**, 122, 1809.
- (12) Alam, T. M.; Nyman, M.; Cherry, B. R.; Segall, J. M.; Lybarger, L. E. *J. Am. Chem. Soc.* **2004**, 126, 5610.
- (13) Pedone, A.; Gambuzzi, E.; Menziani, M. C. *J. Phys. Chem. C* **2012**, 116, 14599.
- (14) Romao, C. P.; Perras, F. A.; Werner-Zwanziger, U.; Lussier, J. A.; Miller, K. J.; Calahoo, C. M.; Zwanziger, J. W.; Bieringer, M.; Marinkovic, B. A.; Bryce, D. L.; White, M. A. *Chem. Mater.* **2015**, 27, 2633.
- (15) Kong, X.; Terskikh, V. V.; Khade, R. L.; Yang, L.; Rorick, A.; Zhang, Y.; He, P.; Huang, Y.; Wu, G. *Angew. Chemie Int. Ed.* **2015**, 54, 4753.
- (16) He, P.; Xu, J.; Terskikh, V. V.; Sutrisno, A.; Nie, H. Y.; Huang, Y. *J. Phys. Chem. C* **2013**, 117, 16953.
- (17) Bignami, G. P. M.; Davis, Z. H.; Dawson, D. M.; Morris, S. A.; Russell, S. E.; McKay, D.; Parke, R. E.; Iuga, D.; Morris, R. E.; Ashbrook, S. E. *Chem. Sci.* **2018**, 9, 850.
- (18) Chen, C.-H.; Gaillard, E.; Mentink-Vigier, F.; Chen, K.; Gan, Z.; Gaveau, P.; Rebière, B.; Berthelot, R.; Florian, P.; Bonhomme, C.; Smith, M. E.; Métro, T.-X.; Alonso, B.; Laurencin, D. *Inorg. Chem.* **2020**, 59, 13050.
- (19) Champouret, Y.; Coppel, Y.; Kahn, M. L. *J. Am. Chem. Soc.* **2016**, 138, 16322.
- (20) Wang, M.; Wu, X. P.; Zheng, S.; Zhao, L.; Li, L.; Shen, L.; Gao, Y.; Xue, N.; Guo, X.; Huang, W.; Gan, Z.; Blanc, F.; Yu, Z.; Ke, X.; Ding, W.; Gong, X. Q.; Grey, C. P.; Peng, L. *Sci. Adv.* **2015**, 1, 1.

- (21) Métro, T.-X.; Gervais, C.; Martinez, A.; Bonhomme, C.; Laurencin, D. *Angew. Chemie Int. Ed.* **2017**, 56, 6803.
- (22) Griffin, J. M.; Clark, L.; Seymour, V. R.; Aldous, D. W.; Dawson, D. M.; Iuga, D.; Morris, R. E.; Ashbrook, S. E. *Chem. Sci.* **2012**, 3, 2293.
- (23) Trease, N. M.; Clark, T. M.; Grandinetti, P. J.; Stebbins, J. F.; Sen, S. J. *Chem. Phys.* **2017**, 146, 184505.
- (24) Pavón, E.; Osuna, F. J.; Alba, M. D.; Delevoye, L. *Solid State Nucl. Magn. Reson.* **2019**, 100, 45.
- (25) Pustogow, A.; Luo, Y.; Chronister, A.; Su, Y.-S.; Sokolov, D. A.; Jerzembeck, F.; Mackenzie, A. P.; Hicks, C. W.; Kikugawa, N.; Raghu, S.; Bauer, E. D.; Brown, S. E. *Nat.* **2019**, 574, 72.
- (26) Peng, L.; Liu, Y.; Kim, N.; Readman, J. E.; Grey, C. P. *Nat. Mater.* **2005**, 4, 216.
- (27) Hung, I.; Uldry, A.-C.; Becker-Baldus, J.; Webber, A. L.; Wong, A.; Smith, M. E.; Joyce, S. A.; Yates, J. R.; Pickard, C. J.; Dupree, R.; Brown, S. P. *J. Am. Chem. Soc.* **2009**, 131, 1820.
- (28) Chen, L.; Lu, X.; Wang, Q.; Lafon, O.; Trébosc, J.; Deng, F.; Amoureux, J. P. *J. Magn. Reson.* **2010**, 206, 269.
- (29) Carnahan, S. L.; Lampkin, B. J.; Naik, P.; Hanrahan, M. P.; Slowing, I. I.; VanVeller, B.; Wu, G.; Rossini, A. J. *J. Am. Chem. Soc.* **2018**, 141, 441.
- (30) Jakobsen, H. J.; Bildsøe, H.; Brorson, M.; Wu, G.; Gor'kov, P. L.; Gan, Z.; Hung, I. *J. Phys. Chem. C* **2015**, 119, 14434.
- (31) Perras, F. A.; Kobayashi, T.; Pruski, M. *J. Am. Chem. Soc.* **2015**, 137, 8336.
- (32) Harris, R. K.; Becker, E. D.; Menezes, S. M. C. de; Goodfellow, R.; Granger, P. *Pure Appl. Chem.* **2001**, 73, 1795.

- (33) Gan, Z.; Hung, I.; Wang, X.; Paulino, J.; Wu, G.; Litvak, I. M.; Gor'kov, P. L.; Brey, W. W.; Lendi, P.; Schiano, J. L.; Bird, M. D.; Dixon, I. R.; Toth, J.; Boebinger, G. S.; Cross, T. A. *J. Magn. Reson.* **2017**, 284, 125.
- (34) Keeler, E. G.; Michaelis, V. K.; Colvin, M. T.; Hung, I.; Gor'kov, P. L.; Cross, T. A.; Gan, Z.; Griffin, R. G. *J. Am. Chem. Soc.* **2017**, 139, 17953.
- (35) Keeler, E. G.; Michaelis, V. K.; Wilson, C. B.; Hung, I.; Wang, X.; Gan, Z.; Griffin, R. G. *J. Phys. Chem. B* **2019**, 123, 3061.
- (36) Hong-Cai, Z.; Long, J. R.; Yaghi, O. M. *Chem. Rev.* **2012**, 112, 673.
- (37) Furukawa, H.; Cordova, K. E.; O'Keeffe, M.; Yaghi, O. M. *Science*, **2013**, 341, 6149.
- (38) Hoffmann, H. C.; Debowski, M.; Müller, P.; Paasch, S.; Senkovska, I.; Kaskel, S.; Brunner, E. *Materials (Basel)*. **2012**, 5, 2537.
- (39) Sutrisno, A.; Huang, Y. *Solid State Nucl. Magn. Reson.* **2013**, 49, 1.
- (40) Lucier, B. E. G.; Chen, S.; Huang, Y. *Acc. Chem. Res.* **2018**, 51, 319.
- (41) Witherspoon, V. J.; Xu, J.; Reimer, J. A. *Chem. Rev.* **2018**, 118, 10033.
- (42) Wong, Y. T. A.; Martins, V.; Lucier, B. E. G.; Huang, Y. *Chem. Eur. J.* **2019**, 25, 1848.
- (43) Lucier, B. E. G.; Zhang, Y.; Huang, Y. *Concepts Magn. Reson. Part A Bridg. Educ. Res.* **2016**, 45A, 1.
- (44) Lucier, B. E. G.; Zhang, Y.; Lee, K. J.; Lu, Y.; Huang, Y. *Chem. Commun.* **2016**, 52, 7541.
- (45) Lu, Y.; Lucier, B. E. G.; Zhang, Y.; Ren, P.; Zheng, A.; Huang, Y. *Phys. Chem. Chem. Phys.* **2017**, 19, 6130.
- (46) Zhang, Y.; Lucier, B. E. G.; Fischer, M.; Gan, Z.; Boyle, P. D.; Desveaux, B.;

- Huang, Y. *Chem. Eur. J.* **2018**, *24*, 7866.
- (47) Loiseau, T.; Serre, C.; Huguenard, C.; Fink, G.; Taulelle, F.; Henry, M.; Bataille, T.; Férey, G. *Chem. Eur. J.* **2004**, *10*, 1373.
- (48) Kitagawa, S.; Uemura, K. *Chem. Soc. Rev.* **2005**, *34*, 109.
- (49) McKinlay, A. C.; Morris, R. E.; Horcajada, P.; Férey, G.; Gref, R.; Couvreur, P.; Serre, C. *Angew. Chemie Int. Ed.* **2010**, *49*, 6260.
- (50) Cai, H.; Huang, Y. L.; Li, D. *Coord. Chem. Rev.* **2019**, *378*, 207.
- (51) Wu, M.-X.; Yang, Y.-W. *Adv. Mater.* **2017**, *29*, 1606134.
- (52) Li, H.; Eddaoudi, M.; O’Keeffe, M.; Yaghi, O. M. *Nature* **1999**, *402*, 276.
- (53) Millange, F.; Serre, C.; Férey, G. *Synthesis, Chem. Commun.* **2002**, *2*, 822.
- (54) Cavka, J. H.; Jakobsen, S.; Olsbye, U.; Guillou, N.; Lamberti, C.; Bordiga, S.; Lillerud, K. P. *J. Am. Chem. Soc.* **2008**, *130*, 13850.
- (55) Rosi, N. L.; Kim, J.; Eddaoudi, M.; Chen, B.; O’Keeffe, M.; Yaghi, O. M. *J. Am. Chem. Soc.* **2005**, *127*, 1504.
- (56) Chui, S. S. Y.; Lo, S. M. F.; Charmant, J. P. H.; Orpen, A. G.; Williams, I. D. *Science*, **1999**, *283*, 1148.
- (57) Ahmed, I.; Jhung, S. H. *Chem. Eng. J.* **2017**, *310*, 197.
- (58) Roberts, J. M.; Fini, B. M.; Sarjeant, A. A.; Farha, O. K.; Hupp, J. T.; Scheidt, K. A. *J. Am. Chem. Soc.* **2012**, *134*, 3334.
- (59) Meng, X.; Wang, H.-N.; Song, S.-Y.; Zhang, H.-J. *Chem. Soc. Rev.* **2017**, *46*, 464.
- (60) Rood, J. A.; Noll, B. C.; Henderson, K. W. *Inorg. Chem.* **2006**, *45*, 5521.
- (61) Fischer, M.; Hoffmann, F.; Fröba, M. *ChemPhysChem* **2010**, *11*, 2220.

- (62) Lian, X.; Fang, Y.; Joseph, E.; Wang, Q.; Li, J.; Banerjee, S.; Lollar, C.; Wang, X.; Zhou, H.-C. *Chem. Soc. Rev.* **2017**, 46, 3386.
- (63) Novio, F.; Simmchen, J.; Vázquez-Mera, N.; Amorín-Ferré, L.; Ruiz-Molina, D. *Coord. Chem. Rev.* **2013**, 257, 2839.
- (64) Xu, J.; Terskikh, V. V.; Chu, Y.; Zheng, A.; Huang, Y. *Chem. Mater.* **2015**, 27, 3306.
- (65) Hu, J.; Sun, T.; Ren, X.; Wang, S. *Microporous Mesoporous Mater.* **2015**, 204, 73.
- (66) Xu, J.; Terskikh, V. V.; Huang, Y. *Chem. Eur. J.* **2013**, 19, 4432.
- (67) Mao, H.; Xu, J.; Hu, Y.; Huang, Y.; Song, Y. *J. Mater. Chem. A* **2015**, 3, 11976.
- (68) Xu, J.; Terskikh, V. V.; Chu, Y.; Zheng, A.; Huang, Y. *Magn. Reson. Chem.* **2020**, 58, 1082.
- (69) Toby, B. H.; Von Dreele, R. B. *IUCr*, **2013**, 46, 544.
- (70) Rood, J. A.; Henderson, K. W. *J. Chem. Educ.* **2012**, 90, 379.
- (71) Massiot, D.; Touzo, B.; Trumeau, D.; Coutures, J. P.; Virlet, J.; Florian, P.; Grandinetti, P. *J. Solid State Nucl. Magn. Reson.* **1996**, 6, 73.
- (72) Hung, I.; Trébossé, J.; Hoatson, G. L.; Vold, R. L.; Amoureux, J. P.; Gan, Z. *J. Magn. Reson.* **2009**, 201, 81.
- (73) Massiot, D.; Fayon, F.; Capron, M.; King, I.; Le Calvé, S.; Alonso, B.; Durand, J. O.; Bujoli, B.; Gan, Z.; Hoatson, G. *Magn. Reson. Chem.* **2002**, 40, 70.
- (74) Kresse, G.; Hafner, J. *Phys. Rev. B*, **1994**, 49, 14251.
- (75) Giannozzi, P.; Baroni, S.; Bonini, N.; Calandra, M.; Car, R.; Cavazzoni, C.; Ceresoli, D.; Chiarotti, G. L.; Cococcioni, M.; Dabo, I.; Corso, A. D.; Gironcoli, S. de; Fabris, S.; Fratesi, G.; Gebauer, R.; Gerstmann, U.; Gougoussis, C.; Kokalj, A.; Lazzeri, M.; Martin-Samos, L.; Marzari, N.; Mauri, F.; Mazzarello, R.; Paolini, S.;

- Pasquarello, A.; Paulatto, L.; Sbraccia, C.; Scandolo, S.; Sclauzero, G.; Seitsonen, A. P.; Smogunov, A.; Umari, P.; Wentzcovitch, R. M. *J. Phys. Condens. Matter* **2009**, *21*, 395502.
- (76) Perdew, J. P.; Burke, K.; Ernzerhof, M. *Phys. Rev. Lett.* **1996**, *77*, 3865.
- (77) Troullier, N.; Martins, J. L. *Phys. Rev. B* **1991**, *43*, 1993.
- (78) Kleinman, L.; Bylander, D. M. *Phys. Rev. Lett.* **1982**, *48*, 1425.
- (79) Charpentier, T. *Solid State Nucl. Magn. Reson.* **2011**, *40*, 1.
- (80) Bonhomme, C.; Gervais, C.; Babonneau, F.; Coelho, C.; Pourpoint, F.; Azaïs, T.; Ashbrook, S. E.; Griffin, J. M.; Yates, J. R.; Mauri, F.; Pickard, C. J. *Chem. Rev.* **2012**, *112*, 5733.
- (81) Pickard, C. J.; Mauri, F. *Phys. Rev. B*, **2001**, *63*, 245101.
- (82) Street, W. T. *J. Am. Chem. Soc.* **1995**, *117*, 5367.
- (83) Amoureux, J. P.; Huguenard, C.; Engelke, F.; Taulelle, F. *Chem. Phys. Lett.* **2002**, *356*, 497.
- (84) Gerothanassis, I. P.; Vakka, C. J. *Org. Chem.* **2002**, *59*, 2341.
- (85) Michaelis, V. K.; Keeler, E. G.; Ong, T.-C.; Craigen, K. N.; Penzel, S.; Wren, J. E. C.; Kroeker, S.; Griffin, R. G. *J. Phys. Chem. B*, **2015**, *119*, 8024.
- (86) Hallock, K. J.; Lee, D. K.; Ramamoorthy, A. J. *Chem. Phys.* **2000**, *113*, 11187.
- (87) Desiraju, G.; Steiner, T. *The Weak Hydrogen Bond: In structural Chemistry and Biology*, 1st Ed.; IUCr, **2010**.
- (88) Bondi, A. J. *Phys. Chem.* **2002**, *68*, 441.
- (89) Trung, T. K.; Trens, P.; Tanchoux, N.; Bourrelly, S.; Llewellyn, P. L.; Loera-Serna, S.; Serre, C.; Loiseau, T.; Fajula, F.; Férey, G. *J. Am. Chem. Soc.* **2008**,

130, 16926.

- (90) Zhang, Y.; Lucier, B. E. G. G.; Huang, Y. *Phys. Chem. Chem. Phys.* **2016**, *18*, 8327.

Chapter 4

4 ^{17}O solid-state NMR at ultrahigh magnetic field of 35.2 T: Resolution of inequivalent oxygen sites in different phases of MOF MIL-53(Al)

4.1 Introduction

Metal–organic frameworks (MOFs) are a class of inorganic–organic hybrid porous materials that have attracted tremendous attention in the last decades.¹ The remarkable variability and tunability of the composition, structure, and property of MOFs are the most striking characteristics, distinguishing themselves from other inorganic porous materials such as zeolites. Flexible MOFs are an important branch of MOF family. They can undergo reversible crystal-to-crystal phase transition upon external stimuli such as host–guest interactions and physical stimuli, resulting in drastic changes in unit cell volume and pore dimension.² The marked change in unit cell volume can be used for applications in sensors, switching devices, micromechanical devices, and so forth. Furthermore, the dynamic switching of MOF channels is ideal for selective adsorption of guest molecules.²

Perhaps, the most prominent member of flexible MOFs is MIL-53. Although many MOF systems exhibit some structural flexibility, the majority of current research is focused on the MIL-53 family due to their superior thermal (up to 500°C) and chemical (in water and many solvents) stability. The structural flexibility of MIL-53 is often demonstrated by the change in pore dimension during MOF activation and subsequent hydration (Figure 4.1).³ By removing the residual linker precursor (1,4-benzenedicarboxylic acid, H_2BDC) molecules occluded inside the MOF channels during synthesis, the pore dimension of MIL-53(Al), a prototypical member of MIL-53, increases from $7.3 \times 7.7 \text{ \AA}^2$ in the as-made phase (i.e., MIL-53(Al)-as) to $8.5 \times 8.5 \text{ \AA}^2$ in the large-pore phase (i.e., MIL-53(Al)-lp). The large-pore phase can adsorb water to yield a narrow-pore phase (i.e., MIL-53(Al)-np) with compressed channels of $2.6 \times 13.6 \text{ \AA}^2$.

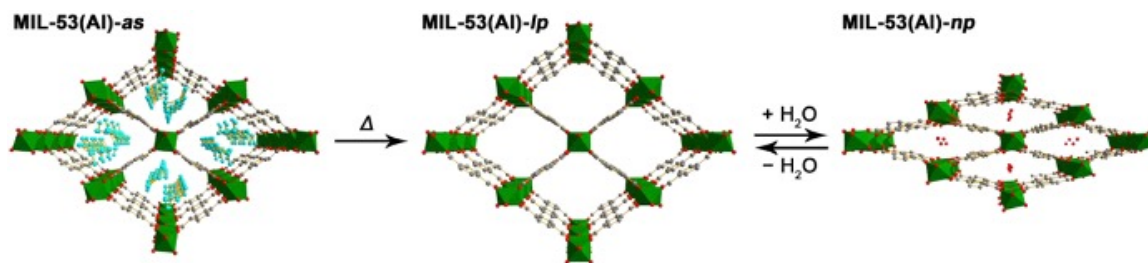


Figure 4.1. Schematic illustrations of the transformation between three MIL-53(Al) phases. Color coding: Al, green; O, red; C, grey; H₂BDC, turquoise. The hydrogen atoms are omitted for clarity.

Despite the drastic changes in channel dimension accompanied by the change in crystal structure, the framework topology is retained during the phase transition. The main driving force for phase transition and dynamic switching of channel size is hydrogen bonding,^{3,4} but other types of host–guest interactions such as π – π stacking and van der Waals forces are also considered to be factors.⁵ These interactions are not only responsible for the structural changes but also play critical roles in their applications such as xylene separation.⁶ Thus, a better understanding of the host–guest interactions in these systems through characterization of different phases are critically important for designing new flexible MOFs. The information on crystal structures of different phases associated with dynamic switching mainly come from the X-ray diffraction (XRD)-based methods. However, more often than not, guest molecules are disordered, and they undergo rapid thermal motions within MOF channels. Furthermore, the details of hydrogen bonding are usually unavailable due to the insensitivity of XRD to hydrogen atoms within the crystal structure.

Solid-state NMR (SSNMR) spectroscopy is a nuclide- and site-specific characterization tool complementary to XRD-based techniques.⁷ It is sensitive to the changes in both long-range ordering upon phase transition and local environment induced by host–guest interactions. Previous SSNMR studies provided valuable information on host–guest interaction and structural change associated with phase transitions in MIL-53(Al).^{1,4,5} The mechanism of dynamic switching during MOF activation and hydration was first rationalized on the basis of ¹H, ¹³C, and ²⁷Al SSNMR data.^{1,4,5} The adsorption of xylene

isomers, aromatic compounds, and nitrogen bases was further examined by ^1H , ^{13}C , ^{27}Al and ^2H SSNMR experiments.⁵ A ^{129}Xe SSNMR study also illustrated that the large-pore to narrow-pore transformation can be triggered by weak van der Waals forces between xenon atoms and the framework.⁵

Oxygen is a key constituent of MIL-53(Al). It exists in two different species within the framework: the carboxylate group ($-\text{COO}^-$), and the μ_2 -hydroxyl group bridging two AlO_6 octahedra ($\text{Al}-\text{OH}-\text{Al}$). These two oxygen-containing functional groups play prominent roles in the phase transition associated with the breathing of MIL-53(Al) and are directly involved in host-guest interactions such as hydrogen bonding.⁴ ^{17}O SSNMR spectroscopy should be ideal for probing phase transitions of MIL-53(Al) that alter the geometric and electronic environments of oxygen as ^{17}O is highly sensitive to both the chemical shift (CS) and quadrupolar interactions.⁸ However, ^{17}O SSNMR is, in general, more challenging than ^1H , ^{13}C , and ^{27}Al SSNMR, due to the fact that ^{17}O has extremely low natural abundance (0.038%) and a relatively low gyromagnetic ratio ($\gamma = -5.774 \text{ MHz T}^{-1}$), although high-resolution proton SSNMR can be challenging as well, but for a different reason. Furthermore, ^{17}O (spin $I = 5/2$) is quadrupolar⁹ and, therefore, often suffers from the line broadening induced by the second-order quadrupolar interaction. ^{17}O isotopic enrichment can dramatically increase the sensitivity.¹⁰ Performing ^{17}O SSNMR experiments at high magnetic fields ($\geq 18.8 \text{ T}$) can significantly improve spectral resolution (as the second-order quadrupolar interaction in frequency is inversely proportional to the strength of magnetic field) and enhances the sensitivity as well.

^{17}O SSNMR has been employed to examine the MIL-53 MOFs. Ashbrook et al. studied the mixed-metal MIL-53(Al and Ga) at 14.1 and 20.0 T. The results provide valuable information on the final composition of the materials, the preference for cation clustering/ordering within the MOFs, and the unusual breathing behavior.¹⁰ Previously, we also acquired ^{17}O SSNMR spectra of MIL-53(Al)-as and MIL-53(Al)-np at 21.1 T.¹⁰ Although significant differences in ^{17}O spectra were observed between the two phases, the multiple crystallographically inequivalent carboxylate oxygen sites in each phase were not resolved.

Very recently, we demonstrated that very high ^{17}O spectral resolution can be achieved for MOF systems at ultrahigh magnetic field of 35.2 T.¹¹ In the abovementioned reference, we examined the effect of activation on the MIL-53(Al) framework oxygen. At this highest magnetic field available to chemists today,¹² significantly higher spectral resolution and sensitivity achieved allowed us to distinguish partially activated from completely activated MIL-53(Al) (note: the completely activated MIL-53(Al) corresponds to MIL-53(Al)-lp phase) and resolve multiple oxygen environments in partially-activated MIL-53(Al). Encouraged by this work, we further carried out an ^{17}O SSNMR study of MIL-53(Al) at 35.2 T. The high spectral resolution and sensitivity at this field permit every inequivalent oxygen site to be differentiated in the MIL-53(Al)-as and MIL-53(Al)-np phases. Both the electric field gradient (EFG) and chemical shift (CS) tensor values for each oxygen site were also extracted.

4.2 Experimental details

4.2.1 Sample preparation

The MIL-53(Al)-as sample was synthesized by the dry gel conversion method described in our previous work.¹⁰ All starting materials were used as received without further purification. A mixture of $\text{Al}(\text{NO}_3)_3 \cdot 9\text{H}_2\text{O}$ (1.6880 g or 4.5 mmol) and 1,4-benzenedicarboxylic acid (H_2BDC , 0.9802 g or 5.9 mmol) was placed in a 23 ml of Teflon-lined autoclave charged with 0.5 ml of ^{17}O -enriched water (CortecNet, 35 atom %), see Figure A4.1 for the reaction vessel. The autoclave was sealed and heated in an oven at 220°C for 3 days. After slowly cooling to room temperature, MIL-53(Al)-as was collected as a white powder under vacuum filtration, washed with DMF, and dried in the air at 80°C. MIL-53(Al)-lp was prepared by first solvent exchanging MIL-53(Al)-as with DMF for 24 h and then activating it at 300°C under dynamic vacuum for 12 h. MIL-53(Al)-np was obtained by exposing MIL-53(Al)-lp to air overnight. The phase purity and crystallinity of ^{17}O -enriched samples were confirmed by powder XRD patterns (Figure A4.2). The degree of ^{17}O exchange is about 5.8% as the abovementioned samples were prepared under exactly the same conditions as those described in He et al.¹⁰

4.2.2 SSNMR spectroscopy

^{17}O SSNMR experiments were conducted at 35.2 T on a series-connected hybrid (SCH) magnet (^{17}O Larmor frequency: 203.4 MHz) at the National High Magnetic Field Laboratory (NHMFL) in Tallahassee, USA.¹² A Bruker Avance NEO console and a 3.2 mm of MAS probe designed and built at the NHMFL were used. The MAS rate was 18 kHz. Because this probe is a single-resonance probe, consequently, the spectra are not ^1H -decoupled. However, because the focal point of this paper is to resolve inequivalent carboxylate oxygen sites, it should be pointed out that the ^1H - ^{17}O dipolar coupling for the carboxylate oxygen in this MOF is relatively weak. In fact, the magnitude of the dipolar coupling between a carboxylate oxygen and a nearby phenyl proton is only about 1 kHz. Furthermore, our previous experience with similar compounds at lower fields indicates that ^1H decoupling does not improve the resolution of carboxylate oxygen drastically.

A pulse delay of 0.1 s was used, which was preoptimized to achieve the highest signal-to-noise (S/N) ratio. When different pulse delays were used, the observed NMR line-shapes did not exhibit significant changes. ^{17}O 1D MAS NMR spectrum of MIL-53(Al)-as was acquired by using a rotor-synchronized spin echo sequence with a 90° pulse of 2 μs and an interpulse delay of one rotor period. ^{17}O 1D MAS NMR spectrum of MIL-53(Al)-lp was acquired by using a one-pulse sequence with a 90° pulse of 2 μs . ^{17}O 1D MAS NMR spectrum of MIL-53(Al)-np was acquired by using a rotor-synchronized spin-echo sequence with a 90° pulse of 5 μs and an interpulse delay of 10 rotor periods for a whole spin-echo signal. ^{17}O 2D rotor-synchronized shifted-echo triple-quantum MAS (3QMAS) spectra were measured by using 3Q excitation and conversion pulses of 3.75 and 1.25 μs , respectively. 2D 3QMAS spectra were processed with the Q-shearing procedure using the MATLAB script (MathWorks Inc.) described in Hung et al.¹³ In general, the choice of a pulse length(s) for a particular experiment is based on the trade-off between the bandwidth and central transition (CT)-selectivity for sites with small C_Q values. Therefore, selection of a pulse length was made during the experimental optimization.

All ^{17}O NMR spectra were referenced to liquid water at 0 ppm. More NMR experimental details can be found in Table A4.1 and Table A4.2.

4.2.3 Spectral simulations

The strong interaction between the electric quadrupole moment of ^{17}O ($I = 5/2$) and the surrounding EFG yields broad powder patterns rather than sharper resonances. Enhanced at high magnetic fields such as 35.2 T, the CS interaction interplays with the quadrupolar interaction, making the line-shape of powder patterns more complicated and difficult to simulate. The dmfit software package was used to simulate ^{17}O SSNMR spectra using the Int2QUAD mode, taking both the quadrupolar and the CS effects into consideration.¹⁴

The EFG tensor is described in dmfit by using three principal components in the following order: $|V_{YY}| \leq |V_{XX}| \leq |V_{ZZ}|$. The quadrupolar coupling constant (C_Q) and asymmetry parameter (η_Q) are defined as follow: $C_Q = (eQV_{ZZ}/h) \times 9.7177 \times 10^{21}$ (in Hz) and $\eta_Q = (V_{YY} - V_{XX})/V_{ZZ}$, where e is the electric charge, Q is the quadrupole moment ($-2.558 \times 10^{-30} \text{ m}^2$),⁹ and a conversion factor of $9.7177 \times 10^{21} \text{ V m}^{-2}$ is used to convert C_Q from atomic units to Hz. C_Q and η_Q describe the spherical and cylindrical symmetry of the EFG tensor, respectively. The CS tensor is described by three principal components such that $|\delta_{22} - \delta_{\text{iso}}| \leq |\delta_{11} - \delta_{\text{iso}}| \leq |\delta_{33} - \delta_{\text{iso}}|$. The isotropic CS $\delta_{\text{iso}} = (\delta_{11} + \delta_{22} + \delta_{33})/3$, and two chemical shift anisotropy (CSA) parameters are defined by $\Delta_{\text{CS}} = \delta_{33} - \delta_{\text{iso}}$ and $\eta_{\text{CS}} = |(\delta_{22} - \delta_{11})/\Delta_{\text{CS}}|$. Three Euler angles (φ , χ , and ψ) describe the orientations of the CS tensor with respect to the EFG principal axis frame. As a result, eight independent parameters, C_Q , η_Q , δ_{iso} , Δ_{CS} , η_{CS} , φ , χ , and ψ , are required to characterize a single ^{17}O site when both the quadrupolar and CSA effects are considered. Only the center transition ($+1/2 \leftrightarrow -1/2$) was considered in spectral simulations of the ^{17}O 1D MAS spectra of MIL-53(AI)-np and MIL-53(AI)-as. For MIL-53(AI)-lp, the spinning sideband (SSB) pattern suggests the observation of satellite transitions. Therefore, the $+3/2 \leftrightarrow +1/2$ and $-1/2 \leftrightarrow -3/2$ transitions were also included to reproduce the SSBs of the 1D MAS spectrum. Seeing the satellite transitions is likely due to the hard 90° excitation pulse used.¹⁵ All uncertainties in NMR parameters were estimated by variation of the parameter of interest in both directions from the best-fit value while holding all other NMR parameters constant.

4.2.4 Theoretical calculations

Input unit cell parameters and atomic coordinates of three MIL-53(Al) phases were taken from the reference.⁴ Due to the disordered nature of H₂BDC in channels of MIL-53(Al)-as, they were removed prior to periodic density functional theory (DFT) calculations. The missing H atoms of BDC²⁻linkers, μ_2 -hydroxyl group, and water molecules in MIL-53(Al)-np were initially positioned to be consistent with the expected structure of the system and all atomic positions were then relaxed with the Vienna Ab-initio Simulation Package (VASP) code,¹⁶ keeping fixed unit cell parameters set to the XRD parameters. The NMR parameters were then calculated by using the QUANTUM-ESPRESSO code,¹⁷ keeping the atomic positions equal to the values previously calculated with VASP. The Gauge-including Projector Augmented Wave (GIPAW) approach involved in QUANTUM-ESPRESSO enables the reproduction of the results of a fully converged all-electron calculation.¹⁸ Calculations were performed using the generalized gradient approximation (GGA) with Perdew, Burke, and Ernserhof (PBE) functionals and norm-conserving pseudopotentials,¹⁹ in the Kleinman–Bylander form.²⁰ The wave functions are expanded on a plane-wave basis set with a kinetic energy cut-off of 80 Ry. For the charge density and CS tensor calculation, the integrals over the first Brillouin zone are performed using Monkhorst–Pack grids of $1 \times 3 \times 1$, $3 \times 1 \times 1$, and $1 \times 3 \times 3$ k-points for MIL-53(Al)-as, MIL-53(Al)-lp, and MIL-53(Al)-np, respectively. The isotropic chemical shift δ_{iso} is defined as $\delta_{\text{iso}} = \sigma_{\text{iso}}(\text{ref}) - \sigma_{\text{iso}}$, where $\sigma_{\text{iso}}(\text{ref})$ is the isotropic chemical shielding of the same nucleus in a reference system. In the present case, the comparison between the experimental ¹⁷O δ_{iso} and calculated σ_{iso} values for Na₂SiO₃, α -Na₂Si₂O₅, α - and γ -glycine, and α -SrSiO₃ enabled the determination of the relation between δ_{iso} and calculated σ_{iso} values for the ¹⁷O nucleus as previously described.¹⁰

4.3 Results and discussion

The framework of MIL-53(Al) is composed of unidimensional chains of μ_2 -OH-bridged AlO₄(OH)₂ octahedra interconnected by BDC²⁻ linkers, exhibiting 1D rhombic channels. Although the framework topology is retained during the dynamic switching of the structure, the crystal symmetry indeed varies from orthorhombic Pnma (#62) for MIL-53(Al)-as, to orthorhombic Imma (#72) for MIL-53(Al)-lp, to eventual monoclinic Cc

(#9) for MIL-53(Al)-np, respectively.⁴ There is only one μ_2 -OH oxygen site present in all three phases. The number of inequivalent $-\text{COO}^-$ oxygen sites, however, varies, depending on the crystal symmetry. Specifically, the numbers of $-\text{COO}^-$ oxygen sites are 2, 1, and 4 for MIL-53(Al)-as, MIL-53(Al)-lp, and MIL-53(Al)-np, respectively (Figure 4.2).

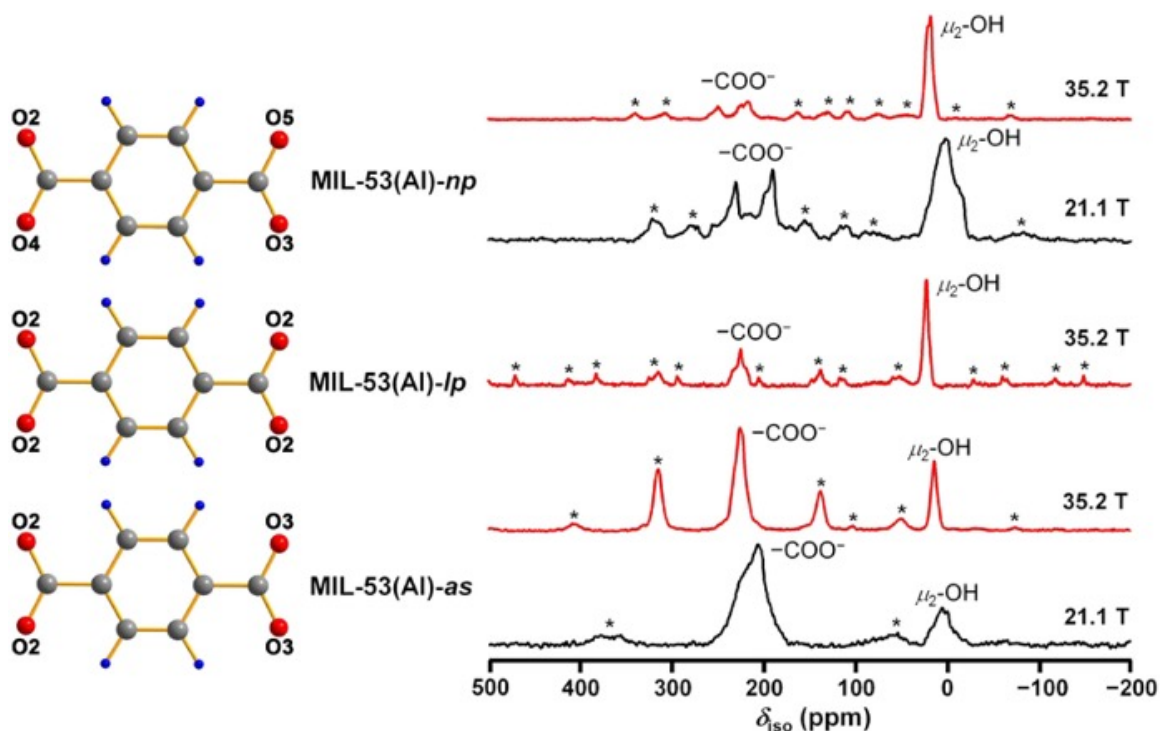


Figure 4.2. Left: The inequivalent $-\text{COO}^-$ oxygen sites in different phases. Color coding: O, red; C, grey; H, blue. Right: ^{17}O 1D MAS NMR spectra of ^{17}O -enriched MIL-53(Al) samples at 35.2 T (red) and 21.1 T (black). MIL-53(Al)-as: the top two spectra; MIL-53(Al)-lp: the middle spectrum; MIL-53(Al)-np: the bottom two spectra. The asterisk (*) denotes spinning sidebands (SSBs). Note: the numbers of transients accumulated for each spectrum at 35.2 T were only 1/4 and 1/8 of those at 21.1 T for MIL-53(Al)-as and MIL-53(Al)-np, respectively. The sample volume ($\sim 36 \mu\text{L}$) at 35.2 T was less than half of that ($\sim 80 \mu\text{L}$) at 21.1 T.

As mentioned earlier, ^{17}O SSNMR experiments of MIL-53(Al)-as and MIL-53(Al)-np were previously performed at magnetic fields lower than 35.2 T.¹⁰ Figure 4.2 shows ^{17}O 1D MAS spectra of MIL-53(Al)-as and MIL-53(Al)-np at 21.1 T.¹⁰ Two ^{17}O spectral envelopes corresponding to $-\text{COO}^-$ (~ 220 ppm) and $\mu_2\text{-OH}$ (~ 20 ppm) oxygen sites are seen in the 1D MAS spectrum of MIL-53(Al)-as. For MIL-53(Al)-np, three signals including two in the $-\text{COO}^-$ and one in the $\mu_2\text{-OH}$ oxygen regions were identified. However, the number of observed $-\text{COO}^-$ signals for each phase is only half of what is expected from the crystal symmetry, implying that not all inequivalent $-\text{COO}^-$ oxygen sites were resolved at this field.

As reported in the recent literature,^{11,12} performing ^{17}O SSNMR measurements at the highest accessible magnetic field strength can drastically enhance both spectral sensitivity and resolution. Therefore, in the present study, we acquired ^{17}O 1D MAS spectra of two MIL-53(Al) phases at 35.2 T (Figure 4.2). At this ultrahigh magnetic field, the signals of both MIL-53(Al)-as and MIL-53(Al)-np phases become considerably narrower due to the reduction of the second order quadrupolar broadening. At 35.2 T, the SSBs are significantly enhanced, especially for the $-\text{COO}^-$ oxygen, indicating the drastically amplified CSA in frequency by the high field.

The ^{17}O spectrum of MIL-53(Al)-lp at 35.2 T was recently published.¹¹ For comparison, it is also included in Figure 4.2. Although ^{17}O signals in the 1D MAS spectra become considerably narrower at 35.2 T, the number of $-\text{COO}^-$ oxygen signals for MIL-53(Al)-as and MIL-53(Al)-np remains the same as seen at 21.1 T, suggesting that even at 35.2 T, the maximum achievable ^{17}O spectral resolution in 1D MAS experiments is still insufficient to resolve all inequivalent oxygen sites. This is because some sites have very similar local environments and simply spinning the sample at the magic angle cannot completely average out the second-order quadrupolar interaction. To achieve higher spectral resolution, we have carried out ^{17}O 3QMAS experiments,²¹ as this technique can completely eliminate the second-order quadrupolar broadening along the indirect F1 dimension and therefore should separate the overlapping signals in the 1D MAS spectrum.

Figure 4.3 illustrates the 3QMAS spectra of MIL-53(Al)-np and MIL-53(Al)-as in the carboxylate oxygen region. Higher spectral resolution was indeed achieved as four and two $-\text{COO}^-$ oxygen sites are resolved along the F1 dimension of the spectra of MIL-53(Al)-np and MIL-53(Al)-as, respectively.

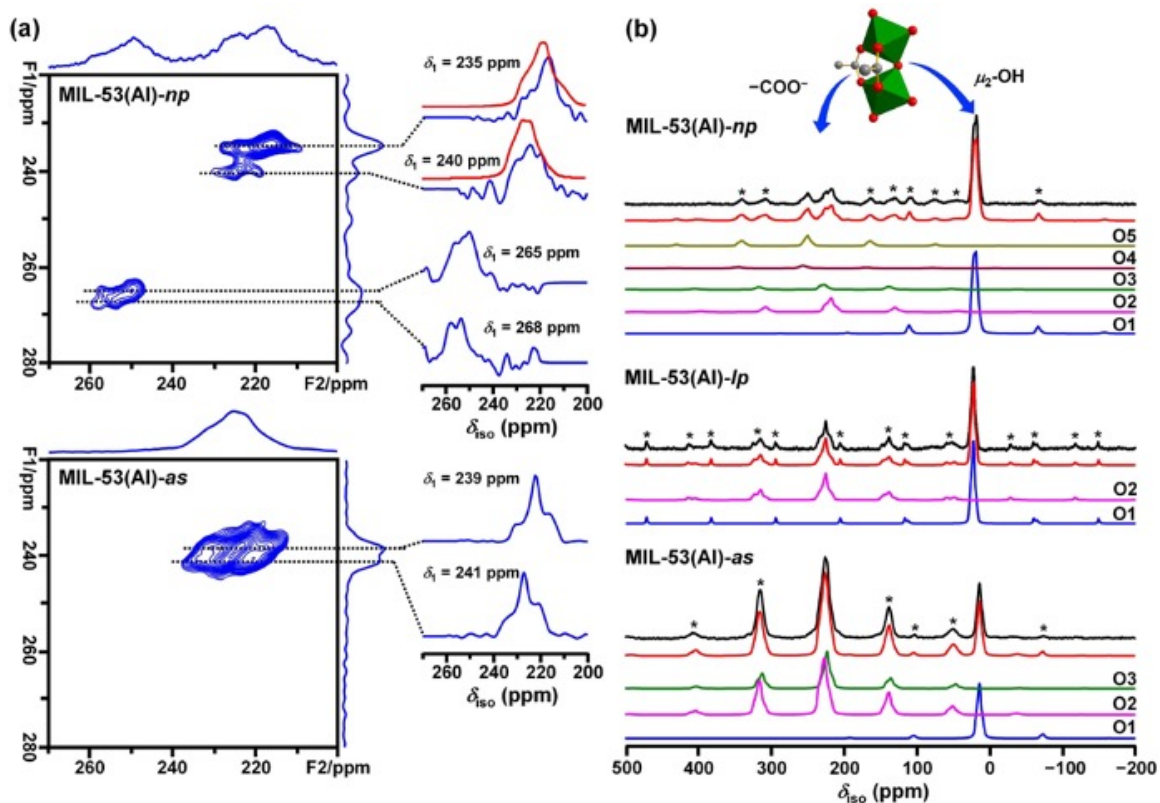


Figure 4.3. (a) ^{17}O 2D 3QMAS NMR spectra of ^{17}O -enriched MIL-53(Al)-as and MIL-53(Al)-np at 35.2 T. Blue and red solid lines denote experimental and simulated spectra, respectively. Only the regions corresponding to $-\text{COO}^-$ oxygen sites are shown. The total experimental times are 1.3 and 3.4 h for MIL-53(Al)-as and MIL-53(Al)-np, respectively. (b) Experimental and simulated ^{17}O 1D MAS NMR spectra of three MIL-53(Al) phases at 35.2 T. Both the quadrupolar and CSA effects are considered in simulation by using the parameters shown in Table 4.1. Asterisks (*) denote SSBs. The two oxygen species in MIL-53(Al) were shown on the top.

For both phases, the number of inequivalent -COO^- oxygen sites seen in the 3QMAS spectra is now consistent with that predicted by the crystal structures.⁴ It should be mentioned that the 3QMAS experiment was also carried out at 21.1 T. However, after 21 h of acquisition, the two inequivalent carboxylate oxygen sites of MIL-53(Al)-as were not resolved in the 3QMAS spectrum (Figure A4.3) at this field.

Analyzing 3QMAS spectra yields the quadrupolar parameters for each oxygen site. For each resolved ^{17}O signal along the F1 dimension, the corresponding F2 cross-section can be extracted at δ_1 (in ppm). The δ_1 and the spectral center of gravity (δ_2 , in ppm) along the F2 dimension can be used to calculate the isotropic chemical shift δ_{iso} (in ppm) and the quadrupolar product, $P_Q = C_Q (1 + \eta_Q^2/3)^{1/2}$ (in MHz) using the following equations:^{10,22}

$$\delta_{\text{iso}} = \frac{17}{27} \delta_1 + \frac{10}{27} \delta_2 \text{ (Equation 4.1)}$$

$$P_Q = \left\{ \frac{170}{81} \frac{[4I(2I-1)^2]}{[4I(I+1)-3]} (\delta_1 - \delta_2) \right\}^{1/2} \nu_0 10^{-3} \text{ (Equation 4.2)}$$

where ν_0 is the Larmor frequency (in MHz) and I is the spin quantum number.

The extracted δ_{iso} and P_Q values of each -COO^- oxygen site of MIL-53(Al)-as and MIL-53(Al)-np are shown in Table A4.3. The values of these two parameters were determined directly from the resonance positions along F1 and F2 dimensions and do not require accurate line-shape fitting along the F2 dimension.

To assign the observed ^{17}O NMR signals to crystallographic -COO^- oxygen sites, the δ_{iso} values of each inequivalent oxygen site were predicted by the GIPAW DFT calculations under periodic boundary conditions (Table A4.4). It has been well established that although the calculated δ_{iso} values may not exactly match the experimental δ_{iso} values, assignments of multiple signals based on relative calculated δ_{iso} values are valid.^{8,10,11,23}

A comparison between calculated and experimental δ_{iso} values permits individual assignment of -COO^- oxygen signals. For instance, the calculated δ_{iso} values of -COO^-

oxygen sites are ordered O4 > O5 > O3 > O2 for MIL-53(Al)-np. The ^{17}O signal with the highest δ_{iso} of 264 ppm is, therefore, assigned to O4, the ^{17}O signal with the second-highest δ_{iso} of 260 ppm is assigned to O5 and so forth. The two $-\text{COO}^-$ oxygen signals of MIL-53(Al)-as are assigned similarly.

For MIL-53(Al)-np, O2 and O3 signals are well resolved in the F2 dimension, and their line-shapes along F2 cross-section are also well defined. Their C_Q , η_Q , and δ_{iso} values can be extracted by fitting the F2 cross-sections (Table A4.3), and they were used as initial inputs to simulate the 1D MAS spectra for final refinement. However, the signals of O4 and O5 sites overlap, and the line-shapes of their F2 cross-sections are not well-defined. For these two sites, using experimentally obtained P_Q and theoretically calculated η_Q , we derived their C_Q values according to their relationship of $P_Q = C_Q(1 + \eta_Q^2/3)^{1/2}$. The C_Q , η_Q , and δ_{iso} values were further refined by simulating the 1D MAS spectra. MIL-53(Al)-np has five oxygen sites including the μ_2 -OH oxygen. Forty parameters in total are required if both the EFG and CSA effects are considered. To reduce the number of parameters, we first simulated the 1D MAS spectrum by only considering the quadrupolar interaction. We have demonstrated previously that at such a high magnetic field of 35.2 T, the EFG anisotropy of a carboxylate oxygen is much smaller than that of the CSA. The EFG is the primary source of line broadening for isotropic peaks, but only makes little contribution to the SSBs.¹¹ Indeed, the isotropic region in the simulated spectrum where only the effect of the EFG is considered matches well with the experimental spectrum (Figure A4.4), but the SSBs are negligible as expected. Figure A4.5 further illustrates an excellent agreement between experimental spectrum of MIL-53(Al)-lp and the simulated one where only the quadrupolar effect is considered, demonstrating that the main source of experimental resonance broadening of the isotropic peaks is the second-order quadrupolar interaction.

To reproduce the SSBs and obtain the CS tensor parameters, we further simulated the 1D spectrum by taking both the EFG and CSA effects into account. Specifically, five additional parameters are incorporated in the simulation: two CSA parameters including the reduced anisotropy Δ_{CS} and the CS asymmetry parameter η_{CS} , as well as three Euler angles (φ , χ , and ψ) describing the orientations of the CS tensor with respect to the EFG

tensor principle axis frame.¹⁴ The calculated Δ_{CS} , η_{CS} , and three Euler angles (ϕ , χ , and ψ) (Table A4.4) along with the C_Q , η_Q , and δ_{iso} values optimized in the previous steps were used as initial inputs for fitting the 1D MAS spectra. The final simulation allows us to refine and determine the final values of the eight parameters describing the EFG and CSA effects for each oxygen site. The final refined NMR parameters are summarized in Table 4.1.

The ^{17}O C_Q , η_Q , and δ_{iso} values of some oxygen sites in MIL-53(Al) were reported previously.¹⁰ However, because the experiments were conducted at the magnetic fields at 21.1 T or lower, the lower sensitivity and resolution did not allow all inequivalent $-\text{COO}^-$ oxygen sites to be resolved. In the present study, we were able to resolve all inequivalent oxygen sites of MIL-53(Al)-as and MIL-53(Al)-np phases and extract ^{17}O C_Q , η_Q , and δ_{iso} values for every site. It should be pointed out that the resolution of all inequivalent sites results from not only the high spectral resolution achieved at 35.2 T but also the significant boost to the sensitivity at this field.

Table 4.1. Refined experimental ^{17}O NMR parameters of three MIL-53(Al) phases.

Site	P_Q (MHz)	C_Q (MHz)	η_Q	δ_{iso} (ppm)	Δ_{CS} (ppm)	η_{CS}	ϕ (°)	χ (°)	ψ (°)
MIL-53(Al)-as									
O1 (μ_2 -OH)		5.78	0.75	19.6	94	0.22	90	0	0
O2 ($-\text{COO}-$)	8.6	7.41	0.74	236.4	-210	0.37	250	80	70
O3 ($-\text{COO}-$)	8.1	6.95	0.84	232.1	-184	0.63	180	85	40
MIL-53(Al)-lp									
O1 (μ_2 -OH)	5.42	0.72	27.4	65	0.72	90	0	0	5.42
O2 ($-\text{COO}-$)	7.45	0.81	235.8	-182	0.82	170	80	45	7.45
MIL-53(Al)-np									
O1 (μ_2 -OH)									
O2 ($-\text{COO}-$)	8.3	6.37	0.5	25.6	-70	0.3	270	0	0
O3 ($-\text{COO}-$)	8.1	7.77	0.75	228	-182	0.72	140	90	80
O4 ($-\text{COO}-$)	7.5	7.36	0.55	235	202	0.95	280	45	160
O5 ($-\text{COO}-$)	8.1	6.95	0.63	258	-201	0.98	170	85	40

The high sensitivity gained at the ultrahigh field has made the ^{17}O 3QMAS experiments performed in this study practically possible in just a matter of hours, not days. Such a gain in sensitivity is very significant, considering the ^{17}O -enriched MOFs used in this work were prepared by using only 35% ^{17}O -enriched water. Furthermore, this is the first time that the CSA parameters and Euler angles are reported for oxygen sites in various MIL-53(Al) phases.

In the present work, ^{17}O 2D 3QMAS experiments at an ultrahigh field of 35.2 T allow us to separate all inequivalent $-\text{COO}^-$ oxygen sites in both MIL-53(Al)-as and MIL-53(Al)-lp. We previously also reported the ^{17}O MAS spectrum of MIL-53(Al)-lp at 35.2 T. Taken together, we have been able to unambiguously identify all chemically and crystallographically inequivalent oxygen sites in all three representative phases of MIL-53(Al) at 35.2 T. The total number of resolved ^{17}O signals now matches the number of inequivalent oxygen sites expected from their crystal symmetry: three for MIL-53(Al)-as, two for MIL-53(Al)-lp, and five for MIL-53(Al)-np.⁴ The experimental C_Q , η_Q , and δ_{iso} values of $-\text{COO}^-$ oxygen sites range from 6.95 to 7.77 MHz, 0.55 to 0.84, and 228.0 to 264.6 ppm, respectively, and these ranges are from 5.42 to 6.37 MHz, 0.50 to 0.75, and 19.6 to 27.4 ppm for $\mu_2\text{-OH}$ oxygen sites. Moreover, the magnitudes of the CSA of $\mu_2\text{-OH}$ oxygen sites ($|\Delta C_S|$: 65 to 94 ppm) are smaller than those of $-\text{COO}^-$ oxygen sites ($|\Delta C_S|$: 176 to 198 ppm), consistent with the literature.⁸

At this point, it is informative to compare the ^{17}O NMR results obtained at 35.2 T with the information extracted from ^1H , ^{13}C , and ^{27}Al MAS NMR data.^{1,4,5,10} In all cases, the changes in NMR spectra have been observed upon the transformation among three MIL-53(Al) phases shown in Figure 4.1. ^1H MAS NMR is sensitive to the existence and identity of guest molecules within MOF channels.^{1,4,10} As a result, the ^1H MAS NMR spectrum of MIL-53(Al)-as looks distinctly different from that of MIL-53(Al)-lp. The ^{13}C cross-polarization (CP) MAS NMR spectra are particularly sensitive to the changes in local electronic environment around carboxylate groups induced by hydrogen bonding.^{4,5,10} Consequently, the phase transition from MIL-53(Al)-lp to MIL-53(Al)-np induced by water adsorption is accompanied by a relatively large chemical shift of carboxylate carbon from 170 to 174 ppm.⁴ The changes in the ^{27}Al MAS NMR spectra

directly reflect the degree of distortion in $\text{AlO}_4(\text{OH})_2$ octahedra during the phase transition.^{4,5} ^{27}Al NMR spectra are particularly sensitive to the phase change between MIL-53(Al)-lp and MIL-53(Al)-np as the C_Q value increases substantially from 8.4 to 10.67 MHz upon adsorption of water.

^{17}O SSNMR can also provide valuable information on structure, phase transition, and host-guest interaction in MIL-53. The chemical shift of the μ_2 -OH oxygen is sensitive to the nature of metals that it bridges in the framework and has been used to confirm and quantify the incorporation of the second framework metal into mixed-metal MIL-53.¹⁰ The current and previous work has shown that ^{17}O SSNMR also has the ability to detect the two phase transitions in MIL-53(Al) involving three phases as shown in Figure 4.1. At 35.2 T, upon activation, MIL-53(Al)-as with the Pnma structure transforms to MIL-53(Al)-lp with the Imma structure, which coincides with a significant change in ^{17}O δ_{iso} of the μ_2 -OH signal from 19.6 to 27.4 ppm (Figure 4.4).

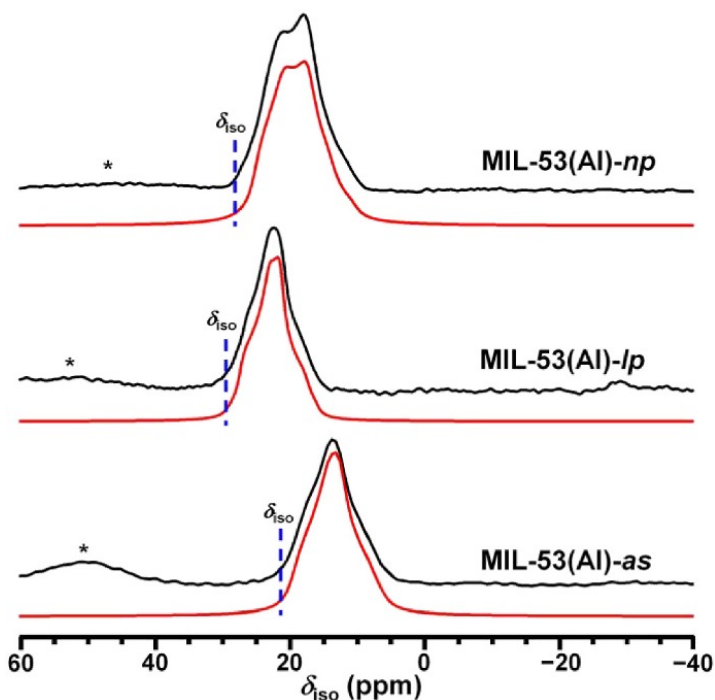


Figure 4.4. ^{17}O 1D experimental (black) and simulated (red) MAS NMR spectra of ^{17}O -enriched MIL-53(Al) samples at 35.2 T. blue dashed lines denote the isotropic chemical shift δ_{iso} . Only the regions corresponding to μ_2 -OH oxygen sites are shown for clarity. Asterisks (*) denote SSBs.

The μ_2 -OH group is involved in the hydrogen bonding with the occluded linker precursor, H₂BDC, in MIL-53(Al)-as. This interaction is responsible for the slightly reduced channel dimension of MIL-53(Al)-as ($7.3 \times 7.7 \text{ \AA}^2$) compared with MIL-53(Al)-lp ($8.5 \times 8.5 \text{ \AA}^2$). Apparently, the significant change in isotropic chemical shift observed upon phase transition is due to the removal of hydrogen bonding interaction by activation. Adsorption of water induces the phase transformation from the MIL-53(Al)-lp to MIL-53(Al)-np phases. It is known that the μ_2 -OH group is not directly involved in hydrogen bonding with water molecules because its ¹H chemical shift does not change upon water adsorption.⁴

Consequently, the change in the ¹⁷O δ_{iso} value of μ_2 -OH oxygen from MIL-53(Al)-lp to MIL-53(Al)-np is subtle. However, the changes in the ¹⁷O C_Q (from 5.42 to 6.37 MHz) and η_Q (from 0.72 to 0.50) values are noticeable. The CSA parameters of μ_2 -OH oxygen also alters upon water adsorption (ΔC_S : 65 to -70 ppm; η_{CS} : 0.72 to 0.30). These observations indicate that the adsorbed water molecules have induced observable differences in local environment of μ_2 -OH, even when hydrogen bonds are not formed.

The phase transformation from MIL-53(Al)-lp to MIL-53(Al)-np upon water adsorption is evidenced from the significant change in the -COO⁻ oxygen region of the ¹⁷O 1D MAS spectra. Specifically, the splitting of the single -COO⁻ oxygen peak in MIL-53(Al)-lp into two signals in the spectrum of MIL-53(Al)-np was observed at 35.2 T and lower fields.¹⁰ Ashbrook et al. identified the signal with lower δ_{iso} value to the -COO⁻ oxygen interacting with water via hydrogen bonding and the one at higher δ_{iso} value to the -COO⁻ oxygen uninvolved in hydrogen bonding.¹⁰ The 3QMAS spectrum acquired at 35.2 T further illustrates that each -COO⁻ oxygen signal seen in the 1D MAS spectrum actually originates from two overlapping signals. The peak with lower chemical shift results from the overlapping of O2 and O3 signals, whereas the higher chemical shift envelop is due to O4 and O5. Crystal structure indicates that the local environments of O2 and O3 are very similar as the bond lengths and angles involving the two oxygen sites are almost identical.⁴ The same is true for O4 and O5. At 35.2 T, each pair of crystallographically inequivalent carboxylate oxygen with very similar local structures can be well distinguished, demonstrating that the very high ¹⁷O spectral resolution and

sensitivity achieved at this ultrahigh magnetic field permit one to differentiate oxygen sites with subtle differences in local geometry. The fact that the ^{17}O isotropic chemical shift values of O4 and O5 differ significantly from O2 and O3 upon adsorption of water confirms the previous results that only half of the $-\text{COO}^-$ oxygen sites are involved in the hydrogen bonding with water in MIL-53(Al)-np.^{1,10} As mentioned earlier, water adsorption indeed induces a shift of $-\text{COO}^-$ carbon towards the deshielded direction.⁴ However, in each carboxylate group, one oxygen is directly involved in hydrogen bonding and the other is not, consequently, the impact of hydrogen bonding with water on each carboxylate carbon is the same. Therefore, the ^{13}C SSNMR data cannot pinpoint exactly which $-\text{COO}^-$ oxygen site participates in the hydrogen bonding.⁴

4.4 Conclusions

In summary, the high ^{17}O spectral resolution and sensitivity achieved at 35.2 T (the highest magnetic field accessible to chemists to date) combined with 2D 3QMAS technique make it possible to resolve all inequivalent $-\text{COO}^-$ oxygen sites in three MIL-53(Al) phases. The crystal structures of MIL-53(Al), originally determined by powder XRD data, are therefore validated by ^{17}O SSNMR data. The enhanced CSA effect at ultrahigh field of 35.2 T allows us to extract the ^{17}O CSA parameters. This work clearly demonstrates that ^{17}O SSNMR at very high magnetic fields is sensitive to the phase transitions in MOFs. Fine information on both MOF structure and host-guest interaction in MIL-53 systems is obtained from ^{17}O NMR spectra at 35.2 T owing to the very high spectral resolution and sensitivity achieved at this field. Such information is complementary to that those obtained from the ^1H , ^{13}C , and ^{27}Al SSNMR spectroscopy. The ability to completely resolve multiple chemically and, more importantly, crystallographically inequivalent oxygen sites in MOFs, as described in this work, greatly increases the potential for using NMR crystallography to determine the structures of new MOFs and refine the crystal structures of existing MOFs.

4.5 References

- (1) a) Zhou, H.-C.; Long, J. R.; Yaghi, O. M. *Chem. Rev.* **2012**, 112, 673. b) Furukawa, H.; Cordova, K. E.; O'Keeffe M.; Yaghi, O. M. *Science*, **2013**, 341, 1230444.
- (2) a) Schneemann, A.; Bon, V.; Schwedler, I.; Senkovska, I.; Kaskel, S.; Fischer, R. A.; *Chem. Soc. Rev.* **2014**, 43, 6062. b) Chang, Z.; Yang, D.-H.; Xu, J.; Hu, T.-L.; Bu, X.-H. *Adv. Mater.* **2015**, 27, 5432.
- (3) Loiseau, T.; Serre, C.; Huguenard, C.; Fink, G.; Taulelle, F.; Henry, M.; Bataille, T.; Férey, G. *Chem. Eur. J.* **2004**, 10, 1373.
- (4) Ortiz, G; Chaplais, G.; Paillaud, J.-L.; Nouali, H.; Patarin J.; Raya, J.; Marichal, C.; *J. Phys. Chem. C*, **2014**, 118, 22021.
- (5) a) Giovine, R.; Volkringer, C.; Trebosc, J.; Amoureux, J.-P.; Loiseau, T.; Lafon, O.; Pourpoint, F. *Acta Crystallogr. C*, **2017**, 73, 176. b) Paula, C.; Wisser, D.; Ranguis, M.; Schwieger, W.; Hovestadt, M.; Kriesten, M.; Vanatalu, K.; Oss, A.; Org, M.-L.; Samoson, A.; Hartmann, M. *J. Phys. Chem. C*, **2020**, 124, 19136. c) Lieder, C.; Opelt S.; Dyballa, M.; Henning, H.; Klemm, E.; Hunger, M.; *J. Phys. Chem. C*, **2010**, 114, 16596. d) Jiang, Y.; Huang, J.; Marx, S.; Kleist, W.; Hunger, M.; Baiker, A. *J. Phys. Chem. Lett.* **2010**, 1, 2886. e) Ibrahim, B.; Lucier, B. E. G.; Xu, J.; He, P.; Huang, Y. *Can. J. Chem.* **2015**, 93, 960. f) Khudozhitkov, A. E.; Jobic, H.; Freude, D.; Haase, J.; Kolokolov, D. I.; Stepanov, A. G. *J. Phys. Chem. C*, **2016**, 120, 21704. g) Khudozhitkov, A. E.; Arzumanov, S. S.; Kolokolov, D. I.; Stepanov, A. G. *Microporous Mesoporous Mater.* **2020**, 300, 110155. h) Li, S.; Li, J.; Tang, J.; Deng, F. *Solid State Nucl. Magn. Reson.* **2018**, 90, 1. i) Springuel-Huet, M.-A.; Nossov, A.; Adem, Z.; Guenneau, F.; Volkringer, C.; Loiseau, T.; Férey, G.; Gédéon, A. *J. Am. Chem. Soc.* **2010**, 132, 11599. j) Trung, T. K.; Trens, P.; Tanchoux, N.; Bourrelly, S.; Llewellyn, P. L.; Loera-Serna, S.; Serre, C.; Loiseau, T.; Fajula, F.; Férey, G.; *J. Am. Chem. Soc.* **2008**, 130, 16926. k) Hamon, L.; Serre, C.; Devic, T.; Loiseau, T.; Millange, F.; Férey, G.; Weireld, G. D. *J. Am. Chem. Soc.* **2009**, 131, 8775. l) Boutin, A.; Coudert, F.-X.; Springuel-Huet, M.-A.; Neimark, A. V.; Férey, G.; Fuchs, A. H. *J. Phys. Chem. C*, **2010**, 114, 22237. m) Coudert, F.-X.; Jeffroy, M.; Fuchs, A. H.; Boutin, A.; Mellot-Draznieks, C. *J. Am. Chem. Soc.* **2008**, 130, 14294. n) Kim, J. Y.; Park, J.; Ha, J.; Jung, M.; Wallacher, D.; Franz, A.; Balderas-

- Xicohténcatl, R.; Hirscher, M.; Kang, S. G.; Park, J. T.; Oh, I. H.; Moon, H. R.; Oh, H. J. *Am. Chem. Soc.* **2020**, 142, 13278.
- (6) a) Alaert, L.; Maes, M.; Giebeler, L.; Jacobs, P. A.; Martens, J. A.; Denayer, J. F. M.; Kirschhock, C. E. A.; De Vos, D. E. *J. Am. Chem. Soc.* **2008**, 130, 14170. b) Finsy, V.; Kirschhock, C. E. A.; Vedts, G.; Maes, M.; Alaerts, L.; De Vos, D. E.; Baron, G. V.; Denayer, J. F. M. *Chem. Eur. J.* **2009**, 15, 7724. c) DeMalsche, W.; Van der Perre, S.; Silverans, S.; Maes, M.; De Vos, D. E.; Lynen, F.; Denayer, J. F. M. *Microporous Mesoporous Mater.* **2012**, 162, 1.
- (7) a) MacKenzie, K. J. D.; Smith, M. E. *Multinuclear Solid-State NMR of Inorganic Materials*, Pergamon, **2002**. b) Freytag, A. I.; Pauric, A. D.; Krachkovskiy, S. A.; Goward, G. R. *J. Am. Chem. Soc.* **2019**, 141, 13758.
- (8) a) Ashbrook, S. E.; Smith, M. E. *Chem. Soc. Rev.* **2006**, 35, 718. b) Wu, G. *Prog. Nucl. Magn. Reson. Spectrosc.* **2019**, 114, 135. c) Yamada, K. *Annu. Rep. NMR Spectrosc.* **2010**, 70, 115. d) Castiglione, F.; Mele, A.; Raos, G. *Annu. Rep. NMR Spectrosc.* **2015**, 85, 143. e) Buannic, L.; Blanc, F.; Middlemiss, D. S.; Grey, C. P. *J. Am. Chem. Soc.* **2012**, 134, 14483. f) Alam, T. M.; Nyman, M.; Cherry, B. R.; Segall, J. M.; Lybarger, L. E. *J. Am. Chem. Soc.* **2004**, 126, 5610. g) Holmes, S. T.; Schurko, R. W. *J. Phys. Chem. C*, **2018**, 122, 1809. h) Romao, C. P.; Perras, F. A.; Werner-Zwanziger, U.; Lussier, J. A.; Miller, K. J.; Calahoo, C. M.; Zwanziger, J. W.; Bieringer, M.; Marinkovic, B. A.; Bryce, D. L.; White, M. A. *Chem. Mater.* **2015**, 27, 2633. i) Champouret, Y.; Coppel, Y.; Kahn, M. L. *J. Am. Chem. Soc.* **2016**, 138, 16322.
- (9) Harris, R. K.; Becker, E. D.; Cabral De Menezes, S. M.; Goodfellow, R.; Granger, P. *Pure Appl. Chem.* **2001**, 73, 1795.
- (10) a) Griffin, J. M.; Clark, L.; Seymour, V. R.; Aldous, D. W.; Dawson, D. M.; Iuga, D.; Morris, R. E.; Ashbrook, S. E. *Chem. Sci.* **2012**, 3, 2293. b) Wang, M.; Wu, X.-P.; Zheng, S.; Zhao, L.; Li, L.; Shen, L.; Gao, Y.; Xue, N.; Guo, X.; Huang, W.; Gan, Z.; Blanc, F.; Yu, Z.; Ke, X.; Ding, W.; Gong, X.-Q.; Grey, C. P.; Peng, L. *Sci. Adv.* **2015**, 1, e1400133. c) Métro, T.-X.; Gervais, C.; Martinez, A.; Bonhomme, C.; Laurencin, D. *Angew. Chem. Int. Ed.* **2017**, 56, 6803. d) He, P.; Xu, J.; Terskikh, V. V.; Sutrisno, A.; Nie, H.-Y.; Huang, Y. *J. Phys. Chem. C*, **2013**, 117, 16953. e)

- Bignami, G. P. M.; Davis, Z. H.; Dawson, D. M.; Morris, S. A.; Russell, S. E.; D.McKay, R. E.; Parke, D.; Iuga, R. E.; Morris, S. A.; Ashbrook, S. E. *Chem. Sci.* **2018**, 9, 850. f) Rice, C. M.; Davis, Z. H.; McKay, D.; Bignami, G. P. M.; Chitac, R. G.; Dawson, D. M.; Morris, R. E.; Ashbrook, S. E. *Phys. Chem. Chem. Phys.* **2020**, 22, 14514.
- (11) Martins, V.; Xu, J.; Wang, X.; Chen, K.; Hung, I.; Gan Z.; Gervais C.; Bonhomme, C.; Jiang, S.; Zheng, A.; Lucier, B. E. G.; Huang, Y. J. *Am. Chem. Soc.* **2020**, 142, 14877.
- (12) a) Keeler, E. G.; Michaelis, V. K.; Colvin, M. T.; Hung, I.; Gor'kov, P. L.; Cross, T. A.; Gan, Z.; Griffin, R. G. *J. Am. Chem. Soc.* **2017**, 139, 17953. b) Gan, Z.; Hung, I.; Wang, X.; Paulino, J.; Wu G.; Litvak, I. M.; Gor'kov, P. L.; Brey, W. W.; Lendi, P.; Schiano, J. L.; Bird, M. D.; Dixon, I. R.; Toth, J.; Boebinger, G. S.; Cross, T. A. *J. Magn. Reson.* **2017**, 284, 125. c) Bonhomme, C.; Wang, X.; Hung I.; Gan, Z.; Gervais C.; Sassoie, C.; Rimsza J.; Du, J.; Smith, M. E.; Hanna J. V.; Sarda S.; Gras, P.; Combes, C.; Laurencin, D. *Chem. Commun.* **2018**, 54, 9591. d) Keeler, E. G.; Michaelis, V. K.; Wilson, C. B.; Hung, I.; Wang, X.; Gan, Z.; Griffin, R. G. *J. Phys. Chem. B*, **2019**, 123, 3061. e) Wang, Q.; Li, W.; Hung, I.; Mentink-Vigier, F.; Wang, X.; Qi, G.; Wang, X.; Gan, Z.; Xu, J.; Deng, F.; *Nat. Commun.* **2020**, 11, 3620.
- (13) Hung, I.; Trébosch, J.; Hoatson, G. L.; Vold, R. L.; Amoureux, J.-P.; Gan, Z. *J. Magn. Reson.* **2009**, 201, 81
- (14) Massiot, D.; Fayon, F.; Capron, M.; King, I.; Le Calve, S.; Alonso, B.; Durand, J.-O.; Bujoli, B.; Gan, Z.; Hoatson, G. *Magn. Reson. Chem.* **2002**, 40, 70.
- (15) Man, P. P., *Encyclopedia of Analytical Chemistry*, John Wiley & Son, Chichester 2000 12224.
- (16) Kresse, G.; Hafner, J. *Phys. Rev. B*, **1994**, 49, 14251.
- (17) Giannozzi, P.; Baroni, S.; Bonini, N.; Calandra, M.; Car, R.; Cavazzoni, C.; Ceresoli, D.; Chiarotti, G. L.; Cococcioni, M.; Dabo, I.; Dal Corso, A.; de Gironcoli, S.; Fabris, S.; Fratesi, G.; Gebauer, R.; Gerstmann, U.; Gougoussis, C.; Kokalj, A.; Lazzeri, M.; Martin-Samos, L.; Marzari, N.; Mauri, F.; Mazzarello, R.; Paolini, S.; Pasquarello, A.; Paulatto, L.; Sbraccia, C.; Scandolo, S.; Sclauzero, G.; Seitsonen, A.

- P.; Smogunov, A.; Umari, P.; Wentzcovitch, R. M. *J. Phys.: Condens. Matter.* **2009**, *21*, 395502
- (18) Pickard, C. J.; Mauri, F. *Phys. Rev. B*, **2001**, *63*, 245101.
- (19) Troullier, N.; Martins, J. L. *Phys. Rev. B*, **1991**, *43*, 1993
- (20) Kleinman, L.; Bylander, D. M. *Phys. Rev. Lett.* **1982**, *48*, 1425.
- (21) Frydman, L.; Harwood, J. S. *J. Am. Chem. Soc.* **1995**, *117*, 5367.
- (22) Amoureux, J.-P.; Huguenard, C.; Engelke, F.; Taulelle, F. *Chem. Phys. Lett.* **2002**, *356*, 497.
- (23) a) Charpentier, T. *Solid State Nucl. Magn. Reson.* **2011**, *40*, 1. b) Bonhomme, C.; Gervais, C.; Babonneau, F.; Coelho, C.; Pourpoint, F.; Azaïs, T.; Ashbrook, S. E.; Griffin, J. M.; Yates, J. R.; Mauri, F.; Pickard, C. J. *Chem. Rev.* **2012**, *112*, 5733. c) Kong, X.; Terskikh, V. V.; Khade, R. L.; Yang, L.; Rorick, A.; Zhang, Y.; He, P.; Huang, Y.; Wu, G. *Angew. Chem., Int. Ed.* **2015**, *54*, 4753. d) Pavón, E.; Osuna, F. J.; Alba, M. D.; Delevoye, L. *Solid State Nucl. Magn. Reson.* **2019**, *100*, 45. e) Pedone, A.; Gambuzzi, E.; Menziani, M. C. *J. Phys. Chem. C*, **2012**, *116*, 14599.

Chapter 5

5 Characterization of oxygen sites in MOF MIL-121 and related materials via ^{17}O SSNMR spectroscopy

5.1 Introduction

Metal–organic frameworks (MOFs) are a class of porous materials that are synthesized via the combination of organic and inorganic building blocks to form three-dimensional frameworks. The most remarkable characteristic of MOFs is that their composition, structure, and physicochemical properties can be fine-tuned for specific applications.^{1–3}

The introduction of new functional groups or metals into the framework can be realized through post-synthetic modification (PSM). PSM can be carried out by a number of approaches such as modifying the organic linker and/or metal node, and adsorption/exchange of guest species. PSM has been widely employed to introduce new features to MOFs, such as enhanced chemical stability, increased gas adsorption capability, and introducing new catalytic sites.^{4–11} MOFs bearing free carboxylic acid groups are ideal platforms for PSM because the CO_2H groups can act as anchor sites for introducing guest metal ions. Additionally, new functional groups can be covalently introduced into the framework via thermolysis for further PSM.^{12–15}

MIL-121 is a prototypical aluminum MOF constructed by combining 1,2,4,5-benzenetetracarboxylic acid (BTC) and aluminum cations to form a three-dimensional porous framework containing free carboxylic acid groups protruding in the pores (Figure 5.1)¹⁶ The BTC ligand contains two carboxylate groups coordinated to the Al^{3+} metal centers and two uncoordinated carboxylic acid groups pointing toward the pore interior. The structure of MIL-121 (Figure 5.1) is composed of infinite chains of $\text{AlO}_4(\text{OH})_2$ octahedra connected by hydroxyl groups. The chains are then linked to each other by bridging pyromellitate ligands. The structure of MIL-121 is similar to that of MIL-53-*lp*, however, in MIL-121 each linker has two carboxylic acid groups (2,5 positions) that remain “free” inside of the pores. The as-made form contains disordered unreacted pyromellitic acid and water occupying the pores, which can then be removed by solvent

exchange and activation, resulting in activated MIL-121-ac with the same crystalline structure, as observed from PXRD.¹⁶

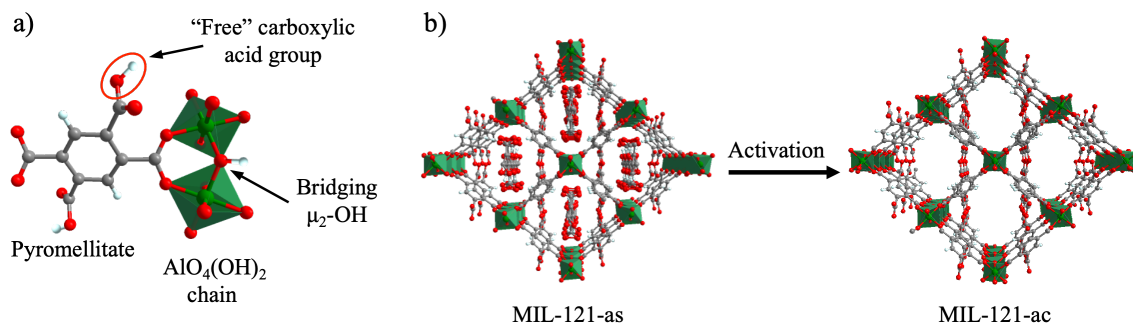


Figure 5.1. a) Building blocks describing the structure of MIL-121; b) The structure of MIL-121-as contains unreacted pyromellitic acid ligands inside of the pores, which are then removed by activation.

MIL-121 is an important MOF in terms of PSM because the free CO_2H groups in the pores allows for the modification and fine-tuning of physico-chemical properties of the material. For example, Chen et al. have shown that hierarchical pores can be created in MIL-121 via PSM. Pore expansion was achieved via thermal decarboxylation of the linker to create larger pores. Decarboxylation and introduction of hierarchical porosity in MIL-121 increased the surface area of the material, enhancing its gas adsorption uptake for industrially relevant gases, such as CO_2 , C_2H_2 , C_2H_4 , and CH_4 .¹⁷ The pores of MIL-121 can also be decorated with highly reactive anhydride groups via thermolysis. This allowed the covalent binding of several types of guest molecules including alcohols, amines, thiols, and even noble metal complexes.¹² The free CO_2H groups in MIL-121 can also be used to introduce non-framework metal ions via cation exchange or acid-base neutralization.^{18–23} Functionalization of MIL-121 with Li^+ , Mg^{2+} , and Ca^{2+} resulted in materials with enhanced uptake of H_2 and CO_2 compared to the parent MIL-121.¹⁸ Lithium-loaded MIL-121 has also shown promising properties as solid-state electrolytes that could potentially be used in solid-state batteries.²⁰ Recognizably, the CO_2H groups

play a fundamental role in the synthesis and structure of MOFs as well as in important technological applications such as catalysis, adsorption, etc.^{24,25}

Therefore, a comprehensive understanding of the interactions of these groups with different functional groups and metals is imperative for the development of new industrial-relevant materials. Solid-state NMR (SSNMR) spectroscopy is a site-specific characterization technique complementary to XRD-based because it can give information on both short and long-range ordering of MOFs.^{26–28} The crystal structure of MIL-121 was solved by refining powder XRD data in combination of ¹H, ¹³C, and ²⁷Al SSNMR results.¹⁶

Furthermore, the carboxylate groups coordinated to the metal centers play a fundamental role in the construction of the framework,^{24,25} and the free CO₂H group is the active site for interaction with guest species as well as catalytic sites.¹⁷ Oxygen exists in three different species within the framework (Figure 5.1): (i) the carboxylate group (CO₂⁻) coordinated to Al, (ii) the hydroxyl group (μ₂-OH) bridging two AlO₆ octahedra, and (iii) the free carboxylic acid (CO₂H) decorating the pores of the framework.

We have recently demonstrated that performing NMR experiments at ultrahigh magnetic field of 35.2 has allowed us to achieve very high ¹⁷O spectral resolution in which 12 crystallographic non-equivalent oxygen sites in the framework of the α-Mg-formate MOF were identified. The increased resolution has allowed us to probe subtle changes during the activation process of this MOF.²⁹ We have also shown that the phase transition of MIL-53 can be followed by ¹⁷O SSNMR spectroscopy at high fields.³⁰ Motivated by this work, we carried out ¹⁷O SSNMR study of MIL-121 at different high magnetic fields (19.6, 21.2, and 35.2 T) in order to fully characterize the structure of this MOF.

Characterization of MIL-121 has been achieved via powder X-ray diffraction, ¹³C, ¹H, and ²⁷Al SSNMR. ¹⁷O can provide additional structural information that can complement the powder X-ray diffraction and previous SSNMR studies and give a further insight into the physico-chemical properties of this material. To further demonstrate the feasibility of using ¹⁷O SSNMR in the characterization of MOFs, specifically MIL-121, we employed

^{17}O SSNMR to probe the local oxygen environments in the MIL-121 loaded with different non-framework metal ions ($M = \text{Na}^+$, Ca^{2+} , Ag^+ , and In^{3+}).

5.2 Experimental details

5.2.1 Sample preparation and characterization

All materials were used from commercial supplies without further purification. Silver and its related silver-exchanged MIL-121(Al) materials were handled in a dark room to avoid oxidation of the silver cations.

Synthesis of ^{17}O -enriched MIL-121

A mixture of 4.80 g of $\text{Al}(\text{NO}_3)_3 \cdot 9\text{H}_2\text{O}$ (Alfa Aesar, 98%) and 1.20 g of 1,2,4,5-benzenetetracarboxylic acid (Sigma-Aldrich, 96%) was dissolved in 3.5 mL of deionized water and 0.5 mL of ^{17}O -enriched H_2O (CortecNet, 35 atom %) in a 23 mL Teflon-lined stainless-steel autoclave. The autoclave was sealed and heated at 90 °C for 24 h. The as-made MIL-121, (MIL-121-as) was collected as a white powder, which was then isolated by centrifugation and dried in an oven at 90 °C overnight.

Solvent exchange and activation

0.20 g of as-made MIL-121 was dispersed in 20.0 mL of methanol (MeOH) and then heated in a sealed Teflon-lined stainless-steel autoclave at 150 °C for 3 days. During this time, the MeOH was decanted and replaced with fresh MeOH three times. The solvent exchanged MIL-121 sample was collected by centrifugation and dried overnight at 80 °C. Finally, the activated MIL-121-ac product was obtained by heating at 250 °C under a dynamic vacuum for 24 h.

Ion exchange experiments

Na@MIL-121: 0.10 g of MIL-121-ac was stirred in 10 mL of 0.2 M Na_2CO_3 for 15 minutes at room temperature. After this time, the solid sample was isolated via centrifugation and washed with deionized water. At the end, the sample was dried at 80 °C overnight.

Ca@MIL-121: 0.10 g of MIL-121-ac was mixed with 10 mL of saturated Ca(OH)₂ for 15 min at room temperature. The solution was then replaced with fresh Ca(OH)₂ saturated solution and stirred for another 10 minutes. At the end, the sample was collected by centrifugation and dried at 80 °C overnight.

Ag@MIL-121: 0.10 g of MIL-121-ac was stirred in 5 mL of 0.08 M Ag(CH₃CO₂) for about 15 hours at 90 °C. The final product was then isolated via centrifugation, washed with deionized water, and dried at 80 °C overnight.

In@MIL-121: 0.10 g MIL-121-ac was mixed with 10 mL of 0.0015 M In(CH₃CO₂)₃ for 3 days. The In(CH₃CO₂)₃ solution was refreshed three times. The resulting solid was then collected by centrifugation, washed with deionized water, and dried at 80 °C overnight.

The approximate guest metal exchange level in each metal-loaded MIL-121 sample has been previously calculated via ¹H SSNMR by comparing the H1/H2 ratio in parent MIL-121 to metal-loaded MIL-121. The estimate exchange levels for the metal-exchange MIL-121 are as follows: Na@MIL-121, 61%; Ca@MIL-121, 43%; Ag@MIL-121, 29%; and In@MIL-121, 17%.¹⁸

Time-of-flight secondary ion mass spectrometry (TOF-SIMS)

Time-of-flight secondary ion mass spectrometry (TOF-SIMS) experiments were carried out to estimate the enrichment of ¹⁷O in the MOF samples.³¹ Experiments were carried out on an ION-TOF (GmbH) TOF-SIMS IV instrument equipped with a Bi cluster liquid metal ion source that was used to estimate the ratio of ¹⁷O to ¹⁶O. A 25 keV Bi³⁺ cluster primary pulsed ion beam (10 kHz, pulse width < 2 ns, target current ~1 pA) was employed to bombard the surface of the sample in order to generate secondary anions. The secondary anions were extracted from the sample surface and separated by their masses and their arrival times were detected via a reflection time-of-flight analyzer. The arrival times were converted to mass/charge ratio (m/z) by calibrating the H⁻ and C⁻ signals. Spectra were collected for 120 s at 128 × 128 pixels by rastering the Bi³⁺ ion beam over an area of 500 × 500 μm²) at three spots on each sample. The samples were pressed in between two silicon wafers coated with an indium layer and then were

separated to obtain a cross section of the pressed particles. To estimate the ^{17}O enrichment level, the relative intensities of the peaks associated with $^{16}\text{O}_2^-$ at m/z 32 and with $^{17}\text{O}_2^-$ at m/z 34 were analyzed in triplicate. First, the average of the $^{16}\text{O}_2^-/^{17}\text{O}_2^-$ ratios were taken. Then, 0.401% was subtracted from the averaged values to account for the contribution from the $^{16}\text{O}^{18}\text{O}^-$ isotopomer at m/z 34 overlapping with the signal from the $^{17}\text{O}_2^-$ isotopomer. Assuming $^{17}\text{O}_2^-/^{16}\text{O}_2^- = ^{17}\text{O}/^{16}\text{O}$, the $^{17}\text{O}/^{16}\text{O}$ isotope ratios are then estimated. Finally, by dividing the measured $^{17}\text{O}/^{16}\text{O}$ ratio by the natural abundance of the ^{17}O isotope (0.037%), one can estimate the increase in enhancement.

Powder X-ray diffraction (PXRD)

Experiments were performed on a Inel CPS powder diffractometer equipped with an Inel CPS 120 detector operating at 40 kV and 40mA (Cu K_α radiation, 1.5418 Å). The diffraction data was collected from 5 to 120 °. The experimental diffractogram was compared with the simulated powder pattern obtained from the reported single-crystal structure (CCDC: 883608).¹⁶

Inductively coupled plasma mass spectrometry (ICP-MS)

The metal exchange level was determined using an Agilent ICP-MS spectrometer model 7700 at the Biotron Research Centre at Western University. The reference method used was EPA 200.8.³²

Thermogravimetric analyses (TGA)

Experiments were carried out on a Mettler Toledo TGA/SDTA851e instrument in the temperature range of 30 to 900 °C under N_2 flow and at a heating rate of 10 °C min^{-1} .

5.2.2 Solid-state NMR measurements

^{17}O and ^1H SSNMR experiments at 19.6 and 35.2 T were performed at the National High Magnetic Field Laboratory (NHMFL) in Tallahassee, FL, USA. SSNMR data at 19.6 T (^{17}O Larmor frequency of 112.7 MHz, and ^1H Larmor frequency of 831.6 MHz) were recorded in a Bruker Avance NEO spectrometer equipped with a HX 3.2 mm low- γ MAS probe along with a spinning frequency of 16 kHz. SSNMR spectra at 35.2 T (^{17}O Larmor

frequency of 203.4 MHz) were collected on the series-connected hybrid (SCH) magnet,³³ a Bruker Avance NEO spectrometer equipped with a costume-made 3.2 mm MAS probe and spinning rate of 18 kHz. The pulse delay was optimized to achieve the highest S/N, and no significant changes in NMR line-shapes were observed when different pulse delays were employed. ¹⁷O 1D MAS spectra were acquired using 1D rotor-synchronized spin echo pulse sequence. ¹⁷O{¹H} Rotational-Echo double-Resonance, REDOR, and heteronuclear correlation, HETCOR, experiments were conducted using standard pulse sequence.³⁴ ¹⁷O 2D 3QMAS spectra were acquired by using a rotor-synchronized shifted-echo triple-quantum MAS pulse sequence³⁵ to avoid spinning sidebands, which are significant due to the chemical shift anisotropy (CSA) at the very high field and 3Q excitation/conversion modulation along the indirect F1 dimension. Therefore, all F1 spinning sidebands are folded back onto the central band, enhancing the overall sensitivity of MQMAS experiments, especially for sites associated with large quadrupole coupling constant and chemical shift anisotropy.^{35–37} The 3Q excitation and conversion pulses were 3.0 and 1.0 μs, respectively. Experiments at 21.1 T (¹⁷O Larmor frequency of 122.0 MHz) were performed at the National Ultrahigh-Field NMR Facility for Solids in Ottawa, Canada, on a Bruker Avance II spectrometer equipped with a Bruker 2.5 mm HX MAS probe along with a spinning rate of 22 kHz. All ¹⁷O NMR spectra were referenced to liquid ¹⁷O-enriched water (18% atom) at 0 ppm. ¹H SSNMR spectra were indirectly referenced to neat tetramethylsilane ($\delta_{\text{iso}} = 0$ ppm) using adamantane ($\delta_{\text{iso}} = 1.82$ ppm). Additional acquisition parameters are listed in

Table A5.2 to Table A5.8.

5.2.3 Spectral simulations

The dmfit software package was used to simulate SSNMR spectra using the Int2QUAD mode, including both the quadrupolar and CSA effects.³⁸ In dmfit, the EFG tensor is described by three principal components in the following order: $|V_{YY}| \leq |V_{XX}| \leq |V_{ZZ}|$. The quadrupolar coupling constant (C_Q) and asymmetry parameter (η_Q) describe the spherical and cylindrical symmetry of the EFG tensor, respectively, and are defined as follows: $C_Q = (eQV_{ZZ}/h) \times 9.7177 \times 10^{21}$ (in Hz) and $\eta_Q = (V_{YY} - V_{XX})/V_{ZZ}$, where e is the electric charge, Q is the quadrupole moment ($-2.558 \times 10^{-30} \text{ m}^2$),³⁹ conversion factor

of $9.7177 \times 10^{21} \text{ V m}^{-2}$ is used during the calculation of C_Q to convert from atomic units to Hz. The chemical shift (CS) tensor is also described by three principal components such that $|\delta_{22} - \delta_{\text{iso}}| \leq |\delta_{11} - \delta_{\text{iso}}| \leq |\delta_{33} - \delta_{\text{iso}}|$, and the isotropic chemical shift $\delta_{\text{iso}} = (\delta_{11} + \delta_{22} + \delta_{33})/3$ is related to the bonding modes. The CSA parameters are defined by $\Delta_{\text{CS}} = \delta_{33} - \delta_{\text{iso}}$ and $\eta_{\text{CS}} = |(\delta_{22} - \delta_{11})/\Delta_{\text{CS}}|$. Three Euler angles (ϕ, χ, ψ) are employed to describe the orientations of the CS tensor with respect to the EFG principal (fixed) axis frame using the ZYZ convention: the corresponding transformation matrix was used to deduce the new directional characteristics of the CS tensor with respect to the EFG system. As a result, eight independent parameters, $C_Q, \eta_Q, \delta_{\text{iso}}, \Delta_{\text{CS}}, \eta_{\text{CS}}, \phi, \chi,$ and ψ , are required to characterize a single ^{17}O site when both the quadrupolar and the CSA effects are considered. All uncertainties in NMR parameters were estimated by bidirectional variation of the parameter in both directions from the best-fit value while all other NMR parameters were held constant.

5.3 Results and discussion

As mentioned before, ^{17}O isotopic enrichment can be very costly. Therefore, we have optimized synthetical conditions to use the least amount of H_2^{17}O (l). Our initial attempt to use the dry gel conversion method failed.^{31,40} Therefore, we followed the synthesis method reported previously¹⁸ but using different amounts of water (10, 8.0, 6.0, and 4.0 mL) to minimize the water content. The ^{17}O isotopic enrichment levels were estimated by using a procedure described previously and are listed in Table A5.1.³¹ The $^{17}\text{O}/^{16}\text{O}$ ratio estimated for the MIL-121 samples are: MIL-121-as, 4.64(11); MIL-121-ac, 5.91(11); Na@MIL-121, 3.07(3); Ca@MIL-121, 4.35(6); Ag@MIL-121, 4.77(24); and In@MIL-121 4.79(12).

The crystallinity and phase purity of the samples were verified by PXRD. The powder pattern of the samples matched well with the simulated pattern based on the crystal structure (Figure A5.1). Therefore, we carried out the syntheses with the least amount, 4.0 mL, of water. In the syntheses of the ^{17}O enriched samples, 3.5 mL of deionized water and 0.5 mL of 35 atom % H_2^{17}O (l). In this case, 9.5 and 0.5 mL of deionized water and H_2^{17}O (l), respectively, was used following the procedure reported in the literature.¹⁸ Solvent exchange and subsequent activation of the sample prior to the metal exchange

was carried out. TGA (Figure A5.2) was used to check the degree of activation of the sample. The TGA curve of the MIL-121-as sample shows a large weight loss attributed to the solvent and unreacted ligands in the pores. The TGA curve of methanol-exchanged MIL-121@MeOH displays a small weight loss. In contrast, the thermogram of the MIL-121-ac did not show any weight loss up to around 300 °C (decomposition of the framework). The metal exchanged materials were characterized via PXRD. The diffractograms of the metal exchanged-MIL-121 samples, Figure A5.3, are in good agreement with the results previously reported by Chen et al.¹⁸ Specifically, the metal-loaded samples retain framework integrity. The crystal structure of MIL-121-as contains 13 crystallographically non-equivalent oxygen atoms, (Figure 5.2): two oxygens from the carboxylate group coordinated to Al³⁺ cations (CO₂⁻, O2 and O3); one hydroxyl oxygen (μ_2 -OH, O1); eight disordered oxygen atoms from the uncoordinated ligands occupying the pores (O21-O28); and two oxygens from the “free” carboxylic acid groups (C=O, O4; COH, O5).¹⁶

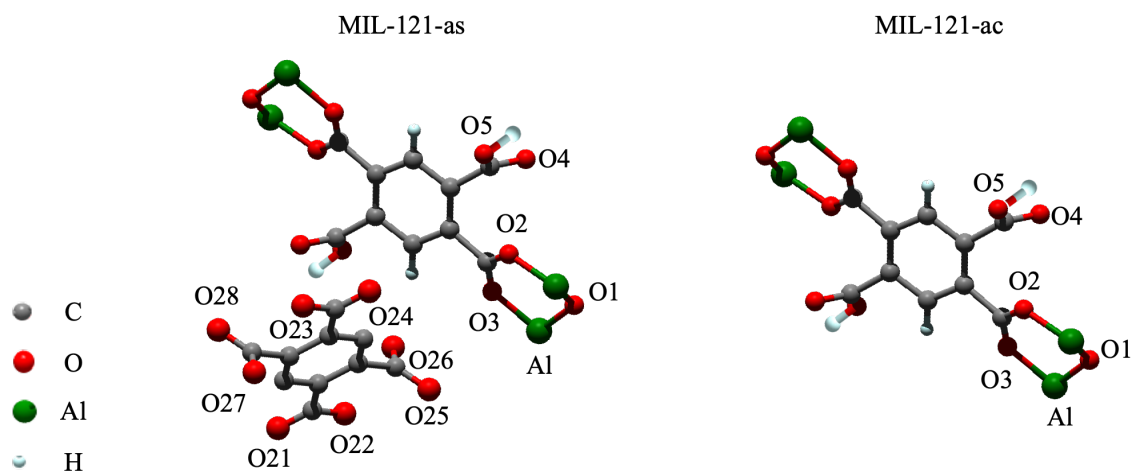


Figure 5.2. Crystallographically non-equivalent oxygen atoms in the crystal structure of MIL-121-as and MIL-121-ac.

The crystal structure of MIL-121-ac has not yet been reported. However, PXRD suggests that the structure of the activated phase remains the same as the structure of the as-made phase upon removal of the uncoordinated organic ligand from the pores. Therefore, we assumed that the crystal structure of MIL-121-ac contains five crystallographic non-equivalent oxygen sites (Figure 5.2): one hydroxyl oxygen (μ_2 -OH, O1); two oxygens from the carboxylate group coordinated to Al^{3+} cations (CO_2^- , O2 and O3); and two oxygens from the “free” carboxylic acid groups (C=O, O4; COH, O5).¹⁶

It was previously mentioned that one of the advantages of ^{17}O SSNMR is that the ^{17}O isotope displays a large chemical shift range.⁴¹ In general, the C=O oxygen site in a carboxylic acid appears in the range 260-340 ppm, the COH oxygen appears between 120 and 200 ppm. In the case of hydrogen-bonded COH and C=O, the chemical shift of both COH and C=O appear in the range of 220 to 300 ppm.^{41,42} Furthermore, the ^{17}O quadrupole coupling and chemical shift tensors are sensitive to chemical environment and molecular interactions such as hydrogen bonding and metal-ligand interactions. One example worth noting is phthalic acid because of its similarity to the pyromellitic acid employed in the synthesis of MIL-121.

The ^{17}O MAS NMR spectrum of phthalic acid is comprised of two resonances at 312 and 180 ppm, which were attributed to the C=O and COH oxygen sites from the carboxylic acid groups, respectively.^{43,44} The ^{17}O parameters of the framework carboxylate group coordinated to the Al^{3+} centers and the bridging hydroxyl, μ_2 -OH, have been previously reported for MIL-53(Al).²⁹ The topology of MIL-121 is similar to that of the large-pore phase of MIL-53. The CO_2^- and μ -OH oxygen signals appear at 236 and 27 ppm, respectively.

The ^{17}O 1D MAS SSNMR spectra of MIL-121-as and MIL-121-ac acquired at 19.6 T are depicted in Figure 5.3. Both spectra display four spectral envelopes centered at around 10, 155, 210, and 300 ppm. Seeing four signals is inconsistent with the crystal structure of the MIL-121-as, which predicts 5 crystallographic non-equivalent sites. Apparently, the two inequivalent CO_2^- sites, O2 and O3 oxygens from the carboxylate groups coordinated to Al^{3+} centers are not resolved in the 1D spectra.

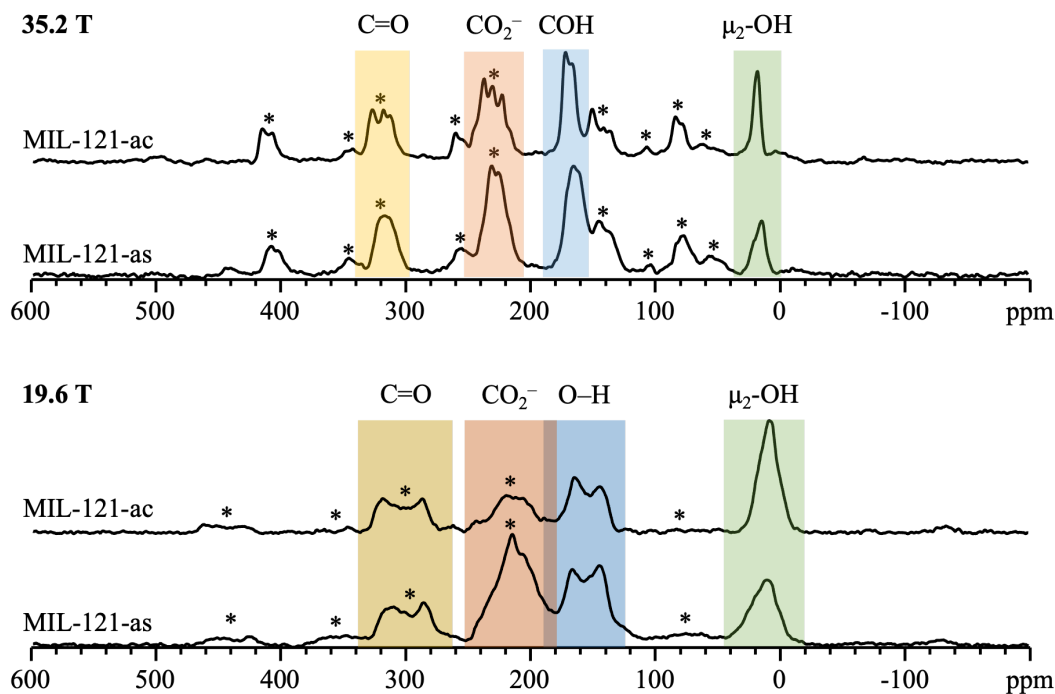


Figure 5.3. ^{17}O 1D MAS SSNMR spectra of MIL-121-as and MIL-121-ac acquired at 19.6 T and 35.2 T with spinning rate of 16 and 18 kHz, respectively. The spinning sidebands are labelled as *.

Based on the crystal structure and the chemical shift values of various oxygen species previously reported in the literature, we tentatively assigned these regions as follows: the signal at 10 ppm is assigned to the bridging $\mu_2\text{-OH}$ group; the signal at 155 is assigned to the COH group of the “free” carboxylic acid groups (O5); the signal at 210 ppm was assigned to the carboxylate CO_2^- group coordinated to the Al^{3+} centers (O2 and O3); finally, the resonance at 300 ppm was assigned to the C=O groups of the “free” carboxylic acid group (O4). To confirm these assignments, ^{17}O observed $^{17}\text{O}\{^1\text{H}\}$ REDOR experiments were carried out. REDOR utilizes heteronuclear dipolar interaction between oxygen and proton and can provide information regarding the O–H distance.⁴⁵ The $^{17}\text{O}\{^1\text{H}\}$ REDOR spectra of MIL-121-as and MIL-121-ac acquired with a dephasing time of two rotor periods (0.062 ms) are shown in Figure 5.4.

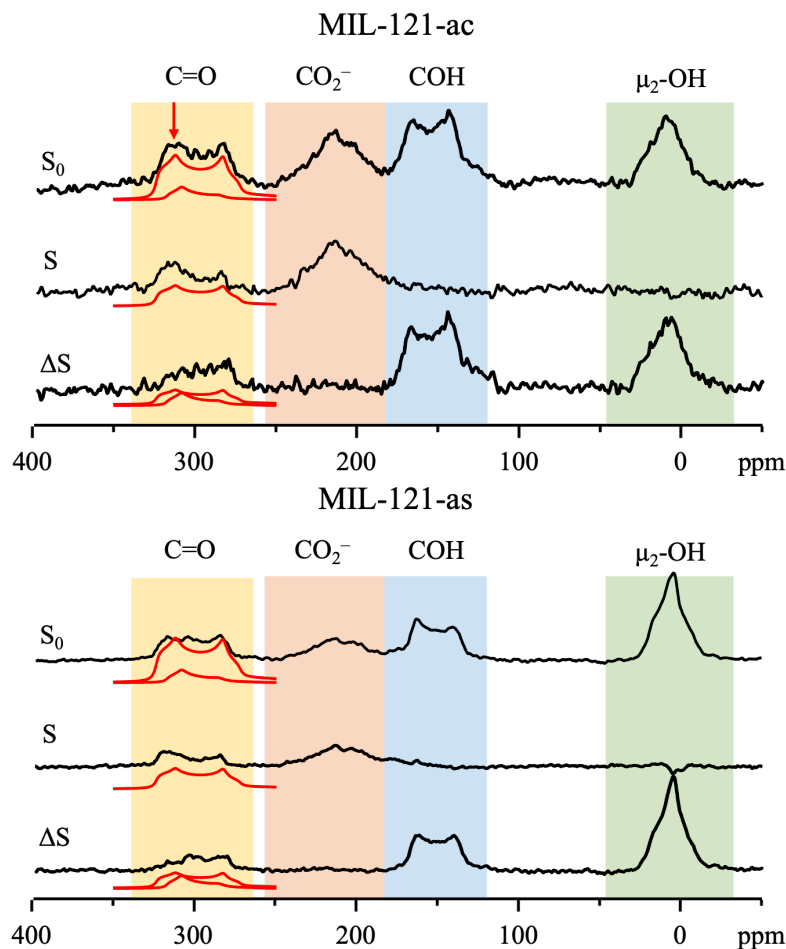


Figure 5.4. $^{17}\text{O}\{^1\text{H}\}$ REDOR spectra of a) MIL-121-as and b) MIL-121-ac acquired at 19.6 T with a spinning frequency of 16 kHz. S_0 , ^{17}O spin-echo; S, REDOR experiment with a dephasing time of 0.062 ms; ΔS , REDOR difference.

The REDOR difference spectra (ΔS) between the control spin echo spectrum (S_0) and the dephased spectrum (S) contains three signals at 10, 155, and 300 ppm. The signal at 10 ppm (O1) displays a REDOR effect ($\Delta S/S_0$) of almost 100%, the signal at 155 (O5) ppm displays a REDOR effect of 90%, and the signal at 300 ppm (O4) displays a REDOR effect of 50%.

Upon close inspection, it is possible to observe the change in intensity and line-shape of the C=O region at around 300 ppm in the dephased spectra. In the control spectrum, the

signal in this region is comprised of the resonance from the C=O oxygens plus an overlapping spinning sideband from the COH signal. In the dephased spectrum, the resonance from the COH oxygens vanished. Consequently, only the resonance from the C=O is observed with a lower intensity due to the REDOR effect. In the difference spectrum, the C=O region is therefore comprised of the spinning sideband from the COH region and the signal from the C=O oxygen with a lower intensity compared to that of the control experiment.

Based on the REDOR effects observed for each signal, it is concluded that the resonance at 10 ppm is indeed due to the hydroxyl group and the signal at 155 ppm originates from the COH groups, since these oxygens are directly bound to a proton, therefore, the shortest OH distance, resulting in the largest REDOR effect. The signal at 300 ppm can be unambiguously assigned to the C=O species since it displays the smallest REDOR effect. The smaller REDOR effect for the C=O groups is due to the larger distance of around 2.40 Å between this oxygen and the adjacent proton of the COH group in the carboxylic acid.

To further corroborate our assignment, 2D ^1H - ^{17}O HETCOR experiments were also carried out. ^1H - ^{17}O HETCOR probes the heteronuclear dipolar interaction between the ^1H and ^{17}O atoms and furnish information regarding the proximity of heteronuclei to one another. The ^1H MAS spectra of MIL-121-ac, Figure 5.5b, display three resonances at around 11, 7, and 2 ppm that are respectively assigned to the proton of the “free” carboxylic acid from the ligand COH, the hydrogen of the aromatic ring of the ligand ArH, and the hydrogen from the bridging hydroxyl groups μ_2 -OH (Figure 5.5a).^{16,18}

The 2D ^1H - ^{17}O HETCOR spectrum of MIL-121-ac (Figure 5.5c) shows a strong correlation between the ^{17}O μ_2 -OH signal and the ^1H μ_2 -OH signal. The ^{17}O signals from the C=O and COH correlate with the ^1H signal from the “free” carboxylic acid groups on the framework pore walls. The ^{17}O signal at 210 ppm does not correlate with any hydrogen in the framework. The results obtained from the HETCOR spectrum are in good agreement with the crystal structure and the previous REDOR results, confirming our assignment is indeed correct.

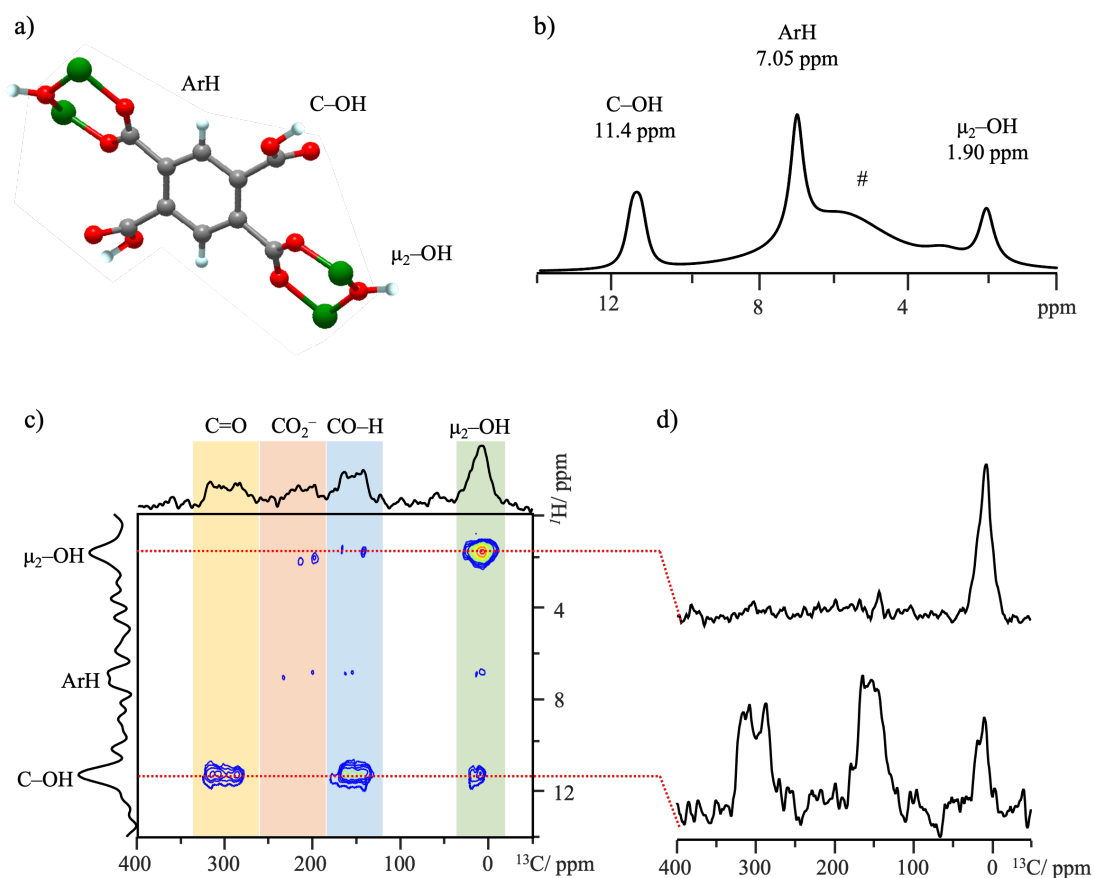


Figure 5.5. a) Representation of the different hydrogen species in the MIL-121-ac; b) ^1H - ^{17}O HETCOR spectrum of MIL-121-ac acquired at 19.6 T with a spinning frequency of 16 kHz; d) slices of the ^{17}O dimension at the ^1H signals. The label # denotes the signal of adsorbed water inside of the pores. Water can be adsorbed during the packing of the sample into the rotor prior to the NMR measurements.

In order to extract the ^{17}O EFG parameters and assign each individual crystallographic site, we have carried out ^{17}O 3QMAS experiments.³⁷ 3QMAS can eliminate the second-order quadrupolar broadening along the indirect F1 dimension and therefore should separate the overlapping signals from the CO_2^- groups (O2 and O3) in the 1D MAS spectrum. The ^{17}O 2D 3QMAS spectra of MIL-121-as and MIL-121-ac 19.6 T are depicted in Figure 5.6. The spectra of the MIL-121-as and MIL-121-ac display 1 signal in

the μ_2 -OH region, one signal in the COH region, two signals in the CO_2^- region, and one signal in the C=O region.

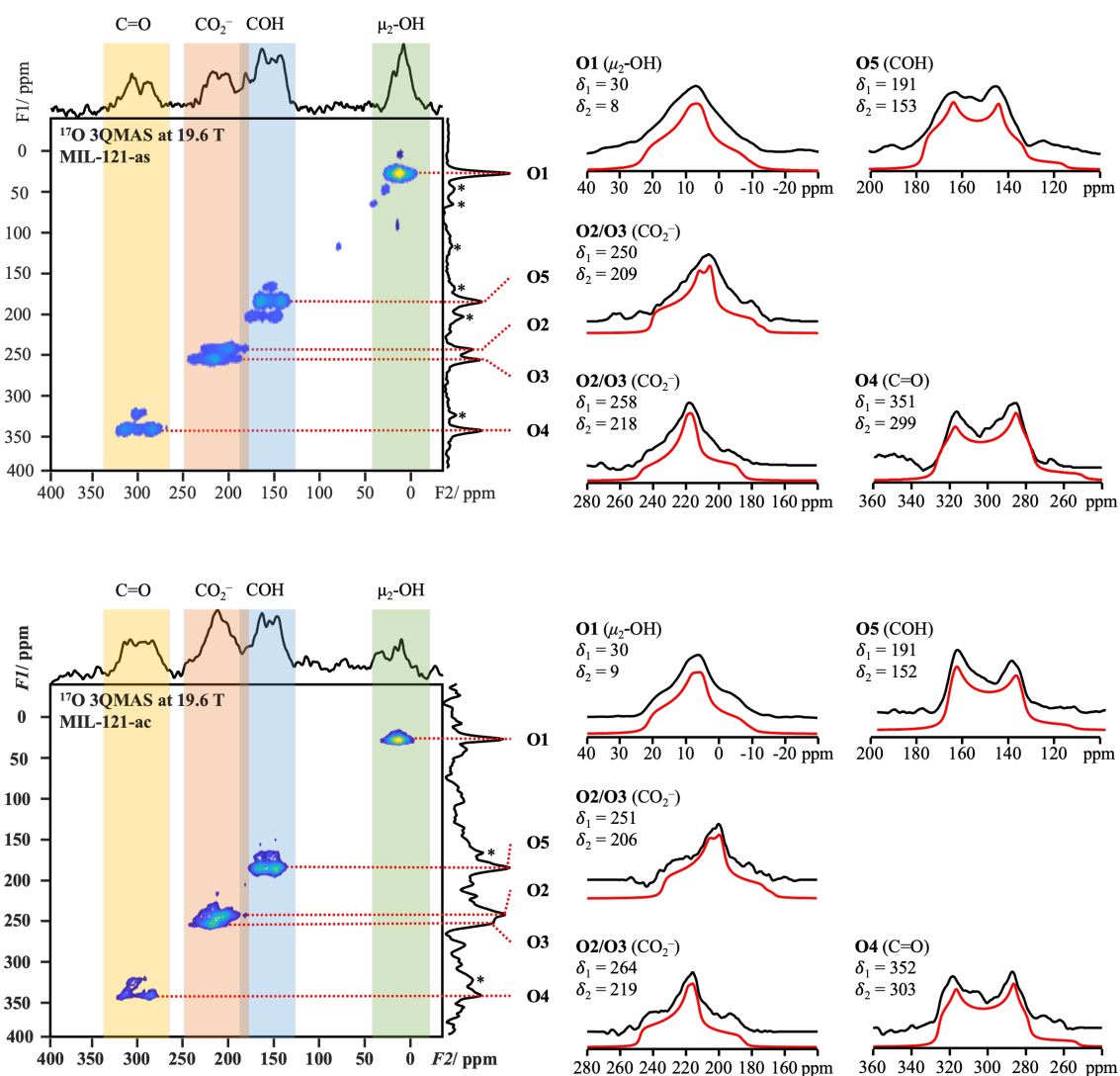


Figure 5.6. ^{17}O 2D 3QMAS NMR spectra of MIL-121-as and MIL-121-ac acquired at 19.6 T with a spinning rate of 16 kHz. The spinning sidebands are denoted as asterisks.

For each F2 cross-section extracted at δ_1 along the F1 dimension, the isotropic chemical shift, δ_{iso} , and the quadrupolar product, P_Q , can be obtained directly from the spectral center of gravity (δ_2) along F2 according to the equations below:

$$\delta_{\text{iso}} = \frac{17}{27} \delta_1 + \frac{10}{27} \delta_2 \text{ (Equation 5.1)}$$

$$P_Q = \left\{ \frac{170}{81} \frac{[4I(2I-1)]^2}{[4I(I+1)-3]} (\delta_1 - \delta_2) \right\}^{1/2} \nu_0 10^{-3} \text{ (Equation 5.2)}$$

where ν_0 is the Larmor frequency and I is the spin quantum number.

The ^{17}O quadrupolar spectral parameters obtained from the 3QMAS spectra acquired at 19.6 T are listed in Table 5.1. The bridging hydroxyl oxygen, O1, displays $\delta_{\text{iso}} = 22$ ppm. The free COH species, O5, displays $\delta_{\text{iso}} = 177$ ppm. The free C=O species, O4, displays $\delta_{\text{iso}} = 332$ ppm signal. Finally, the two overlapping CO_2^- , O2 and O3, display $\delta_{\text{iso}} = 235$ ppm and $\delta_{\text{iso}} = 243$ ppm, respectively. The 3QMAS spectra allowed us to resolve the two overlapping resonances from the O3 and O2.

Table 5.1. Experimental ^{17}O NMR parameters and peak assignments of MIL-121-as and MIL-121-ac.

Sample	O site	O type	δ_1 (ppm)	δ_2 (ppm)	P_Q (MHz)	δ_{iso} (ppm)
MIL-121-as	O1	μ_2 -OH	30	8	5.3	22
	O5	COH	191	153	7.0	178
	O2	CO_2^-	250	209	7.4	235
	O3	CO_2^-	258	218	7.3	243
	O4	C=O	351	299	8.2	332
MIL-121-ac	O1	μ_2 -OH	30	9	5.2	22
	O5	COH	191	152	7.1	177
	O2	CO_2^-	251	206	7.7	234
	O3	CO_2^-	264	219	7.7	247
	O4	C=O	352	303	8.1	334

As reported in the recent literature, performing ^{17}O SSNMR measurements at the highest accessible magnetic field strength can drastically enhance both spectral sensitivity and resolution. Therefore, we acquired ^{17}O 1D MAS spectra of MIL-121-as and MIL-121-ac at 35.2 T (Figure 5.3). The signals in the 1D MAS spectra at a higher field of 35.2 T

become considerably narrower and exhibit well-defined features compared to those at 19.6 T due to the reduction of the second order quadrupolar broadening at a much higher magnetic field. In addition, at a higher field, the spinning sidebands become significantly enhanced because the CS interaction increases with increasing magnetic field. This is clearly seen in the spectra acquired at 35.2 T.

It is possible to take advantage of the enhanced CS interaction at ultrahigh magnetic field of 35.2 T because the intense spinning side bands resulting from the CS interaction allow the extraction of the CSA parameters more accurately. ^{17}O 3QMAS spectrum of MIL-121-as was also acquired at 35.2 T (Figure A5.5). However, the signal-to-noise ratio of the spectra at 35.2 T are rather poor due to the limited magnet time available.

In general, to simulate a 1D MAS spectrum with 5 inequivalent sites requires 40 parameters when both the EFG and the CSA are considered. To reduce the number of parameters for simulation, the following procedure was used:

(1) The 1D MAS spectrum at 19.6 T was first simulated using the quadrupolar coupling constant, C_Q , the asymmetry parameter, η_Q , and the isotropic chemical shift, δ_{iso} values obtained from 3QMAS experiments at 19.6 T as initial inputs (Table A5.9). At this point, only EFG is taken into consideration as the SSBs at this field is relatively weak. These parameters were optimized via simulating 1D MAS spectra at 19.6 T.

(2) The refined C_Q , η_Q , and δ_{iso} values were used for simulating 1D MAS spectra at 35.2 T to extract the CSA info. The initial CSA parameter values (including the reduced anisotropy, Δ_{CS} , and the chemical shift asymmetry parameter, η_{CS}) were taken from the literature used for oxalic acid (Table A5.10).^{30,41} They were varied to fit the spinning sideband pattern at 35.2 T. Finally, the EFG and CSA parameters were slightly adjusted to fit the spectra at 19.6 and 35.2 T individually.

(3) The average was taken as the final EFG and CSA parameters. These values are given in Table 5.2. The 1D MAS spectra of MIL-121-as and MIL-121-ac at 19.6 T and 35.2 T were calculated using a single set of the EFG and CSA parameters and are depicted in Figure 5.7. They are in good agreement with the experimental spectra.

We were not able to identify the oxygen signals from the unreacted ligand. This is because the amount of unreacted ligand in the framework is very small, ca. 0.07 equivalent of unreacted ligand per metal, which translates to around 8% in mass percentage of the sample. Our TGA results (Figure A5-2) show that there is a weight loss of about 18%, in which 9% is attributed to the desorption of water (around 273 K) and the other 9% is attributed to the ligand.

It has been shown that ^{17}O SSNMR can probe activation process of MOFs. The removal of guest molecules is accompanied by the changes in the NMR parameters. The ^{17}O signals are particularly sensitive to hydrogen bonding.^{29,30}

There is a good correlation between the isotropic chemical shift and the hydrogen bonding strength. In general, for a C=O oxygen in a carboxylic acid group, δ_{iso} increases as the H-bond strength decreases. In contrast, δ_{iso} of the COH oxygen decreases as the H-bond strength decreases. The COH oxygen experiences a greater decrease in δ_{iso} when it acts as proton donor.⁴⁶

In the crystal structure of MIL-121-as (Figure 5.8), there are three types of hydrogen bonding (HB): (i) hydrogen bonding between the uncoordinated carboxylic acid groups of the framework in the pores, C=O4 \cdots HO5C characterized by a short distance of 2.55 Å and an angle C5–O5 \cdots O4 of 117 °; (ii) HB interaction between the hydroxyl O1 oxygen and the disordered oxygens from the unreacted ligand; and (iii) head-to-tail HB interaction between the oxygens of the unreacted ligands in the pores. Upon activation, the removal of the unreacted ligand in the pores affect these interactions causing small changes in the spectral parameters.

1 **Table 5.2.** Refined ^{17}O EFG and CSA parameters of the MIL-121-as and MIL-121-ac.

Sample	Site	O type	Intensity	δ_{iso} (ppm)	C_Q (MHz)	η_Q	Δ_{CS} (ppm)	η_{CS}	ϕ ($^\circ$)	χ ($^\circ$)	ψ ($^\circ$)
MIL-121-as	O1	$\mu_2\text{-OH}$	23	23	0.8	0.80	-120	0.20	180	20	0
	O5	COH	25	173	1.0	0.20	160	1.00	110	60	100
	O2	CO_2^-	19	235	1.0	0.90	200	1.00	30	60	0.0
	O3	CO_2^-	19	244	1.0	0.90	210	1.00	30	0	0
	O4	C=O	14	328	1.2	0.20	-200	0.50	30	30	0
MIL-121-ac	O1	$\mu_2\text{-OH}$	46	22	0.7	0.80	120	1	0	30	30
	O5	COH	21	177	1.1	0.15	180	0	0	0	30
	O2	CO_2^-	9	235	1.1	0.80	200	1	30	60	0
	O3	CO_2^-	9	248	1.0	0.90	210	1	30	0	0
	O4	C=O	14	333	1.2	0.20	-200	1	90	60	0

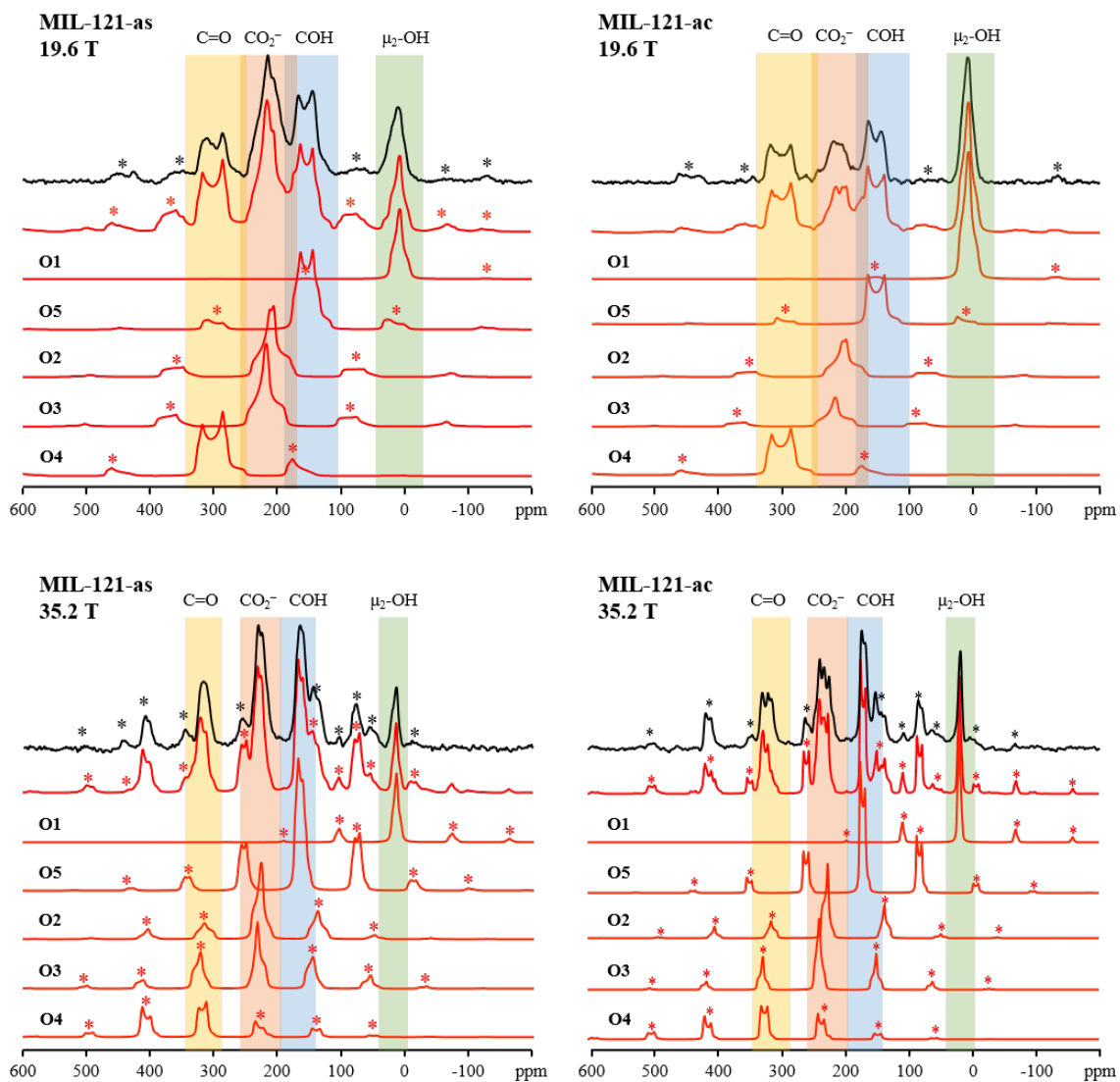


Figure 5.7. Experimental and simulated ^{17}O 1D MAS spectra of MIL-121-ac and MIL-121-as acquired at 19.2 T and 35.2 T with spinning rate of 16 and 18 kHz, respectively. Spinning sidebands are denoted by asterisk.

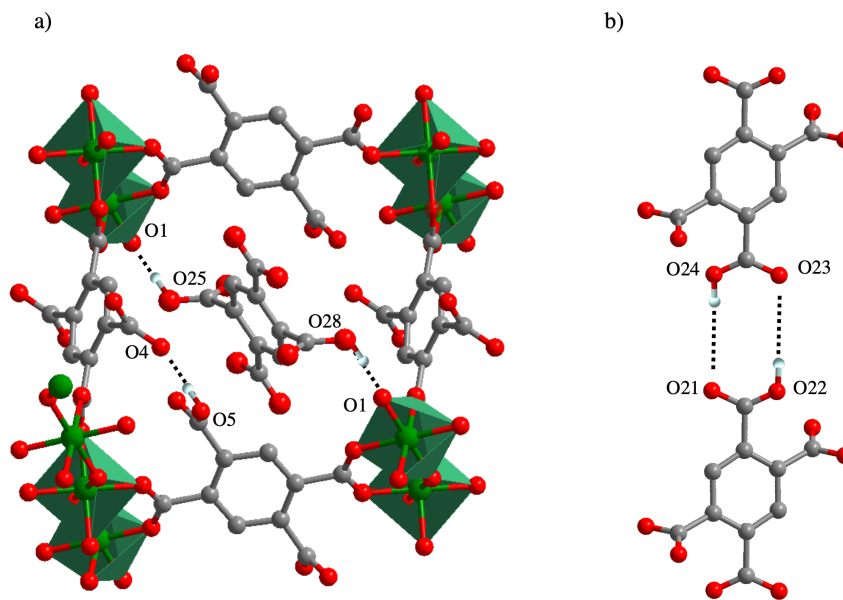


Figure 5.8. a) Representation of the main hydrogen bonding interactions taking place in the crystal structure of the MIL-121-as. b) Hydrogen bonding.

The changes in spectral parameters upon activation are listed in Table 5.2. The largest changes in δ_{iso} are observed for O3, O4 and O5, with an upfield shift of 4, 5, and 4 ppm, respectively, suggesting that the removal of the unreacted ligand affects the local environment of these sites. The small change in δ_{iso} suggest that the HB interactions are relatively weak.

Table 5.2. Comparison between the experimental ^{17}O NMR parameters upon activation of MIL-121-as at 19.6 T.

O site	O type	$\Delta\{\delta_{\text{iso}}\}$ (ppm)	$\Delta\{C_Q\}$ (MHz)	$\Delta\{\eta_Q\}$ (MHz)
O1	μ_2 -OH	1	0.1	0
O5	COH	-4	-0.2	0
O2	CO_2^-	0	-0.1	0.1
O3	CO_2^-	-4	0.1	0
O4	C=O	-5	-0.4	0

The reasoning for these changes is the following: upon removal of the ligand from the pores, the unreacted carboxylic acid group might possess a higher degree of freedom, allowing the O5 to interact with O3, as shown in Figure 5.9. A decrease in δ_{iso} for the coordinated CO_2^- group has been observed for $\alpha\text{-Mg}_3(\text{HCOO})_6$ MOF which was associated with removal of DMF molecules inside of the pores.²⁹ In the MIL-121, the chemical shift of O5 decreases by 4 ppm, indicating a decrease in HB.

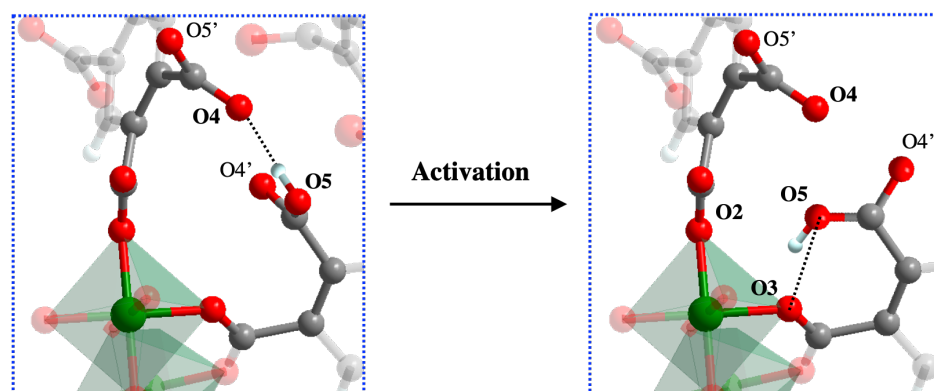


Figure 5.9. Representation of possible intramolecular hydrogen bonding before and after activating MIL-121.

Another important change in the spectra of the MIL-121-as and MIL-121-ac upon activation is that the intensity of the CO_2^- signal seems to decrease relatively to the free CO_2H signal. As mentioned previously, the uncoordinated ligands occupying the pores can participate in a head-to-tail HB fashion. A similar configuration was observed for solid benzoic acid, in which the ^{17}O MAS spectra display one signals at $\delta_{\text{iso}} = 236$ ppm, assigned to both COH and C=O signals. Clearly, these signals overlap with the CO_2^- resonances, resulting in a higher intensity in the 1D MAS spectra of MIL-121-as.

Loading non-framework guest metal ions into MOFs can affect host–guest interactions, enhancing MOFs capabilities. Therefore, it is important to gain information on the location and environment of guest species inside of the pores.

^{17}O SSNMR is advantageous because it offers direct structural information regarding the interaction between the metal cations and the free carboxylic acid groups protruding in the pores. Besides, it has been shown that the ^{17}O EFG and CS tensors are sensitive to even subtle structural changes, which allows for the study of metal-carbonyl interactions in organic and biological molecules.⁴⁷ For example, ^{17}O SSNMR has been employed to study the influence of the metal cation size on the ^{17}O CSA and EFG parameters of group I hydrogen dibenzoates, furnishing important structural information complementary to X-ray diffraction. In general terms, removing the acidic proton in a CO_2H group by acid-based neutralization or ion-exchange leads to the formation of a CO_2^- group whose chemical shift is in between the $\text{C}=\text{O}$ and COH .^{44,48} For example, the ^{17}O 1D MAS spectra of phthalic acid is comprised of two resonances at 312 and 180 ppm which were assigned to the $\text{C}=\text{O}$ and COH species, respectively. Upon exchange of the acidic protons from the appending carboxylate groups with lithium, the ^{17}O NMR spectrum displayed only one CO_2^- signal at 272 ppm. Similar results have also been reported in the literature.^{43,44,49} Herein, we selected the MIL-121 MOF loaded with several different metals (MIL-121@M , $\text{M} = \text{Na}^+$, Ca^{2+} , Ag^+ , In^{3+}) to explore if ^{17}O SSNMR can be employed to probe metal-exchange in metal-organic frameworks.

The degree of metal ion exchange for each sample was measured by ICP-MS. The metal exchange degrees for Na@MIL-121 , Ca@MIL-121 , Ag@MIL-121 , and In@MIL-121 are 42, 5, 30, and 6 %, respectively (Table A5.12). ^1H - ^{13}C CP/MAS SSNMR spectra of Na^+ , Ca^{2+} , Ag^+ , and In^{3+} -loaded MIL-121 are sensitive to the presence of non-framework cations and this is particularly true in the $\text{CO}_2^-/\text{CO}_2\text{H}$ region at around 170 ppm. The SSNMR spectra of the metal ions provide the info on the state of ions inside the MOF channels.^{50,51} The ^{17}O 1D MAS spectra of all metal-loaded MIL-121 can be found in (Figures A5-8). The ^{17}O 1D MAS spectra of Na@MIL-121 and Ag@MIL-121 exhibit the largest changes compared to that of the active MOF and are depicted in Figure 5.10.

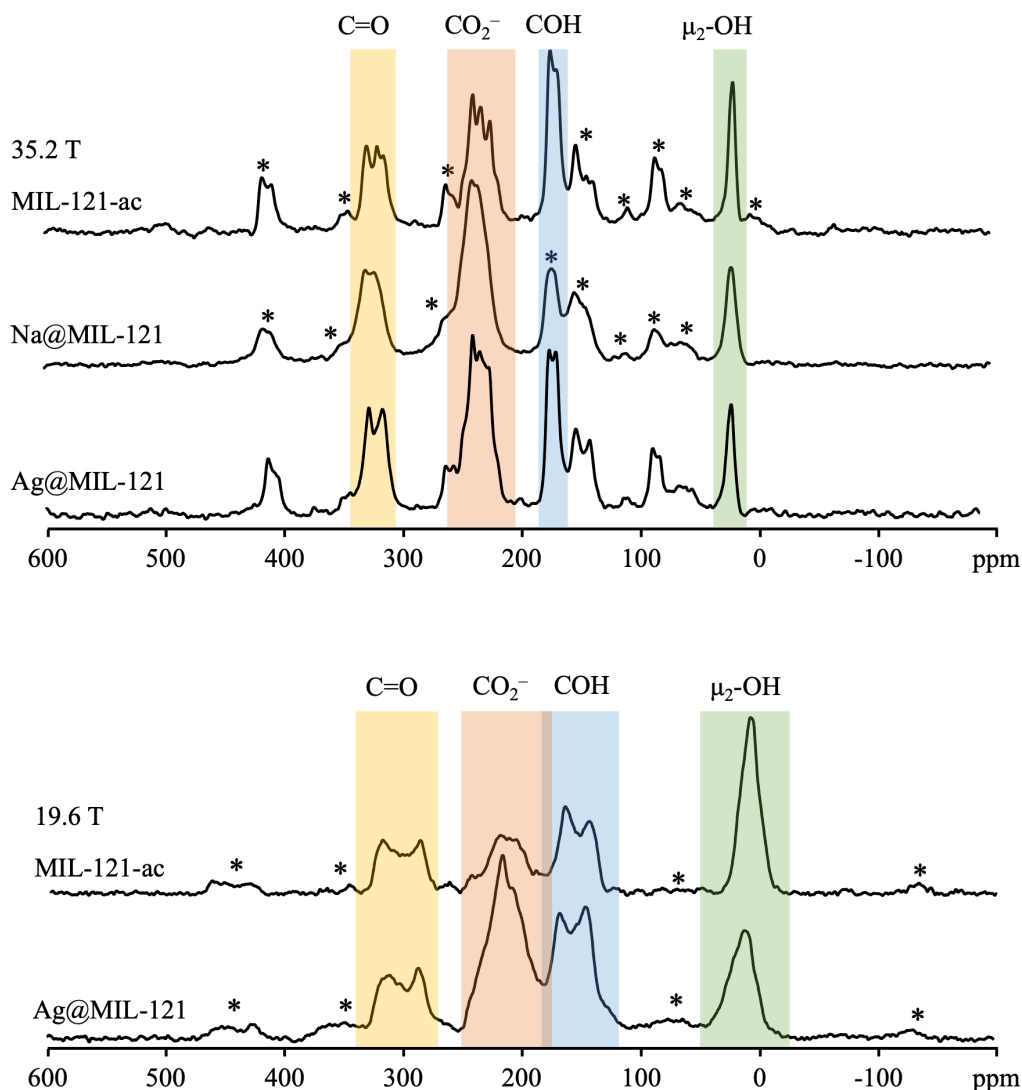


Figure 5.10. Experimental ^{17}O 1D MAS spectra of MIL-121-ac and $\text{Na}^+/\text{Ag}^+@$ MIL-121 acquired at different magnetic fields with spinning rate of 16 kHz (19.6 T) and 18 kHz (35.2T). Spinning sidebands are denoted by asterisk.

For Na^+ and Ag^+ -loaded samples, a clear change in relative intensity between the COH and CO_2^- signals was observed. The peak due to the COH is stronger than that of the CO_2^- signals in MIL-121-ac and the intensity ratio is 20/18. Upon Na^+ exchange, the intensity of the CO_2^- signal increases significantly at the expense of the peak due to COH. The decrease in the intensity in COH peak indicates that some of acidic protons

have been replaced by incoming Na^+ ions. As mentioned earlier, upon ion-exchange C=O and C-OH in the same carboxylate group become CO_2^- . This newly formed species has a chemical shift very similar to the CO_2^- coordinated to the framework Al,⁴⁰ resulting in an overlapping with the framework CO_2^- and, therefore, an increased intensity of the profile in the 230 ppm region. Similar trend was also seen for Ag-exchanged MIL-121. ¹⁷O 3QMAS experiments (Figures A5.9 and A5.10) were also carried out in attempt to separate the CO_2^- groups bound to Al and those associated with the non-framework cations. Unfortunately, the spectra are very similar to that of activated MIL-121 and there are only 2 signals observed in the CO_2^- region.

An analysis of the intensity data (Table 5.3) reveals that the intensity ratio between COH to CO_2^- is 1.2 (21/18) and this value changed to 0.5 (21/42), suggesting a Na^+ exchange level is around 50%, which is in relatively good agreement with the measured exchange degree of 42%. Upon Ag^+ exchange, the COH / CO_2^- intensity ratio decreased from 1.1 to 0.75, suggesting a metal exchange level of around 25%, which is also in good agreement with the value found from ICP-MS measurement (30%). Furthermore, upon loading, the signals in the CO_2^- and COH regions become featureless in comparison with that of the activated sample, which is particularly true for Na^+ exchanged sample.

Table 5.3. Difference in the intensities in the oxygen signals upon metal-exchange.

O site	O type	Before metal exchange	After Na^+ exchange	After Ag^+ exchange
O1	μ_2 -OH	46	27	23
O5	COH	21	21	29
O2/O3	CO_2^-	9	21	23
O2/O3	CO_2^-	9	21	17
O4	C=O	14	11	8

This suggests a distribution of similar environments around the dangling carboxylate group resulting from the distribution of cations. This also corroborates the previous ²³Na SSNMR results which show the Na^+ ions are randomly distributed around carboxylate

groups.¹⁸ In the case of Ca^{2+} and In^{3+} -loaded MIL-121, no significant change in the COH and CO_2^- region and their ratios remained the same as that of the activated MOF.

It is likely that the degrees of ion-exchange in these two samples are too low to be identified by our ^{17}O NMR experiments. Indeed, the metal-loading levels for Ca@MIL-121 and In@MIL-121 were only 5 and 6%, respectively. Their 3QMAS spectra are also very similar to that of the activated MIL-121 (Figure A5.9 and Figure A5.10) for the same reason mentioned above.

A comparison of the chemical shifts of metal ion-exchanged MIL-121 obtained from ^{17}O 3QMAS experiments (Table A5.11) with those of activated MIL-121 leads to the following information:

- Na@MIL-121 : Upon Na-loading, the δ_{iso} of O1 displayed a downfield shift of 4 ppm and O2, O3, and O4 displayed a downfield shift of 2 ppm. Thus, suggesting that Na^+ cations are interacting with the μ_2 -OH groups in the framework (Figure 5.11).

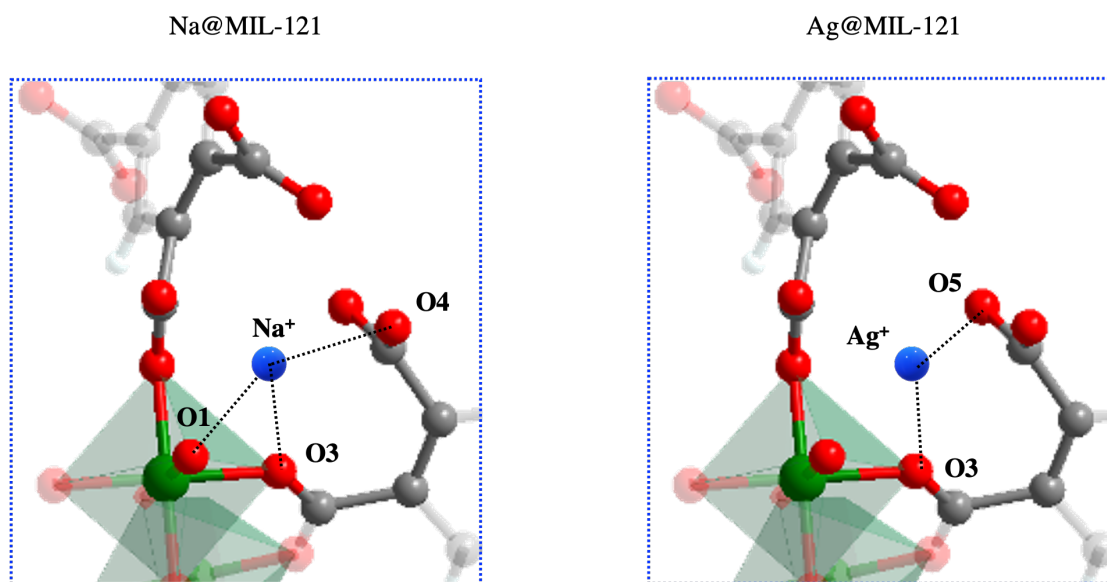


Figure 5.11. Representation of possible interactions between the loaded metal cations and the MOF framework.

- Ag@MIL-121: In the case of Ag@MIL-121, the largest shift in δ_{iso} is observed for O5 and O3. For Ag@MIL-121, the δ_{iso} of O5 and O3 display a downfield shift of 3 and 2 ppm, respectively. This suggests that the silver cations interact with the free carboxylate group (Figure 5.11).

5.4 Conclusions

In summary, in this work, we further demonstrate how ^{17}O SSNMR has allowed us to characterize the oxygen local environments upon activation and metal-exchange of the MIL-121 MOF. The 1D MAS ^{17}O SSNMR spectra acquired at 19.6, 21.1, and the ultrahigh 35.2 T magnetic fields displayed spectral differences upon activation and metal-exchange of the material.

This further shows that ^{17}O SSNMR is a sensitive probe for subtle structural changes in MOFs. Assignment of the resonances were confirmed via $^1\text{H}\rightarrow^{17}\text{O}$ HETCOR, and $^1\text{H}\rightarrow^{17}\text{O}$ REDOR experiments. In addition to confirming the signal assignments, these experiments also provided important information regarding the hydrogen bonding interactions in the framework. A complete set of spectral parameters for each crystallographic non-equivalent sites in the crystal structure (O1, O2, O3, O4, and O5) was obtained, which includes both the quadrupolar and the chemical shift anisotropy parameters. ^{17}O 3QMAS at 19.6 T provided the EFG parameters while the increase of the CSA interaction at the highest 35.2 T field provided the CSA parameters. The parameters were refined using the 1D MAS data. Metal ion-exchange process was also studied via ^{17}O SSNMR and the degree of ion-exchange can also be estimated from ^{17}O NMR.

Our results suggest that Na^+ interacts with the hydroxyl group from the MIL-121 framework. In the case of Ag^+ , the metal cations are exchanged with the hydrogens from both the free carboxylic acid and hydroxyl group from the framework. This work demonstrates that ^{17}O SSNMR can probe the intermolecular interactions governing the activation of MIL-121 and can also probe the metal-exchange PSM in MOFs.

5.5 References

- (1) Yuan, S.; Feng, L.; Wang, K.; Pang, J.; Bosch, M.; Lollar, C.; Sun, Y.; Qin, J.; Yang, X.; Zhang, P.; Wang, Q.; Zou, L.; Zhang, Y.; Zhang, L.; Fang, Y.; Li, J.; Zhou, H. C. *Adv. Mater.* **2018**, 30, 1.
- (2) Cui, Y.; Li, B.; He, H.; Zhou, W.; Chen, B.; Qian, G. *Acc. Chem. Res.* **2016**, 49, 483.
- (3) Hong-Cai, Z.; Long, J. R.; Yaghi, O. M. *Chem. Rev.* **2012**, 112, 673.
- (4) Mandal, S.; Natarajan, S.; Mani, P.; Pankajakshan, A. *Adv. Funct. Mater.* **2021**, 31, 1.
- (5) Taylor-Pashow, K. M. L.; Rocca, J. Della; Xie, Z.; Tran, S.; Lin, W. J. *Am. Chem. Soc.* **2009**, 131, 14261.
- (6) Tanabe, K. K.; Cohen, S. M. *Chem. Soc. Rev.* **2011**, 40, 498.
- (7) Islamoglu, T.; Goswami, S.; Li, Z.; Howarth, A. J.; Farha, O. K.; Hupp, J. T. *Acc. Chem. Res.* **2017**, 50, 805.
- (8) Wang, Z.; Cohen, S. M. *J. Am. Chem. Soc.* **2007**, 129, 12368.
- (9) Kim, M.; Cahill, J. F.; Su, Y.; Prather, K. A.; Cohen, S. M. *Chem. Sci.* **2011**, 3, 126.
- (10) Yin, Z.; Wan, S.; Yang, J.; Kurmoo, M.; Zeng, M. H. *Coord. Chem. Rev.* **2019**, 378, 500.
- (11) Ji, G.; Gao, X.; Zheng, T.; Guan, W.; Liu, H.; Liu, Z. *Inorg. Chem.* **2018**, 57, 10525.
- (12) Chen, S.; Song, Z.; Lyu, J.; Guo, Y.; Lucier, B. E. G.; Luo, W.; Workentin, M. S.; Sun, X.; Huang, Y. J. *Am. Chem. Soc.* **2020**, 142, 4419.
- (13) Carboni, M.; Lin, Z.; Abney, C. W.; Zhang, T.; Lin, W. *Chem. Eur. J.* **2014**, 20,

14965.

- (14) Custelcean, R.; Gorbunova, M. G. *J. Am. Chem. Soc.* **2005**, 127, 16362.
- (15) Bhadra, B. N.; Ahmed, I.; Lee, H. J.; Jhung, S. H. *Coord. Chem. Rev.* **2022**, 450, 214237.
- (16) Volkringer, C.; Loiseau, T.; Guillou, N.; Férey, G.; Haouas, M.; Taulelle, F.; Elkaim, E.; Stock, N. *Inorg. Chem.* **2010**, 49, 9852.
- (17) Chen, S.; Mukherjee, S.; Lucier, B. E. G.; Guo, Y.; Wong, Y. T. A.; Terskikh, V. V.; Zaworotko, M. J.; Huang, Y. *J. Am. Chem. Soc.* **2019**, 141, 14257.
- (18) Chen, S.; Lucier, B. E. G.; Luo, W. across the P. T. I. 14 D. M. I. to E. M.-O. F. P.; Xie, X.; Feng, K.; Chan, H.; Terskikh, V. V.; Sun, X.; Sham, T. K.; Workentin, M. S.; Huang, Y. *ACS Appl. Mater. Interfaces*, **2018**, 10, 30296.
- (19) Ji, C.; Wu, D.; Lu, J.; Shan, C.; Ren, Y.; Li, T.; Lv, L.; Pan, B.; Zhang, W. *Water Res.* **2021**, 189.
- (20) Zettl, R.; Lunghammer, S.; Gadermaier, B.; Boulaoued, A.; Johansson, P.; Wilkening, H. M. R.; Hanzu, I. *Adv. Energy Mater.* **2021**, 11, 2003542.
- (21) Wei, Q.; Shi, B.; Wang, F.; Shao, S.; Zhu, L.; Zhao, X. *Coatings*, **2021**, 11, 854.
- (22) Ou, R.; Zhang, H.; Wei, J.; Kim, S.; Wan, L.; Nguyen, N. S.; Hu, Y.; Zhang, X.; Simon, G. P.; Wang, H. *Adv. Mater.* **2018**, 30, 1.
- (23) Hao, J. N.; Yan, B. *New J. Chem.* **2016**, 40, 4654.
- (24) Loiseau, T.; Volkringer, C.; Haouas, M.; Taulelle, F.; Férey, G. *Comptes Rendus Chim.* **2015**, 18, 1350.
- (25) Martins, V.; Resende, J. A. L. C.; Ronconi, C. M. *CrystEngComm.* **2017**, 19, 3103.
- (26) Sutrisno, A.; Huang, Y. *Solid State Nucl. Magn. Reson.* **2013**, 49, 1.

- (27) Lucier, B. E. G.; Chen, S.; Huang, Y. *Acc. Chem. Res.* **2018**, 51, 319.
- (28) Li, S.; Lafon, O.; Wang, W.; Wang, Q.; Wang, X.; Li, Y.; Xu, J.; Deng, F. *Adv. Mater.* **2020**, 32, 1.
- (29) Martins, V.; Xu, J.; Wang, X.; Chen, K.; Hung, I.; Gan, Z.; Gervais, C.; Bonhomme, C.; Jiang, S.; Zheng, A.; Lucier, B. E. G.; Huang, Y. *J. Am. Chem. Soc.* **2020**, 142, 14877.
- (30) Martins, V.; Xu, J.; Hung, I.; Gan, Z.; Gervais, C.; Bonhomme, C.; Huang, Y. *Magn. Reson. Chem.* **2020**, 53, 1.
- (31) He, P.; Xu, J.; Terskikh, V. V.; Sutrisno, A.; Nie, H. Y.; Huang, Y. *J. Phys. Chem. C*, **2013**, 117, 16953.
- (32) U.S. EPA. **1994**. "Method 200.8: Determination of Trace Elements in Waters and Wastes by Inductively Coupled Plasma-Mass Spectrometry," Revision 5.4. Cincinnati, OH.
- (33) Gan, Z.; Hung, I.; Wang, X.; Paulino, J.; Wu, G.; Litvak, I. M.; Gor'kov, P. L.; Brey, W. W.; Lendi, P.; Schiano, J. L.; Bird, M. D.; Dixon, I. R.; Toth, J.; Boebinger, G. S.; Cross, T. A. *J. Magn. Reson.* **2017**, 284, 125.
- (34) Chou, F. C.; Tsai, T. W. T.; Chan, J. C. C. *Solid State Nucl. Magn. Reson.* **2010**, 38, 58.
- (35) Massiot, D.; Touzo, B.; Trumeau, D.; Coutures, J. P.; Virlet, J.; Florian, P.; Grandinetti, P. J. *Solid State Nucl. Magn. Reson.* **1996**, 6, 73.
- (36) Massiot, D. *J. Magn. Reson. Ser. A* **1996**, 122, 240.
- (37) Frydman, L.; Harwood, J. S. *J. Am. Chem. Soc.* **1995**, 117, 5367.
- (38) Massiot, D.; Fayon, F.; Capron, M.; King, I.; Le Calvé, S.; Alonso, B.; Durand, J. O.; Bujoli, B.; Gan, Z.; Hoatson, G. *Magn. Reson. Chem.* **2002**, 40, 70.

- (39) Antoniadou, M. A.; Eleftheriades, G. V. Proc. 5th Eur. Conf. Antennas Propagation, **2011**, 73, 2406.
- (40) Demong, D. E.; Ng, I.; Miller, M. W.; Stamford, A. W. Org. Lett. **2013**, 15, 2830.
- (41) Wu, G. Prog. Nucl. Magn. Reson. Spectrosc. **2008**, 52, 118.
- (42) Wu, B.; Wong, Y. T. A.; Lucier, B. E. G.; Boyle, P. D.; Huang, Y. ACS Omega **2019**, 4, 4000.
- (43) Hagaman, E. W.; Chen, B.; Jiao, J.; Parsons, W. Solid State Nucl. Magn. Reson. **2012**, 41, 60.
- (44) Rees, G. J.; Day, S. P.; Lari, A.; Howes, A. P.; Iuga, D.; Pitak, M. B.; Coles, S. J.; Threlfall, T. L.; Light, M. E.; Smith, M. E.; Quigley, D.; Wallis, J. D.; Hanna, J. V. CrystEngComm **2013**, 15, 8823.
- (45) Schaefer, J. J. Magn. Reson. **2011**, 213 (2), 421.
- (46) Wong, A.; Pike, K. J.; Jenkins, R.; Clarkson, G. J.; Anupold, T.; Howes, A. P.; Crout, D. H. G.; Samoson, A.; Dupree, R.; Smith, M. E. J. Phys. Chem. A, **2006**, 110, 1824.
- (47) Ashbrook, S. E.; Smith, M. E. Chem. Soc. Rev. **2006**, 35, 718.
- (48) Wu, B.; Wong, Y. T. A.; Lucier, B. E. G.; Boyle, P. D.; Huang, Y. ACS Omega **2019**, 4, 4000.
- (49) Wong, A.; Pike, K. J.; Jenkins, R.; Clarkson, G.; Anupold, T.; Howes, A. P.; Crout, D. H. G.; Samoson, A.; Dupree, R.; Smith, Mark E. J. Phys. Chem. A, **2006**, 110, 1824.
- (50) Penner, G. H.; Liu, X. Prog. sNucl. Magn. Reson. Spectrosc. **2006**, 49, 151.
- (51) and, G. H. P.; Li, W. Inorg. Chem. **2004**, 43, 5588.

Chapter 6

6 Probing the behavior of CO₂ adsorbed in an ultramicroporous MOF under humid conditions using multinuclear solid-state NMR spectroscopy

6.1 Introduction

The climate change has become, perhaps, the greatest challenge of human civilization due to the unprecedented amount of carbon dioxide (CO₂) released into the atmosphere.¹ In order to mitigate global warming, extensive efforts are being deployed for the development of materials and processes to achieve more efficient CO₂ capture capabilities as well as CO₂ storage and utilization.² Metal-organic frameworks (MOFs) are crystalline porous materials that have emerged as promising adsorbents for CO₂ capture. MOFs are hybrid organic-inorganic materials synthesized via the assembly of building blocks with specific geometries that can be combined to form 3D frameworks with high porosity.³⁻⁵

However, application of these materials is still limited by the low chemical stability of some MOFs in the presence of water. Furthermore, a more detailed understanding of the effects of water on CO₂ adsorption in MOFs is still required.^{6,7} For example, while water can negatively affect the CO₂ adsorption capacity of MOF based materials and even cause the collapse of the framework,⁸ it can also enhance the CO₂ adsorption capacity of some MOFs such as in the case of MOF-100,⁹ HKUST-1,¹⁰ and MIL-101.¹¹ Therefore, it is critically important to understand the different roles that water may play in CO₂ adsorption, which may have implications on designing new MOF materials as well as selecting existing MOFs for carbon capture and storage.

Most experimental studies employed to investigate the effect of humidity on the CO₂ adsorption capacity of MOFs involve the approaches to measure multicomponent CO₂ uptake, including thermogravimetric analysis, infrared spectroscopy (IR), gas chromatography (GC), dynamic column-breakthrough techniques with accurate flow measurements, and multicomponent equilibrium adsorption isotherms.¹²

SSNMR is an excellent technique to probe the dynamics of guest molecules inside of MOFs and should be a good probe for investigating effects of water on the dynamics of CO₂ adsorbed in MOFs.¹³ However, most of the studies regarding the dynamics of CO₂ in MOFs have been carried out under dry conditions and only with the pure CO₂ gas. In these cases, SSNMR provided important structural information regarding the dynamics, adsorption sites, and host-guest interactions involving the CO₂ adsorbed inside of the pores of MOFs.¹⁴ To the best of our knowledge, there has been no report on the study of the dynamics of CO₂ and water co-adsorbed in MOFs using SSNMR spectroscopy. Motivated by this, we aimed at characterizing the co-adsorption of carbon dioxide and water in an ultra-microporous MOF, namely ZnAtzOx (Figure 6.1).

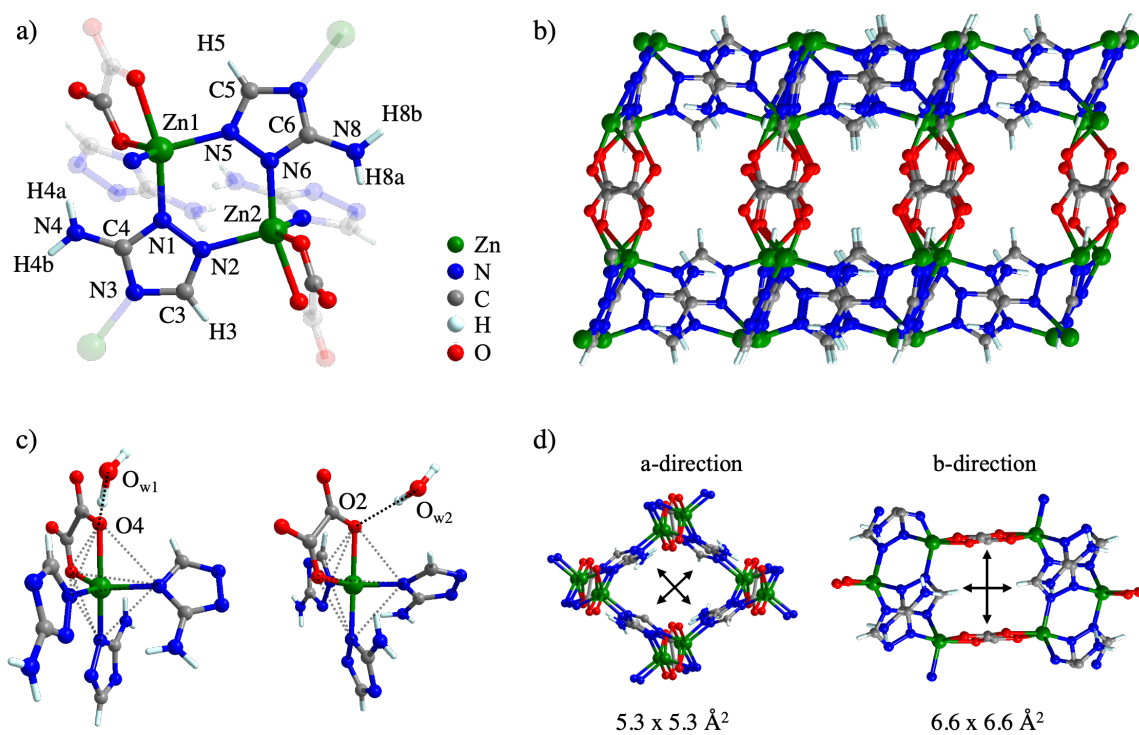


Figure 6.1. a) Asymmetric unit of the crystal structure of ZnAtzOx-as; b) ZnAtz layers pillared by oxalate ligands; c) coordination environment of Zn metal centers; d) cross-sections of the channels in ZnAtzOx. CCDC 1428296.

Our goals are (i) to demonstrate that SSNMR spectroscopy can be a useful technique for the study of co-adsorption of water and CO₂; (ii) to obtain important structural information on the behavior of water and CO₂ co-adsorbed in the MOF framework.

ZnAtzOx is synthesized by combining zinc metal centers with 3-amino-1,2,4- triazolate (Atz) and oxalate (Ox) ligands to form an ultramicroporous 3D framework. ZnAtzOx crystallizes in the monoclinic space group P2₁/c (14). The asymmetric unit of the as-made ZnAtzOx (Figure 6.1) is comprised of two crystallographic non-equivalent metal sites, two Atz ligands and one Ox ligand coordinated to the metal, and two adsorbed water molecules. The Zn sites are penta-coordinated and adopt a distorted trigonal bipyramidal geometry with two oxygen atoms from the oxalate ligand chelated in a cis-fashion and three nitrogen atoms from the Atz ligands. The Zn–O/Zn–N bond lengths and angles are listed in Table A6.1 and Table A6.2. The ligand Atz adopts a tridentate bridging coordination with the metal centers. Topologically, dimeric ZnAtz secondary building units acting as six-connected nodes are linked by Atz and Ox units acting as vertices forming a **pcu** network. The ZnAtz dimers form two-dimensional sheet that is then “pillared” into three dimensions. This arrangement creates channels with dimensions of 5.3 x 5.3 Å² in the a-direction, 6.6 x 6.6 Å² in the b-direction, and 5.8 x 5.2 Å² in the [0 1 1] direction (Figure 6.1).¹⁵ We selected the ZnAtzOx framework for the following reasons:

- (i) It is commercially relevant and synthesized from cheap sources.
- (ii) It exhibits high stability in water, which means it maintains its porosity under humid conditions.
- (iii) The ultramicroporous nature of ZnAtzOx is responsible for the high selectivity towards CO₂ and is ideal for the study of intermolecular interactions experienced by the guest molecules in confined space.
- (iv) The pores of ZnAtzOx contain “free” amino groups that can potentially interact with the CO₂ molecules and enhance the adsorption capacity of the material.

6.2 Experimental details

6.2.1 Sample preparation and characterization

Materials

The following materials were used without further purification: zinc carbonate basic ($[\text{ZnCO}_3]_2 \cdot [\text{Zn}(\text{OH})_2]_3$, 97%, Alfa Aesar), oxalic acid ($\text{C}_2\text{O}_4\text{H}_2$, 98%, Alfa Aesar), 3-amino-1,2,4-triazole ($\text{C}_2\text{N}_4\text{H}_4$, 95%, Aldrich), butanol (99%, Alfa Aesar), methanol (99%, Fischer Chemicals), deuterium oxide (D_2O , 99.9 %), and ^{13}C isotopically enriched carbon dioxide ($^{13}\text{CO}_2$, denoted as CO_2 herein for simplicity, 99% ^{13}C , Sigma- Aldrich).

Synthesis of ZnAtzOx

ZnAtzOx was synthesized as described elsewhere.¹⁵ Briefly, zinc carbonate basic (0.11 g, 0.20 mmol), oxalic acid (0.090g, 1.0 mmol) and 3-amino-1,2,4-triazole (0.42 g, 5.0 mmol) were added into a 6.0 mL solution of distilled water and butanol (50:50 v/v) in a 23 mL Teflon-lined stainless-steel autoclave. The mixture was stirred for 30 minutes at room temperature and the autoclave was then sealed and heated at 180 °C for two days. The colorless microcrystalline product was collected and washed three times with 15 mL of a solution of water and methanol (50:50 v/v) and then dried in air at 80 °C overnight.

Powder X-ray diffraction (PXRD)

Powder X-ray diffraction experiments were carried out to verify the MOF structure and phase purity of the material. PXRD diffractograms were recorded on an Inel CPS powder diffractometer operating with $\text{CuK}\alpha$ radiation ($\lambda=1.5406 \text{ \AA}$). Reflections were collected at 2θ values ranging from 5 to 120°. The experimental PXRD patterns are depicted in Figure A6.2. The experimental patterns are consistent with that calculated from the reported crystal structure (CCDC: 1428296 for the as-made sample, 1428296 for the activated sample), confirming the phase purity and stability of the synthesized ZnAtzOx materials.

Activation and guest loading

To prepare the sample for the NMR experiments, ZnAtxOx was loaded into a L-shaped 5 mm glass tube connected to a Schlenk line, where it was heated at 160 °C for 12 h under vacuum. After cooling to room temperature, D₂O was loaded into the sample by using a syringe. Finally, the sample was exposed to 40-90 mbar of ¹³CO₂ in the calibrated volume (83 mL) and then condensed at liquid nitrogen temperature (77 K). After the adsorption of all ¹³CO₂, the tube was flame sealed and left to equilibrate at 60 °C for 12 h. A detailed table with the amount of guest loading are given in Table A6.3.

CO₂ adsorption measurements

CO₂ adsorption isotherm of the activated ZnAtzOx sample was collected in order to confirm the structural integrity and permanent porosity. Experiments were carried out on a Micromeritics ASAP 2020 porosity analyzer at a temperature of 77 K. The CO₂ adsorption isotherm, Figure A6.3, is similar to that obtained from the literature, showing an adsorption capacity that is comparable to that of previously measured in the literature (4.5 mmol g⁻¹ versus 5.0 mmol g⁻¹).¹⁵ Therefore, confirming that the ²H isotope enrichment and activation does not affect the porosity of the material.

6.2.2 Solid-state NMR

¹H, ¹³C, and ²H SSNMR experiments were performed on a Varian Infinity Plus SSNMR spectrometer operating at a magnetic field of 9.4 T and equipped with a Varian VT temperature control unit. Temperatures were measured to ±2 K. ¹³C and ²H 1D static experiments were conducted with a 5 mm HX Varian/Chemagnetics probe. ¹³C and ²H 1D and 2D MAS experiments were conducted with a 4 mm HXY Varian/Chemagnetics probe at a spinning rate of 8 kHz. ¹³C (Larmor frequency: 100.45 MHz) static NMR spectra were collected using the DEPTH-echo pulse sequence¹⁶ with an optimized ¹³C 90° pulse length of 2.2 μs and pulse delay of 3 s. Spectra were referenced to tetramethylsilane using the methylene carbon in ethanol as a secondary reference at 58.05 ppm.¹⁷ ¹H-¹³C cross polarization (CP) spectra¹⁸ were acquired using contact times varying from 0.5 ms to 10 ms. In the case of ¹H-¹³C CP MAS, the ¹H spectra were

referenced to tetramethylsilane using the CH₂ sites in solid adamantane as a secondary reference with a chemical shift of 1.85 ppm. ¹H-¹³C heteronuclear correlation (HETCOR) experiments were performed using the FSLG-HETCOR pulse sequence¹⁹ with a pulse delay of 5 seconds and a contact time of 0.5 ms. The ²H (Larmor frequency of 61.32 MHz) static SSNMR spectra were acquired using the quadrupolar echo sequence.²⁰ A 90° pulse length of 5.25 μs, a pulse delay of 0.5 s, and a delay time, τ, of 40 μs were used. The chemical shift of ²H was referenced to D₂O at 4.8 ppm, relative to tetramethylsilane.¹⁷ ⁶⁷Zn and ²H MAS experiments were carried out at a magnetic field of 21.1 T on a Bruker II Avance spectrometer at the National Ultrahigh-field NMR facility for Solids in Ottawa, Canada. ⁶⁷Zn (Larmor frequency: 56.24 MHz) SSNMR spectra were acquired on a home-built 7 mm HX probe using a solid-echo pulse sequence with a pulse delay of 0.5 s and a delay time τ of 70 μs.²⁰ The spectra were referenced to 1.0 M aqueous Zn(NO₃)₂, at 0 ppm. ²H MAS spectra were collected on a 2.5 mm HX MAS Bruker probe at a spinning rate of 30 kHz and using the quadrupolar echo sequence.²⁰ A 90° pulse length of 2 μs, a pulse delay of 5 s were used. The chemical shift of ²H was referenced to D₂O at 4.8 ppm, relative to neat tetramethylsilane.¹⁷

6.2.3 Spectral simulations

Analytical simulations of the experimental SSNMR spectra were performed using WSolids NMR simulations package to obtain the observed spectral parameters.²¹ EXPRESS software was employed to simulate the effects of different types and rates of dynamic motions on the observed SSNMR spectra and to obtain the motionally averaged spectral parameters.²² The known parameters for static CO₂ are δ_{iso} = 125 ppm, Ω = 335 ppm, and κ = 1.²³ The known parameters for static D₂O and ND₂ are C_Q(²H) = 225 kHz and η_Q = 0, and C_Q(²H) = 200 kHz and η_Q = 0, respectively.^{24,25}

6.3 Results and discussion

Behavior of CO₂ adsorbed in ZnAtzOx

The dynamics of CO₂ in MOFs is an important phenomenon that directly affects the sorption capacity of the material and therefore affects its practical applications.

Understanding the dynamics of adsorbed CO₂ is therefore essential for the rational design

of MOF materials with enhanced physicochemical properties.^{26–28} SSNMR is a valuable tool that can provide complementary information about guest dynamics across a large range of time scale. CO₂ dynamics in MOFs is typically studied via ¹³C solid-state NMR (SSNMR) experiments using ¹³C-enriched ¹³CO₂ gas.^{29–31} ¹³C is a spin-1/2 nucleus associated with broad powder patterns that exhibit line-shapes dominated by the chemical shielding (CS) interaction, which is sensitive to the local environment and dynamics of adsorbed CO₂.³² Therefore, spectral simulations of the observed variable-temperature NMR parameters can reveal the dynamics of CO₂ molecules, along with motional angles and rates.^{22,33}

To understand the dynamics of adsorbed CO₂ molecules in the ZnAtzOx, variables temperature (VT) static ¹³C SSNMR experiments were performed on ZnAtzOx loaded with different amounts (0.1, 0.2 and 0.5 molar equivalent per metal) of ¹³C-labelled CO₂. The complete set of experimental and simulated SSNMR powder patterns are depicted in Figure A6.4 to Figure A6.5. The static VT ¹³C SSNMR spectrum of ZnAtzOx loaded with 0.5 equivalent ¹³CO₂ (Figure 6.2) displays a broad powder pattern that was simulated using three signals at temperatures below 293 K and two signals at temperatures above 293 K. These signals are denoted as Site 1, Site 2, and Site 3. The spectral parameters for each site are listed in Table 6.1. At low temperatures (below 300 K), the CSA pattern is comprised of two broad signals (Site 1 and Site 2) and one narrow signal (Site 3). As temperature increases and reach 300 K, the CSA pattern can be simulated by considering only Site 1 and Site 2.

The CO₂ molecules located at Sites 1, 2, and 3 display chemical shift of 125, 124, and 125 ppm, respectively. The known parameters of solid CO₂ are: $\delta_{\text{iso}} = 126$ ppm, $\Omega = 335$ ppm, and $\kappa = 1.00$.²³ Therefore, we tentatively attribute these three signals to CO₂ species adsorbed in the framework. Similar values of δ_{iso} have also been reported for CO₂ adsorbed in other MOF materials, corroborating our attribution.^{34,35,44–46,36–43} For CO₂ at Site 1, the Ω ranges from 290 ppm at 193 K to 260 ppm at 333 K. When compared with the Ω value of solid CO₂, the large Ω of 290 ppm indicates that the CO₂ molecules are relatively immobile in the pores. This can be attributed to the small pore dimensions of ZnAtzOx ($5.3 \times 5.3 \text{ \AA}^2$),¹⁵ which limits the motion of the CO₂.

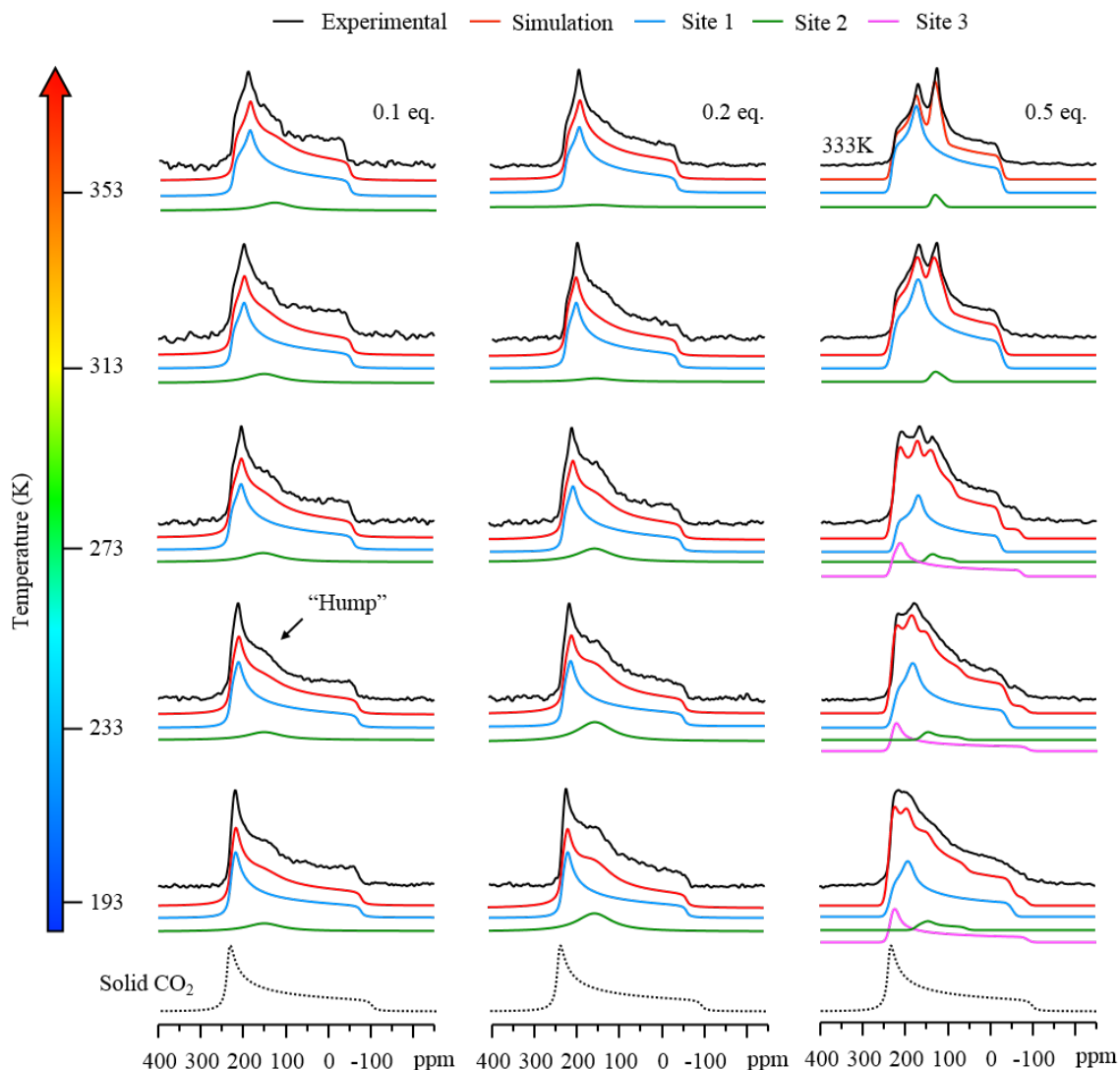


Figure 6.2. Experimental and simulated VT static ^{13}C NMR spectra of $^{13}\text{CO}_2$ -loaded ZnAtzOx at selected temperatures and gas loadings.

For comparison, a Ω of 300 ppm has been found for CO_2 adsorbed in the ultramicroporous SIFSIX-3-Zn with a pore diameter of 3.8 \AA ,⁴⁷ and a small Ω of 100 ppm for the relatively mobile CO_2 molecules in the Mg-MOF-74 material with pore diameter of 15 \AA .⁴⁴ The κ parameters ranges from 0.70 at 193 K to 0.55 at 333K suggest that, although the CO_2 molecules are relatively immobile, they still display some type of dynamics. The CO_2 molecules only occupy Site 2 at temperatures below 300 K.

Table 6.1. Experimental ^{13}C CSA parameters of $^{13}\text{CO}_2$ adsorbed within ZnAtzOx at 0.5 equivalent loading (or 5 atm). Parameters were obtained from analytical simulations of static ^{13}C SSNMR spectra.

Temperature (K)	Relative intensity (%)	δ_{iso} (ppm)	Ω (ppm)	κ	α ($^\circ$)	β ($^\circ$)
Site 1						
333	88(1)	126(1)	260(2)	0.55(1)	10(1)	25(1)
313	90(1)	126(1)	260(2)	0.52(1)	10(1)	26(1)
293	49(1)	125(2)	240(5)	0.64(2)	20(1)	22(1)
273	57(1)	125(2)	250(5)	0.54(2)	15(1)	25(1)
253	58(1)	125(2)	260(5)	0.60(2)	13(1)	24(1)
233	64(1)	125(2)	270(5)	0.64(2)	13(1)	22(1)
213	67(1)	125(2)	290(5)	0.70(2)	8(1)	21(1)
193	57(1)	125(2)	290(5)	0.70(2)	7(1)	21(1)
Site 2						
293	44(1)	124(2)	300(5)	0.90(2)	12(1)	15(1)
273	33(1)	124(2)	310(5)	0.84(2)	7(1)	15(1)
253	35(1)	124(2)	315(5)	0.94(2)	5(1)	12(1)
233	28(1)	124(2)	315(5)	1.00(2)	5(1)	11(1)
213	25(1)	124(2)	310(5)	1.00(2)	5(1)	11(1)
193	34(1)	124(2)	320(5)	1.00(2)	4(1)	11(1)
Site 3						
333	12(1)	125(5)	30(10)	0.50(5)	50(1)	29(1)
313	10(1)	125(5)	40(10)	0.50(5)	48(1)	29(1)
293	7(1)	130(5)	50(10)	0.60(5)	47(1)	28(1)
273	8(1)	125(5)	70(10)	0.50(5)	44(1)	27(1)
253	7(1)	125(5)	80(10)	0.50(5)	42(1)	27(1)
233	8(1)	125(5)	100(10)	0.65(5)	40(1)	26(1)
213	8(1)	120(5)	120(10)	0.50(5)	37(1)	27(1)
193	9(1)	125(5)	120(10)	0.50(5)	36(1)	27(1)

The span ranges from 320 ppm at 193 K to 300 ppm to at 333K and the skew ranges from 1.00 at 193 K to 0.90 at 333 K. The large span value and almost symmetrical skew of CO_2 at Site 2 indicate that at low temperature and high concentration of CO_2 , the molecules can be tightly packed inside of the framework, with very small mobility. At Site 3, CO_2 has a low intensity and the Ω is considerably smaller compared to those of

CO₂ located at Site 1 and Site 2, ranging from 120 ppm at 193 K to 30 ppm at 333K. This suggests that the CO₂ molecules at Site 3 have a much higher degree of motion.

The framework of ZnAtzOx can undergo what is called gate-opening, which is responsible for a sharp increase in the CO₂ adsorption capacity from 3 mmol g⁻¹ at around 0.5 atm to more than 5 mmol g⁻¹ at pressures above 1 atm and at 298 K. Vaidhyathan and collaborators have demonstrated that the gate opening process in ZnAtzOx is associated with a subtle molecular motion that opens an additional site for CO₂ to fill up, thus increasing the adsorption uptake. The authors suggested that the CO₂ molecules occupying the site at low pressure interact with the amino groups and that at high pressure the CO₂ molecules interact with the framework and other CO₂ molecules. Furthermore, they showed that the gate opening effect is dependent on temperature. At higher temperatures above 300 K, only one site is available for the CO₂ adsorption.¹⁵ Accordingly, we can tentatively attribute the Site 1 to the CO₂ adsorbed in the framework, interacting with the amino groups. The Site 2 can be tentatively assigned to the CO₂ molecules occupying the site created after the gate opening and interacting with the CH and oxalate groups from the ligand. The Site 3 can be tentatively assigned to the CO₂ adsorbed on the surface of the material. At low temperature, CO₂ can occupy both Site 1 and Site 2. As temperature increases and reaches 300 K, the gate closes again, and CO₂ can only occupy Site 1. Some CO₂ previously occupying Site 2 is now forced to adsorb outside of the pore, on the surface of the material.

To investigate the effect of concentration of the CO₂ on the adsorption capacity of the material, VT static ¹³C NMR experiments were carried out in the samples loaded with 0.1 and 0.2 equivalent of CO₂. The spectra are depicted in Figure 6.2 and the spectral parameters are listed in Table 6.2. At a loading of 0.2 equivalent, one signal was observed throughout all temperatures. This signal is very similar to that observed for Site 1 at a loading of 0.5 eq., therefore we tentatively assigned it to the CO₂ site interacting with the amino groups. The span ranges from 305 ppm at 173 K to 262 ppm at 373 K. The skew, ranges from 0.96 at 173 K to 0.69 at 373 K.

Table 6.2. Experimental ^{13}C CSA parameters of $^{13}\text{CO}_2$ adsorbed within ZnAtzOx at 0.2 (2 atm) and 0.1 equivalent (1.5 atm) loading in Site 1. Parameters were obtained from analytical simulations of static ^{13}C SSNMR spectra. Site 2 was simulated using a gaussian curve with $\delta_{\text{iso}} = 150$ ppm and FWHM 100 ppm.

Temperature (K)	Relative intensity (%)	δ_{iso} (ppm)	Ω (ppm)	κ	α ($^\circ$)	β ($^\circ$)
0.2 equivalent CO_2						
373	100(1)	125(1)	262(2)	0.69(1)	14(1)	22(1)
353	99(1)	124(1)	264(2)	0.74(1)	15(1)	21(1)
333	99(1)	124(1)	266(2)	0.77(1)	14(1)	21(1)
313	99(1)	124(1)	266(2)	0.77(1)	14(1)	19(1)
293	97(1)	123(1)	280(2)	0.80(1)	15(1)	17(1)
273	96(1)	125(1)	282(2)	0.82(1)	14(1)	16(1)
253	94(1)	124(1)	292(2)	0.87(1)	12(1)	16(1)
233	94(1)	124(2)	290(5)	0.88(2)	12(1)	16(1)
213	94(1)	125(2)	295(5)	0.90(2)	12(1)	14(1)
193	94(1)	124(2)	295(5)	0.90(2)	11(1)	14(1)
173	94(1)	124(2)	305(5)	0.96(2)	10(1)	12(1)
0.1 equivalent CO_2						
373	97(1)	123(1)	272(2)	0.69(1)	12(1)	22(1)
353	98(1)	123(1)	274(2)	0.71(1)	12(1)	21(1)
333	98(1)	122(1)	278(2)	0.75(1)	12(1)	20(1)
313	97(1)	123(1)	284(2)	0.77(1)	13(1)	18(1)
293	97(1)	124(1)	286(2)	0.78(1)	12(1)	18(1)
273	97(1)	123(1)	292(2)	0.81(1)	9(1)	18(1)
253	96(1)	123(1)	298(2)	0.83(1)	7(1)	17(1)
233	97(1)	123(1)	302(2)	0.86(1)	6(1)	16(1)
213	97(1)	123(1)	306(2)	0.89(1)	5(1)	15(1)
193	97(1)	123(1)	308(2)	0.92(1)	3(1)	14(1)
173	97(1)	123(1)	312(2)	0.95(1)	2(1)	13(1)

It is worth noting a “hump” at around 160 ppm of the total signal. This signal was simulated using a Gaussian line-shape centered at 160 ppm with full width at half maximum (FWHM) of 120 ppm and low intensity of around 5%. The breadth of this signal is comparable to the span of CO_2 at Site 3 observed at a loading of 0.5 equivalent,

suggesting that some CO₂ might be adsorbed on the surface of the material. However, we were not able to confidently assign this signal because of the large error associated with the low intensity. Furthermore, this signal can be also from the signals of the framework, which have expected chemical shift values between 161 ppm and 140 ppm and centered at around 150 ppm.

The static ¹³C spectra of the as-made and activated materials can be reasonably simulated with the same parameters used to simulate the Gaussian signal with FWHM of 120 ppm (Figure 6.3). At a loading of 0.1 equivalent, the ¹³C NMR spectra are similar to those previously described. The CO₂ at Site 1 displays span ranging from 312 ppm at 173 to 272 ppm at 373 K and skew ranging from 0.95 at 173 K to 0.69 at 373 K.

Analytical simulations of the line-shapes can furnish details about the types of motions that CO₂ undergoes. The effects of motion on the line-shape can be deduced from the span, which has been found to be affected by hopping motions around the molecular axis of CO₂, and the skew, which is affected by hopping motions inside of the pores. The wobbling motion (Figure 6.4) is described by a six-fold rotation of the CO₂ molecule at an angle α . The hopping motion (Figure 6.4) is described by a two-fold rotation with an angle β . An increase of α indicates an increase in the wobbling motion and an increase of β indicates increase in the hopping motion.²⁹⁻³¹

The parameters obtained from dynamic simulations are listed in Table 6.1 and Table 6.2. For CO₂ at Site 1, it was found that the wobbling motion (angle of around 10 °) is only slightly affected by the concentration of CO₂ and the temperature. The hopping motion is also similar for all concentrations and temperatures, ranging from around 12 ° at 173 K to around 22 ° at 373 K. The small change of wobbling and hopping angles with temperature suggests that the CO₂ molecules are interacting strongly with the framework. For CO₂ at Site 2, which only appears when the sample is loaded with 0.5 equivalent CO₂ and at low temperatures, the wobbling and hopping angles are around 10 and 12 °, respectively. This indicates that the CO₂ molecules at Site 2 are almost immobile and are also dependent on the concentration of CO₂ inside of the pores.

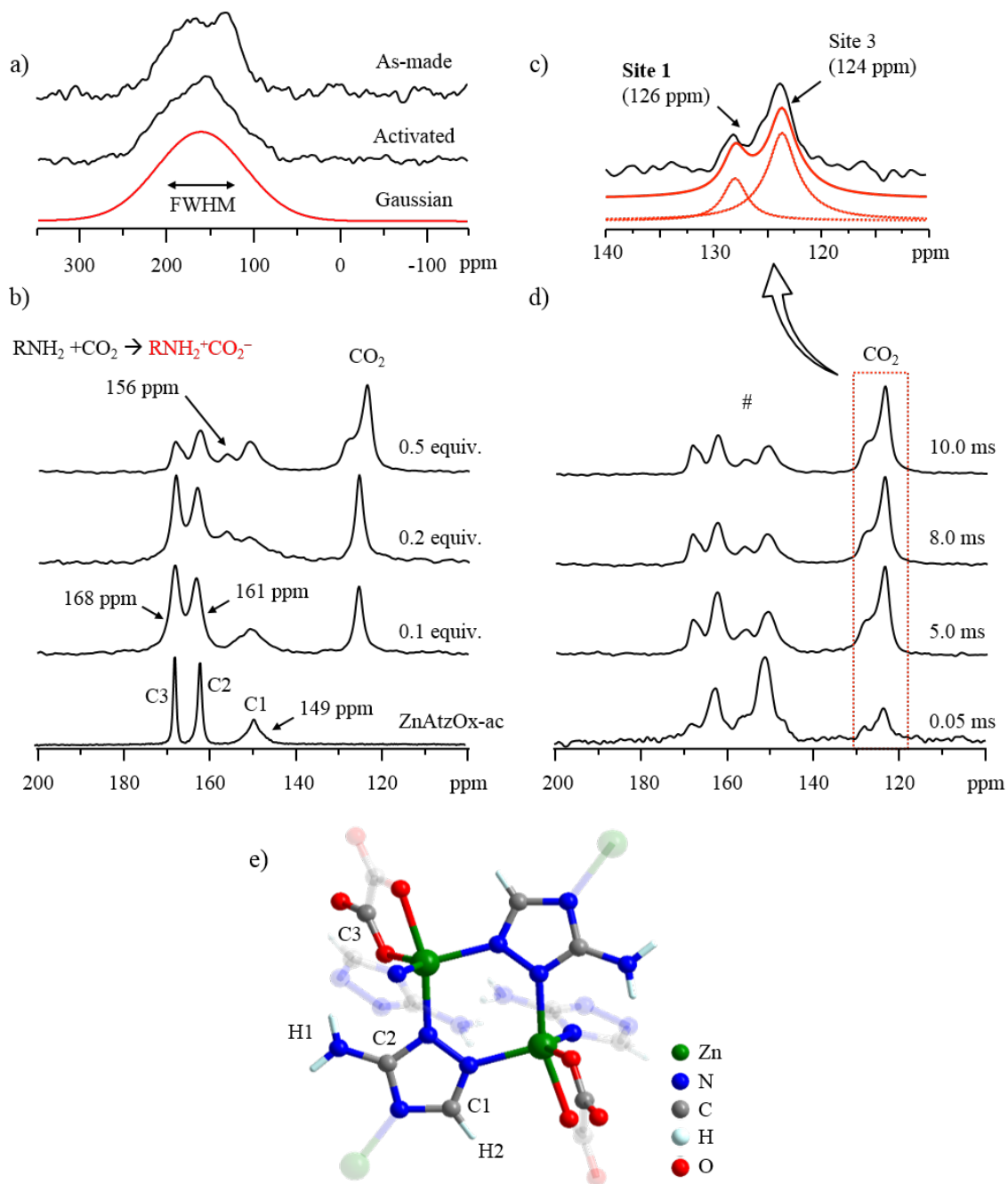


Figure 6.3. a) Experimental and simulated static ^{13}C SSNMR spectra of ZnAtzOx-as and ZnAtzOx-ac; b) ^1H - ^{13}C CP MAS spectra of ZnAtzOx loaded with different loadings of CO_2 (spinning rate of 10 kHz and contact time of 8 ms); c) Zoomed in region of adsorbed CO_2 ; and d) ^1H - ^{13}C CP MAS spectra of ZnAtzOx loaded 0.5 equivalent of CO_2 acquired with a spinning rate of 10 kHz and different contact times; e) Asymmetric unit of ZnAtzOx.

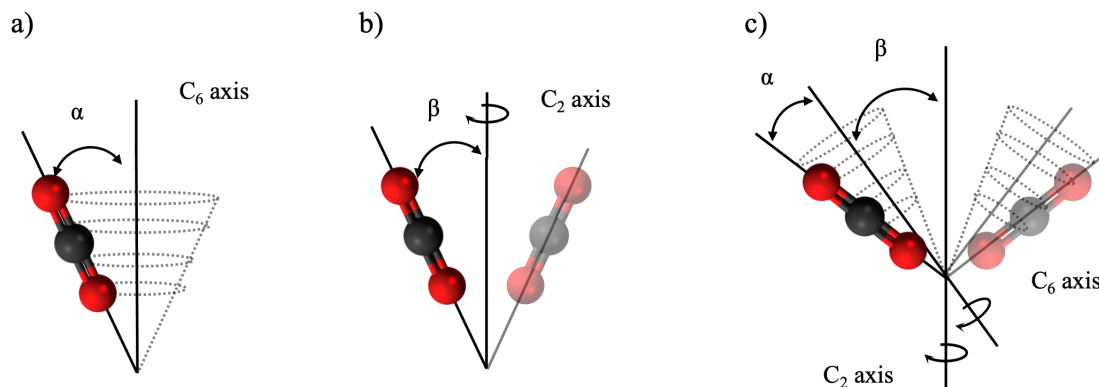


Figure 6.4. Representation of the a) wobbling, b) hopping and c) combined wobbling and hopping motions of a CO₂ molecule. The motions are described by the angles α and β respectively. Wobbling motions are modelled by a six-fold rotation, while hopping motions are modelled by a two-fold rotation.

In order to confirm the number of adsorption sites found from the simulation of the static ¹³C spectra, ¹H-¹³C cross-polarization MAS (CPMAS) experiments were carried out. ¹H-¹³C CP experiments involve the transfer of magnetization from ¹H to ¹³C nuclei through the heteronuclear dipolar interaction. In addition to sensitivity enhancement, it also provides information on distance and, by extension, the connectivity between two unlike spins involved.⁴⁸ The ¹H-¹³C CPMAS spectra of ZnAtzOx loaded with different CO₂ concentrations are depicted in Figure 6.3

The ¹H-¹³C CPMAS spectrum of the activated ZnAtzOx displays three signals at 149, 161, and 168 ppm. The resonances at 149 and 161 are assigned to the C1 and C2 carbon atoms in the triazole ring and the signal centered at 168 ppm is assigned to the carbon atoms from the oxalate ligands. Oxalic acid has a reported ¹³C chemical shift of 168 ppm and 3-amino-1,2,4-triazole has reported ¹³C chemical shifts of 155 ppm for C2 and 140 ppm for C1.⁴⁹ Upon loading of CO₂ at 0.1 and 0.2 equivalent, the ¹H-¹³C CPMAS spectra display two additional signals at around 125 ppm and 156 ppm. Interestingly, the signal at 156 is suggestive of the Gaussian signal observed at loadings of 0.1 and 0.2 equivalent of CO₂. Since this signal is not present in the as-made and activated materials, it might

suggest the formation of carbamate species upon CO₂ adsorption. Previous literature has shown that MOFs containing amino groups can adsorb CO₂ via a mechanism involving the formation of carbamate species. ¹³C MAS experiments have shown that these species have a chemical shift varying from 159 to 165 ppm.^{50,51} This signal could also be the reason for the “hump” observed in the ¹³C static spectra.

The signal at 125 is attributed to the CO₂ adsorbed in the framework. Upon increasing the CO₂ loading to 0.5 equivalent, two CO₂ signals appear at 126 and 124 ppm instead of one signal. ¹H-¹³C CPMAS experiments were then carried out using different contact times. At very small contact time of 0.05 ms, the two CO₂ sites were still present, suggesting that the carbon atoms in the CO₂ molecules must be very close to the hydrogens in the framework. The ¹³C CPMAS results are in good agreement with the ¹³C SSNMR static results. The ¹³C static spectrum of ZnAtzOx loaded with 0.5 equivalent of CO₂ displayed three sites and the ¹³C CPMAS indicated that at least two sites are present. The resolution might not be enough to resolve all signals under the experimental conditions employed. Nevertheless, the δ_{iso} of the two signals obtained from CPMAS are in good agreement with those of the signals obtained from static experiments. Specifically, CO₂ molecules adsorbed at Sites 1 and 2 display large span, which indicates a strong interaction with the framework. These two signals have been observed in the ¹H-¹³C CPMAS spectra. Moreover, the signal of CO₂ loosely adsorbed at Site 3 in the static experiments was absent in the ¹H-¹³C CPMAS spectra. This confirms that the CO₂ is weakly interacting with the framework in Site 3, considering that the CO₂ was desorbed during the spinning experiments.

To determine the location and proximity of the CO₂ molecules to the protons of the framework, two-dimensional correlation spectroscopy ¹H-¹³C HETCOR was employed (Figure 6.5). ¹H-¹³C HETCOR allows for the ¹H and ¹³C signals to be correlated with one another. HETCOR essentially functions as two-dimensional CP experiments, which is based on the strength of their dipolar interactions.⁴⁸

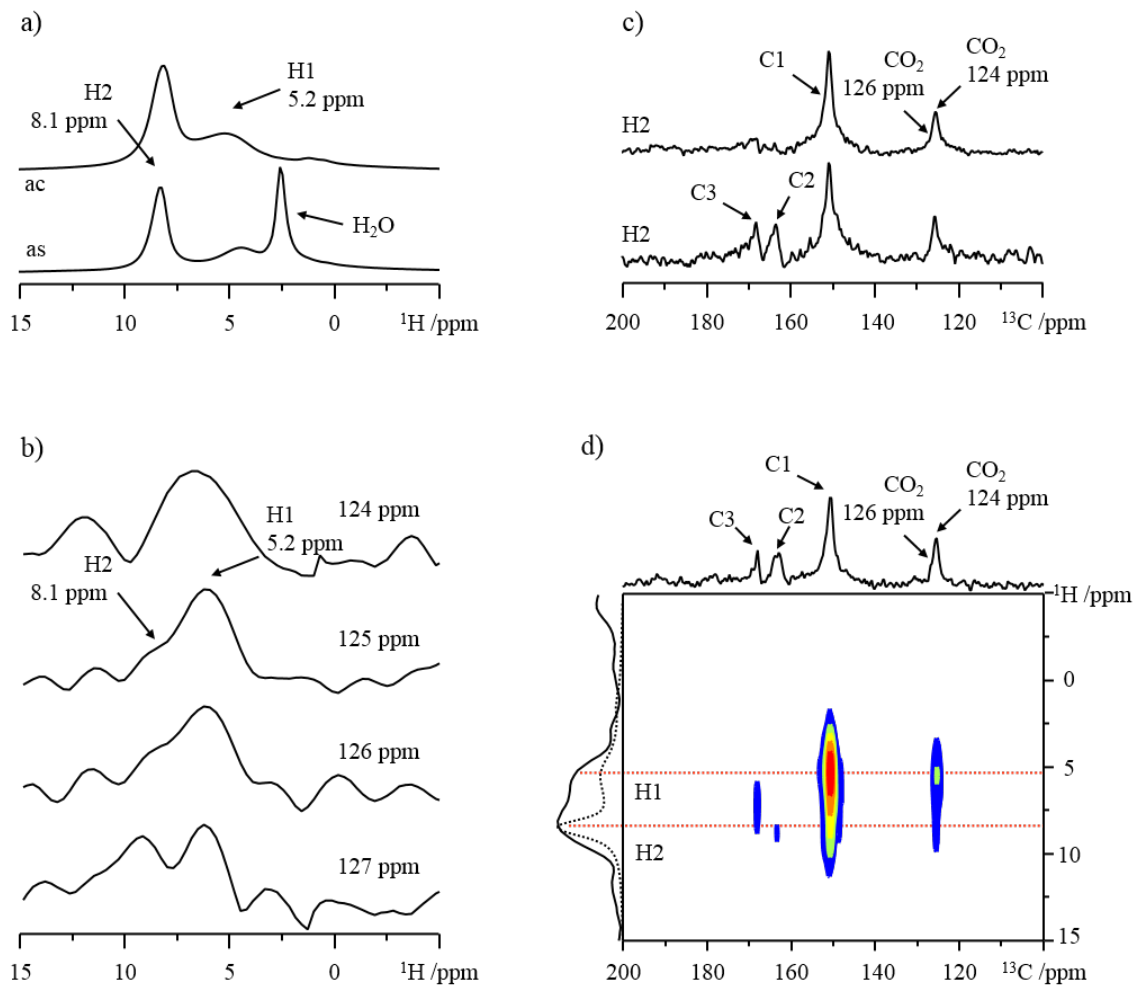


Figure 6.5. a) ^1H MAS spectra of ZnAtzOx-as and ZnAtzOx-ac acquired at 9.4 T with a spinning rate of 10 kHz; b) F2 cross-sections; c) F1 cross-sections; d) HETCOR Spectrum of ZnAtzOx loaded with 0.5 equivalent of CO_2 . Spectra were acquired with spinning rate of 8 kHz and contact time of 8 ms.

The ^1H spectrum of ZnAtzOx-ac displays two signals at 5.2 and 8.1 ppm, which are assigned to the NH_2 (H1) and CH (H2) protons from the framework, respectively (Figure 6.5.a). The ^1H - ^{13}C HETCOR spectrum (Figure 6.5.e) indicates a strong correlation between the amino (H1) and the CH (H2) protons from the triazole ring and with the CO_2 . In Figure 6.5.c, projections of the F2 dimension at the chemical shift of H1 and H2 are depicted. The amino proton interacts with all carbon species in the framework as well

as the adsorbed CO₂ molecules. The H2 protons correlate with the CH and the adsorbed CO₂. This suggests that the CO₂ molecules interact with both the CH and amino groups. To further investigate the location and interaction of CO₂, cross-sections in the F1 dimension at a ¹³C chemical shift ranging from 124 to 127 ppm were analyzed (Figure 6.5.b). The CO₂ signal at 124 ppm correlates with both protons of the amino and CH groups. Suggesting that the CO₂ interacts with both groups. The signal of CO₂ molecules at Site 2 with chemical shift of 126 ppm correlates mostly with the CH groups, indicating that the CO₂ molecules at Site 2 interact mostly with the CH groups. In the crystal structure of ZnAtzOx,¹⁵ the distance between H1 and C1 is 0.95 Å. The distance between the H2 and C1 is 3.8 Å, between H2 and C3 is 3.4 Å, and the distance between H2 and C2 is 1.9 Å.

Based on our NMR results, a tentative model for the CO₂ adsorption in ZnAtzOx can be realized (Figure 6.6). At low concentration of CO₂ (0.1 and 0.2 eq.), most of the molecules occupy one site inside of the framework and a few can be adsorbed at Site 3 or formed carbamate. The CO₂ molecules adsorbed inside of the pores occupy Site 1 and are located near the amino groups in the framework. This is consistent with the relatively high enthalpy of adsorption of 46 kJ mol⁻¹ for Site 1, which was attributed to the relatively strong interactions between the CO₂ molecules and amino groups in the framework.^{15,52} At these CO₂ loadings (0.1 and 0.2 eq.), we only expect the CO₂ to occupy one site because the amount of CO₂ is lower than the capacity of the sample. For example, the maximum CO₂ capacity of ZnAtzOx based on the CO₂ adsorption isotherm is 4.5 mmol per gram of MOF. The maximum CO₂ that can be loaded for the 0.1 equivalent sample is around 0.7 mmol (0.16 g of activated ZnAtzOx was used). The actual amount of CO₂ loaded was 0.5 mmol of CO₂ per gram of MOF, which is much smaller than the maximum capacity of 4.5 mmol g^s. The values for the theoretical maximum loading of CO₂ can be found on Table A6.3. For the sample loaded with 0.2 equivalent of CO₂, the actual CO₂ loaded is 1 mmol g⁻¹.

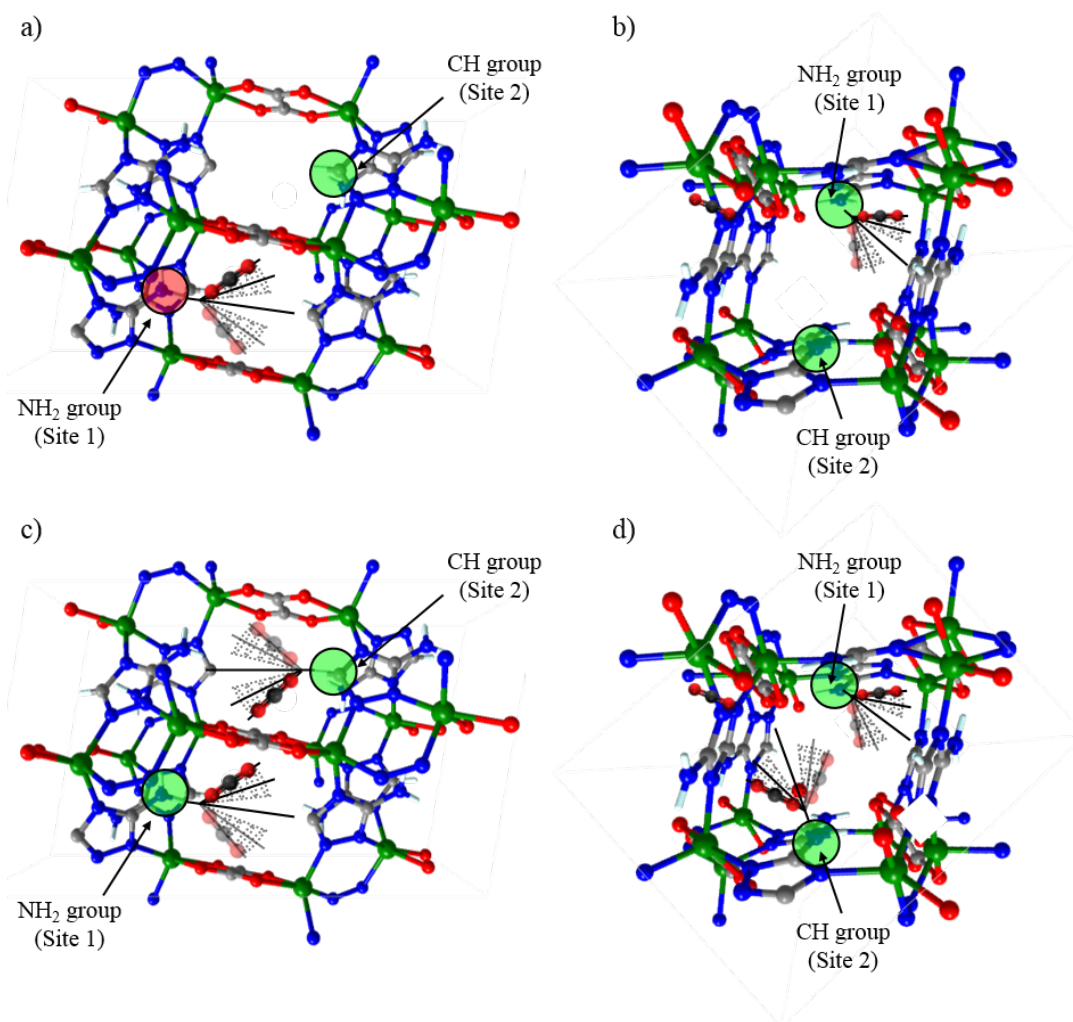


Figure 6.6. Representation of CO₂ sites in ZnAtzOx. a) model of low CO₂ loading viewed from a-axis; b) model of low CO₂ loading viewed from b-axis; c) model of high CO₂ loading viewed from a-axis; d) model of high CO₂ loading viewed from b-axis.

At high concentration of CO₂ of 0.5 eq., the actual CO₂ loading is 2.6 mmol g⁻¹. This implies that there are enough CO₂ molecules to occupy both Site 1 and Site 2. At Site 1, the CO₂ molecules interact with the amino groups, while at Site 2 the CO₂ molecules interact with the CH groups and other CO₂ molecules. At the same CO₂ loading of 0.5

equivalent but at high temperature, only one site is observed for CO₂ adsorbed in the pores. This is expected because the gate opening only occurs at temperatures below 303 K. At temperatures above 303 K, the CO₂ adsorbed at Site 2 is, therefore, desorbed.

Finally, it is important to highlight that the ¹³C static NMR results also demonstrated to be an interesting probe for the gate opening process in ZnAtzOx and other similar MOFs. The ¹³C static NMR spectrum of the sample loaded with high concentration of CO₂ is distinctively different at 293 and 313 K. The gate opening process occurs at around 303 K. This means that there are two possible sites below 303 K and that there is only one site above this temperature.¹⁵ Indeed, the spectrum at 293 K displays two signals for adsorbed CO₂ and the spectrum at 313 K displays only one site for adsorbed CO₂.

Behavior of H₂O adsorbed in ZnAtzOx

The sensitivity of MOF structure to water is a major issue when considering these materials for adsorption applications.^{12,53,54} It is well known that water can affect the structural stability as well as the adsorption performance of MOFs.^{6,12,55–58} Therefore, a better understanding of the effect of water on MOF stability and adsorption properties is crucial to the development of new water-stable adsorbents.¹³

However, although high-resolution SSNMR is a powerful technique for such characterization, only a few studies have been reported so far on the stability^{59–61} and water adsorption in MOFs.^{59,62} To investigate the dynamics of adsorbed water molecules in the ZnAtzOx, variable temperature (VT) static ²H SSNMR experiments were conducted on ²H₂O-loaded ZnAtzOx at loading levels of 2, 4, and 8 weight percent, %. Spectral simulations were carried out. The experimental and simulated ²H powder patterns at selected temperatures are depicted in Figure 6.7. The complete set of experimental and simulated SSNMR powder patterns from 173 to 373 K are depicted in Figure A6.7 to Figure A6.9 and the complete set of parameters are listed in Table A6.4 to Table A6.6. The static VT ²H SSNMR spectra of ZnAtzOx loaded 2% D₂O (Figure 6.7) exhibit a broad pattern composed of two signals: a broad powder pattern and a narrower pattern. The broad resonance was attributed to the ND₂ groups of the framework.

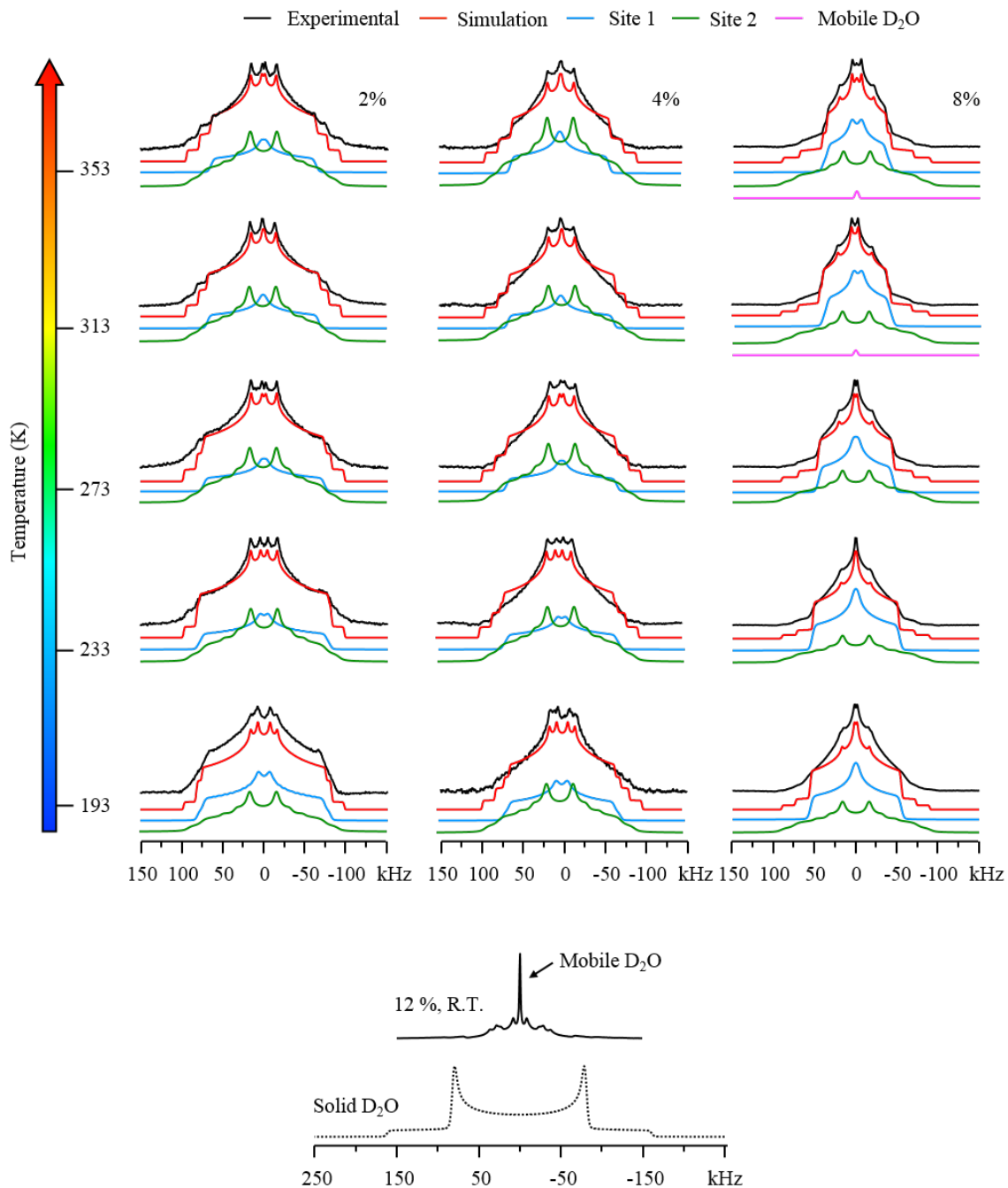


Figure 6.7. Experimental and simulated ^2H static VT NMR spectra of D_2O -loaded ZnAtzOx at selected temperatures and loading. Static pattern of solid D_2O was simulated using $C_Q = 225$ kHz and $\eta_Q = 0$.^{24,25} R.T. stands for room temperature.

Upon D₂O loading, the ²H protons atoms of the D₂O can exchange with the protons of the amino groups. To confirm this assignment, a simple ²H isotope enrichment approach was used in which the activated MOF sample was immersed in a small amount of ²H₂O (heavy water) overnight and then the sample was activated. To evaluate the level of exchange, ¹H MAS spectra of the ZnAtzOx-ac and ²H-exchanged ZnAtzOx-ac were acquired (Figure A6.6). The intensity ratio between the NH₂ and CH groups from the framework before ²H exchange is 2.7, which is in excellent agreement with the crystal structure. Upon ²H exchange, the ratio decreased to 2.3, which indicates an enrichment of around 14%. ²H VT static experiments were then carried out to probe the behavior of ND₂ and the spectra of activated ²H-exchanged ZnAtzOx is depicted in Figure A6.6.

The powder pattern of activated ²H-exchanged ZnAtzOx is characterized by a broad signal with apparent C_Q of 133 kHz and η_Q of 0.75. The signal remains unchanged to temperatures up to 233 K and then the ²H powder pattern becomes broader below 233 K. Analysis of spectral parameters and line-shape suggest that the ND₂ groups undergo a fast π flip-flop rotation around its molecular axis accompanied by libration motions.^{22,63}

The narrow line-shape of the static VT ²H SSNMR spectra of ZnAtzOx loaded 2% of D₂O is similar to those found in the literature for the π flip-flop of D₂O adsorbed in other porous materials.^{24,25,64} However, it displays a smaller value of C_Q, ranging from 110 kHz at 173 K to 85 kHz at 333 K. Furthermore, the line-shape is much narrower than that of static water.²⁴ This indicates that additional dynamics must be taking place and that the water molecules are relatively mobile inside of the framework. The η_Q ranges from 0.82 at 173 K to 0.90 at 373 K. The static VT ²H SSNMR spectra of ZnAtzOx loaded with 4% D₂O are similar to those of ZnAtzOx loaded 2% D₂O. However, the resonances are slightly narrower, with C_Q ranging from 95 kHz at 173 K to 80 kHz at 333 K, and η_Q ranging from 0.82 at 173 K to 0.90 at 373 K (Figure 6.7).

At the maximum loading of 8%, the intensity of the signal from the water molecules increases in comparison with the signal from the framework ND₂ groups. The C_Q ranges from 80 kHz at 173 K to 55 kHz at 373 K and the η_Q ranges from 0.69 at 173 K to 0.90 at 373 K. At 293 K, an additional sharp signal attributed to “mobile” water appears. This

sharp signal is also present in the ^2H spectrum of the sample loaded with 12% D_2O (Figure 6.7).

It is well known in the literature that water can undergo vibrational libration modes that cause a decrease in the effective quadrupolar constant.⁶⁵ Considering a D–O–D angle of 109 degrees, a C_Q of 215 kHz and η_Q of 0, we were able to simulate the experimental powder pattern by modelling the motion of the water molecules as a combination of π -flip rotation and libration motions.^{24,25,66} The libration angles (γ) of the water molecules loaded in ZnAtzOx at different levels are depicted in Figure 6.8 and listed in Table 6.3. At a loading level of 2% and low temperatures, the water molecules only undergo the π -flip rotation and the librational angle increases to 38 ° at 373 K from 0 ° at 173 K.^{65,67}

Table 6.3. Librational angles (γ) of the water molecules loaded in ZnAtzOx at different levels.

Temperature	2% D_2O	4% D_2O	8% D_2O
373 K	38 °	42 °	60 °
353 K	36 °	40 °	60 °
333 K	34 °	38 °	59 °
313 K	32 °	36 °	59 °
293 K	28 °	34 °	57 °
273 K	24 °	32 °	55 °
253 K	14 °	30 °	52 °
233 K	0	28 °	50 °
213 K	0	26 °	48 °
193 K	0	28 °	46 °
173 K	0	28 °	42 °

At a 4% D_2O loading, γ varies from 28 ° at 173 K to 42 ° at 373 K. At a loading of 8%, γ ranges from 42 ° at 173 K to 60 ° at 373 K. This might suggest that at high concentrations the interaction between the water molecules in the pores weakens the interaction between the water molecules and the framework. Consequently, the molecules can rotate more freely.

^2H MAS experiments of ZnAtzOx loaded with 4 and 8% D_2O were carried out to identify the number of possible sites of adsorption in the framework. At very high spinning rates such as the one employed for the ^2H MAS experiments ($\nu_r = 30$ kHz), the frictional heating of the rotor can strongly affect the temperature of the sample.⁶⁸ Therefore, ^2H MAS experiments were carried out at both room temperature and under cooling with nitrogen gas purging. The ^2H MAS spectra of ZnAtzOx loaded with 8% D_2O (Figure 6.8) displays at least 6 different signals, with chemical shift ranging from 3.5 to 1.0 ppm. For the 8% loaded sample, at least five sites are present in the same region. We can tentatively attribute the signal at around -3 ppm to the ND_2 species. The other signals are tentatively attributed to the D_2O adsorbed in the MOF.

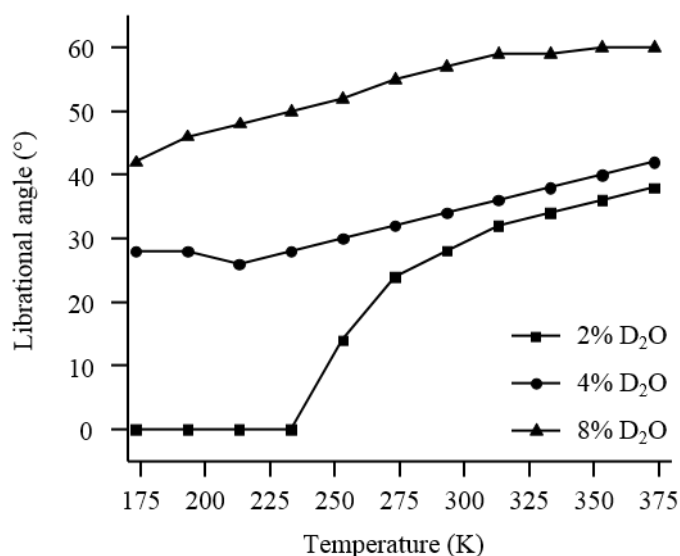


Figure 6.7. Dependence of librational angle on the temperature for D_2O -loaded ZnAtzOx .

The presence of several signals suggests that the water molecules are dispersed in the pores instead of interacting strongly with the framework. It is noteworthy to mention that the ^2H MAS spectra without cooling looks distinctively different. As mentioned previously, this is because the frictional heating of the rotor can strongly affect the

temperature of the sample. Nevertheless, these results indicate that the water molecules are rather distributed in the pores instead of localized. The simulated ^2H static pattern using the signals with different chemical shifts (Figure 6.8) matches with that obtained experimentally, corroborating the ^2H MAS results.

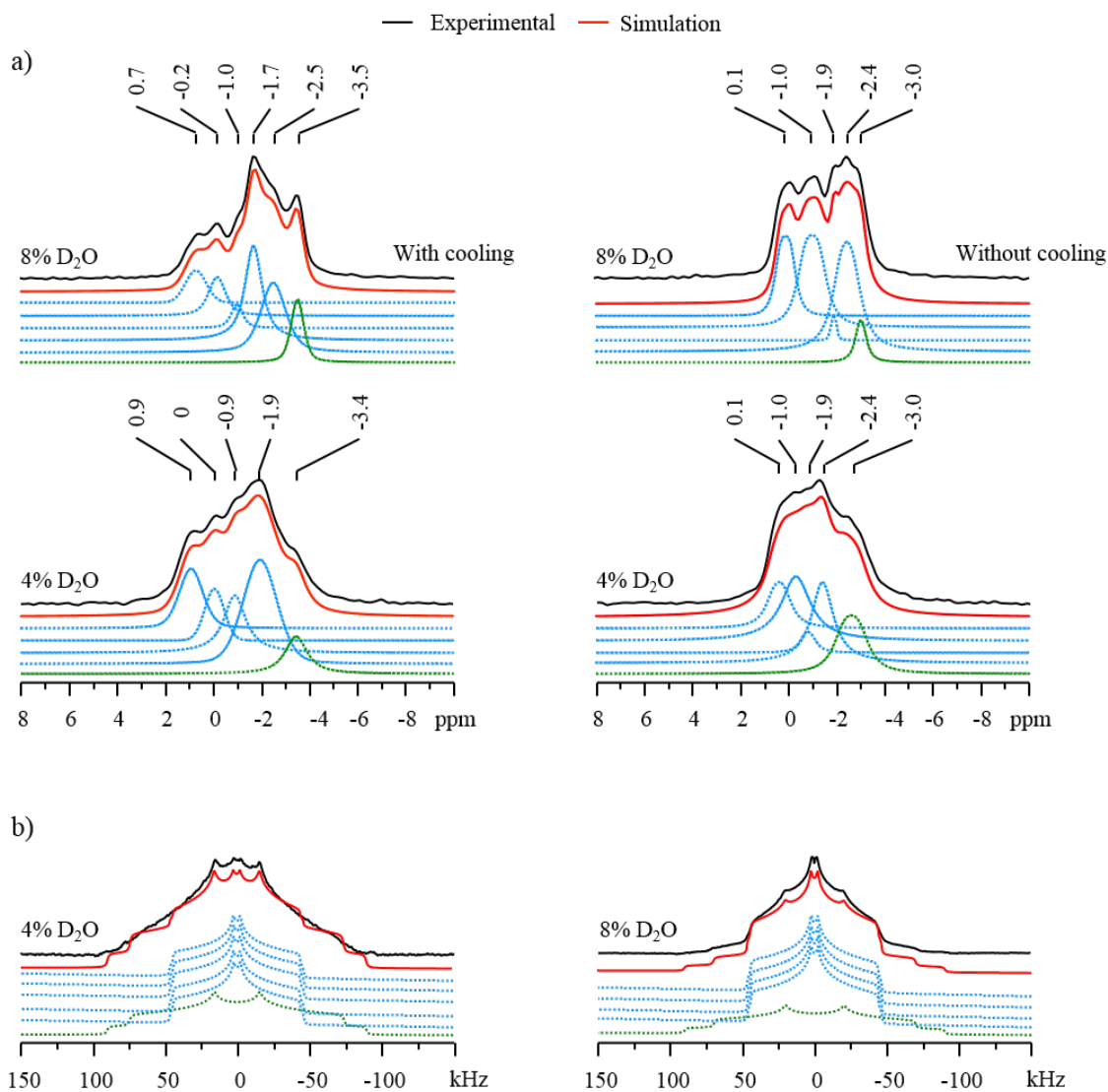


Figure 6.8. a) ^2H MAS spectra of ZnAtzOx loaded with 4 and 8% D_2O acquired at 21.1 T with a spinning rate of 30 kHz; b) Experimental and simulated ^2H static VT NMR spectra of D_2O -loaded ZnAtzOx.

The adsorption of water molecules around the metal centers of MOFs can often lead to change in polarization of the electronic structure, which can trigger the distortion of the molecular structure and eventually contribute to the destabilization of the material or even change in the CO₂ adsorption capacity of the material.¹²

Water may also coordinate to metal centers and eventually insert into the metal-ligand bond. Furthermore, water can dissociate into OH⁻ and H⁺ fragments that can attach to the metal center and/or the linker, respectively. Both the water insertion and the water dissociation reactions can cause the metal-ligand bonds to weaken, which may lead to the collapse of the MOF framework.^{12,53,54} Therefore, it is important to understand the effect of the water on the metal environment of the metal centers in the framework.

Herein, we decided to investigate the local environment around the Zn centers in ZnAtzOx via the changes in the ⁶⁷Zn SSNMR spectra associated with the effect of water. The only NMR-active isotope of zinc is ⁶⁷Zn (I = 5/2) which is a quadrupolar nucleus. The quadrupolar nature makes the acquisition of high-quality SSNMR spectra challenging because of its quadrupole moment (150 mb), low gyromagnetic ratio (1.68 rad·T⁻¹·s⁻¹, 6.3% of the ¹H value), and low natural abundance (4.1%).⁶⁹⁻⁷¹ Consequently, only a few ⁶⁷Zn NMR spectroscopic studies have been reported on MOFs.⁷²⁻⁷⁴ The 1D ⁶⁷Zn static spectra of the activated ZnAtzOx and D₂O-loaded (8%) ZnAtzOx are depicted in Figure 6.9. The spectrum of the activated sample displays a broad resonance (≈ 40 kHz). The spectrum can be well fitted with two Zn sites and the simulations generated a set of ⁶⁷Zn EFG tensor parameters for each site.

For Zn(1), the δ_{iso} , C_Q and η_Q are 170 ppm, 5.0 MHz, and 0.85, respectively. For Zn(2), the δ_{iso} , C_Q and η_Q are, respectively, 170 ppm, 5.2 MHz, and 0.45, respectively. This is in good agreement with the crystal structure, which displays two crystallographic non-equivalent Zn sites.¹⁵ Furthermore, the C_Q and η_Q values from experimental spectra are similar to those found in the literature for penta-coordinated zinc.⁷⁵

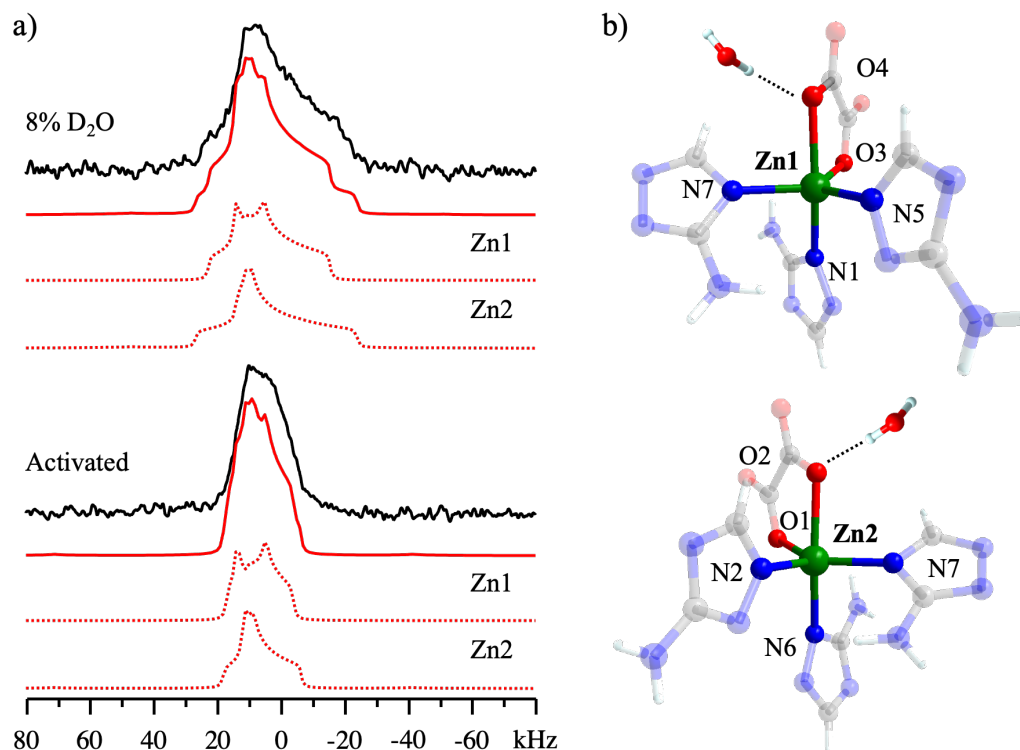


Figure 6.9. a) Experimental and simulated ^{67}Zn static spectra of activated and D_2O -loaded (8%) ZnAtzOx ; b) Illustration of the coordination environment around the zinc centers in the crystal structure of ZnAtzOx .

Upon water adsorption, the 1D ^{67}Zn static spectrum displays a broader signal with larger values of C_Q . For Site 1, C_Q increases from 5.0 to 6.5 MHz and η_Q decreases from 0.85 to 0.75. For Site 2, C_Q increases from 5.2 to 7.0 MHz and η_Q increases from 0.45 to 0.95. The larger value of C_Q indicates that the local Zn environments in the activated sample are significantly distorted upon adsorption of water.

These results suggest that the adsorption of water leads to the changes in the Zn coordination environment and that the variations in the observed ^{67}Zn spectra are due to the distributions of guest molecules. 1D ^{67}Zn static experiments were also carried out for the as-made sample and the spectrum is depicted in Figure A6.10. Unsurprisingly, the spectrum is very similar to that of the activated sample D_2O loaded sample because the

as-made MOF contains water molecules (8% w/w H₂O) in the pores of the MOF based on our results and on the crystal structure reported in the literature,¹⁵ it is possible to tentatively model the behavior of D₂O inside of the pores of ZnAtzOx. In the crystal structure, there are two non-equivalent crystallographic water sites, as depicted in Figure 6.10.

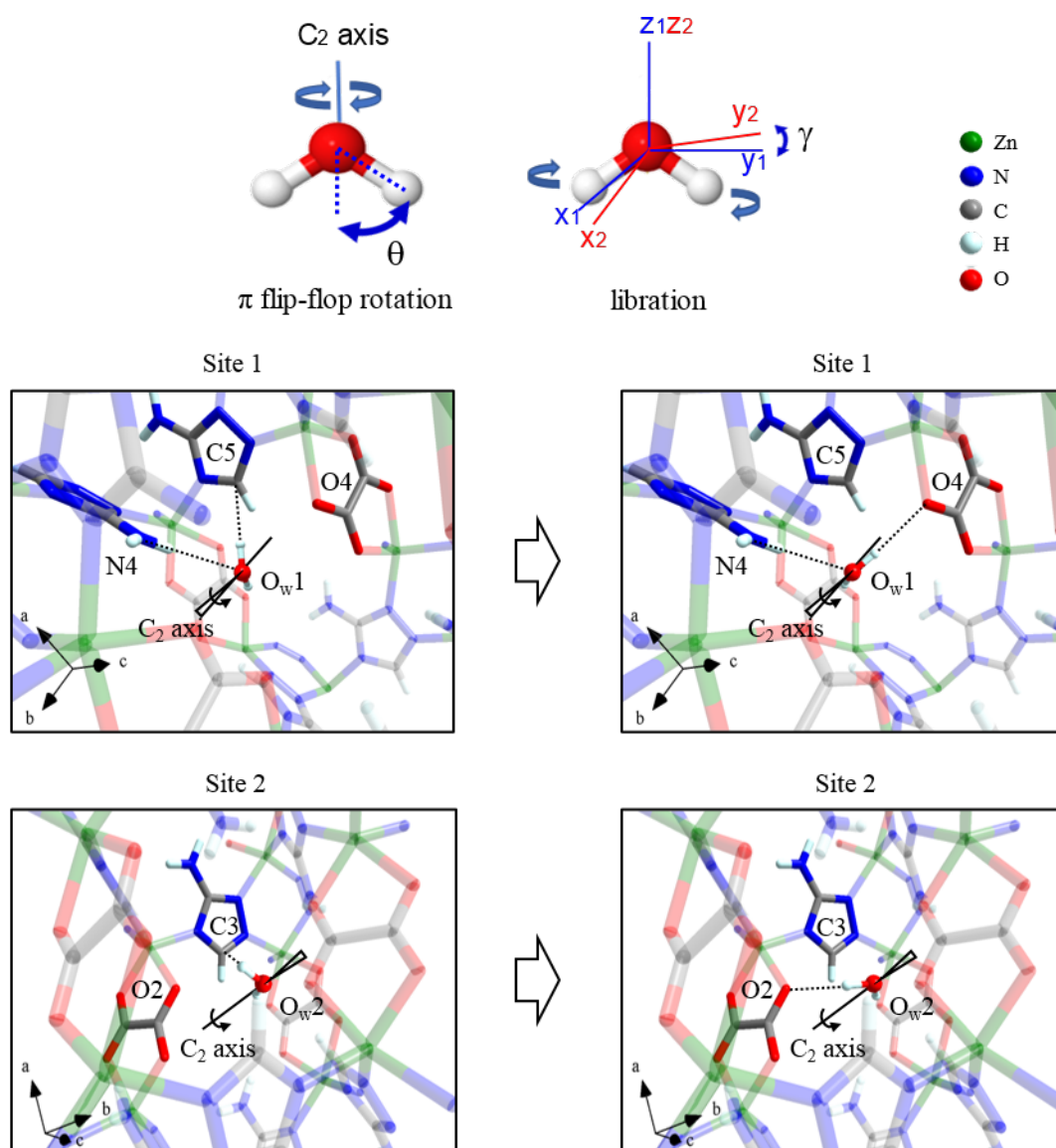


Figure 6.10. Representation of the π -flips and librational motion of D₂O groups inside of the framework of ZnAtzOx for two crystallographic non-equivalent water sites.

In Site 1, the water molecules interact with the nitrogen, N4, in the amino group, the CH group (C5), and the oxygen, O4, from the oxalate ligand. The distances are as follows: $O_{w1} \cdots N4$, 3.04 Å; $O_{w1} \cdots O4$, 3.04 Å; and $O_{w1} \cdots C5$, 3.24 Å. In contrast, the water molecules in Site 2 interact only with the CH groups, C3, and the oxalate ligand, O2. The $O_{w2} \cdots C3$ and $O_{w2} \cdots O2$ distances are, respectively, 3.33 and 3.02 Å.

The librational angle obtained is consistent with the geometry of the pore structure. The water can partially rotate to interact with the oxalate and the CH groups, with an angle of about 60°. For comparison, the spectral analysis indicated a maximum libration angle of 60° for the ZnAtzOx loaded with 8% of D₂O at 373 K. Furthermore, the relatively small C_Q indicated that the water is relatively mobile inside of the framework.

Behavior of CO₂ adsorbed in ZnAtzOx under humid conditions

To understand the possible effects of water on the adsorption of CO₂, we performed ¹³C static experiments on a series of ZnAtzOx loaded with varied concentrations of D₂O and ¹³CO₂ (Figure 6.11). The complete set of ¹³C VT spectra are shown in Figure A6.11 and Figure A6.12, and the parameters are listed on Table A6.7 to Table A6-10.

The ²H static spectra of the co-loaded samples are depicted in Figure A6.13 Figure A6.14. At a low loading level of 0.1 and 0.2 equivalent of CO₂ and 4% of D₂O, the spectra are very similar to those observed for the pure CO₂. The concentration of water seems to have a small effect on the dynamics of carbon dioxide, suggesting very little interaction between CO₂ and D₂O. This is reasonable given that the framework can accommodate all guest species. When the concentration of water is increased to 8%, all CO₂ is still adsorbed, even if all pores are “saturated” with water. Interestingly, at a concentration of 0.2 equivalent of CO₂ and 8% of D₂O, the CO₂ molecules seem to be totally adsorbed inside the framework at Site 1. This might suggest that the CO₂ molecules adsorb preferentially at the amino group. At high loading levels of pure CO₂, the molecules can occupy Site 1 (near the amino groups) and Site 2 (near the Ox oxygens), and some CO₂ molecules adsorbed on the surface or has been converted into carbamate.

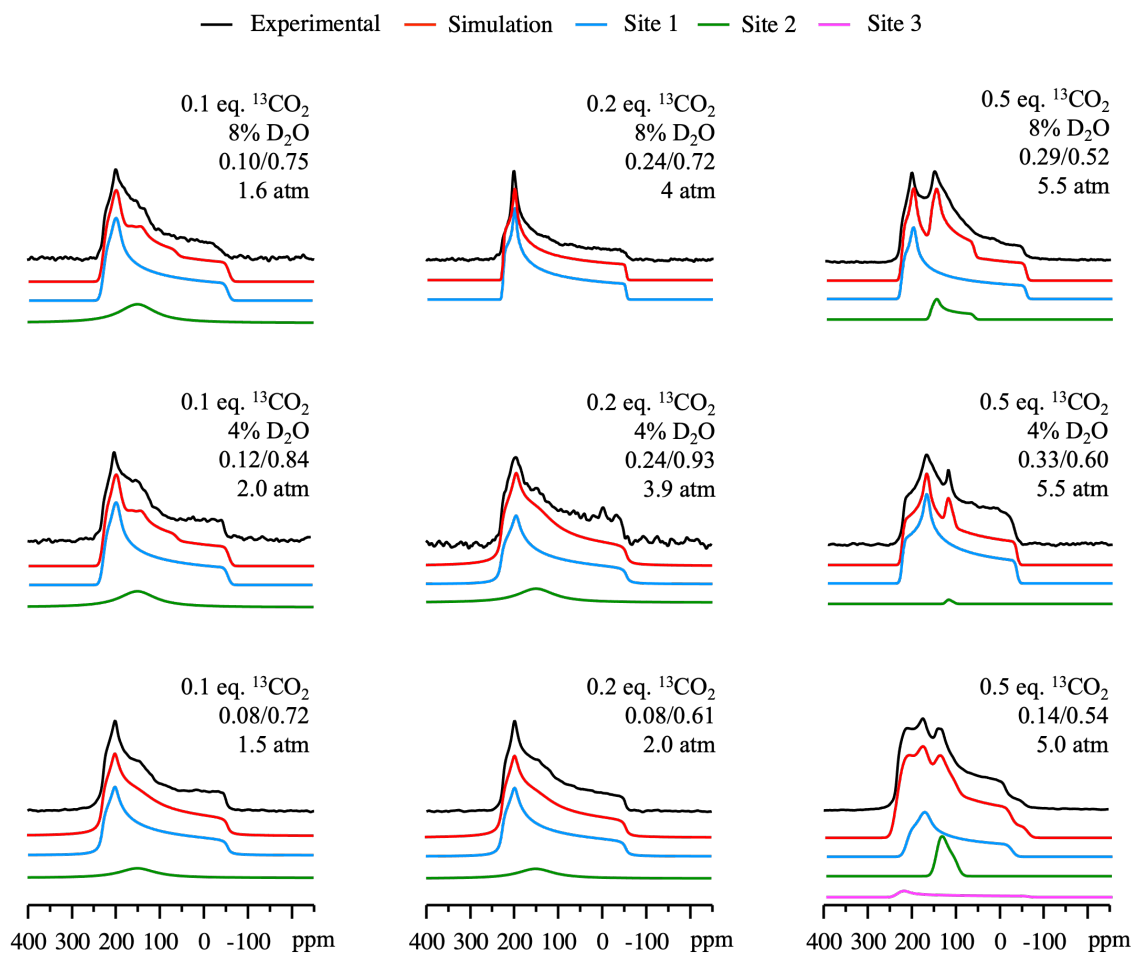


Figure 6.11. Experimental and simulated static ^{13}C NMR spectra of ZnAtzOx loaded with different concentrations of $^{13}\text{CO}_2$ and D_2O at 298 K.

In contrast, the sample loaded with 4% of water only displays one ^{13}C CO_2 signal (Site 1), Figure 6.11. This suggests that the water is somehow limiting the location of the CO_2 molecules to Site 1, next to the amino groups, while it occupies the site next to the CH groups. When the D_2O concentration is increased to 8%, one site is also observed in the spectra.

This suggests that when the concentration of D₂O is high, the water molecules occupy Site 2 while forcing all CO₂ to be adsorbed around the amino groups in the framework (at Site 1).

Based on the above, the following observations can be made, and a tentative model is depicted in (Figure 6.12):

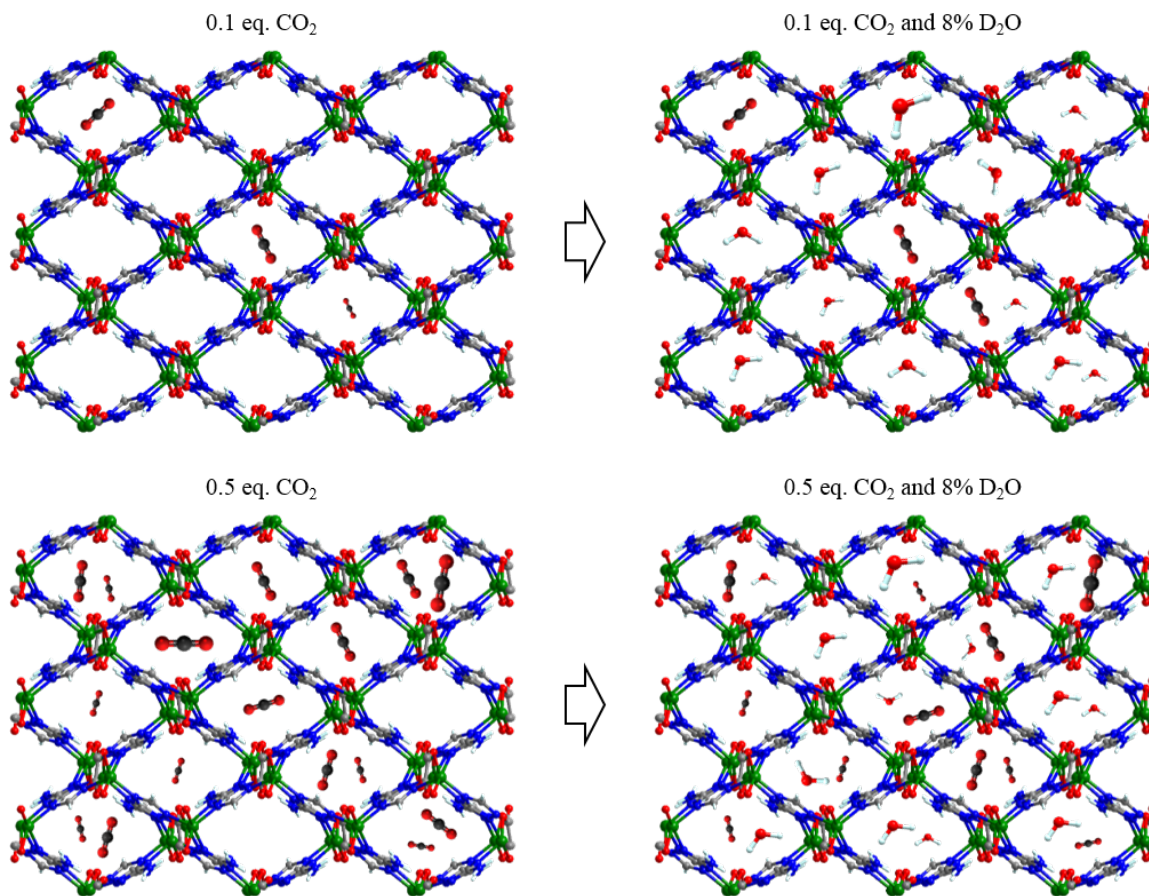


Figure 6.12. Representation of behavior of CO₂ and water inside of the pores of ZnAtzOx.

- (i) Even at the highest concentration of D₂O and CO₂, all the CO₂ molecules were still adsorbed (as suggested by the relatively large span of the sites. This leads to the suggestion that the adsorption capacity of ZnAtzOx under humid conditions is not drastically affected at this loading.

- (ii) The presence of several sites in the framework suggests that both water and CO₂ are rather randomly distributed inside of the pores instead of localized in specific locations in the framework.

- (iii) The dynamics of the CO₂ molecules inside of the framework are not affected to an observable extent by the presence of water. The wobbling and hopping angles under humid conditions is similar to those found under dry conditions.

6.4 Conclusions

Herein, we have used multinuclear SSNMR experiments to probe the CO₂ motional behavior and guest-host interactions in the ultramicroporous ZnAtzOx MOF. Static ¹³C SSNMR experiments and simulations revealed that the adsorbed CO₂ molecules undergo hopping and wobbling motions. ¹H-¹³C CP/MAS and 2D ¹H-¹³C HETCOR SSNMR were used to probe the host-guest interactions and to furnish information regarding the location of the CO₂ molecules in the pores. Our results suggests that the CO₂ molecules can occupy two sites in the framework, being one interacting with the amino groups and the other one interacting with the CH groups of the triazole ligands. ²H static SSNMR experiments were carried out to investigate the dynamics of water molecules by probing D₂O. Our results shows that the adsorbed water molecules undergo a 180 flip-flop and libration motions and are located in the pores interacting with the oxalate ligands. Additional ⁶⁷Zn SSNMR experiments revealed insight into the changes in Zn nuclei symmetry upon adsorption of water in the framework, activation. We have found an increase in the C_Q value for the Zn(1) site and a decreasing C_Q value for the Zn(2) site after activation of the as made structure. Finally, we have shown that the behavior of CO₂ in MOFs under humid conditions can be studied via SSNMR spectroscopy. Experiments using different concentrations of both water and CO₂ were carried out. Interestingly, our results suggest that the ZnAtzOx MOF can probably be a good candidate for CO₂ removal in humid conditions. Specifically, we have found that the CO₂ and D₂O

molecules can be co-adsorbed in the framework. The CO₂ molecules interact with the amino groups of the framework while the water molecules interact with the CH groups.

6.5 References

- (1) Masson-Delmotte, V.; Zhai, P.; Pirani, A.; Connors, S. L.; Péan, C.; Berger, S.; Caud, N.; Chen, Y.; Goldfarb, L.; Gomis, M. I.; Huang, M.; Leitzell, K.; Lonnoy, E.; Matthews, J. B. R.; Maycock, T. K.; Waterfield, T.; Yelekçi, O.; Yu, R.; Zhou, B. IPCC, 2021: Climate Change 2021: The Physical Science Basis. Contribution of Working Group I to the Sixth Assessment Report of the Intergovernmental Panel on Climate Change.
- (2) Osman, A. I.; Hefny, M.; Abdel Maksoud, M. I. A.; Elgarahy, A. M.; Rooney, D. W. *Environ. Chem. Lett.* **2020**, 19, 797.
- (3) Liu, Y.; Wang, Z. U.; Zhou, H.-C. *Greenh. Gases Sci. Technol.* **2012**, 2, 239.
- (4) Li, J. R.; Ma, Y.; McCarthy, M. C.; Sculley, J.; Yu, J.; Jeong, H. K.; Balbuena, P. B.; Zhou, H.-C. *Coord. Chem. Rev.* **2011**, 255, 1791.
- (5) Zhou, H.-C.; Long, J. R.; Yaghi, O. M. *Chem. Soc. Rev.* **2012**, 112, 673.
- (6) Li, P.; Chen, J.; Zhang, J.; Wang, X. *Sep. Purif. Rev.* **2015**, 44, 19.
- (7) Furukawa, H.; Gándara, F.; Zhang, Y. B.; Jiang, J.; Queen, W. L.; Hudson, M. R.; Yaghi, O. M. *J. Am. Chem. Soc.* **2014**, 136, 4369.
- (8) Canivet, J.; Fateeva, A.; Guo, Y.; Coasne, B.; Farrusseng, D. *Chem. Soc. Rev.* **2014**, 43, 5594.
- (9) Soubeyrand-Lenoir, E.; Vagner, C.; Yoon, J. W.; Bazin, P.; Ragon, F.; Hwang, Y. K.; Serre, C.; Chang, J.-S.; Llewellyn, P. L. *J. Am. Chem. Soc.* **2012**, 134, 10174.
- (10) Yazaydın, A. Ö.; Benin, A. I.; Faheem, S. A.; Jakubczak, P.; Low, J. J.; Willis, R. R.; Snurr, R. Q. *Chem. Mater.* **2009**, 21, 1425.

- (11) Chen, Y. F.; Babarao, R.; Sandler, S. I.; Jiang, J. W. *Langmuir* **2010**, 26, 8743.
- (12) Kolle, J. M.; Fayaz, M.; Sayari, A. *Chem. Rev.* **2021**, 121, 7280.
- (13) Bertmer, M. *Annu. Reports NMR Spectrosc.* **2020**, 101, 1.
- (14) Witherspoon, V. J.; Xu, J.; Reimer, J. A. *Chem. Rev.* **2018**, 118, 10033.
- (15) Banerjee, A. M.; Nandi, S.; Nasa, P.; Vaidhyanathan, R. *Chem. Commun.* **2016**, 52, 1851.
- (16) Cory, D. G.; Ritchey, W. M. *J. Magn. Reson.* **1988**, 80, 128.
- (17) Fulmer, G. R.; Miller, A. J. M.; Sherden, N. H.; Gottlieb, H. E.; Nudelman, A.; Stoltz, B. M.; Bercaw, J. E.; Goldberg, K. I. *Organometallics* **2010**, 29, 2176.
- (18) Pines, A.; Gibby, M. G.; Waugh, J. S. *J. Chem. Phys.* **1972**, 56, 1776.
- (19) Bielecki, A.; Kolbert, A. C.; Levitt, M. H. *Chem. Phys. Lett.* **1989**, 155, 341.
- (20) Antonijevic, S.; Wimperis, S. *J. Magn. Reson.* **2003**, 164, 343.
- (21) Eichele, K.; Wasylishen, R. E. *WSolids1: Solid-State NMR Spectrum Simulation Package*. Universität Tübingen: Tübingen 2009.
- (22) Vold, R. L.; Hoatson, G. L. *J. Magn. Reson.* **2009**, 198, 57.
- (23) Beeler, A. J.; Orendt, A. M.; Grant, D. M.; Cutts, P. W.; Michl, J.; Zilm, K. W.; Downing, J. W.; Facelli, J. C.; Schindler, M. S.; Kutzelnigg, W. *Chem. Informationsd.* **1985**, 16, 15.
- (24) Stepanov, A. G.; Shegai, T. O.; Luzgin, M. V.; Essayem, N.; Jovic, H. *J. Phys. Chem. B*, **2003**, 107, 12438.
- (25) Long, J. R.; Ebelhäuser, R.; Griffin, R. G. *J. Phys. Chem. A*, **2002**, 101, 988.
- (26) Younas, M.; Rezakazemi, M.; Daud, M.; Wazir, M. B.; Ahmad, S.; Ullah, N.;

- Inamuddin; Ramakrishna, S. *Prog. Energy Combust. Sci.* **2020**, 80.
- (27) Li, H.; Wang, K.; Sun, Y.; Lollar, C. T.; Li, J.; Zhou, H.-C. *Mater. Today* **2018**, 21, 108.
- (28) Yu, J.; Xie, L. H.; Li, J. R.; Ma, Y.; Seminario, J. M.; Balbuena, P. B. *Chem. Rev.* **2017**, 117, 9674.
- (29) Fu, Y.; Guan, H.; Yin, J.; Kong, X. *Coord. Chem. Rev.* **2021**, 427, 213563.
- (30) Brunner, E.; Rauche, M. *Chem. Sci.* **2020**, 11, 4297.
- (31) Wong, Y. T. A.; Martins, V.; Lucier, B. E. G.; Huang, Y. *Chem. Eur. J.* **2019**, 25, 1848.
- (32) Levitt, M. H. *Spin Dynamics: Basics of Nuclear Magnetic Resonance*, 2nd Ed. John Wiley and Sons, **2009**.
- (33) Melix, P.; Heine, T. *ChemPhysChem.* **2021**, 22, 2336.
- (34) Zhang, Y.; Lucier, B. E. G.; McKenzie, S. M.; Arhangelskis, M.; Morris, A. J.; Frišćić, T.; Reid, J. W.; Terskikh, V. V.; Chen, M.; Huang, Y. *ACS Appl. Mater. Interfaces*, **2018**, 10, 28582.
- (35) Peksa, M.; Burrekaew, S.; Schmid, R.; Lang, J.; Stallmach, F. *Microporous Mesoporous Mater.* **2015**, 216, 75.
- (36) Kong, X.; Scott, E.; Ding, W.; Mason, J. A.; Long, J. R.; Reimer, J. A. *J. Am. Chem. Soc.* **2012**, 134, 14341.
- (37) Lin, L.-C.; Kim, J.; Kong, X.; Scott, E.; McDonald, T. M.; Long, J. R.; Reimer, J. A.; Smit, B. *Angew. Chemie Int. Ed.* **2013**, 52, 4410.
- (38) Wang, W.; Waang, W. D.; Lucier, B. E. G.; Terskikh, V. V.; Huang, Y. *J. Phys. Chem. Lett.* **2014**, 5, 3360.
- (39) Zhang, Y.; Lucier, B. E. G. G.; Huang, Y. *Phys. Chem. Chem. Phys.* **2016**, 18,

8327.

- (40) Lu, Y.; Lucier, B. E. G.; Zhang, Y.; Ren, P.; Zheng, A.; Huang, Y. *Phys. Chem. Chem. Phys.* **2017**, *19*, 6130.
- (41) Marti, R. M.; Howe, J. D.; Morelock, C. R.; Conradi, M. S.; Walton, K. S.; Sholl, D. S.; Hayes, S. E. *J. Phys. Chem. C*, **2017**, *121*, 25778.
- (42) Forse, A. C.; Gonzalez, M. I.; Siegelman, R. L.; Witherspoon, V. J.; Jawahery, S.; Mercado, R.; Milner, P. J.; Martell, J. D.; Smit, B.; Blümich, B.; Long, J. R.; Reimer, J. A. *J. Am. Chem. Soc.* **2018**, *140*, 1663.
- (43) Bon, V.; Pallmann, J.; Eisbein, E.; Hoffmann, H. C.; Senkovska, I.; Schwedler, I.; Schneemann, A.; Henke, S.; Wallacher, D.; Fischer, R. A.; Seifert, G.; Brunner, E.; Kaskel, S. *Microporous Mesoporous Mater.* **2015**, *216*, 64.
- (44) Gul-E-Noor, F.; Michel, D.; Krautscheid, H.; Haase, J.; Bertmer, M. *J. Chem. Phys.* **2013**, *139*, 034202.
- (45) Peksa, M.; Lang, J.; Stallmach, F. *Microporous Mesoporous Mater.* **2015**, *205*, 11.
- (46) Wu, B.; Wong, Y. T. A.; Lucier, B. E. G.; Boyle, P. D.; Huang, Y. *ACS Omega* **2019**, *4*, 4000.
- (47) Desveaux, B. E.; Wong, Y. T. A.; Lucier, B. E. G.; Terskikh, V. V.; Boyle, P. D.; Jiang, S.; Huang, Y. *J. Phys. Chem. C*, **2019**, *123*, 17798.
- (48) Laws, D. D.; Bitter, H.; Jerschow, L. *Angew. Chem. Int. Ed. Engl.* **2002**, *41*, 3096.
- (49) Desveaux, B. *Adsorbed Gas Behaviour and Guest-Host Interactions in Ultramicroporous Metal-Organic Frameworks.* **2018**.
- (50) Milner, P. J.; Siegelman, R. L.; Forse, A. C.; Gonzalez, M. I.; Runčevski, T.; Martell, J. D.; Reimer, J. A.; Long, J. R. *J. Am. Chem. Soc.* **2017**, *139*, 13541.
- (51) Forse, A. C.; Milner, P. J.; Lee, J. H.; Redfean, H. N.; Oktawiec, J.; Siegelman, R.

- L.; Martell, J. D.; Dinakar, B.; Porter-Zasada, L. B.; Gonzalez, M. I.; Neaton, J. B.; Long, J. R.; Reimer, J. A. *J. Am. Chem. Soc.* **2018**, 140, 18016.
- (52) Vaidhyanathan, R.; Iremonger, S. S.; Dawson, K. W.; Shimizu, G. K. H. *Chem. Commun.* **2009**, 35, 5230.
- (53) Kalmutzki, M. J.; Diercks, C. S.; Yaghi, O. M. *Adv. Mater.* **2018**, 30, 1.
- (54) Liu, X.; Wang, X.; Kapteijn, F. *Chem. Rev.* **2020**, 120, 8303.
- (55) Chanut, N.; Bourrelly, S.; Kuchta, B.; Serre, C.; Chang, J.-S.; Wright, P. A.; Llewellyn, P. L. *ChemSusChem* **2017**, 10, 1543.
- (56) Burtch, N. C.; Jasuja, H.; Walton, K. S. *Chem. Rev.* **2014**, 114, 10575.
- (57) Liu, B.; Vikrant, K.; Kim, K.-H.; Kumar, V.; Kailasa, S. K. *Environ. Sci. Nano* **2020**, 7, 1319.
- (58) Chanut, N.; Bourrelly, S.; Kuchta, B.; Serre, C.; Chang, J.-S.; Wright, P. A.; Llewellyn, P. L. *ChemSusChem*, **2017**, 10, 1543.
- (59) Birsa Čelič, T.; Mazaj, M.; Guillou, N.; Elkaïm, E.; El Roz, M.; Thibault-Starzyk, F.; Mali, G.; Rangus, M.; Čendak, T.; Kaučič, V.; Zabukovec Logar, N. *J. Phys. Chem. C*, **2013**, 117, 14608.
- (60) Gul-E-Noor, F.; Jee, B.; Pöppel, A.; Hartmann, M.; Himsl, D.; Bertmer, M. *Phys. Chem. Chem. Phys.* **2011**, 13, 7783.
- (61) Gul-E-Noor, F.; Michel, D.; Krautscheid, H.; Haase, J.; Bertmer, M. *Microporous Mesoporous Mater.* **2013**, 180, 8.
- (62) E. Khudozhitkov, A.; S. Arzumanov, S.; V. Toktarev, A.; V. Cherepanova, S.; A. Gabrienko, A.; I. Kolokolov, D.; G. Stepanov, A. *Phys. Chem. Chem. Phys.* **2021**, 23, 18925.
- (63) Khudozhitkov, A. E.; Kolokolov, D. I.; Stepanov, A. G. *J. Phys. Chem. C*, **2018**,

- 122, 12956.
- (64) Kolokolov, D. I.; Glaznev, I. S.; Aristov, Y. I.; Stepanov, A. G.; Jovic, H. J. *Phys. Chem. C*, **2008**, 112, 12853.
- (65) Tong, Y.; Kampfrath, T.; Campen, R. K. *Phys. Chem. Chem. Phys.* **2016**, 18, 18424.
- (66) Gonzalez-Nelson, A.; Coudert, F.-X.; Veen, M. A. van der. *Nanomater.* **2019**, 9, 330.
- (67) Keeler, E. G.; Michaelis, V. K.; Griffin, R. G. J. *Phys. Chem. B*, **2016**, 120, 7851.
- (68) Thurber, K. R.; Tycko, R. J. *Magn. Reson.* **2009**, 196, 84.
- (69) Wu, G. *Chem. Phys. Lett.* **1998**, 298, 375.
- (70) Smith, M. E. *Magn. Reson. Chem.* **2021**, 59, 864.
- (71) Leroy, C.; Bryce, D. L. *Prog. Nucl. Magn. Reson. Spectrosc.* **2018**, 109, 160.
- (72) Madsen, R. S. K.; Qiao, A.; Sen, J.; Hung, I.; Chen, K.; Gan, Z.; Sen, S.; Yue, Y. *Science*, **2020**, 367, 1473.
- (73) Sutrisno, A.; Terskikh, V. V.; Shi, Q.; Song, Z.; Dong, J.; Ding, S. Y.; Wang, W.; Provost, B. R.; Daff, T. D.; Woo, T. K.; Huang, Y. *Chem. Eur. J.* **2012**, 18, 12251.
- (74) He, P.; Lucier, B. E. G.; Terskikh, V. V.; Shi, Q.; Dong, J.; Chu, Y.; Zheng, A.; Sutrisno, A.; Huang, Y. J. *Phys. Chem. C*, **2014**, 118, 23728.
- (75) Huang, Y.; Sutrisno, A. *Annu. Reports NMR Spectrosc.* **2014**, 81, 1.

Chapter 7

7 Summary, perspectives, and future work

7.1 Summary

In the last three decades, metal-organic frameworks and related materials have attracted enormous attention of the scientific community owing to their tunable porosity and physicochemical properties. Furthermore, MOFs are promising materials for several applications such as, carbon capture and utilization, gas separation, catalysis, and water harvesting. To realize the full potential of MOFs in such applications, a deep understanding of MOF structure and the interactions between guest species and framework is crucial. In this thesis, multinuclear SSNMR spectroscopy was employed along with other techniques to characterize the structure of MOFs and their properties including framework flexibility, effect of activation on framework structure, host-guest interaction, and the behavior of guests inside of the pores. Specifically, it was demonstrated that (i) ^{17}O SSNMR spectra of MOFs acquired at ultra-high magnetic field of 35.2 T provide ultra-high resolution, leading to ultra-fine structural information; (ii) ^{17}O SSNMR is a viable complementary technique to XRD that provides important information on phase transition; (iii) ^{17}O SSNMR is an excellent method for investigating ion-exchanged MOFs and can be used to estimate the degree of exchange. (iv) ^{17}O SSNMR is particularly sensitive to hydrogen bonding interaction in MOF systems. (v) multinuclear SSNMR spectroscopy can be used to successfully probe the adsorptive and dynamic behavior of guest species in MOFs, specifically, the co-adsorption of water and carbon dioxide.

In Chapters 1 and 2, the fundamentals about MOFs and SSNMR spectroscopy are described. In Chapter 1, the most recent definitions and terminologies of MOFs were described, along with the most commonly used synthetic approaches and characterization methods including SSNMR. In Chapter 2, the physical background and the NMR spectroscopic methods used in the characterizations are described.

Chapter 3 describes an advance in ^{17}O SSNMR spectroscopy. The very high resolution achieved in 3QMAS spectra at an ultra-high magnetic field of 35.2 T enabled the observation of subtle changes in ^{17}O SSNMR spectra of as-made and activated α - $\text{Mg}_3(\text{HCOO})_6$ phases, providing crucial information on the effect of activation on MOF structure, revealing the weak site-specific interaction between DMF guests and the MOF framework such as hydrogen bonding and van der Waals forces. The advantage of performing ^{17}O SSNMR experiments at 35.2 T for MOF characterization is further illustrated by the activation of MIL-53(Al). The partially and fully activated phases of MIL-53(Al) can be unambiguously distinguished. This chapter illustrates that a wide variety of organic and inorganic compounds are now viable targets for ^{17}O SSNMR at an ultrahigh magnetic field of 35.2 T. The sensitivity and resolution afforded at this field strength greatly extend the volume and quality of structural and chemical information available from ^{17}O SSNMR spectroscopy, as much of these data are unavailable at or lower magnetic fields.

Furthermore, we have shown in Chapter 4 that the high ^{17}O spectral resolution and sensitivity achieved at 35.2 T allows the resolution of all inequivalent $-\text{COO}^-$ oxygen sites in three MIL-53(Al) phases, validating the crystal structures of MIL-53(Al) originally determined by powder XRD data. Additionally, fine information on both MOF flexibility and host-guest interaction in MIL-53 systems were obtained from ^{17}O NMR spectra at 35.2 T.

In Chapter 5, we further demonstrate how ^{17}O SSNMR has allowed us to characterize the oxygen local environments in activated and ion-exchanged MIL-121 MOFs. The 1D MAS ^{17}O SSNMR spectra acquired at 19.6, 21.1, and the ultrahigh 35.2 T magnetic fields displayed spectral differences upon activation and metal-exchange of the material. Chemically and crystallographically inequivalent oxygen sites were largely resolved, allowing spectral assignment of the resonances. The assignments were further confirmed via $^1\text{H} \rightarrow ^{17}\text{O}$ HETCOR, and $^{17}\text{O} \{^1\text{H}\}$ REDOR experiments. In addition to confirming the signal assignments, these experiments also provided important information regarding the hydrogen bonding interactions in the framework. Metal ion-exchange process was also studied via ^{17}O SSNMR and the degree of ion-exchange can also be estimated from ^{17}O

NMR and the results are consistent with those from ICP measurements. Our results suggested Na^+ ions interact with the hydroxyl groups from the MIL-121 framework, and Ag^+ cations interact with the hydrogens from both the free carboxylic acid and hydroxyl group from the framework.

In Chapter 6, we demonstrated that multinuclear SSNMR spectroscopy can be used to investigate the co-adsorption of water and carbon dioxide in ultramicroporous MOF ZnAtzOx. The dynamics of pure water and CO_2 were first investigated via static ^{13}C and ^2H SSNMR experiments. It was found that the CO_2 molecules undergo a combination of wobbling and hopping motions inside of the pores of the framework. The water molecules undergo π -flip motions alongside with librational dynamics. The effect of concentration of guest was studied. 2D ^1H - ^{13}C HTECOR technique was employed to shed light on the adsorption sites and host-guest interaction. Our results show that the co-adsorption effects of water and CO_2 in MOFs can be well studied by SSNMR spectroscopy. It was shown that the adsorption behavior of the CO_2 adsorbed in the ZnAtzOx material is not drastically affected by humidity under our experimental conditions.

7.2 Perspectives

Chapters 3, 4, and 5 demonstrate that ^{17}O SSNMR spectroscopy is an excellent technique for the characterization of metal-organic frameworks. This work represents an advance on the characterization of MOF based materials. The importance of this work lies in the fact that oxygen plays a fundamental role in not only the structure of MOFs, but also the applications in adsorption, catalysis, and drug delivery. If employed with other techniques, ^{17}O SSNMR spectroscopy can provide crucial structural information that can be used to design novel MOF based materials with optimized capabilities for several technological applications.

In Chapter 6, we demonstrated that multinuclear SSNMR spectroscopy can be used to understand the effects of water on the adsorption of carbon dioxide of ZnAtzOx. To the best of our knowledge, this is the first time SSNMR spectroscopy has been employed to

study the co-adsorption of water and CO₂. This work is important because water can impact the structure and adsorption capacity of MOFs.

Furthermore, a detailed understanding of the effect that humidity has on the MOF adsorption capacity is still lacking. Consequently, new approaches and techniques that provide such information can further help develop the next generation of MOFs that can work under humid conditions without compromising of their properties.

7.3 Future work

In Chapters 3, 4, and 5, we have demonstrated the potential of ¹⁷O SSNMR spectroscopy in the characterization of MOFs. The high resolution achieved allowed us to better understand activation processes, phase transition, supramolecular interactions, host-guest interaction, among other characteristics of MOFs. For future work, it would be interesting to carry out a systematic investigation regarding the ¹⁷O enrichment of MOFs. A systematic understanding about the exchange process would allow a better control over the labelling of the oxygen sites in the framework. In chapter 5, we have shown that the ion-exchange in MOFs can be probed via ¹⁷O SSNMR, provided that the degree of enrichment is high enough. It would be interesting to increase the degree of metal-exchange in order to see a more accurate picture on the ¹⁷O spectral changes that took place upon metal-loading.

Furthermore, other applications of MOFs and other materials can be studied. Oxygen is vital for the chemistry of MOF and this is shown by their role in the formation of secondary building blocks which dictate the structure of the MOF. One interesting class of SBUs is the two-dimensional metal-oxide sheets that are pillared by organic ligands to form MOFs based on metals of the Group 1 of the periodic chart. MOFs based on Group 1 metals are relatively underexplored compared to MOFs based on transition metals. This is because that the structures of Group I MOFs are hard to predict. By probing the local environment of oxygen in these types of SBUs, it is possible to gain further insight into the chemistry of these materials.

Finally, in Chapter 7 we have shown that SSNMR spectroscopy can provide important information regarding the adsorption of CO₂ under humid conditions. It would be very important to apply the same approach used in the work to other materials in order to show that this methodology can indeed be applied to other systems. One interesting class of MOFs that are similar to ZnAtzOx are the ZnTzL series. The ZnTzL series are isorecticular MOFs composed of two-dimensional Zinc-Triazole sheet pillared by dicarboxylate ligands (L = fumarate, benzedicarboxylate, benzedicarboxylate). This MOFs is very similar to ZnAtzOx but without the amino groups. It is very stable under humid conditions. The fact that the ZnTzL series can be functionalized with several different groups is what attracts the attention.

Appendices

Copyright permissions

License Details

This Agreement between Mr. Vinicius Martins ("You") and Springer Nature ("Springer Nature") consists of your license details and the terms and conditions provided by Springer Nature and Copyright Clearance Center.

[Print](#) [Copy](#)

License Number	5218921236400
License date	Dec 30, 2021
Licensed Content Publisher	Springer Nature
Licensed Content Publication	Nature
Licensed Content Title	Reticular synthesis and the design of new materials
Licensed Content Author	Omar M. Yaghi et al
Licensed Content Date	Jun 12, 2003
Type of Use	Thesis/Dissertation
Requestor type	academic/university or research institute
Format	electronic
Portion	figures/tables/illustrations
Number of figures/tables/illustrations	1
High-res required	no
Will you be translating?	no
Circulation/distribution	1 - 29
Author of this Springer Nature content	no
Title	SSNMR of MOFs
Institution name	UWO
Expected presentation date	Jan 2022
Portions	Figure 1

This is an open access article published under an ACS AuthorChoice License, which permits copying and redistribution of the article or any adaptations for non-commercial purposes.



Cite This: *ACS Cent. Sci.* 2018, 4, 440–450

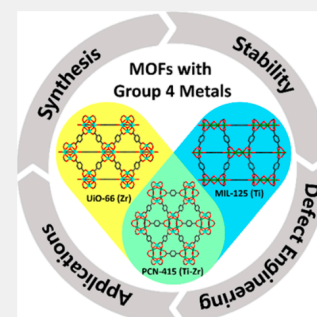
Stable Metal–Organic Frameworks with Group 4 Metals: Current Status and Trends

Shuai Yuan,[‡] Jun-Sheng Qin,[‡] Christina T. Lollar,[‡] and Hong-Cai Zhou^{*,‡,§,ID}

[‡]Department of Chemistry, Texas A&M University, College Station, Texas 77843-3255, United States

[§]Department of Materials Science and Engineering, Texas A&M University, College Station, Texas 77843-3003, United States

ABSTRACT: Group 4 metal-based metal–organic frameworks (M^{IV}-MOFs), including Ti-, Zr-, and Hf-based MOFs, are one of the most attractive classes of MOF materials owing to their superior chemical stability and structural tunability. Despite being a relatively new field, M^{IV}-MOFs have attracted significant research attention in the past few years, leading to exciting advances in syntheses and applications. In this outlook, we start with a brief overview of the history and current status of M^{IV}-MOFs, emphasizing the challenges encountered in their syntheses. The unique properties of M^{IV}-MOFs are discussed, including their high chemical stability and strong tolerance toward defects. Particular emphasis is placed on defect engineering in Zr-MOFs which offers additional routes to tailor their functions. Photocatalysis of M^{IV}-MOF is introduced as a representative example of their emerging applications. Finally, we conclude with the perspective of new opportunities in synthesis and defect engineering.



CCC | Marketplace™

This is a License Agreement between Vinicius Martins ("User") and Copyright Clearance Center, Inc. ("CCC") on behalf of the Rightsholder identified in the order details below. The license consists of the order details, the CCC Terms and Conditions below, and any Rightsholder Terms and Conditions which are included below. All payments must be made in full to CCC in accordance with the CCC Terms and Conditions below.

Order Date	11-Dec-2021	Type of Use	Republish in a thesis/dissertation
Order License ID	1167769-1	Publisher	ROYAL SOCIETY OF CHEMISTRY
ISSN	1463-9076	Portion	Image/photo/illustration

LICENSED CONTENT

Publication Title	Physical chemistry chemical physics : PCCP	Rightsholder	Royal Society of Chemistry
Article Title	H ₂ storage in isostructural UiO-67 and UiO-66 MOFs.	Publication Type	Journal
Author/Editor	Royal Society of Chemistry (Great Britain), Deutsche Bunsen-Gesellschaft für Physikalische Chemie., Koninklijke Nederlandse Chemische Vereniging., Società chimica italiana.	Start Page	1614
Date	01/01/1999	End Page	1626
Language	English	Issue	5
Country	United Kingdom of Great Britain and Northern Ireland	Volume	14

REQUEST DETAILS

Portion Type	Image/photo/illustration	Distribution	Canada
Number of images / photos / illustrations	1	Translation	Original language of publication
Format (select all that apply)	Print	Copies for the disabled?	No
Who will republish the content?	Academic institution	Minor editing privileges?	No
Duration of Use	Current edition and up to 5 years	Incidental promotional use?	No
Lifetime Unit Quantity	Up to 499	Currency	CAD

License Details

This Agreement between Mr. Vinicius Martins ("You") and John Wiley and Sons ("John Wiley and Sons") consists of your license details and the terms and conditions provided by John Wiley and Sons and Copyright Clearance Center.

[Print](#)[Copy](#)

License Number	5206171393675
License date	Dec 11, 2021
Licensed Content Publisher	John Wiley and Sons
Licensed Content Publication	Angewandte Chemie International Edition
Licensed Content Title	Rapid Guest Exchange and Ultra-Low Surface Tension Solvents Optimize Metal–Organic Framework Activation
Licensed Content Author	Adam J. Matzger, Antek G. Wong-Foy, Andre P. Kalenak, et al
Licensed Content Date	Oct 20, 2017
Licensed Content Volume	56
Licensed Content Issue	46
Licensed Content Pages	4
Type of Use	Dissertation/Thesis
Requestor type	University/Academic
Format	Print
Portion	Figure/table
Number of figures/tables	1
Will you be translating?	No
Title	SSNMR of MOFs
Institution name	UWO
Expected presentation date	Jan 2022
Portions	Figure 1

License Details

This Agreement between Mr. Vinicius Martins ("You") and John Wiley and Sons ("John Wiley and Sons") consists of your license details and the terms and conditions provided by John Wiley and Sons and Copyright Clearance Center.

[Print](#)[Copy](#)

License Number	5206180380282
License date	Dec 11, 2021
Licensed Content Publisher	John Wiley and Sons
Licensed Content Publication	Advanced Materials
Licensed Content Title	Stable Metal–Organic Frameworks: Design, Synthesis, and Applications
Licensed Content Author	Hong-Cai Zhou, Jialuo Li, Yu Fang, et al
Licensed Content Date	Feb 12, 2018
Licensed Content Volume	30
Licensed Content Issue	37
Licensed Content Pages	35
Type of Use	Dissertation/Thesis
Requestor type	University/Academic
Format	Electronic
Portion	Figure/table
Number of figures/tables	1
Will you be translating?	No
Title	SSNMR of MOFs
Institution name	UWO
Expected presentation date	Jan 2022
Portions	Figure 15

License Details

This Agreement between Mr. Vinicius Martins ("You") and John Wiley and Sons ("John Wiley and Sons") consists of your license details and the terms and conditions provided by John Wiley and Sons and Copyright Clearance Center.

[Print](#) [Copy](#)

License Number	5206190374532
License date	Dec 11, 2021
Licensed Content Publisher	John Wiley and Sons
Licensed Content Publication	Chemistry - A European Journal
Licensed Content Title	A Rationale for the Large Breathing of the Porous Aluminum Terephthalate (MIL-53) Upon Hydration
Licensed Content Author	Thierry Loiseau, Christian Serre, Clarisse Huguénard, et al
Licensed Content Date	Mar 15, 2004
Licensed Content Volume	10
Licensed Content Issue	6
Licensed Content Pages	10
Type of Use	Dissertation/Thesis
Requestor type	University/Academic
Format	Print
Portion	Figure/table
Number of figures/tables	1
Will you be translating?	No
Title	SSNMR of MOFs
Institution name	UWO
Expected presentation date	Jan 2022
Portions	Figure 6



[Home](#)
[Help](#)
[Live Chat](#)
[Sign in](#)
[Create Account](#)

CO2 Dynamics in a Metal–Organic Framework with Open Metal Sites



Author: Xueqian Kong, Eric Scott, Wen Ding, et al
Publication: Journal of the American Chemical Society
Publisher: American Chemical Society
Date: Sep 1, 2012

Copyright © 2012, American Chemical Society

PERMISSION/LICENSE IS GRANTED FOR YOUR ORDER AT NO CHARGE

This type of permission/license, instead of the standard Terms and Conditions, is sent to you because no fee is being charged for your order. Please note the following:

- Permission is granted for your request in both print and electronic formats, and translations.
- If figures and/or tables were requested, they may be adapted or used in part.
- Please print this page for your records and send a copy of it to your publisher/graduate school.
- Appropriate credit for the requested material should be given as follows: "Reprinted (adapted) with permission from {COMPLETE REFERENCE CITATION}. Copyright {YEAR} American Chemical Society." Insert appropriate information in place of the capitalized words.
- One-time permission is granted only for the use specified in your RightsLink request. No additional uses are granted (such as derivative works or other editions). For any uses, please submit a new request.

If credit is given to another source for the material you requested from RightsLink, permission must be obtained from that source.

[BACK](#)

[CLOSE WINDOW](#)

Capturing Guest Dynamics in Metal–Organic Framework CPO-27-M (M = Mg, Zn) by 2H Solid-State NMR Spectroscopy



Author: Jun Xu, Regina Sinelnikov, Yining Huang

Publication: Langmuir

Publisher: American Chemical Society

Date: Jun 1, 2016

Copyright © 2016, American Chemical Society

PERMISSION/LICENSE IS GRANTED FOR YOUR ORDER AT NO CHARGE

This type of permission/license, instead of the standard Terms and Conditions, is sent to you because no fee is being charged for your order. Please note the following:

- Permission is granted for your request in both print and electronic formats, and translations.
- If figures and/or tables were requested, they may be adapted or used in part.
- Please print this page for your records and send a copy of it to your publisher/graduate school.
- Appropriate credit for the requested material should be given as follows: "Reprinted (adapted) with permission from {COMPLETE REFERENCE CITATION}. Copyright {YEAR} American Chemical Society." Insert appropriate information in place of the capitalized words.
- One-time permission is granted only for the use specified in your RightsLink request. No additional uses are granted (such as derivative works or other editions). For any uses, please submit a new request.

If credit is given to another source for the material you requested from RightsLink, permission must be obtained from that source.

[BACK](#)

[CLOSE WINDOW](#)

Multiple-Quantum Magic-Angle Spinning NMR: A New Method for the Study of Quadrupolar Nuclei in Solids



Author: Ales Medek, John S. Harwood, Lucio Frydman

Publication: Journal of the American Chemical Society

Publisher: American Chemical Society

Date: Dec 1, 1995

Copyright © 1995, American Chemical Society

PERMISSION/LICENSE IS GRANTED FOR YOUR ORDER AT NO CHARGE

This type of permission/license, instead of the standard Terms and Conditions, is sent to you because no fee is being charged for your order. Please note the following:

- Permission is granted for your request in both print and electronic formats, and translations.
- If figures and/or tables were requested, they may be adapted or used in part.
- Please print this page for your records and send a copy of it to your publisher/graduate school.
- Appropriate credit for the requested material should be given as follows: "Reprinted (adapted) with permission from {COMPLETE REFERENCE CITATION}. Copyright {YEAR} American Chemical Society." Insert appropriate information in place of the capitalized words.
- One-time permission is granted only for the use specified in your RightsLink request. No additional uses are granted (such as derivative works or other editions). For any uses, please submit a new request.

If credit is given to another source for the material you requested from RightsLink, permission must be obtained from that source.

[BACK](#)

[CLOSE WINDOW](#)

Issue 26, 2020

[Previous Article](#)[Next Article](#)

From the journal:
Physical Chemistry Chemical Physics

Following the unusual breathing behaviour of ^{17}O -enriched mixed-metal (Al,Ga)-MIL-53 using NMR crystallography†

[Cameron M. Rice](#),^{‡a} [Zachary H. Davis](#),^{‡a} [David McKay](#),^{id a} [Giulia P. M. Bignami](#),^a [Ruxandra G. Chitac](#),^a
[Daniel M. Dawson](#),^{id a} [Russell E. Morris](#),^{id *ab} and [Sharon E. Ashbrook](#),^{id *a}

[+ Author affiliations](#)

Abstract

The breathing behaviour of ^{17}O -enriched (Al,Ga)-MIL-53, a terephthalate-based metal-organic framework, has been investigated using a combination of solid-state nuclear magnetic resonance (NMR) spectroscopy, powder X-ray diffraction (PXRD) and first-principles

[About](#)[Cited by](#)[Related](#)

Following the unusual breathing behaviour of ^{17}O -enriched mixed-metal (Al,Ga)-MIL-53 using NMR crystallography

C. M. Rice, Z. H. Davis, D. McKay, G. P. M. Bignami, R. G. Chitac, D. M. Dawson, R. E. Morris and S. E. Ashbrook, *Phys. Chem. Chem. Phys.*, 2020, **22**, 14514 DOI: 10.1039/D0CP02731F

This article is licensed under a [Creative Commons Attribution 3.0 Unported Licence](#). You can use material from this article in other publications without requesting further permissions from the RSC, provided that the correct acknowledgement is given.

Read more about [how to correctly acknowledge RSC content](#).



Higher Magnetic Fields, Finer MOF Structural Information: ^{17}O Solid-State NMR at 35.2 T

Author: Vinicius Martins, Jun Xu, Xiaoling Wang, et al
Publication: Journal of the American Chemical Society
Publisher: American Chemical Society
Date: Sep 1, 2020

Copyright © 2020, American Chemical Society

PERMISSION/LICENSE IS GRANTED FOR YOUR ORDER AT NO CHARGE

This type of permission/license, instead of the standard Terms and Conditions, is sent to you because no fee is being charged for your order. Please note the following:

- Permission is granted for your request in both print and electronic formats, and translations.
- If figures and/or tables were requested, they may be adapted or used in part.
- Please print this page for your records and send a copy of it to your publisher/graduate school.
- Appropriate credit for the requested material should be given as follows: "Reprinted (adapted) with permission from {COMPLETE REFERENCE CITATION}. Copyright {YEAR} American Chemical Society." Insert appropriate information in place of the capitalized words.
- One-time permission is granted only for the use specified in your RightsLink request. No additional uses are granted (such as derivative works or other editions). For any uses, please submit a new request.

If credit is given to another source for the material you requested from RightsLink, permission must be obtained from that source.

[BACK](#)

[CLOSE WINDOW](#)

Identification of Nonequivalent Framework Oxygen Species in Metal–Organic Frameworks by 17O Solid-State NMR

Author: Peng He, Jun Xu, Victor V. Terskikh, et al

Publication: The Journal of Physical Chemistry C

Publisher: American Chemical Society

Date: Aug 1, 2013

Copyright © 2013, American Chemical Society

PERMISSION/LICENSE IS GRANTED FOR YOUR ORDER AT NO CHARGE

This type of permission/license, instead of the standard Terms and Conditions, is sent to you because no fee is being charged for your order. Please note the following:

- Permission is granted for your request in both print and electronic formats, and translations.
- If figures and/or tables were requested, they may be adapted or used in part.
- Please print this page for your records and send a copy of it to your publisher/graduate school.
- Appropriate credit for the requested material should be given as follows: "Reprinted (adapted) with permission from {COMPLETE REFERENCE CITATION}. Copyright {YEAR} American Chemical Society." Insert appropriate information in place of the capitalized words.
- One-time permission is granted only for the use specified in your RightsLink request. No additional uses are granted (such as derivative works or other editions). For any uses, please submit a new request.

If credit is given to another source for the material you requested from RightsLink, permission must be obtained from that source.

[BACK](#)[CLOSE WINDOW](#)**Identification of Nonequivalent Framework Oxygen Species in Metal–Organic Frameworks by 17O Solid-State NMR**

Author: Peng He, Jun Xu, Victor V. Terskikh, et al

Publication: The Journal of Physical Chemistry C

Publisher: American Chemical Society

Date: Aug 1, 2013

Copyright © 2013, American Chemical Society

PERMISSION/LICENSE IS GRANTED FOR YOUR ORDER AT NO CHARGE

This type of permission/license, instead of the standard Terms and Conditions, is sent to you because no fee is being charged for your order. Please note the following:

- Permission is granted for your request in both print and electronic formats, and translations.
- If figures and/or tables were requested, they may be adapted or used in part.
- Please print this page for your records and send a copy of it to your publisher/graduate school.
- Appropriate credit for the requested material should be given as follows: "Reprinted (adapted) with permission from {COMPLETE REFERENCE CITATION}. Copyright {YEAR} American Chemical Society." Insert appropriate information in place of the capitalized words.
- One-time permission is granted only for the use specified in your RightsLink request. No additional uses are granted (such as derivative works or other editions). For any uses, please submit a new request.

If credit is given to another source for the material you requested from RightsLink, permission must be obtained from that source.

[BACK](#)[CLOSE WINDOW](#)

License Details

This Agreement between Mr. Vinicius Martins ("You") and John Wiley and Sons ("John Wiley and Sons") consists of your license details and the terms and conditions provided by John Wiley and Sons and Copyright Clearance Center.

[Print](#) [Copy](#)

License Number	5218940579680
License date	Dec 30, 2021
Licensed Content Publisher	John Wiley and Sons
Licensed Content Publication	Magnetic Resonance in Chemistry
Licensed Content Title	17O solid-state NMR at ultrahigh magnetic field of 35.2 T: Resolution of inequivalent oxygen sites in different phases of MOF MIL-53(AI)
Licensed Content Author	Vinicius Martins, Jun Xu, Ivan Hung, et al
Licensed Content Date	Feb 8, 2021
Licensed Content Volume	59
Licensed Content Issue	9-10
Licensed Content Pages	11
Type of Use	Dissertation/Thesis
Requestor type	Author of this Wiley article
Format	Electronic
Portion	Full article
Will you be translating?	No
Title	SSNMR of MOFs
Institution name	UWO
Expected presentation date	Jan 2022

CCC | Marketplace™

This is a License Agreement between Vinicius Martins ("User") and Copyright Clearance Center, Inc. ("CCC") on behalf of the Rightsholder identified in the order details below. The license consists of the order details, the CCC Terms and Conditions below, and any Rightsholder Terms and Conditions which are included below. All payments must be made in full to CCC in accordance with the CCC Terms and Conditions below.

Order Date	30-Dec-2021	Type of Use	Republish in a thesis/dissertation
Order License ID	1173174-1	Publisher	Royal Society of Chemistry
ISSN	2041-6539	Portion	Image/photo/illustration

LICENSED CONTENT

Publication Title	Chemical science	Rightsholder	Royal Society of Chemistry
Article Title	Ionothermal 17O enrichment of oxides using microlitre quantities of labelled water	Publication Type	e-Journal
Author/Editor	Royal Society of Chemistry (Great Britain)	Start Page	2293
Date	01/01/2010	Issue	7
Language	English	Volume	3
Country	United Kingdom of Great Britain and Northern Ireland	URL	http://www.rsc.org/Publishing/Journals/S...

REQUEST DETAILS

Portion Type	Image/photo/illustration	Distribution	Canada
Number of images / photos / illustrations	1	Translation	Original language of publication
Format (select all that apply)	Electronic	Copies for the disabled?	No
Who will republish the content?	Academic institution	Minor editing privileges?	No
Duration of Use	Current edition and up to 5 years	Incidental promotional use?	No
Lifetime Unit Quantity	Up to 499	Currency	CAD
Rights Requested	Main product		

Appendix A3

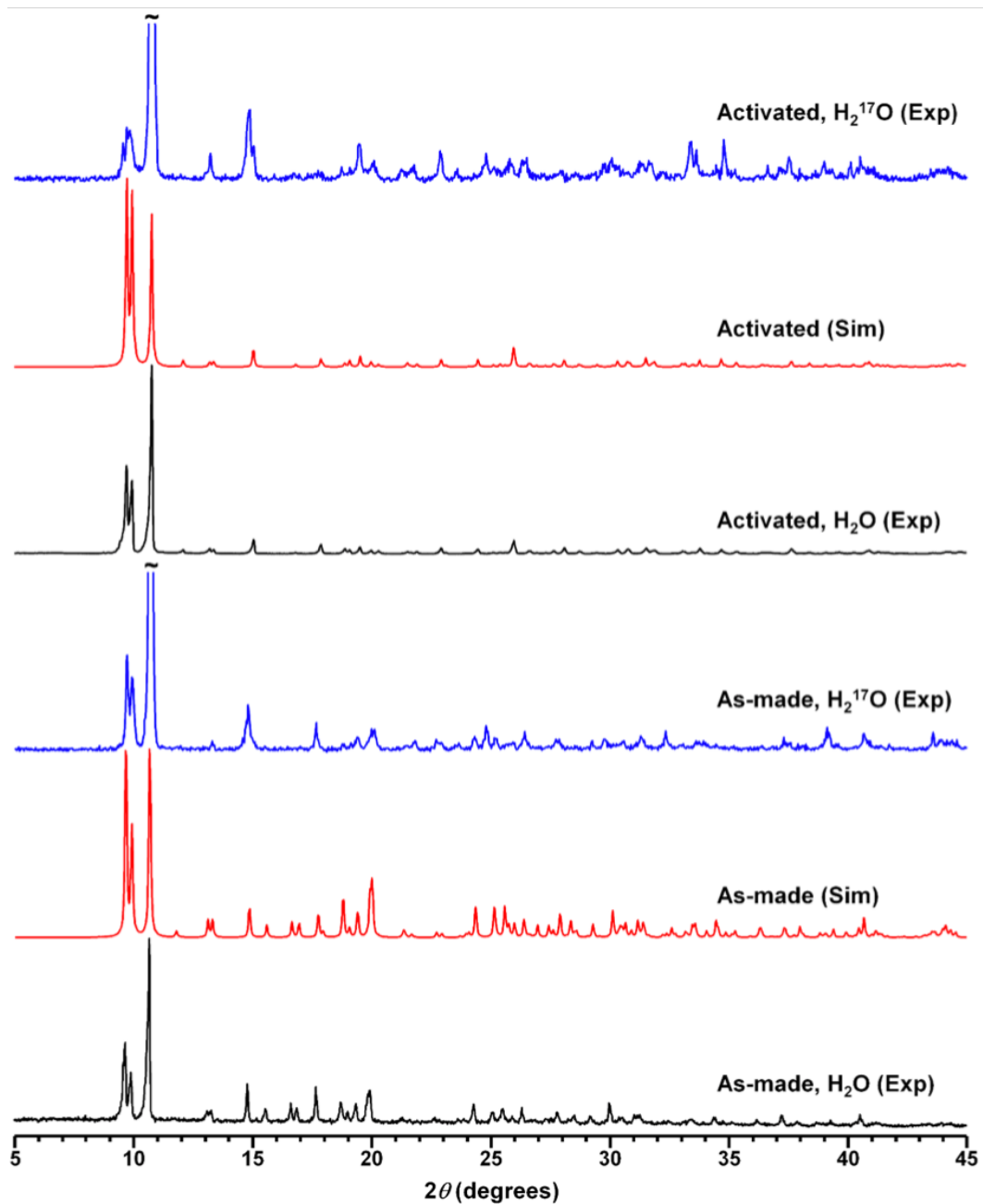


Figure A3.1. Experimental (Exp) and simulated (Sim) PXRD patterns of $\alpha\text{-Mg}_3(\text{HCO}_2)_6$. The ~ symbol denotes an intense reflection truncated for clarity. The simulated patterns were calculated based on the reported single crystal XRD structures.

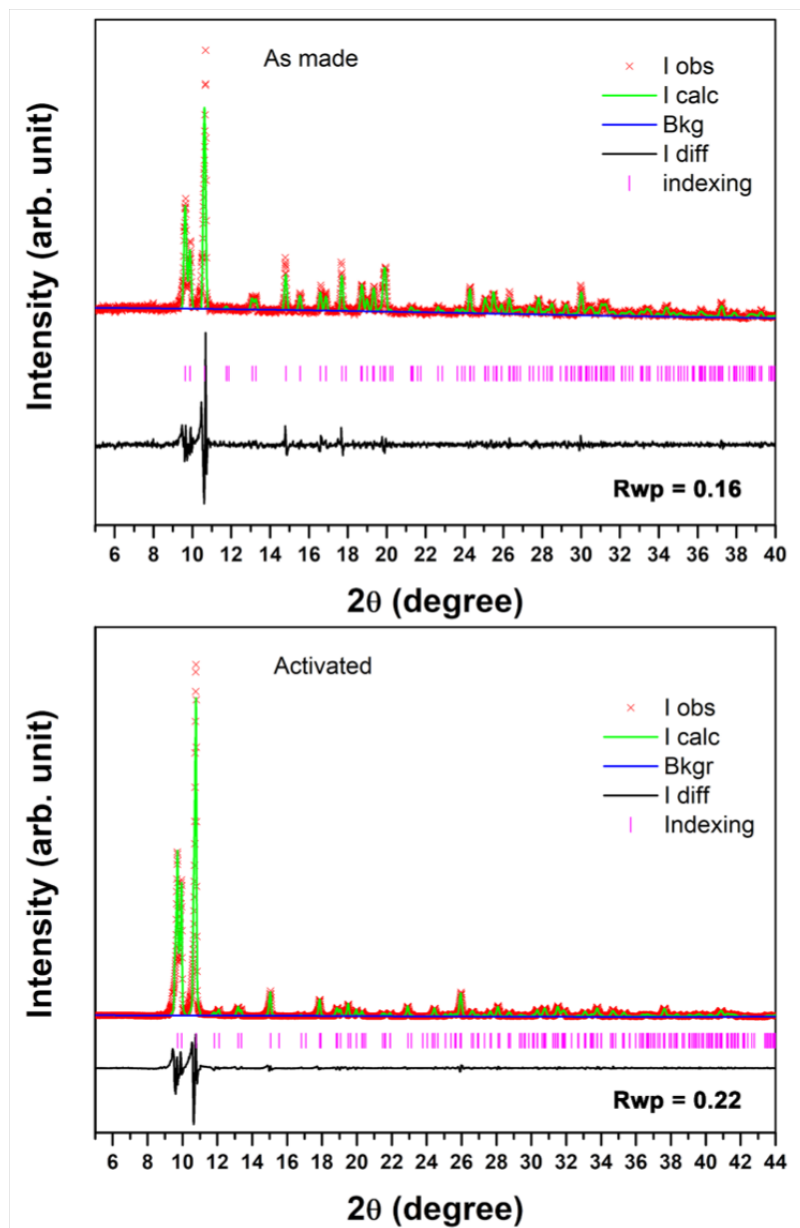


Figure A3.2. Le Bail refinement of unit cell parameters for the as-made (top) and the activated (bottom) α -Mg₃(HCOO)₆.

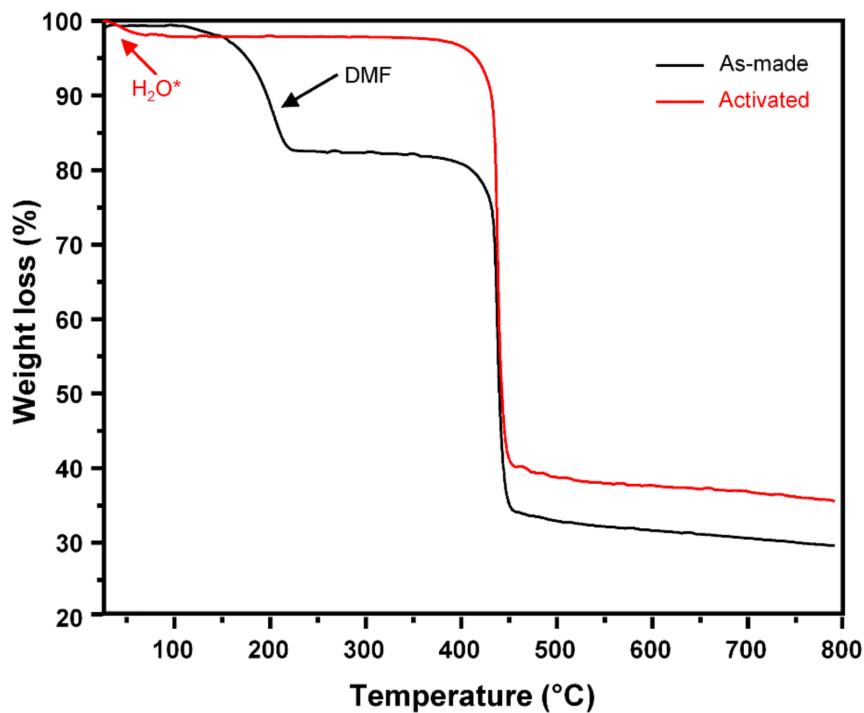


Figure A3.3. TGA profiles for the as-made and activated α - $\text{Mg}_3(\text{HCOO})_6$.

Thermogravimetric analysis

Thermogravimetric analysis (TGA) measurements were performed under a N_2 atmosphere. The samples used for TGA measurements were prepared using normal H_2O and were heated from 25° to 800°C at a rate of $10^\circ\text{C}/\text{min}$ under a N_2 atmosphere on a Mettler Toledo TGA/DTA851e instrument. The TGA profile of the as-made sample shows a weight loss at around 150°C due to the departure of the DMF. This weight loss is absent in the graph of the activated phase. Note: a very small weight loss at very low temperature is due to a small amount of water adsorbed on the activated sample surfaces during the sample preparation.

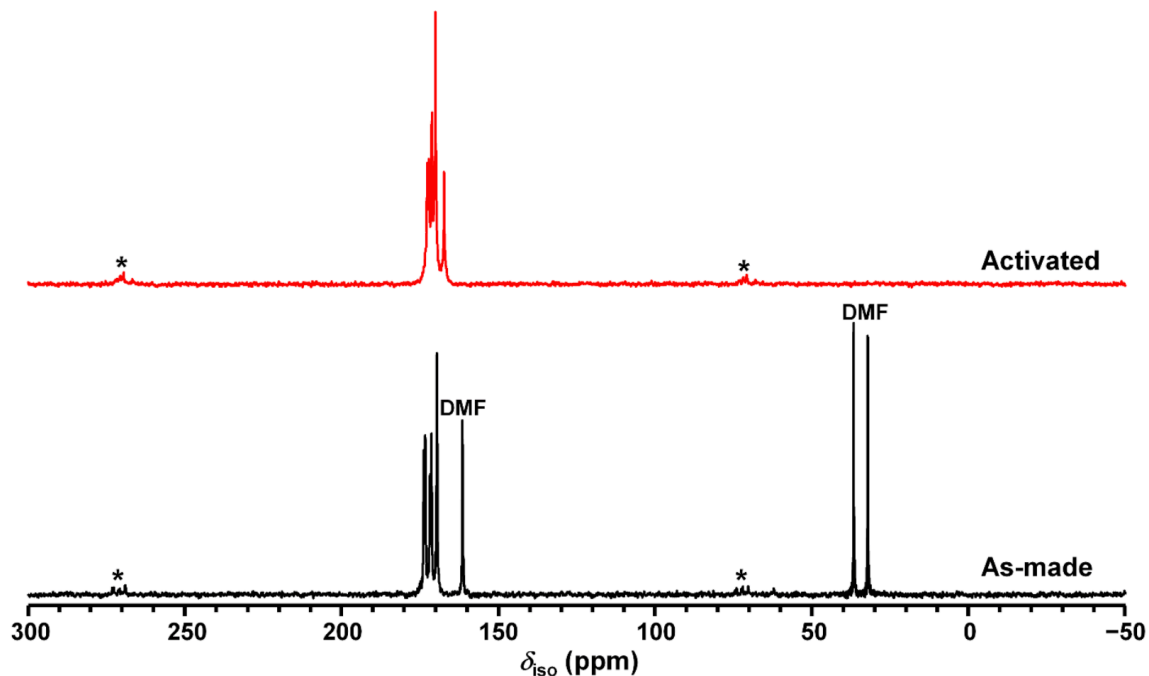


Figure A3.4. ^{13}C CP MAS NMR spectra of the as-made and activated $\alpha\text{-Mg}_3(\text{HCOO})_6$. The “DMF” label highlights resonances arising from guest DMF molecules, while the asterisk (*) denotes spinning sidebands (SSBs).

^{13}C SSNMR measurements

^{13}C SSNMR experiments were performed on a Bruker Avance III HB spectrometer by using a 4.0 mm Bruker $^1\text{H}/^{31}\text{P}\text{-}^{15}\text{N}$ MAS probe, with a spinning frequency of 10 kHz. ^{13}C chemical shifts were referenced to the methylene signal of solid adamantane at 38.48 ppm.³ The Hartmann-Hahn match conditions for $^1\text{H}\text{-}^{13}\text{C}$ cross-polarization (CP) experiments were optimized on solid 1,2- ^{13}C -glycine, using a TPPM ^1H decoupling field strength of 62.5 kHz. The contact time was 5 ms and the recycle delay was 4 s. The samples used for these experiments were those prepared using ordinary H_2O . The ^{13}C CP MAS spectra clearly indicate that upon activation, the three resonances from DMF disappear completely, signifying the absence of DMF guests.

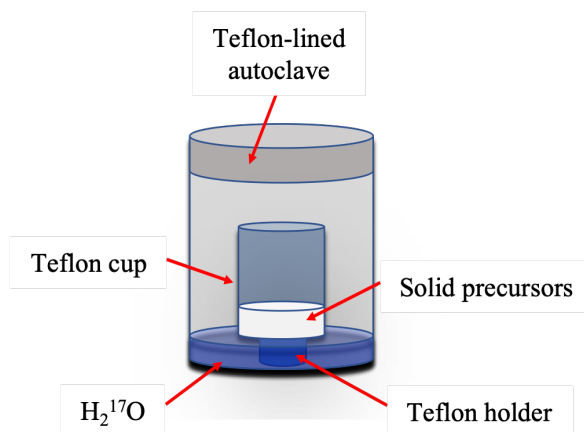


Figure A3.5. Schematic illustration of the reaction vessel used in the dry gel conversion method.

Synthesis of ¹⁷O-enriched MIL-53(Al)

As-made ¹⁷O-enriched MIL-53(Al) samples were synthesized via the dry gel conversion method described elsewhere.⁴ All starting materials were used as received without further purification. A mixture of Al(NO₃)₃·9H₂O (4.5 mmol, Aldrich) and 1,4-benzenedicarboxylic acid (H₂BDC, 5.9 mmol, Aldrich) was placed in a 23 mL Teflon-lined autoclave containing a small amount (0.5–1.0 mL) of ¹⁷O-enriched water (CortecNet, 35 atom%). The autoclave was sealed and then heated in an oven at 493 K for 3 days. After slowly cooling down to room temperature, as-made ¹⁷O-enriched MIL-53(Al) in the form of a white powder was collected, washed with DMF, and dried at 353 K. Activated ¹⁷O-enriched MIL-53(Al) samples were prepared by first solvent exchanging as-made ¹⁷O-enriched MIL-53(Al) with DMF in an autoclave at 423 K for 24 and 12 h for Samples A and B, respectively. These samples were then activated at 573 K under dynamic vacuum for 12 h.

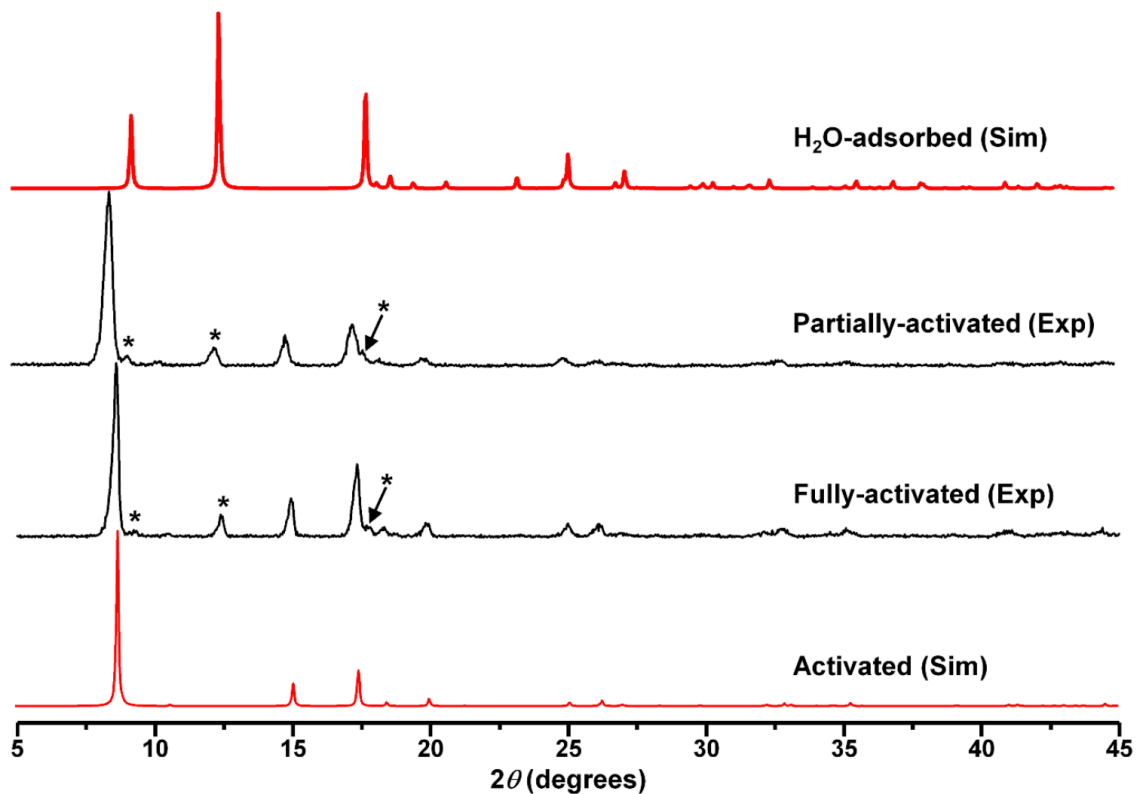


Figure A3.6. Experimental (Exp) and simulated (Sim) PXRD patterns of ^{17}O -enriched MIL-53(Al). The simulated patterns were calculated based on the reported PXRD structures.⁵ The asterisk denotes a very small amount of the H_2O -adsorbed MIL-53(Al) phase.

Sample preparation for PXRD

Both fully- and partially-activated samples were briefly exposed to ambient conditions during PXRD experiments. Since activated MIL-53(Al) is hydrophilic, a small amount of the sample adsorbed water. With this knowledge in hand, the activated samples for NMR measurements were packed inside a glove box and the samples were never exposed to air, preventing formation of the H_2O -adsorbed MIL-53(Al) phase.

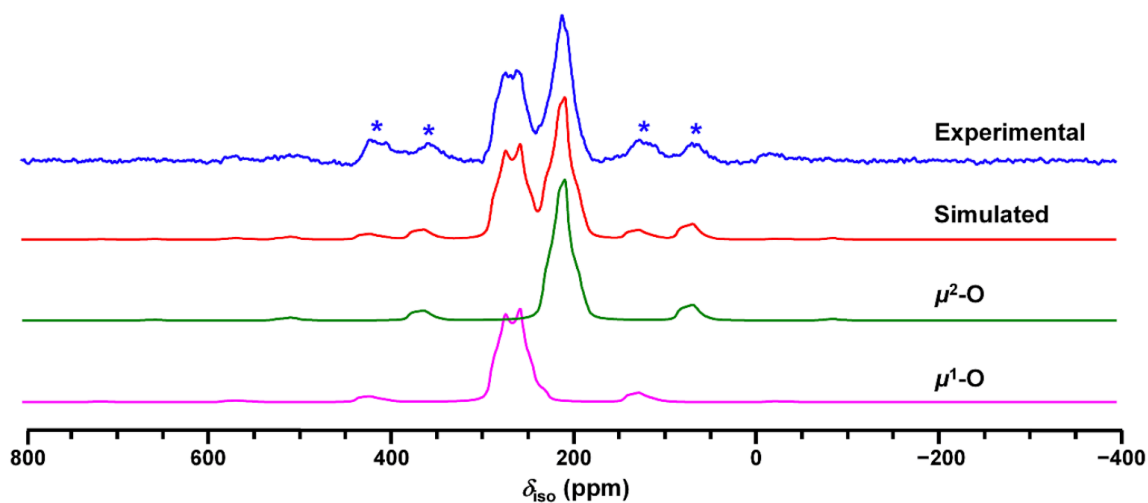


Figure A3.7. Experimental and simulated ^{17}O 1D MAS NMR spectra of ^{17}O -enriched as-made $\alpha\text{-Mg}_3(\text{HCOO})_6$ at 21.1 T, acquired at a spinning frequency of 18 kHz. Only the quadrupolar interaction is considered in the simulations. The asterisk (*) denotes SSBs.

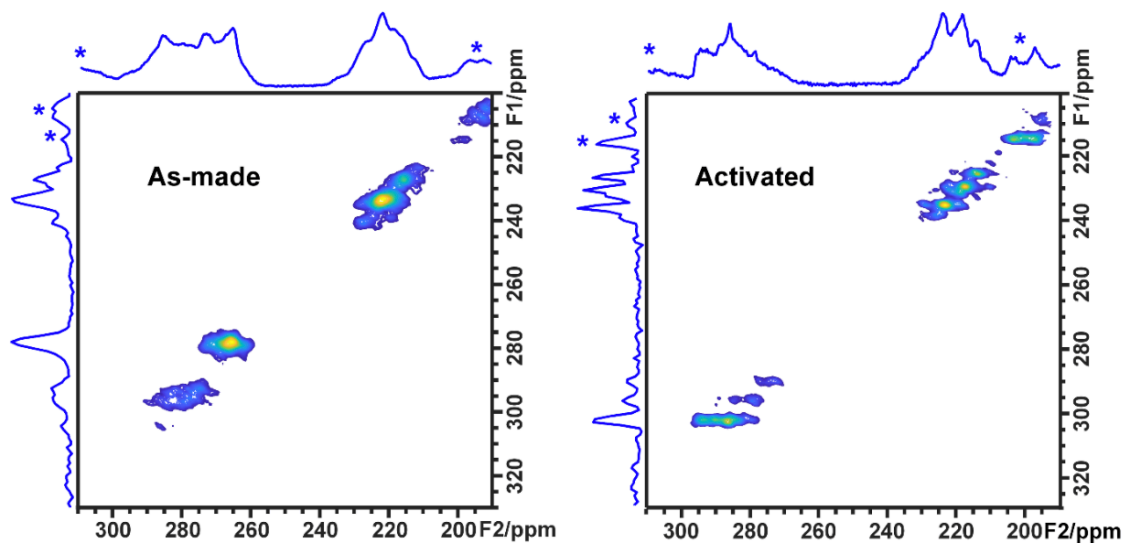


Figure A3.8. ^{17}O 2D 3QMAS NMR spectra of ^{17}O -enriched $\alpha\text{-Mg}_3(\text{HCOO})_6$ at 35.2 T without the markups present in Figure 3.2 of the main text. The asterisk (*) denotes spinning sidebands (SSBs).

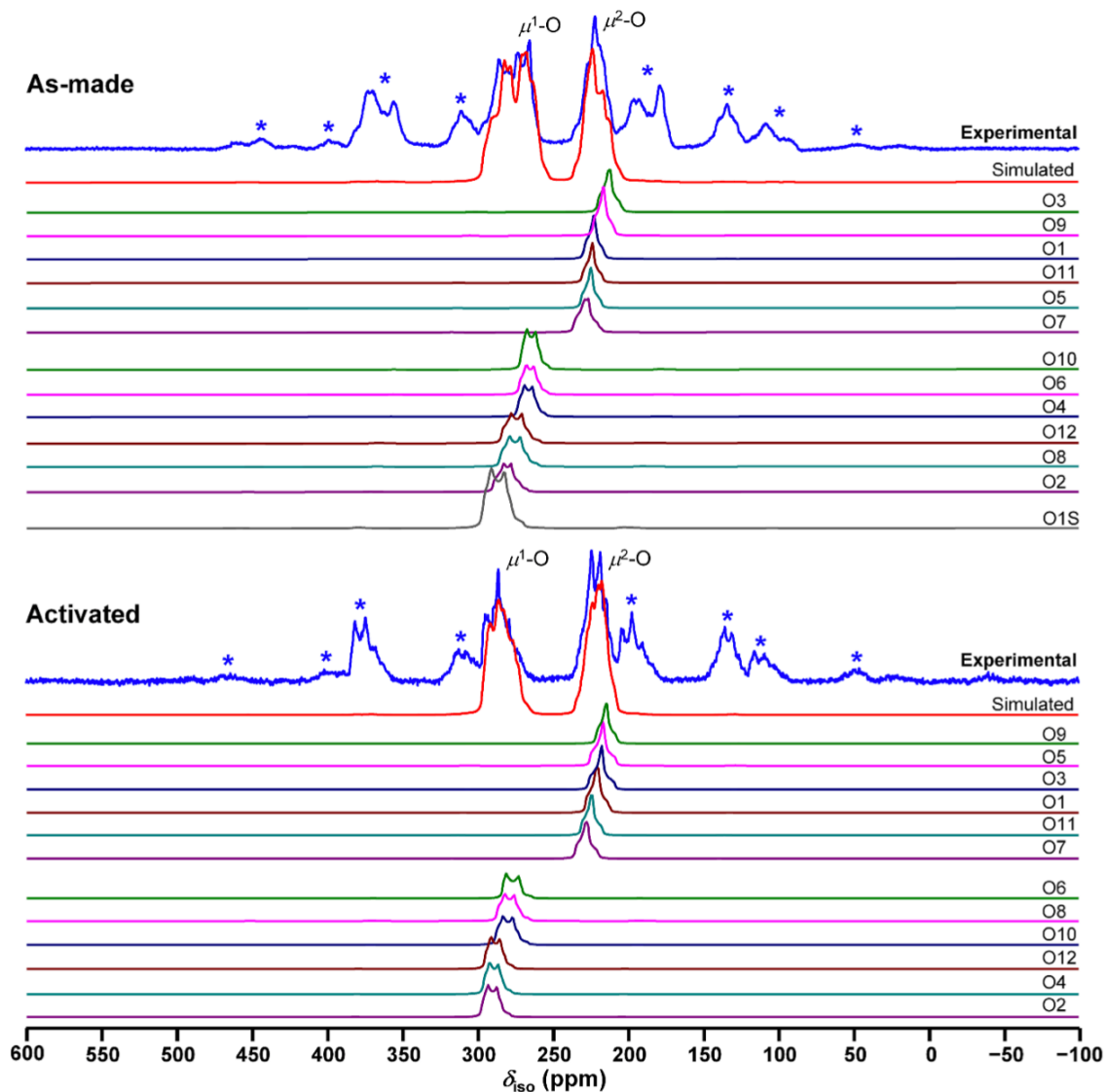


Figure A3.9. Experimental and simulated ^{17}O 1D MAS NMR spectra of ^{17}O -enriched $\alpha\text{-Mg}_3(\text{HCOO})_6$ at 35.2 T acquired at a spinning frequency of 18 kHz. The spectra were simulated by considering only the quadrupolar effect. The asterisk (*) denotes SSBs. Note: the intensities of the spinning sidebands in simulated spectra are very weak if only the quadrupolar interaction is considered.

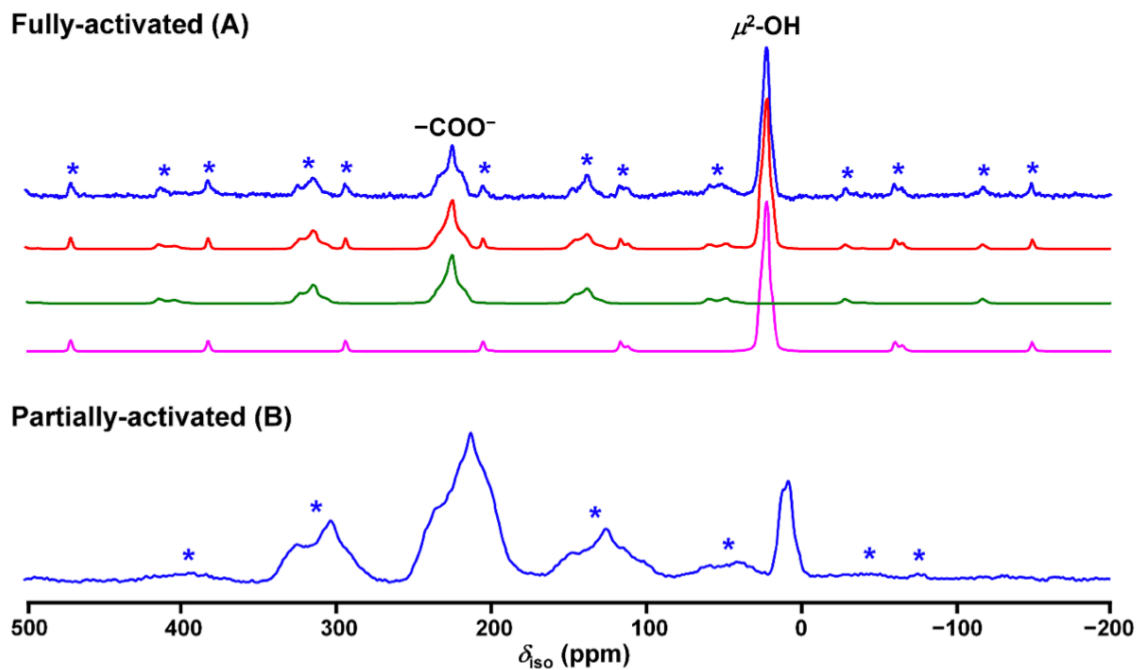


Figure A3.10. The ^{17}O 1D MAS NMR spectra of (A) fully- and (B) partially-activated ^{17}O -enriched MIL-53(AI) at 35.2 T. The asterisk (*) denotes SSBs.

Table A3.1. Comparison between unit cell parameters of α -Mg₃(HCOO)₆ determined in this work and those previously reported.²

Sample	a (Å)	a (Å)	b (Å)	b (Å)	c (Å)	c (Å)	b (°)a	b (°)a
	This work	Lit.	This work	Lit.	This work	Lit.	This work	Lit.
As-made	11.40(1)	11.4007(6)	10.02(1)	9.9047(4)	14.91(1)	14.5357(6)	91.5(1)	91.317(2)
Activated	11.40(1)	11.324(2)	9.91(1)	9.847(1)	16.42(1)	14.623(1)	91.4(1)	91.150(3)

Table A3.2. Calculated ^{17}O NMR parameters of $\alpha\text{-Mg}_3(\text{HCOO})_6$.

Sample	O Site	$ C_Q $ (MHz) ^a	η_Q	δ_{iso} (ppm)	Δ_{CS} (ppm)	η_{CS}	φ (°)	χ (°)	ψ (°)
As-made	O1 ($\mu^2\text{-O}$)	7.02	0.86	236.1	-196	0.97	-155	-95	90
	O3 ($\mu^2\text{-O}$)	6.89	0.90	227.1	194	0.84	90	65	5
	O5 ($\mu^2\text{-O}$)	6.67	0.92	239.4	-196	0.95	110	90	-90
	O7 ($\mu^2\text{-O}$)	7.18	0.98	256.4	-208	0.90	-65	-90	85
	O9 ($\mu^2\text{-O}$)	6.75	0.87	230.5	195	0.83	90	-110	5
	O11 ($\mu^2\text{-O}$)	6.54	0.99	238.9	-195	0.93	-115	90	-90
	O2 ($\mu^1\text{-O}$)	8.56	0.41	306.5	-284	0.45	150	90	90
	O4 ($\mu^1\text{-O}$)	8.44	0.42	293.2	-277	0.44	35	-90	90
	O6 ($\mu^1\text{-O}$)	8.37	0.45	291.2	-280	0.43	-40	90	-90
	O8 ($\mu^1\text{-O}$)	8.40	0.43	297.2	-293	0.41	-145	90	-90
	O10 ($\mu^1\text{-O}$)	8.42	0.36	288.7	-283	0.43	40	-90	-90
	O12 ($\mu^1\text{-O}$)	8.49	0.44	295.5	-277	0.46	145	90	90
	O1S (DMF) ^a	8.64	0.35	308.3	-354	0.47	70	90	-90
Activated	O1 ($\mu^2\text{-O}$)	7.08	0.90	234.7	199	0.93	-80	-25	170
	O3 ($\mu^2\text{-O}$)	6.76	0.99	232.0	201	0.86	-80	-155	-170
	O5 ($\mu^2\text{-O}$)	6.70	0.92	232.0	-188	0.99	110	-90	95
	O7 ($\mu^2\text{-O}$)	7.04	0.94	243.5	-202	0.91	155	85	90
	O9 ($\mu^2\text{-O}$)	6.66	0.89	227.7	189	0.89	90	-110	5
	O11 ($\mu^2\text{-O}$)	6.66	0.96	238.7	193	0.94	-90	115	0
	O2 ($\mu^1\text{-O}$)	8.56	0.36	298.5	-284	0.47	145	90	95
	O4 ($\mu^1\text{-O}$)	8.48	0.37	296.5	-280	0.50	40	90	90
	O6 ($\mu^1\text{-O}$)	8.39	0.42	285.3	-276	0.46	-40	-90	90
	O8 ($\mu^1\text{-O}$)	8.36	0.41	288.0	-284	0.47	145	-90	90
	O10 ($\mu^1\text{-O}$)	8.58	0.39	289.9	-280	0.44	140	90	-90
	O12 ($\mu^1\text{-O}$)	8.44	0.36	296.4	-276	0.50	-35	-90	90

Table A3.3. ^{17}O NMR parameters used in the simulation of 1D ^{17}O MAS spectra of ^{17}O -enriched $\alpha\text{-Mg}_3(\text{HCOO})_6$.

Sample	O Site	C_Q (MHz)	η_Q	δ_{iso} (ppm)	Δ_{CS} (ppm)	η_{CS}	φ ($^\circ$)	χ ($^\circ$)	ψ ($^\circ$)
As-made	O1 ($\mu^2\text{-O}$)	5.9	0.86	229	130	0.97	-155	-95	90
	O3 ($\mu^2\text{-O}$)	6.5	0.80	220	130	0.84	90	65	5
	O5 ($\mu^2\text{-O}$)	5.8	0.92	231	130	0.95	110	90	-90
	O7 ($\mu^2\text{-O}$)	7.0	0.70	236	130	0.90	-65	-90	85
	O9 ($\mu^2\text{-O}$)	6.0	0.88	223	130	0.83	90	-110	5
	O11 ($\mu^2\text{-O}$)	5.7	0.99	230	130	0.93	-115	90	-90
	O2 ($\mu^1\text{-O}$)	7.9	0.55	290	-180	0.45	150	90	90
	O4 ($\mu^1\text{-O}$)	7.3	0.42	274	-180	0.44	35	-90	90
	O6 ($\mu^1\text{-O}$)	7.3	0.45	273	-180	0.43	-40	90	-90
	O8 ($\mu^1\text{-O}$)	8.5	0.43	286	-180	0.41	-145	90	-90
	O10 ($\mu^1\text{-O}$)	7.3	0.36	272	-180	0.43	40	-90	-90
	O12 ($\mu^1\text{-O}$)	8.5	0.44	285	-180	0.46	145	90	90
	O1S (DMF) ^a	8.9	0.35	298	-200	0.47	70	90	-90
Activated	O1 ($\mu^2\text{-O}$)	6.5	0.80	228	170	0.93	-80	-25	170
	O3 ($\mu^2\text{-O}$)	6.5	0.99	226	170	0.86	-80	-155	-170
	O5 ($\mu^2\text{-O}$)	6.6	0.92	225	170	0.99	110	-90	95
	O7 ($\mu^2\text{-O}$)	6.4	0.80	235	170	0.91	155	85	90
	O9 ($\mu^2\text{-O}$)	6.0	0.85	221	170	0.89	90	-110	5
	O11 ($\mu^2\text{-O}$)	6.1	0.85	231	170	0.94	-90	115	0
	O2 ($\mu^1\text{-O}$)	7.4	0.36	298	-220	0.47	145	90	95
	O4 ($\mu^1\text{-O}$)	7.4	0.37	297	-220	0.50	40	90	90
	O6 ($\mu^1\text{-O}$)	7.7	0.20	285	-220	0.46	-40	-90	90
	O8 ($\mu^1\text{-O}$)	7.9	0.41	288	-220	0.47	145	-90	90
	O10 ($\mu^1\text{-O}$)	7.9	0.39	289	-220	0.44	140	90	-90
	O12 ($\mu^1\text{-O}$)	7.4	0.36	296	-220	0.50	-35	-90	90

Table A3.4. Experimental ^{17}O NMR parameters and tentative resonance assignments of carboxylate oxygen sites in two different MIL-53(Al) samples.

Sample	δ_{i} (ppm)	P_{Q} (MHz)	δ_{iso} (ppm)	Assignment	C_{Q} (MHz)	η_{Q}
Fully-activated			236(2)	Activated MIL-53(Al)	7.5(4)	0.81(10)
Partially-activated	212(1)	7.5(5)	207(2)	H ₂ BDC		
	217(1)	7.5(5)	212(2)	H ₂ BDC		
	226(1)	7.5(5)	221(2)	Occupied channels		
	237(1)	7.5(5)	232(2)	Empty channels		
	244(1)	7.2(5)	240(2)	Occupied channels		

Appendix A4

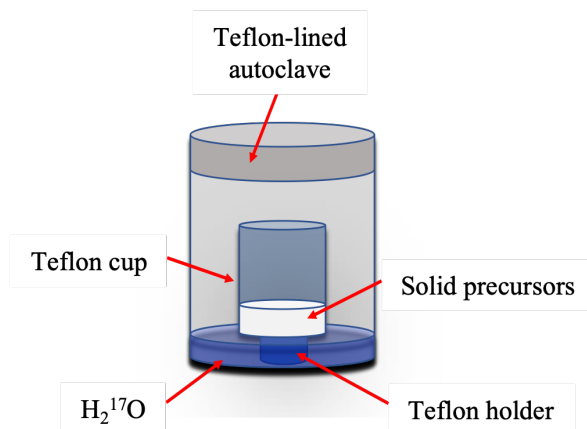


Figure A4.1. Illustration of the reaction vessel for the dry gel conversion method.

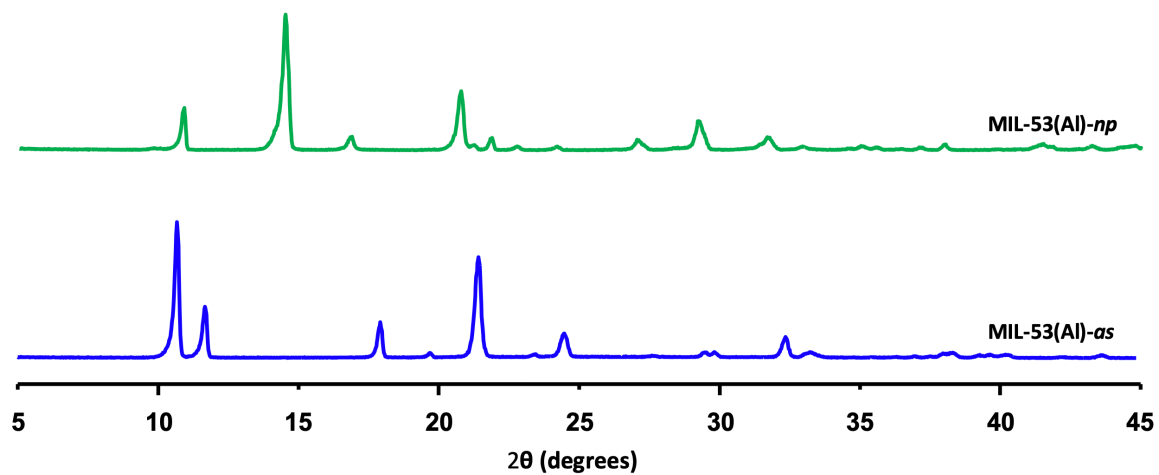


Figure A4.2. Powder XRD patterns of the MIL-53(Al)-as and MIL-53(Al)-np.

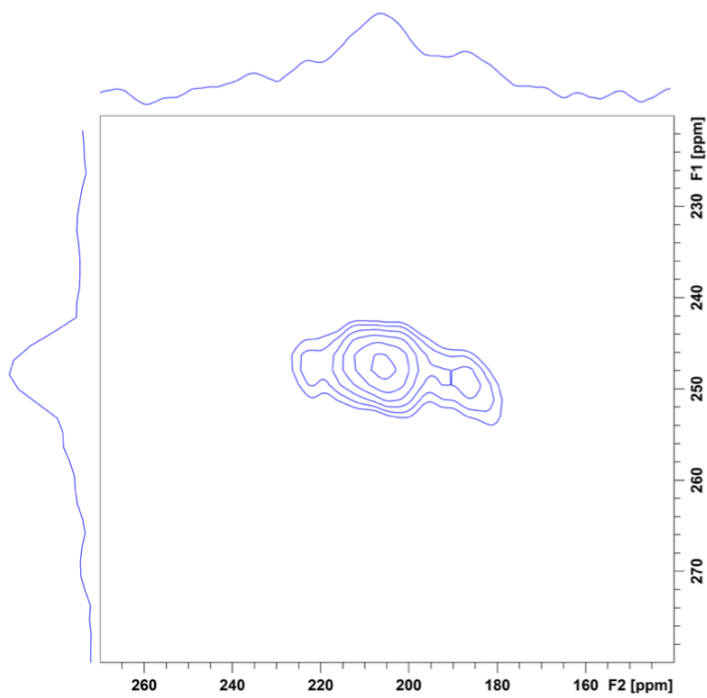


Figure A4.3. ^{17}O 2D 3QMAS NMR spectrum of ^{17}O -enriched MIL-53(Al)-as at 21.1 T.

Only the regions corresponding to $-\text{COO}^-$ oxygen sites are shown for clarity.

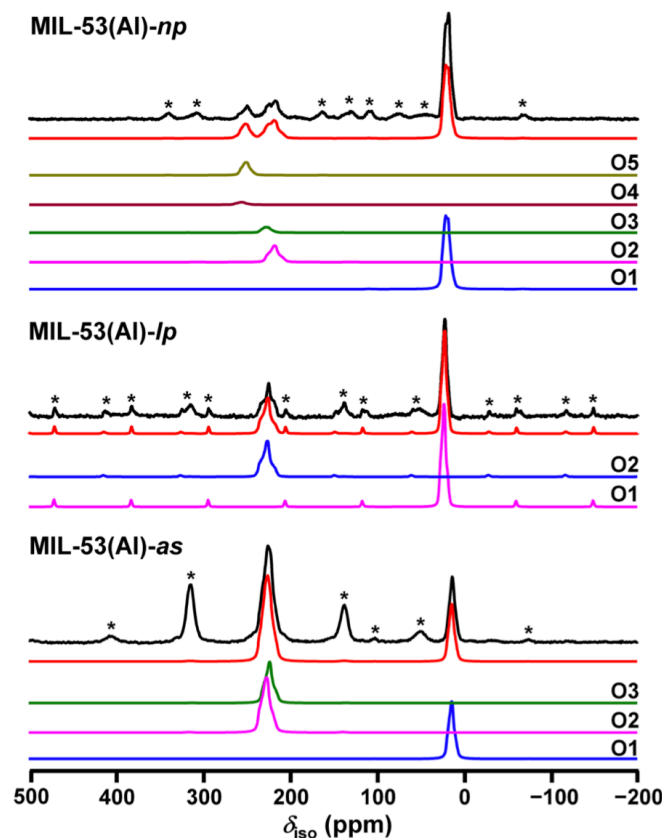


Figure A4.4. Experimental and simulated ^{17}O 1D MAS NMR spectra of three ^{17}O -enriched MIL-53(Al) phases at 35.2 T. Only the quadrupolar effects are considered in simulation by using the parameters shown in Table 4.1. The asterisk (*) denotes SSBs. The satellite transitions were also observed in the spectrum of MIL-53(Al)-lp due to the use of a one-pulse sequence with a hard 90° excitation pulse.⁴

Figure S3 shows that if only the quadrupolar interaction is taken into consideration, the simulated spectra in isotropic region match well with those of experimental ones. However, the intensities of the spinning sidebands are extremely weak. These results indicate that the ^{17}O EFG anisotropy at 35.2 T is rather small and the CSA is the major contributor to the SSBs. When the quadrupolar and CSA effects are both considered, the simulated ^{17}O 1D MAS NMR spectra match the observed ones much better, indicating that both the quadrupolar and CSA effects influence the ^{17}O line-shape significantly.

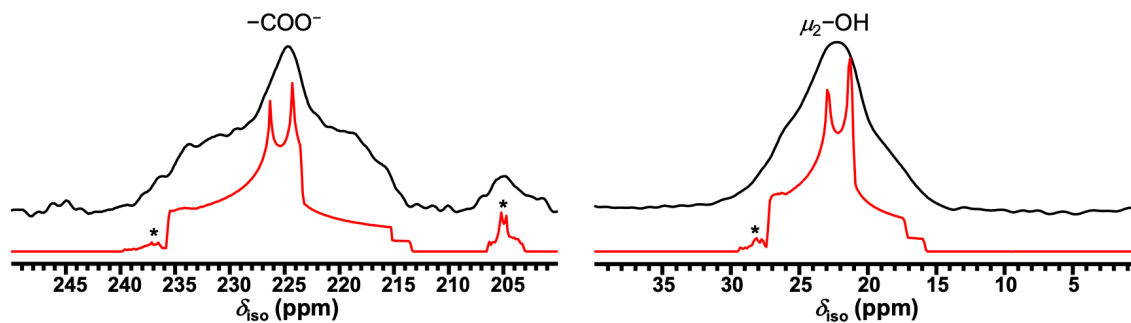


Figure A4.5. Experimental and simulated ^{17}O 1D MAS NMR spectrum of ^{17}O -enriched MIL-53(Al)-lp in isotropic region at 35.2 T. Only the quadrupolar effect is considered in simulation and no line broadening is applied. The regions of two oxygen sites are expanded to compare the linewidth. The simulations were constructed using calculated C_Q and η_Q values with experimentally determined δ_{iso} values. Note the striking similarity in resonance widths between experimental and DFT-calculated spectra, suggesting that the main source of experimental resonance broadening in isotropic region is the second-order quadrupolar interaction.

Table A4.1. Additional details for ^{17}O 1D MAS NMR experiments.

Phase	# of scans	Acquisition time	Apodization	Line broadening (LB)
MIL-53(Al)- <i>as</i>	256	26 s	Exponential	100 Hz
MIL-53(Al)- <i>lp</i>	1024	17 min	Exponential	100 Hz
MIL-53(Al)- <i>np</i>	512	51 s	Exponential	20 Hz

Table A4.2. Additional details for ^{17}O 3QMAS NMR experiments.

Phase	# of scans	Acquisition time	Apodization	Line broadening: F2/F1
MIL-53(Al)- <i>as</i> ($-\text{COO}^-$)	1920 \times 24	77 min	Exponential	150/300 Hz
MIL-53(Al)- <i>np</i> ($-\text{COO}^-$)	960 \times 128	205 min	Exponential	200/100 Hz

Table A4.3. Experimental ^{17}O NMR parameters, calculated^a δ_{iso} values, and assignments of $-\text{COO}^-$ oxygen sites for MIL-53(Al)-*as* and MIL-53(Al)-*np*.

Phase	O type	δ_1 (ppm)	P_Q (MHz)	δ_{iso} (ppm)	$\delta_{\text{iso,calc}}$ (ppm)	O site	C_Q (MHz)	η_Q
MIL-53(Al)- <i>as</i>	$-\text{COO}^-$	239	8.6	233	244.5	O3		
	$-\text{COO}^-$	241	8.1	235	248.0	O2		
MIL-53(Al)- <i>np</i>	$-\text{COO}^-$	235	8.3	229	233.8	O2	7.8	0.8
	$-\text{COO}^-$	240	8.1	234	241.6	O3	7.4	0.6
	$-\text{COO}^-$	265	7.5	260	275.6	O5		
	$-\text{COO}^-$	268	8.1	264	286.3	O4		

The estimated uncertainties are 1 ppm for δ_1 and δ_{iso} , 0.5 MHz for P_Q and C_Q , 0.1 for η_Q , respectively. ^aThe complete calculated ^{17}O NMR parameters are shown in Table A4.4.

3QMAS Experiments at 21.1 T

The rotor-synchronized ^{17}O 3QMAS spectrum of MIL-53(Al)- as with a spinning rate of 18 kHz was acquired by using the soft-pulse-added-mixing (SPAM) MQMAS sequence under the echo/anti-echo mode.³ The durations of excitation, conversion, and soft selective pulses were 3.9, 2.0, and 18.0 μs , respectively. 960 scans were acquired for each t_1 increment, with 16 increments in F1 dimension accumulated. The recycle delay was 5 s. The total acquisition time was approximately 21 h.

Table A4.4. Calculated ^{17}O NMR parameters of three MIL-53(Al) phases.

Phase	O site	$ C_Q $ (MHz)	η_Q	δ_{iso} (ppm)	Δ_{CS} (ppm)	η_{CS}	φ ($^\circ$)	χ ($^\circ$)	ψ ($^\circ$)
MIL-53(Al)- <i>as</i>	O1 (μ^2 -OH)	8.80	0.72	6.5	24	0.32	-10	-85	90
	O2 ($-\text{COO}^-$)	7.54	0.89	248.0	-246	0.43	-90	80	0
	O3 ($-\text{COO}^-$)	7.57	0.91	244.5	-234	0.28	165	90	90
MIL-53(Al)- <i>lp</i>	O1 (μ^2 -OH)	8.97	0.71	7.8	26	0.29	90	90	0
	O2 ($-\text{COO}^-$)	7.49	0.90	243.1	-240	0.32	15	90	90
MIL-53(Al)- <i>np</i>	O1 (μ^2 -OH)	7.45	0.88	3.5	16	0.88	-20	95	15
	O2 ($-\text{COO}^-$)	8.70	0.75	233.8	-237	0.21	-160	80	-90
	O3 ($-\text{COO}^-$)	8.46	0.79	241.6	-243	0.16	-165	80	-90
	O4 ($-\text{COO}^-$)	7.61	0.75	286.3	-278	0.16	10	95	-90
	O5 ($-\text{COO}^-$)	7.43	0.82	275.6	-269	0.20	-175	-95	90
	O6 (H_2O)	9.68	0.74	-34.5	-39	0.45	-20	-100	-165

^aOnly the absolute values of C_Q can be determined in the experiments performed in this work. Therefore, the absolute value of calculated C_Q values are reported as $|C_Q|$.

Appendix A5

Table A5.1. ^{17}O -enrichment details of the MIL-121 materials^a.

Sample	A $\{^{16}\text{O}_2\}$	A $\{^{17}\text{O}_2\}$	R	wR	R $\{^{17}\text{O}/^{16}\text{O}\}$
MIL-121-as	4.69x10 ⁴	2.21x10 ³	4.72		
	4.24x10 ⁴	1.99x10 ³	4.70		
	4.44x10 ⁴	2.00x10 ³	4.51	4.6(1)	4.24(1)
MIL-121-ac	2.11x10 ⁴	1.24x10 ³	5.88		
	4.27x10 ⁴	2.58x10 ³	6.03		
	3.24x10 ⁴	1.89x10 ³	5.82	5.9(1)	5.51(1)
Na@MIL-121	1.03x10 ⁴	3.17x10 ³	3.09		
	1.37x10 ⁴	4.17x10 ³	3.04		
	1.03x10 ⁴	3.17x10 ³	3.09	3.1(1)	2.67(1)
Ca@MIL-121	1.05x10 ⁴	4.55x10 ³	4.32		
	1.13x10 ⁴	5.00x10 ³	4.42		
	1.68x10 ⁴	7.24x10 ³	4.31	4.4(1)	3.95(1)
Ag@MIL-121	1.71x10 ⁴	8.13x10 ³	4.76		
	1.33x10 ⁴	6.04x10 ³	4.53		
	2.17x10 ⁴	1.09x10 ³	5.02	4.7(2)	4.37(1)
In@MIL-121	2.89x10 ⁴	1.34x10 ³	4.65		
	1.21x10 ⁴	5.88x10 ³	4.87		
	4.82x10 ⁴	2.34x10 ³	4.86	4.8(1)	4.39(1)

^aThe A values represent the intensity of the isotopomer. The ratio, R, between the $^{17}\text{O}/^{16}\text{O}$ obtained in triplicate is then averaged and the value wR is obtained. To account for the intensity from the signal of the naturally abundant $^{17}\text{O}/^{16}\text{O}$, the final ^{17}O -exchange rate, R $\{^{17}\text{O}/^{16}\text{O}\}$, was given by the subtraction of wR by 0.041%.

Table A5.2. Additional details for ^{17}O 1D MAS experiments at 19.6 T.

Sample	# of scans	SW	pw90 (μs)	pd (s)	t (h)	LB
MIL-121-as	10240	250 kHz	4.5	1.0	2.8	200
MIL-121-ac	19200	250 kHz	3.0	0.1	0.5	200
Na@MIL-121	19200	250 kHz	3.0	0.1	0.5	200
Ag@MIL-121	10240	250 kHz	4.5	1.0	2.8	200
In@MIL-121	19200	250 kHz	3.0	0.1	0.5	200

Table A5.3. Additional details for ^1H 1D MAS experiments at 19.6 T.

Sample	# of scans	SW	pw90 (μs)	pd (s)	t (s)	LB
MIL-121-as	4	200 kHz	5.0	2.0	8	200
MIL-121-ac	4	200 kHz	5.0	2.0	8	200

Table A5.4. Additional details for ^{17}O 1D MAS experiments at 21.1 T.

Sample	# of scans	SW	pw90 (μs)	pd (s)	t (h)	LB
MIL-121-as	24576	250 kHz	3.0	5.0	34	200
MIL-121-ac	32768	250 kHz	3.0	5.0	45	200

Table A5.5. Additional details for ^{17}O 1D MAS experiments at 35.2 T.

Sample	# of scans	SW	pw90 (μs)	pd (s)	t (min)	LB
MIL-121-as	4095	500 kHz	4.6	0.5	34	200
MIL-121-ac	16384	500 kHz	4.0	0.5	136	200
Na@MIL-121	4095	500 kHz	4.0	0.5	34	200
Ca@MIL-121	4095	500 kHz	4.5	0.3	20	200
Ag@MIL-121	1024	500 kHz	4.6	0.5	8.5	200

Table A5.6. Additional details for ^{17}O 3QMAS experiments at 19.6 T.

Sample	# of scans	SW	^{17}O pw90 (μs)	^1H pw90 (μs)	pd (s)	TD(F1)	t (h)	LB
MIL-121-as	8192	250 kHz	3.0	5.0	0.1	12	2.7	200
MIL-121-ac	8192	500 kHz	3.0	5.0	0.1	4	0.9	200

Table A5.7. Additional details for ^{17}O 3QMAS experiments at 19.6 T.

Sample	^{17}O pw90 (μs)	# scans	TD(F1)	pd (s)	t (h)
MIL-121-as	5.0	8192	12	0.1	2.7
MIL-121-ac	5.0	65536	2	0.1	3.6
Na@MIL-121	5.0	8192	4	0.1	0.91
Zn@MIL-121	5.0	8192	8	0.1	1.8
In@MIL-121	5.0	8192	4	0.1	0.91

Table A5.8. Additional details for ^{17}O 3QMAS experiments at 35.2 T.

Sample	^{17}O pw90 (μs)	SW	# scans	TD(F1)	pd (s)	t (h)
MIL-121-as	5.0	500	960	32	0.1	0.8
Na@MIL-121	4.0	500	12000	14	0.1	4.6
Ca@MIL-121	4.0	500	12000	14	0.1	4.6
Ag@MIL-121	5.0	500	960	32	0.1	0.8

Table A5.9. Experimental ^{17}O EFG of MIL-121-as and MIL-121-ac obtained from 3QMAS spectra acquired at 19.6 T. ^aObtained from simulation of F1 cross-sections of 3QMAS.

Sample	Site	O type	δ_1 (ppm)	δ_2 (ppm)	P_Q (MHz)	δ_{iso} (ppm)	δ_{iso}^a (ppm)	C_Q (MHz)	η_Q (ppm)
MIL-121-as	O1	μ_2 -OH	30	8	5.3	22	23	5.0	0.80
	O5	COH	191	153	7.0	177	177	7.0	0.30
	O2/O3	CO_2^-	250	209	7.4	235	239	7.1	0.90
	O2/O3	CO_2^-	258	218	7.3	243	249	7.1	0.90
	O4	C=O	351	299	8.2	332	329	7.9	0.20
MIL-121-ac	O1	COH	30	9	5.2	22	21	4.9	0.80
	O5	CO_2^-	191	152	7.1	177	177	7.3	0.15
	O2/O3	CO_2^-	251	206	7.7	234	235	7.2	0.80
	O2/O3	C=O	264	219	7.7	247	248	7.0	0.90
	O4	μ_2 -OH	352	303	8.1	334	332	8.3	0.20

Table A5.10. ^{17}O EFG and CSA parameters of MIL-121-as and MIL-121-ac used as input for refinement of spectral parameters.

Sample	Site	O type	Intensity	δ_{iso} (ppm)	C_Q (MHz)	η_Q	Δ_{CS} (ppm)	η_{CS}	ϕ ($^\circ$)	χ ($^\circ$)	ψ ($^\circ$)
MIL-121-as	O1	$\mu_2\text{-OH}$	23	22	5.0	0.80	65	0.7	90	0	0
	O5	COH	25	172	7.0	0.20	252	1.0	0	0	0
	O2	CO_2^-	19	235	7.1	0.90	-182	0.8	170	80	45
	O3	CO_2^-	19	243	7.1	0.90	-182	0.8	170	80	45
	O4	C=O	14	327	7.9	0.20	-434	0	0	0	0
MIL-121-ac	O1	$\mu_2\text{-OH}$	46	22	4.9	0.80	65	0.7	90	0	0
	O5	COH	21	177	7.3	0.15	252	1.0	0	0	0
	O2	CO_2^-	9	235	7.2	0.80	-182	0.8	170	80	45
	O3	CO_2^-	9	248	7.0	0.90	-182	0.8	170	80	45
	O4	C=O	14	333	8.3	0.20	-434	0	0	0	0

Table A5.11. ^{17}O EFG parameters of Na@MIL-121 and Ag@MIL-121.

Sample	Site	O type	δ_1 (ppm)	δ_2 (ppm)	P_Q (MHz)	δ_{iso} (ppm)	δ_{iso}^a (ppm)	C_Q (MHz)	η_Q (ppm)
MIL-121-as	O1	$\mu_2\text{-OH}$	30	8	5.3	21	26	5.0	0.70
	O5	COH	191	153	7.0	177	178	7.0	0.20
	O2	CO_2^-	250	209	7.4	235	237	7.1	0.95
	O3	CO_2^-	258	218	7.3	243	250	7.1	0.85
	O4	C=O	-	-	-	-	335	7.9	0.20
MIL-121-ac	O1	COH	30	9	5.2	22	23	4.9	0.85
	O5	CO_2^-	191	152	7.1	177	178	7.3	0.25
	O2	CO_2^-	251	206	7.7	234	235	7.2	0.80
	O3	C=O	264	219	7.7	247	251	7.0	0.80
	O4	$\mu_2\text{-OH}$	352	303	8.1	334	333	8.3	0.25

Table A5.12. Metal exchange percentage of the metal-loaded MIL-121 samples.

Sample	ICP-MS	^{17}O NMR
Na@MIL-121	42	50
Ca@MIL-121	5	-
Ag@MIL-121	30	25
In@MIL-121	6.5	-

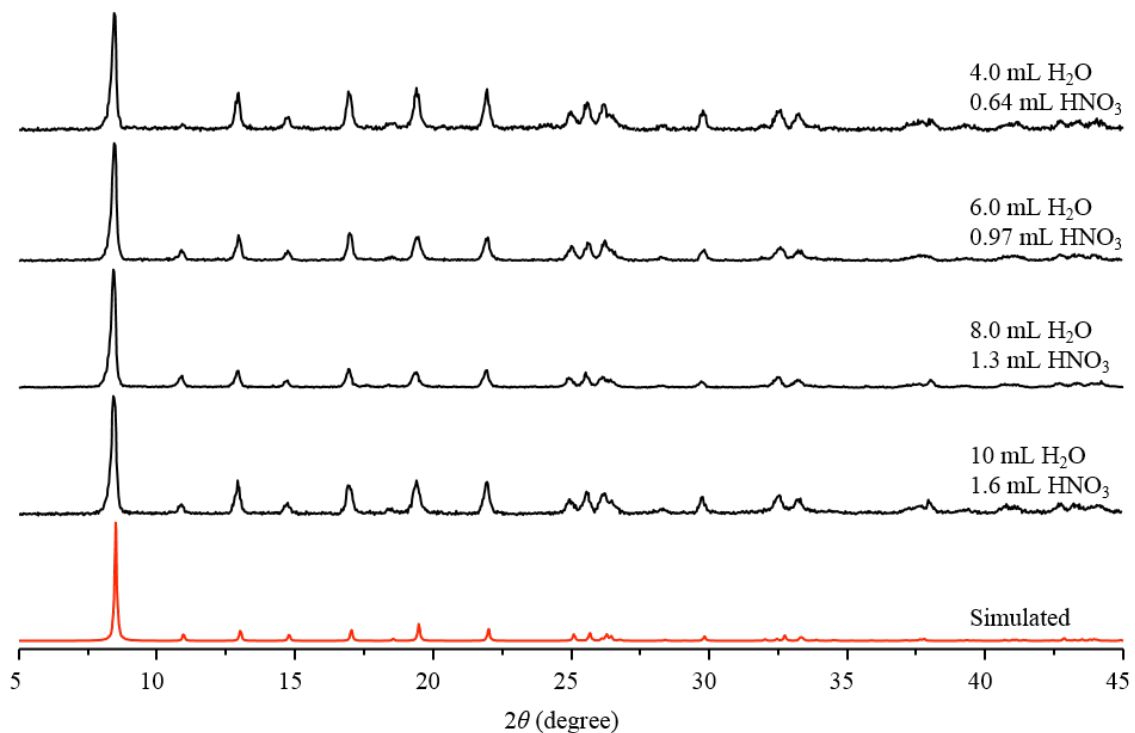


Figure A5.1. Powder X-ray diffraction pattern of MIL-121 samples synthesized with varied amounts of water. Cu-K α ($\lambda = 1.541 \text{ \AA}$). The water volume was varied from 10 mL (original method) to 2 mL, while keeping the volume of 4.0 M HNO₃ at a 10/1.6 (H₂O/HNO₃ v/v).

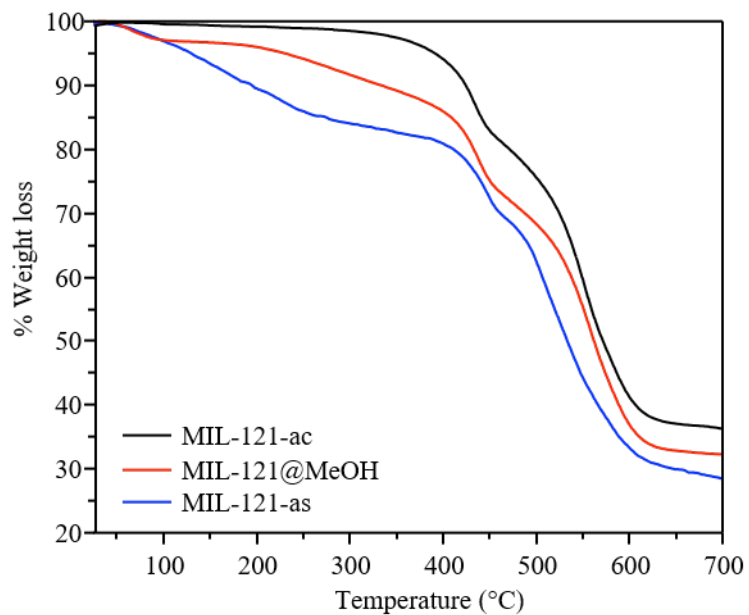


Figure A5.2. Thermogravimetric weight loss profiles for MIL-121 samples. As-made sample shows a constant weight loss rate up to around 300 °C.

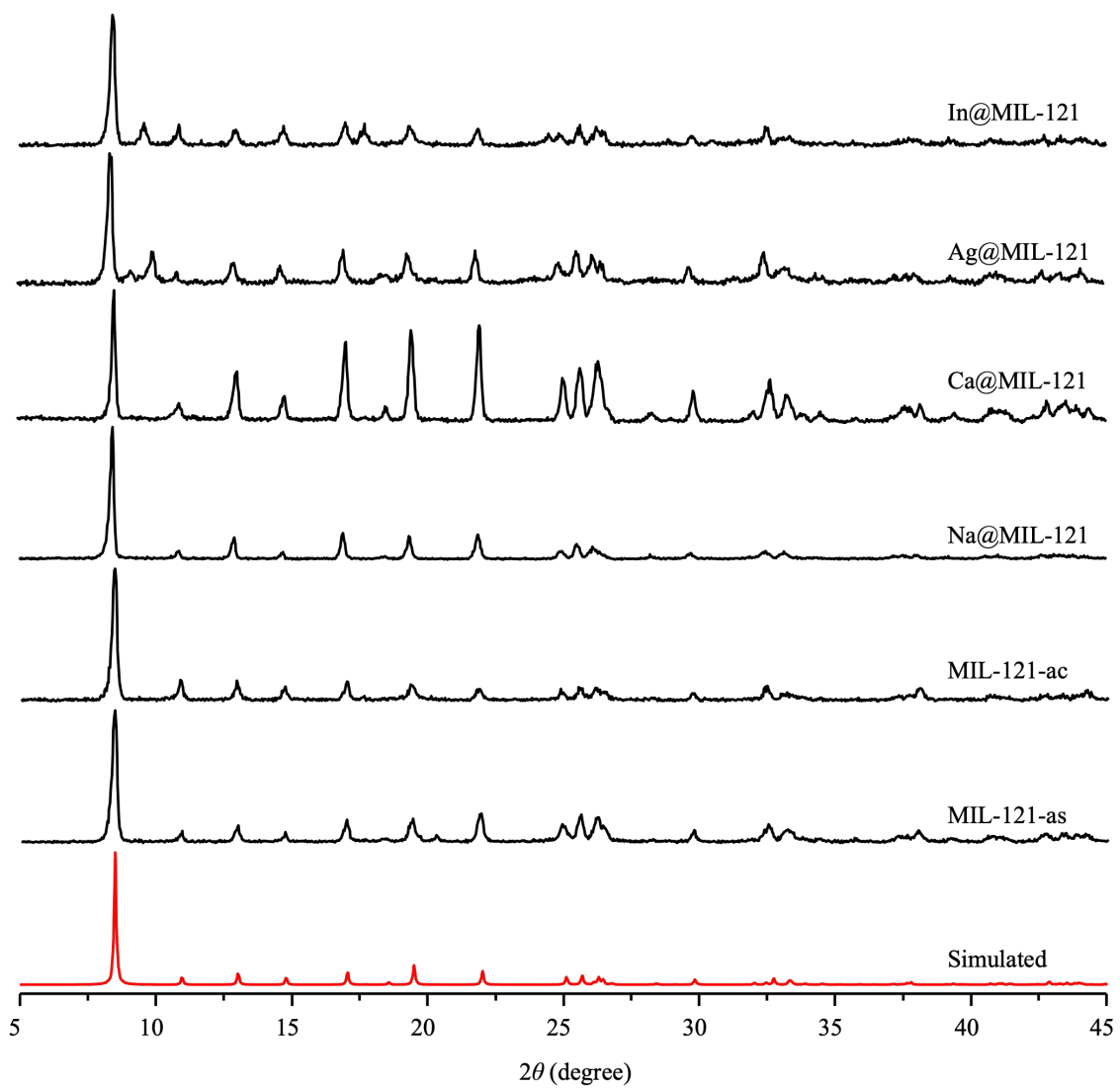


Figure A5.3. Powder X-ray diffraction pattern of ^{17}O -labelled MIL-121 samples. Cu-K α ($\lambda = 1.540 \text{ \AA}$).

Crystallographic non-equivalent H species

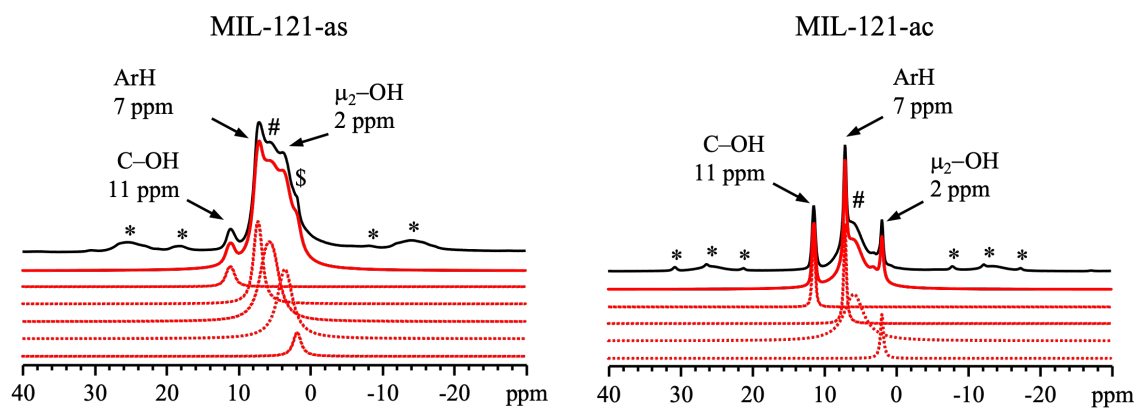
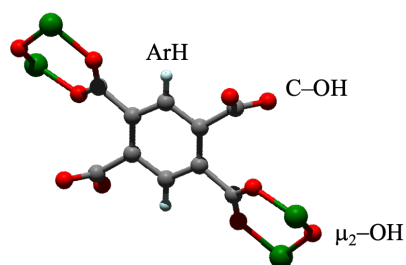


Figure A5.4. ¹H MAS SSNMR spectra of MIL-121 samples acquired at 19.5 T using a spinning speed of 16.0 kHz. The * label denotes spinning sidebands. The # label denotes adsorbed water within the pores. The \$ label denotes water adsorbed on the surface of the sample. Adsorption of water might occur during the packing of samples in the rotor.

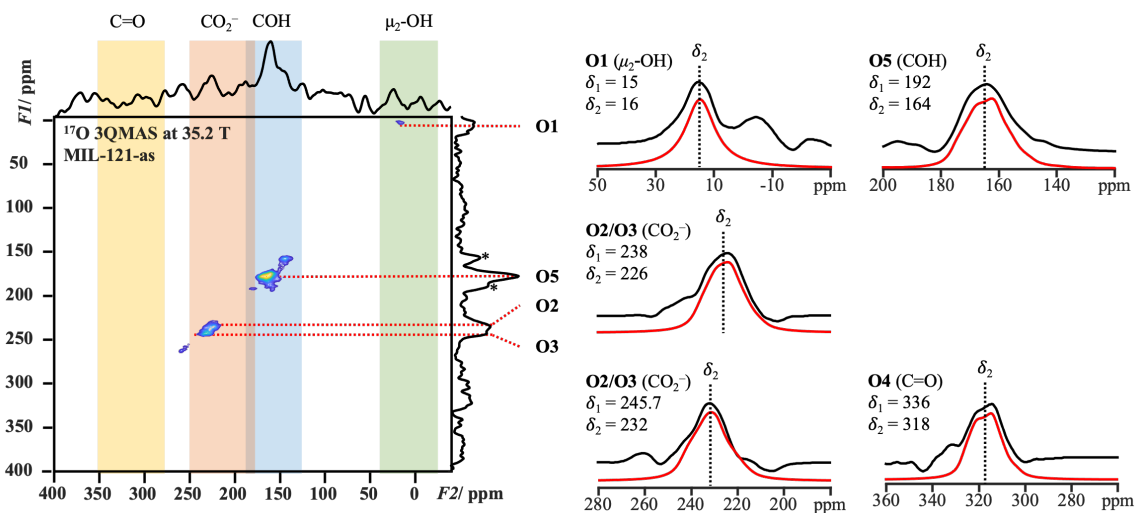


Figure A5.5. ^{17}O 3QMAS spectrum of MIL-121-as acquired at 35.2 T using a spinning speed of 16.0 kHz. The * label denotes spinning sidebands.

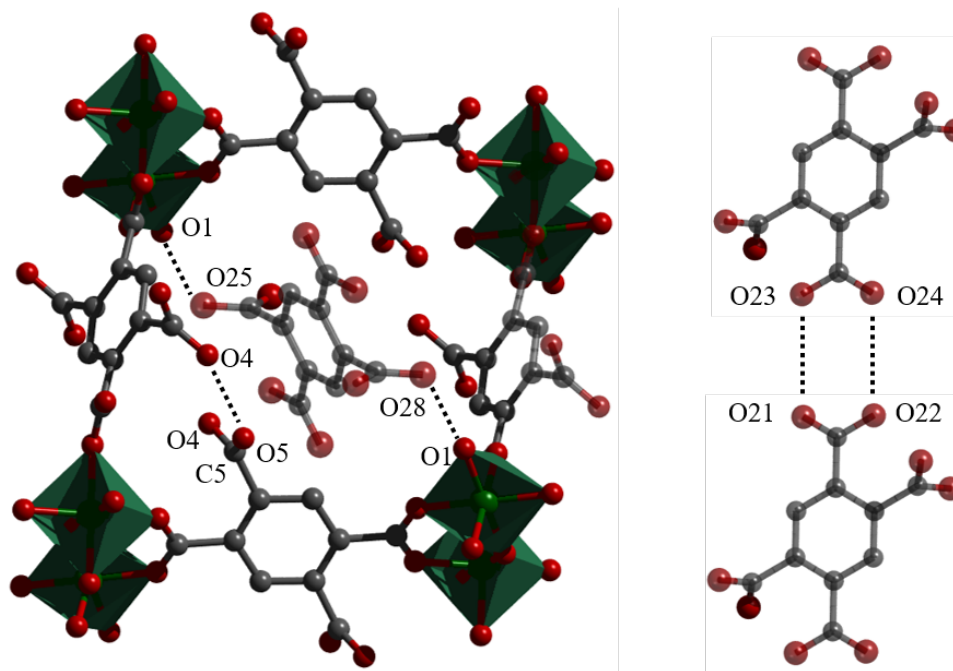


Figure A5.6. Representation of the main hydrogen bonding interactions taking place in the crystal structure of the MIL-121-as.

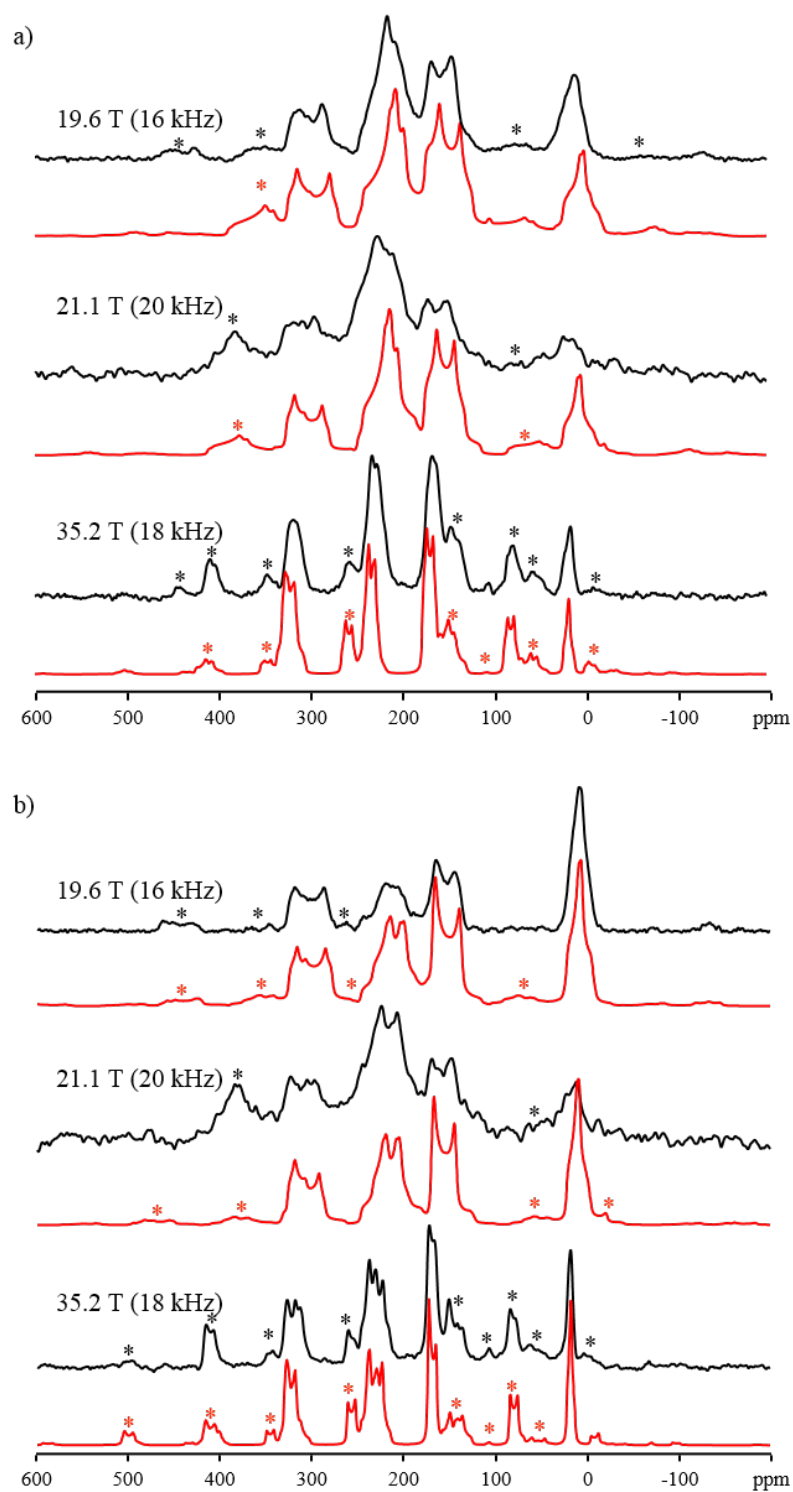


Figure A5.7. ^{17}O parameters for a) MIL-121-as and b) MIL-121-ac at different magnetic fields. Blue lines represent experimental and red lines represent simulated.

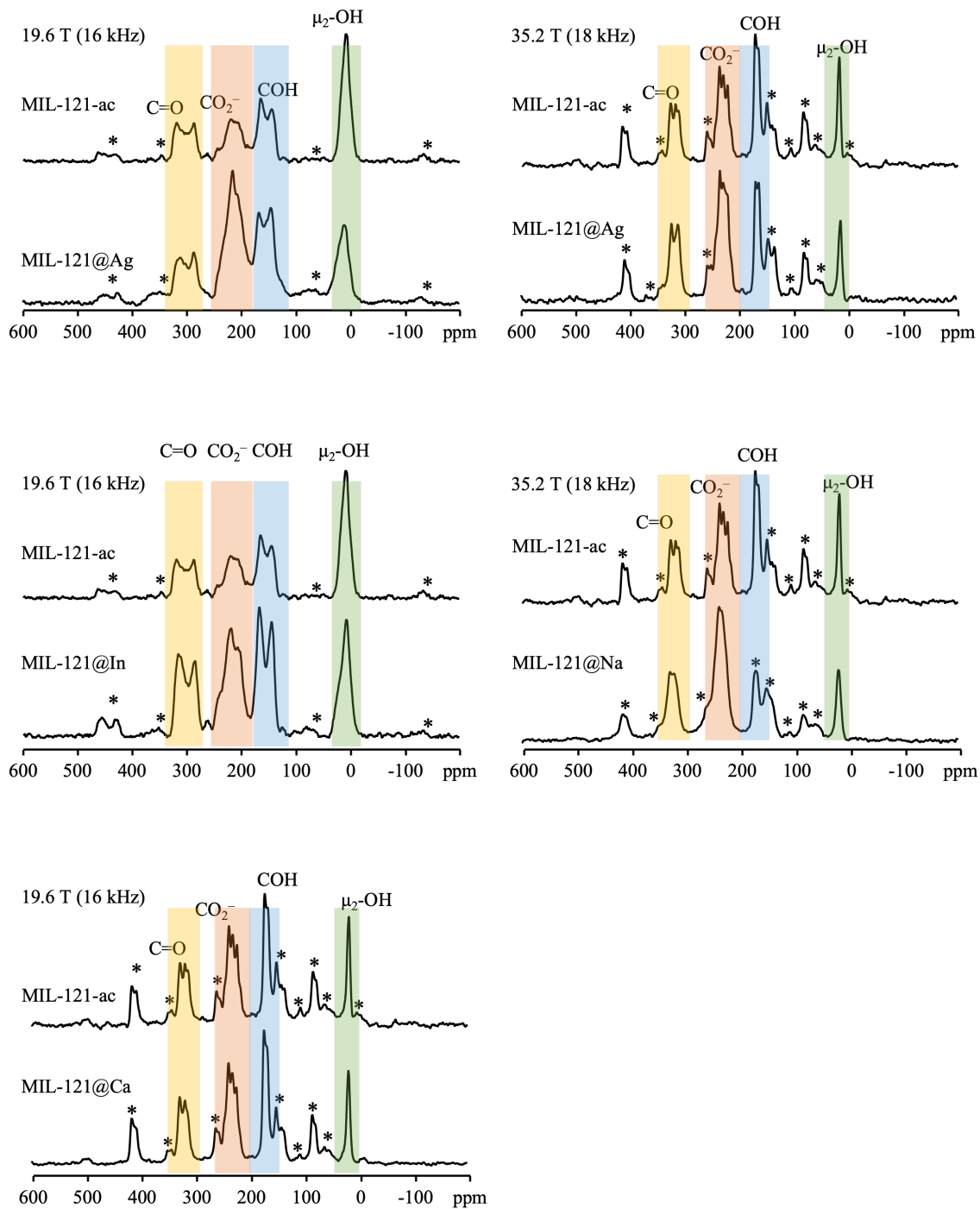


Figure A5.8. Experimental and simulated ^{17}O 1D MAS spectra of metal-loaded acquired at 19.2 T with spinning rate of 16 kHz and at 35.2 and spinning rate of 18 kHz. Spinning sidebands are denoted by asterisk.

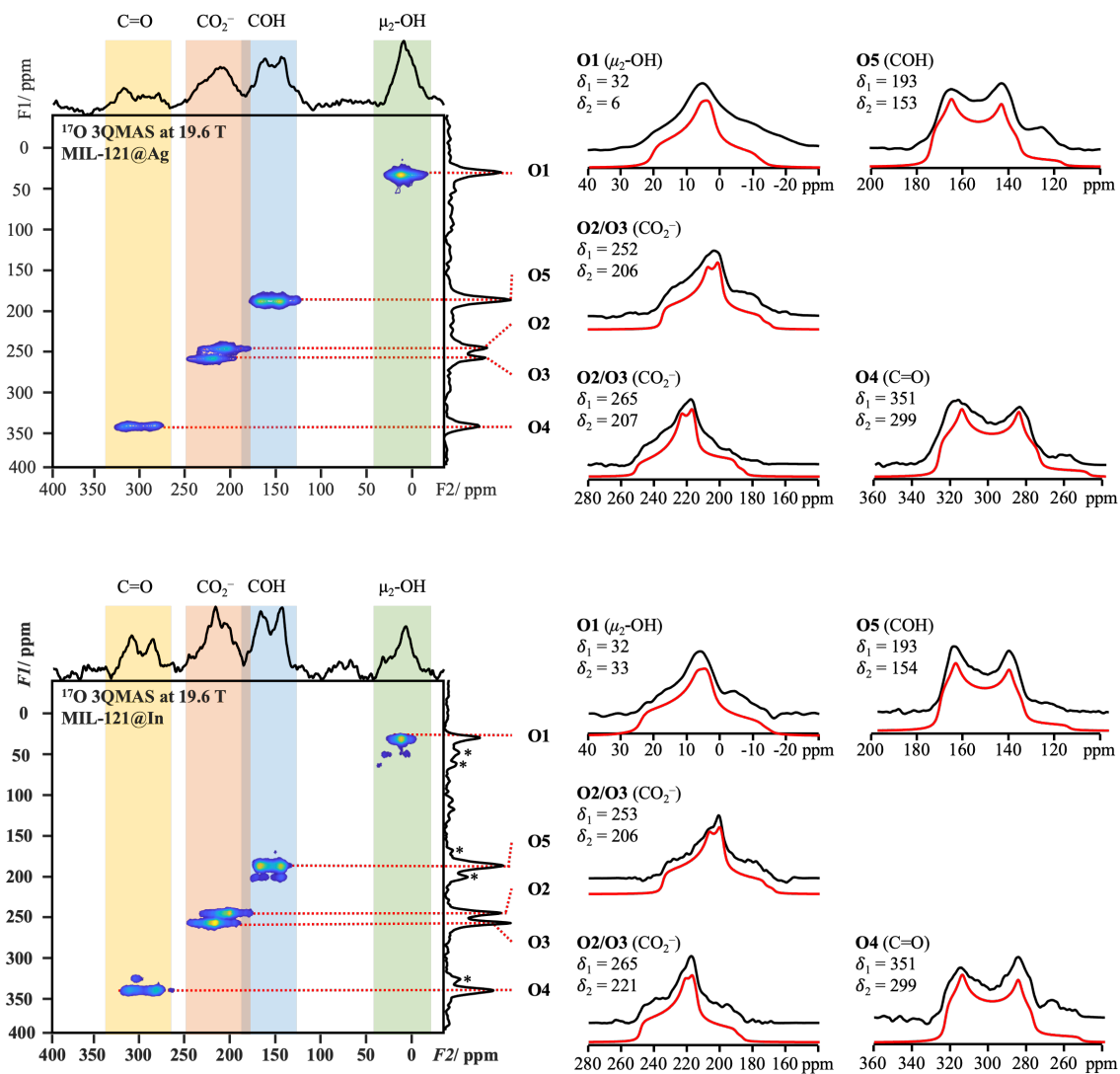


Figure A5.9. ^{17}O 3QMAS spectra of Ag@MIL-121 and In@MIL-121 acquired at 19.6 T with a spinning rate of 16 kHz.

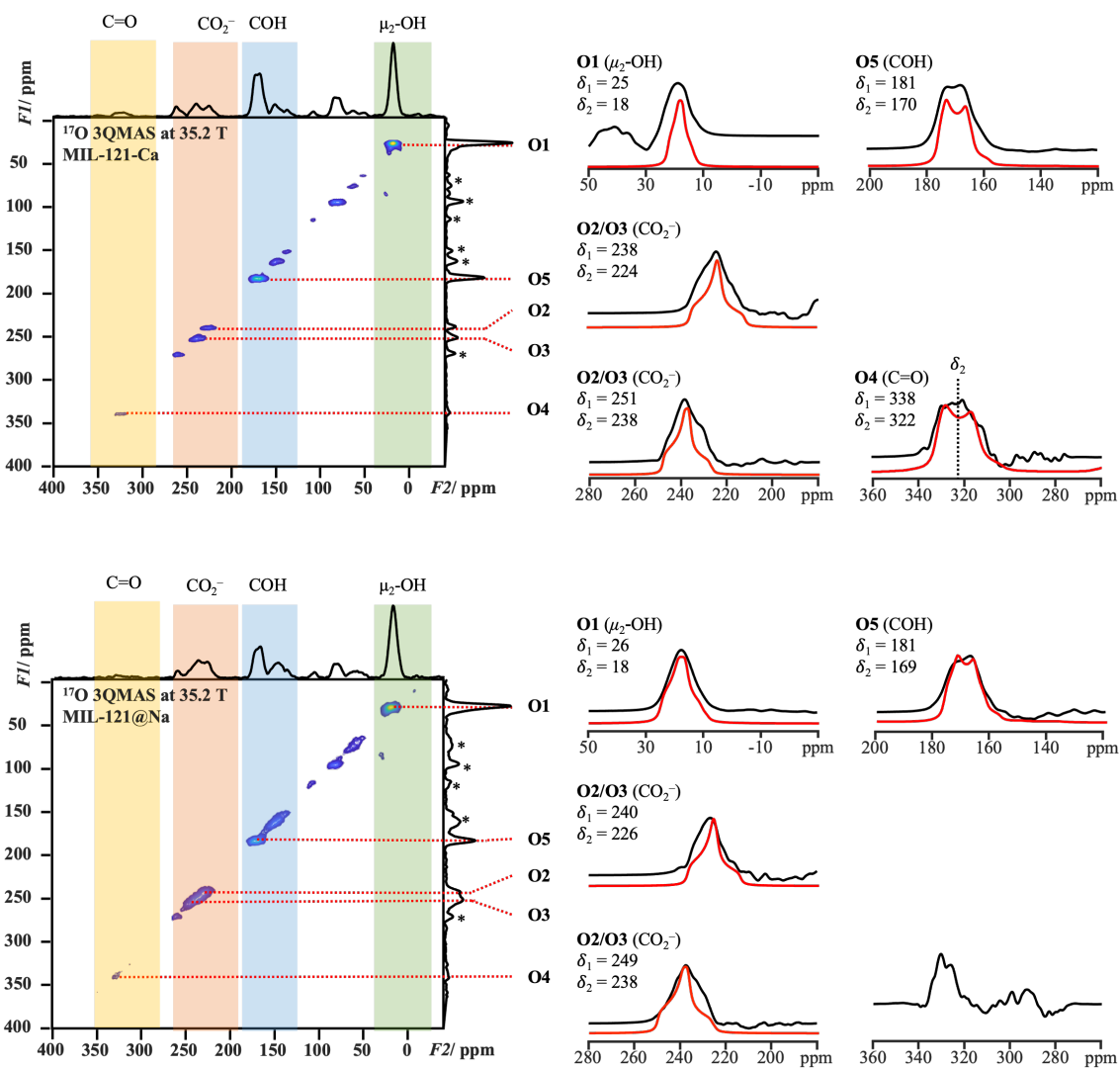


Figure A5.10. ^{17}O 3QMAS spectra of Na@MIL-121 and Ca@MIL-121 acquired at 19.6 T with a spinning rate of 16 kHz.

Appendix A6

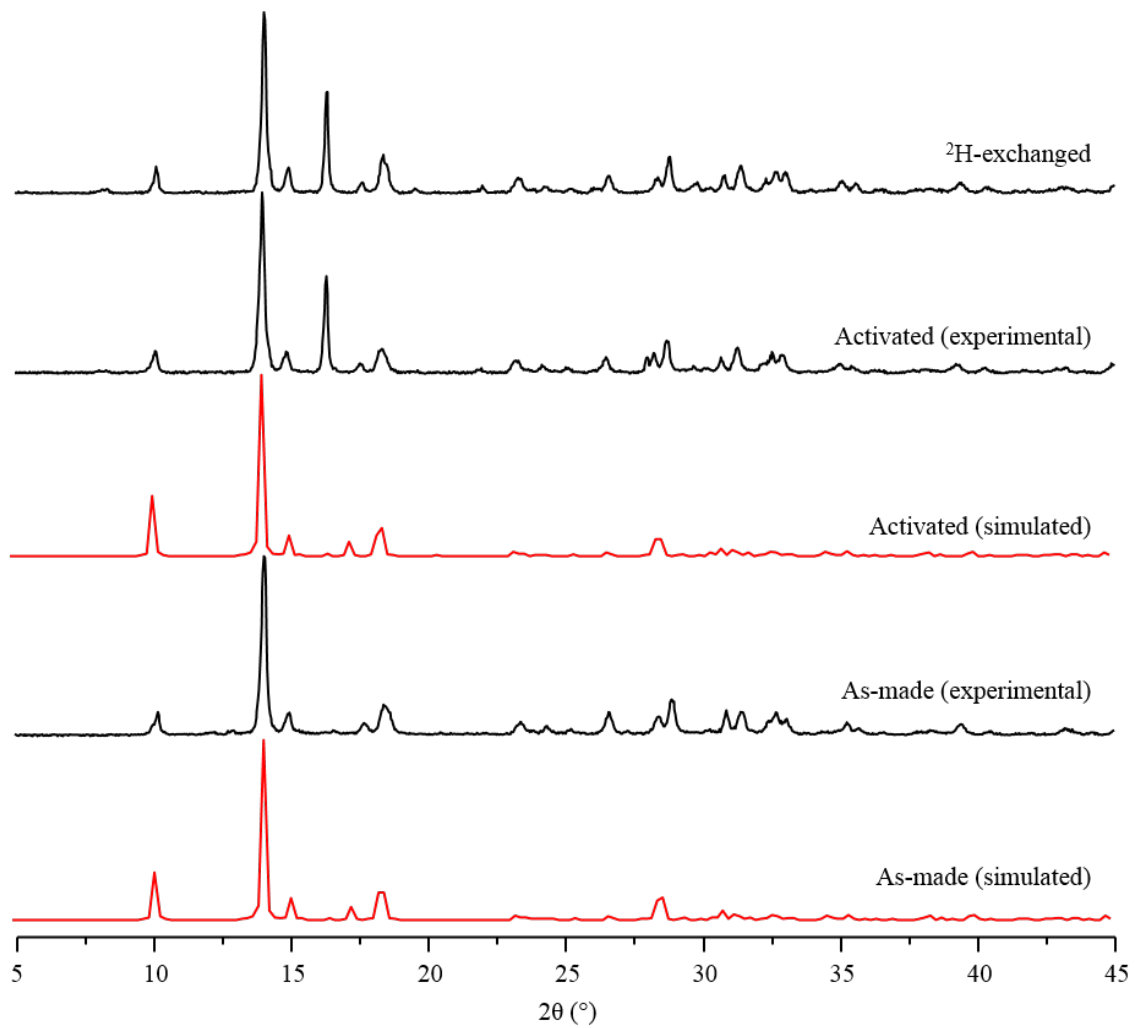


Figure A6.2. Powder XRD diffractograms of ZnAtzOx samples.

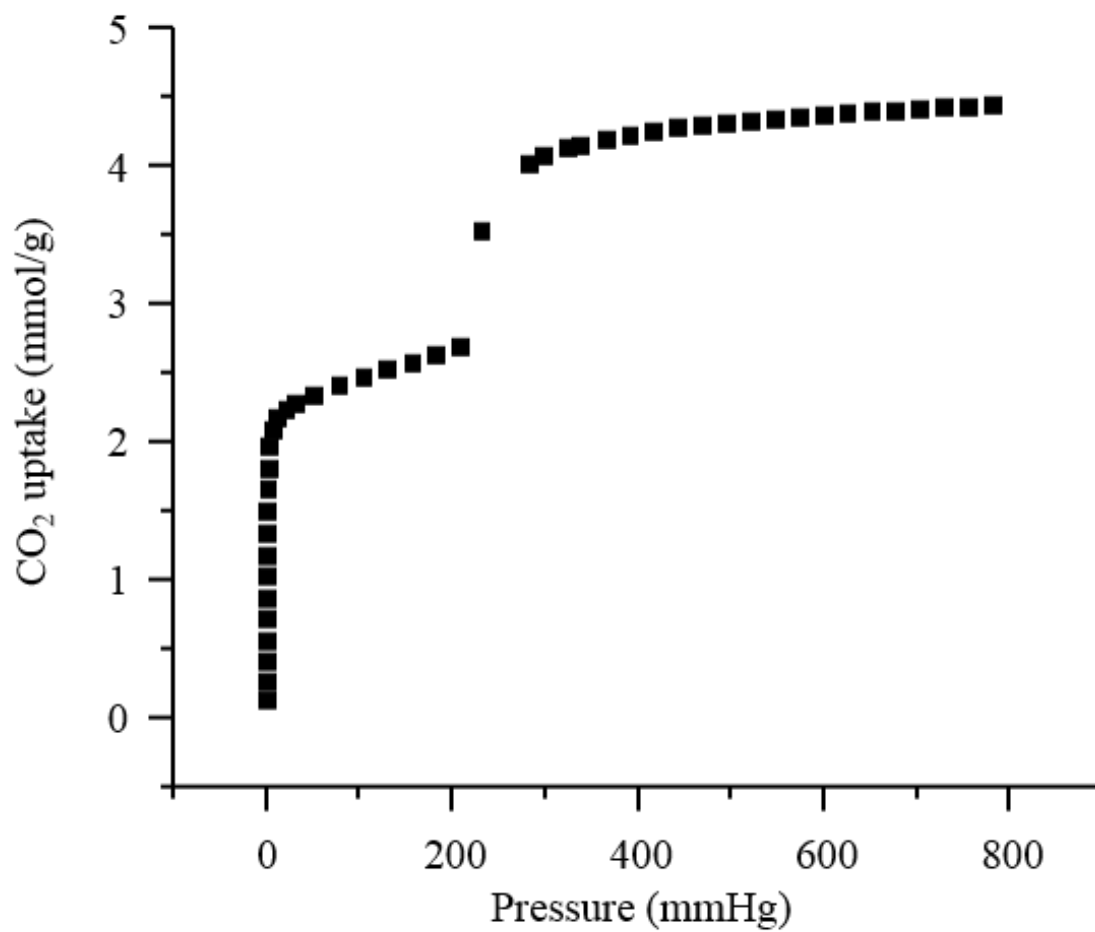


Figure A6.3. CO₂ adsorption isotherm of ZnAtzOx measured at 77 K.

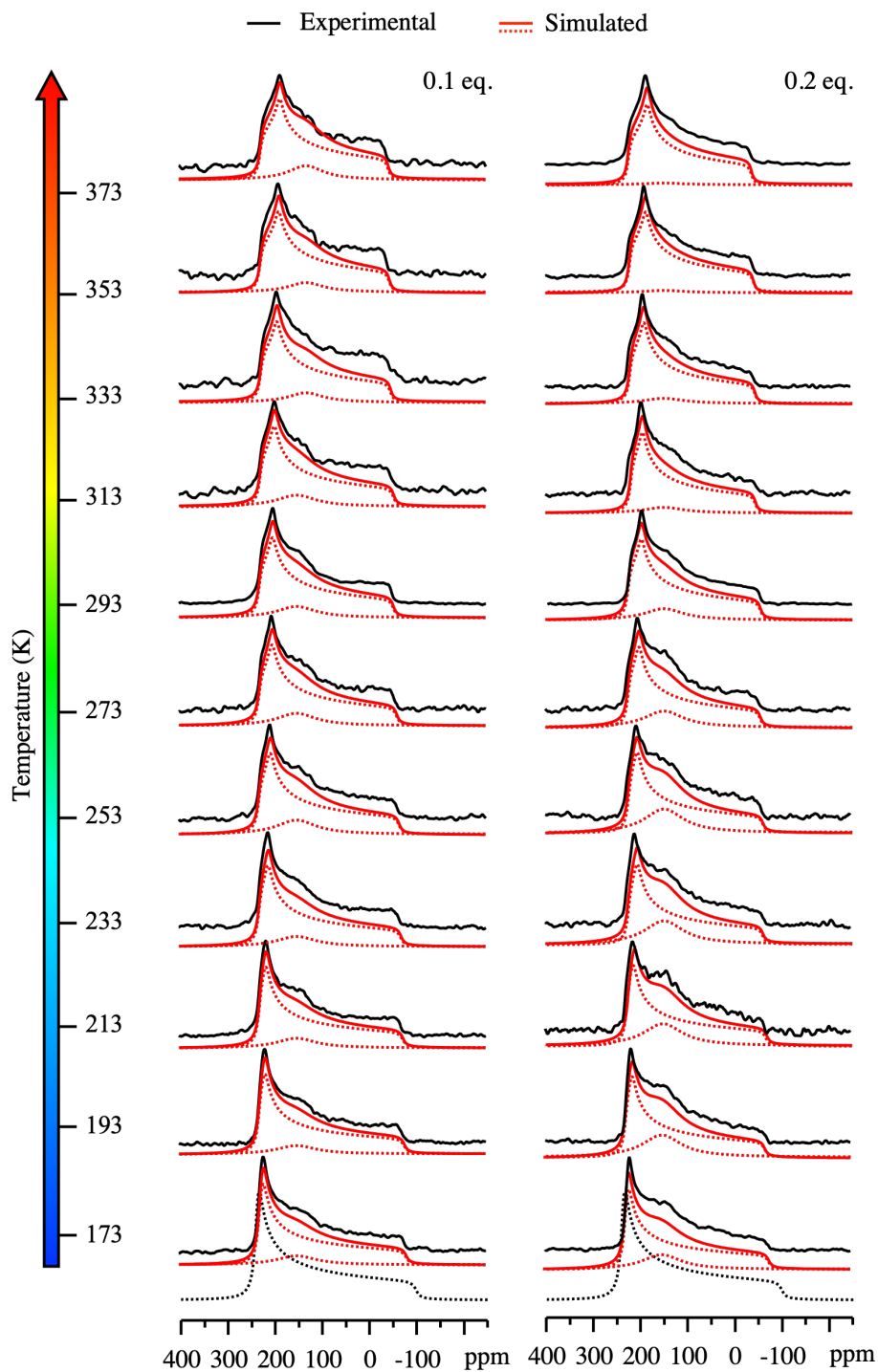


Figure A6.4. Experimental and simulated VT static ^{13}C NMR spectra of ZnAtzOx loaded with 0.1, and 0.2 equivalent of $^{13}\text{CO}_2$.

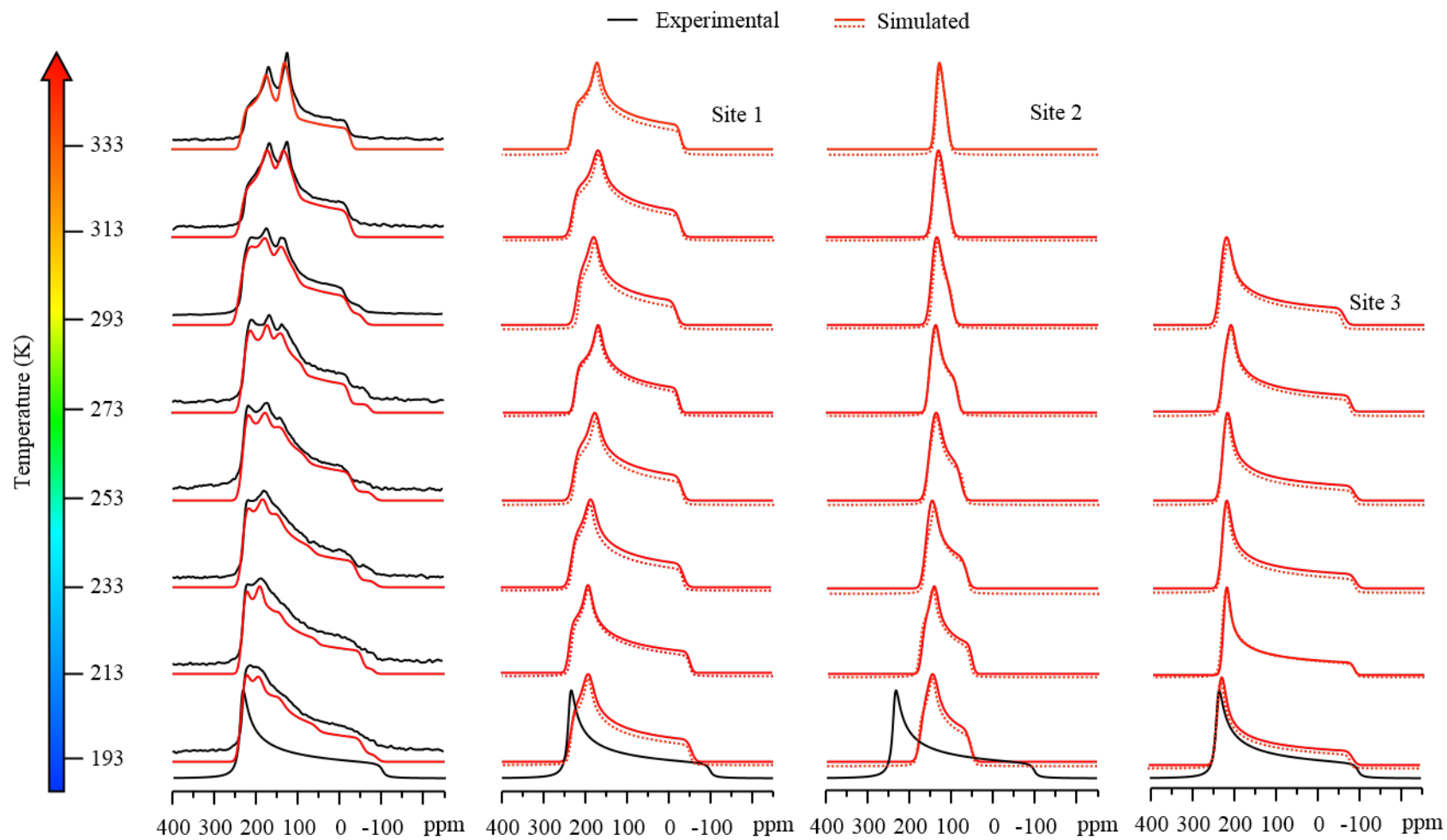


Figure A6.5 Experimental and simulated VT static ^{13}C NMR spectra of ZnAtzOx loaded with 0.5 equivalent $^{13}\text{CO}_2$.

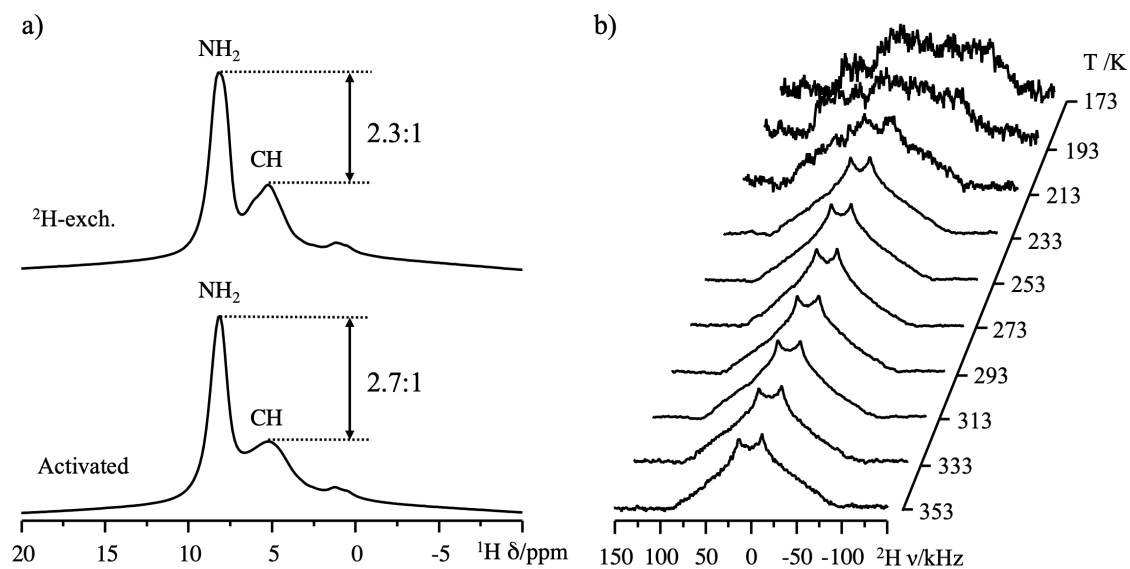


Figure A6.6. a) ^1H MAS spectra of ZnAtzOx-ac and ^2H -exchanged ZnAtzOx-ac (spinning rate of 8 kHz); b) Experimental and simulated ^2H static VT spectra of ^2H -exchanged ZnAtzOx-ac.

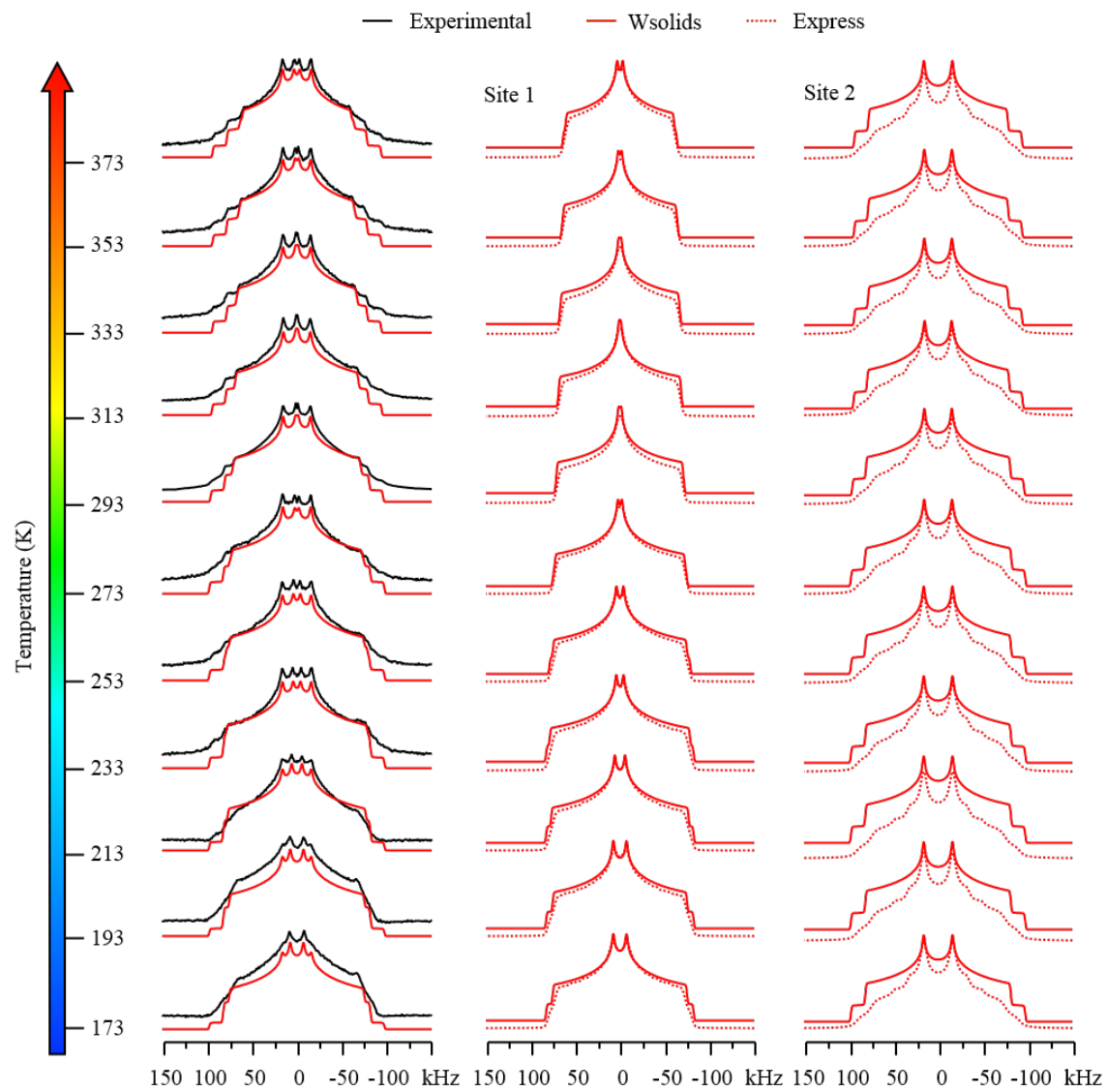


Figure A6.7. Experimental and simulated VT static ^2H NMR spectra of ZnAtzOx loaded with 2% D_2O .

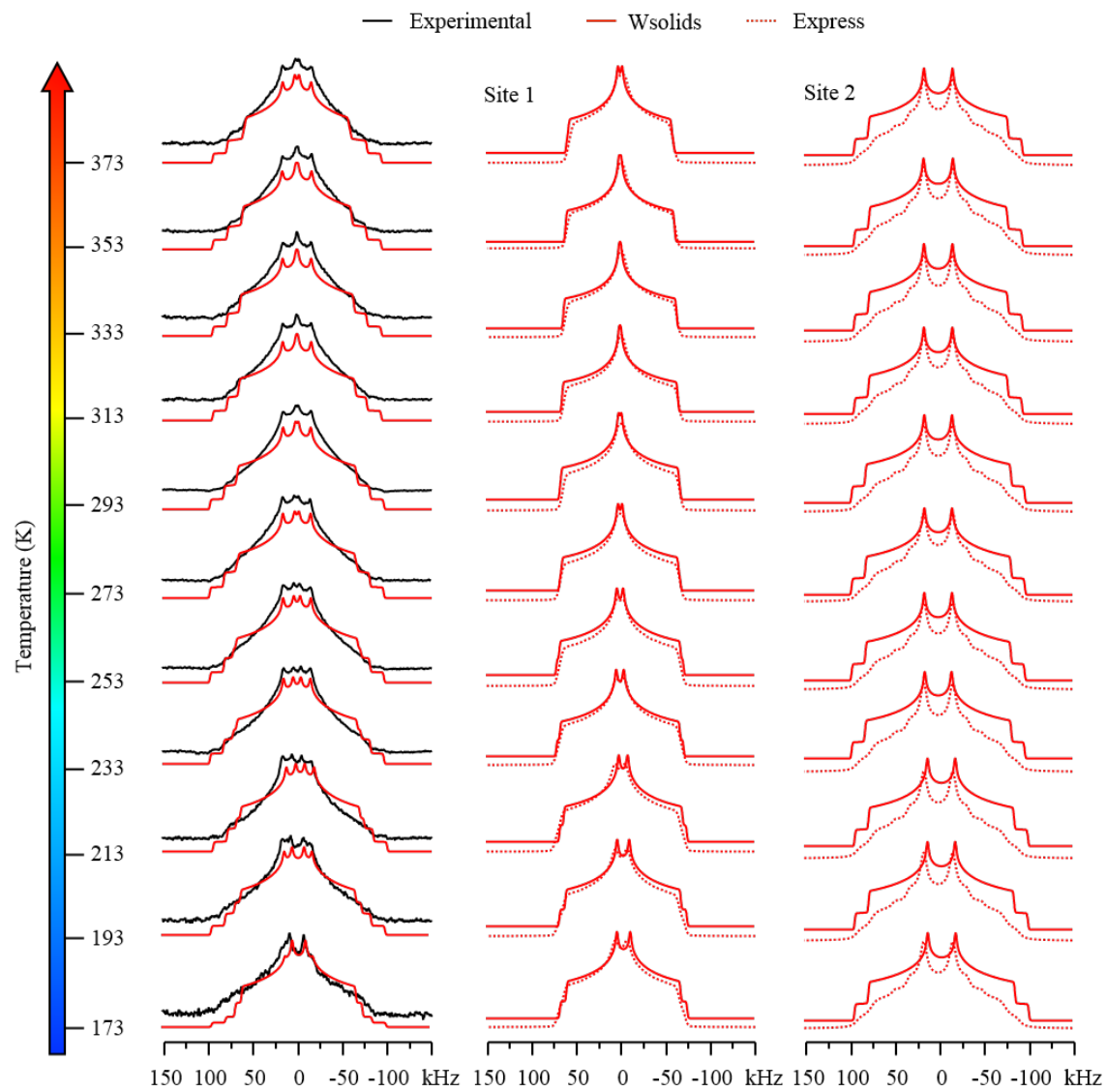


Figure A6.8. Experimental and simulated VT static ^2H NMR spectra of ZnAtzOx loaded with 4% D_2O .

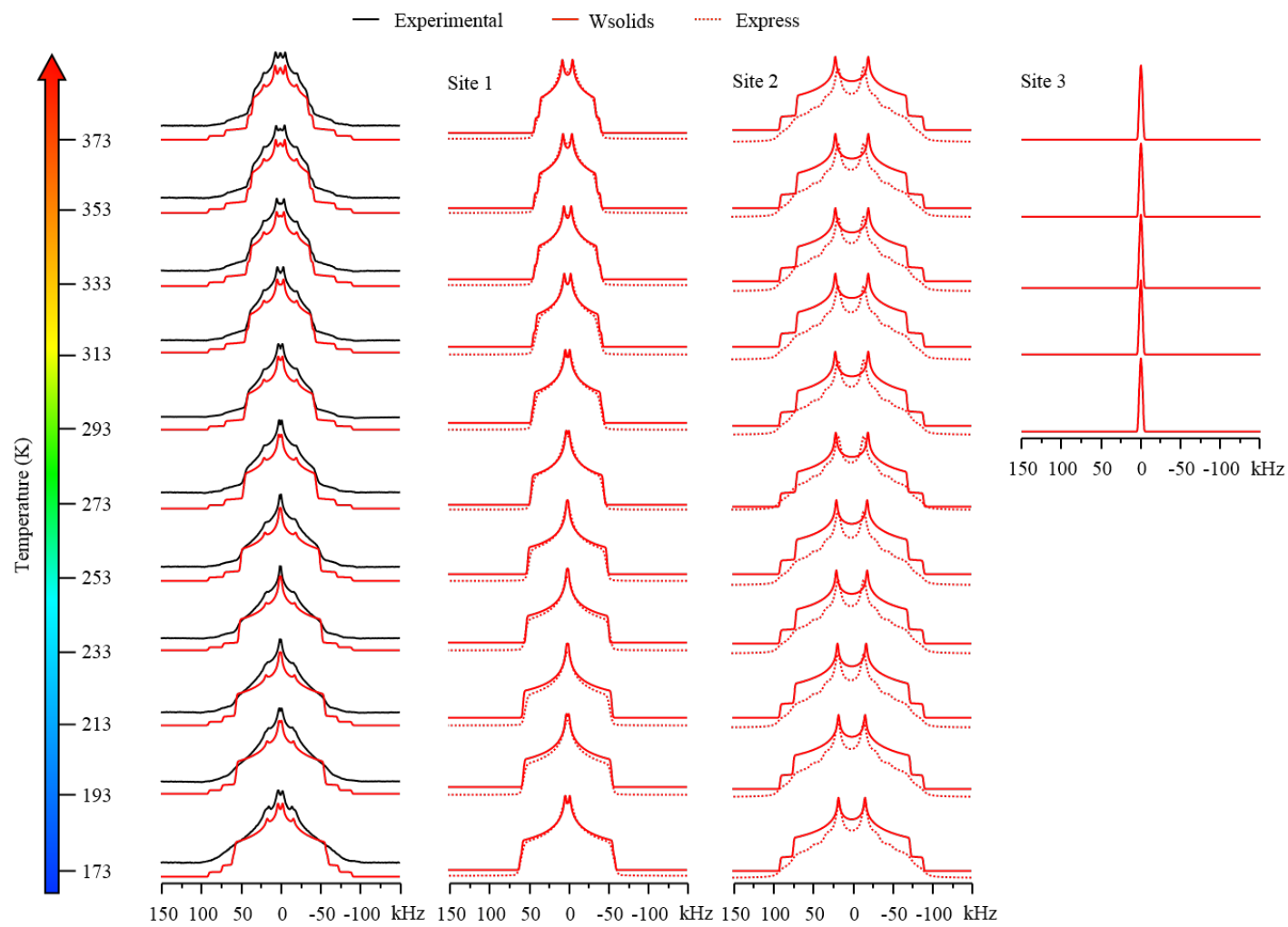


Figure A6.9. Experimental and simulated VT static ^2H NMR spectra of ZnAtzOx loaded with 8% D_2O .

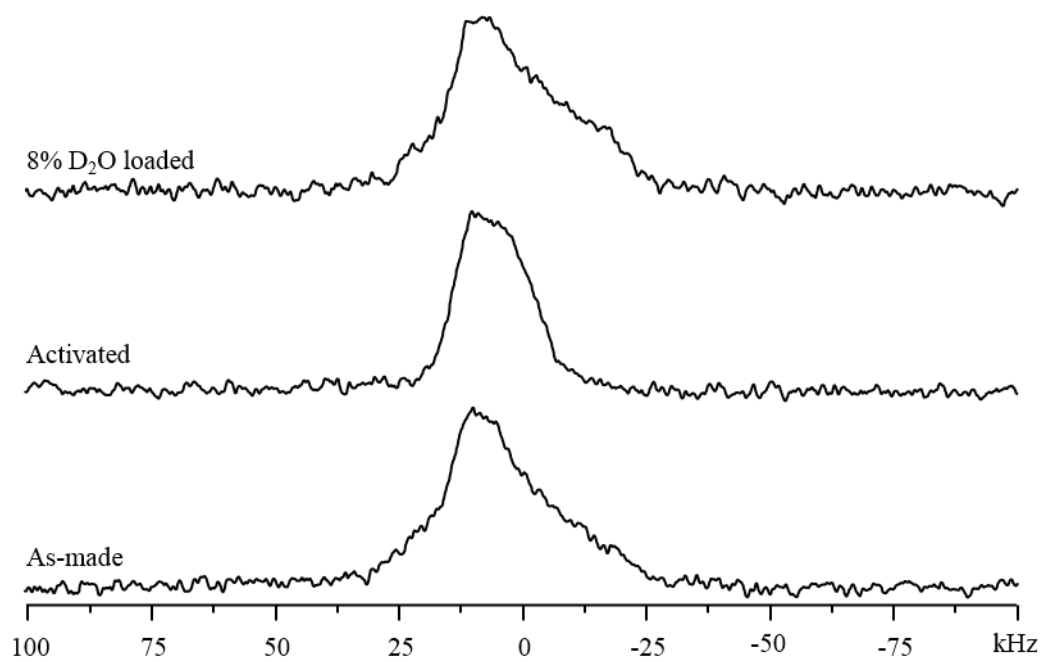


Figure A6.10. Experimental ^{67}Zn static spectra of ZnAtzOx samples.

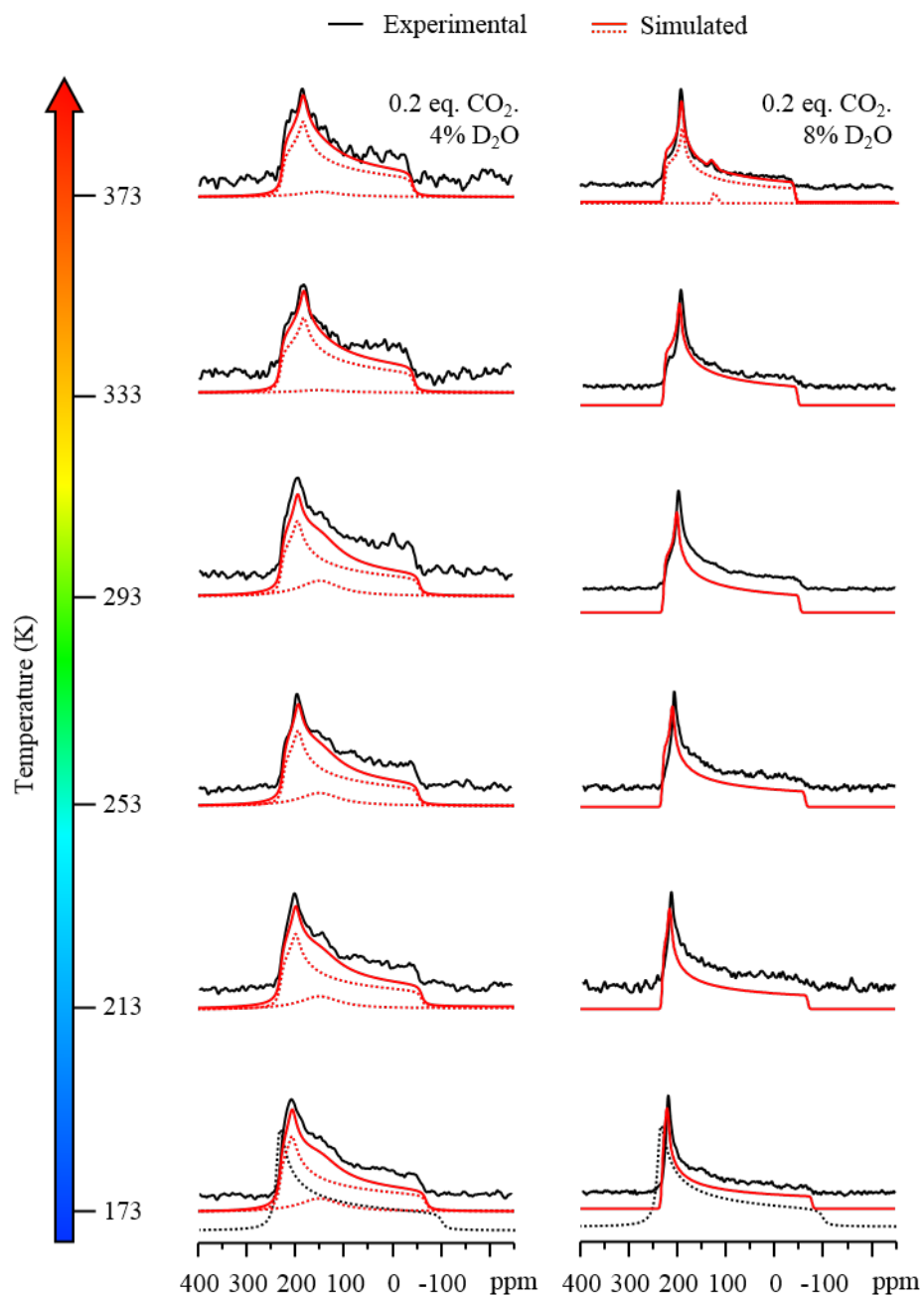


Figure A6.11. Experimental and simulated VT static ¹³C NMR spectra of ZnAtzOx loaded with 0.2 equivalent ¹³CO₂ and different amount of D₂O.

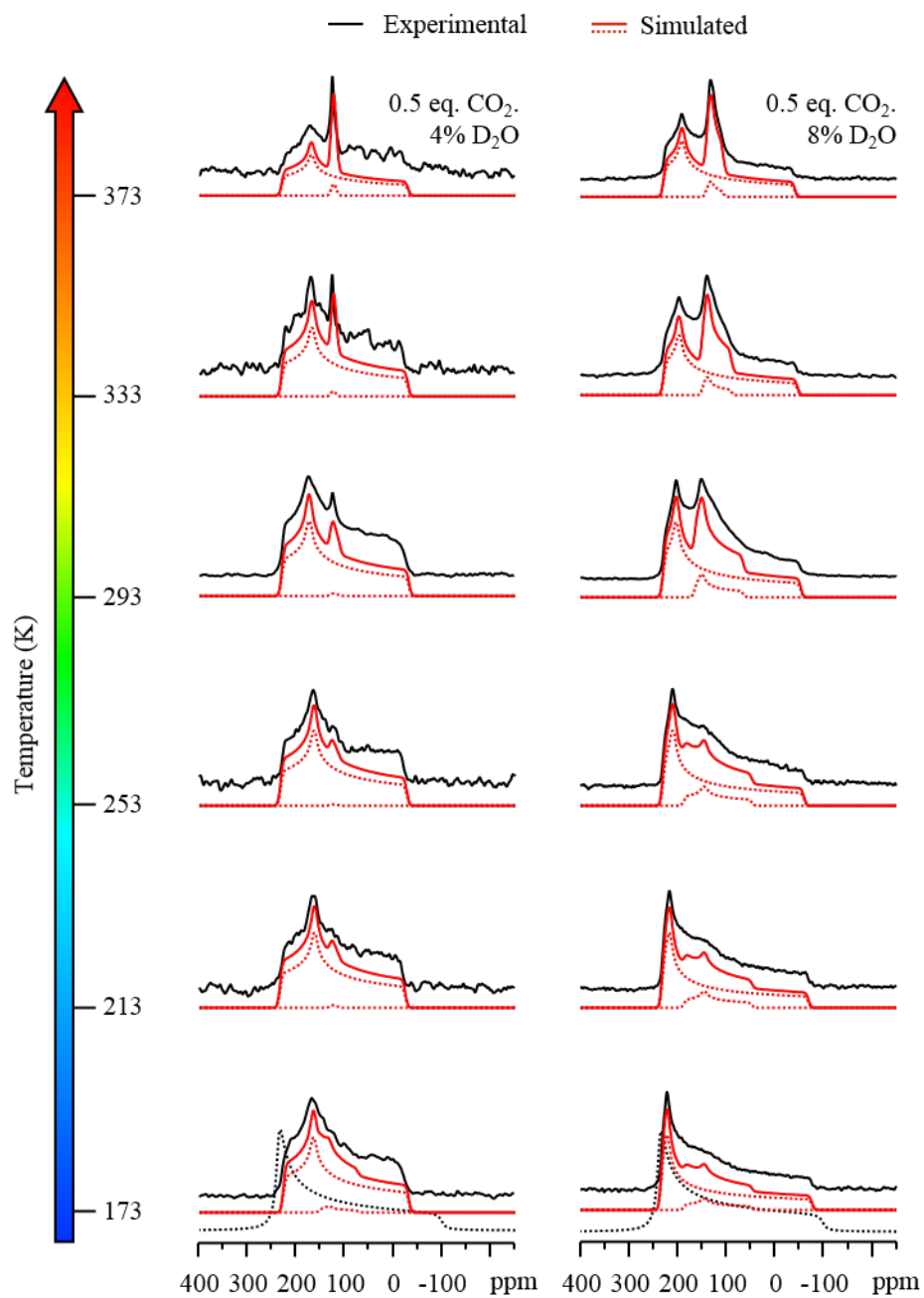


Figure A6.12. Experimental and simulated VT static ¹³C NMR spectra of ZnAtzOx loaded with 0.2 equivalent ¹³CO₂ and different amount of D₂O.

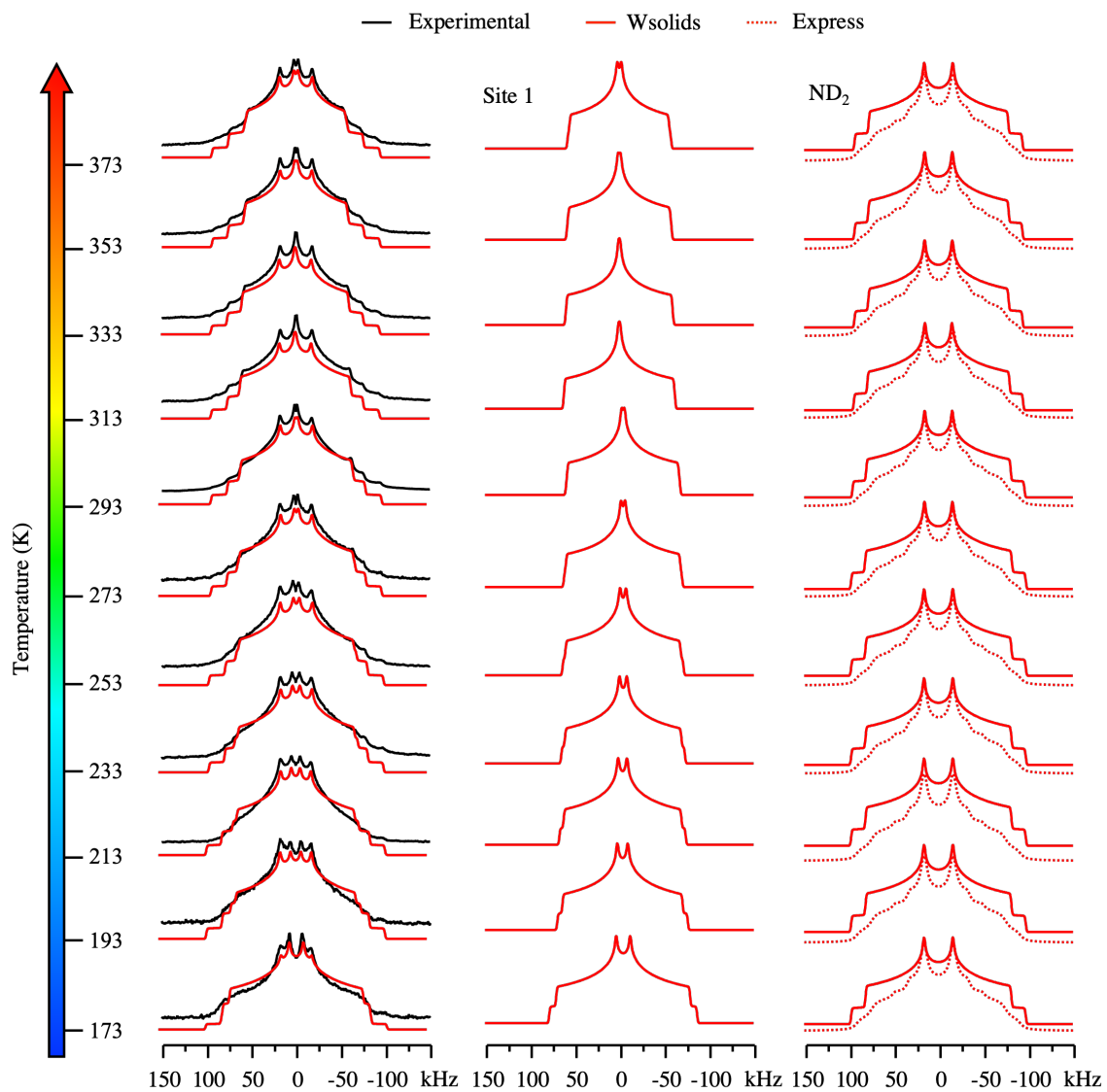


Figure A6.13. Experimental and simulated VT static ^2H NMR spectra of ZnAtzOx co-loaded with 4% D_2O and 0.2 equivalent of CO_2 .

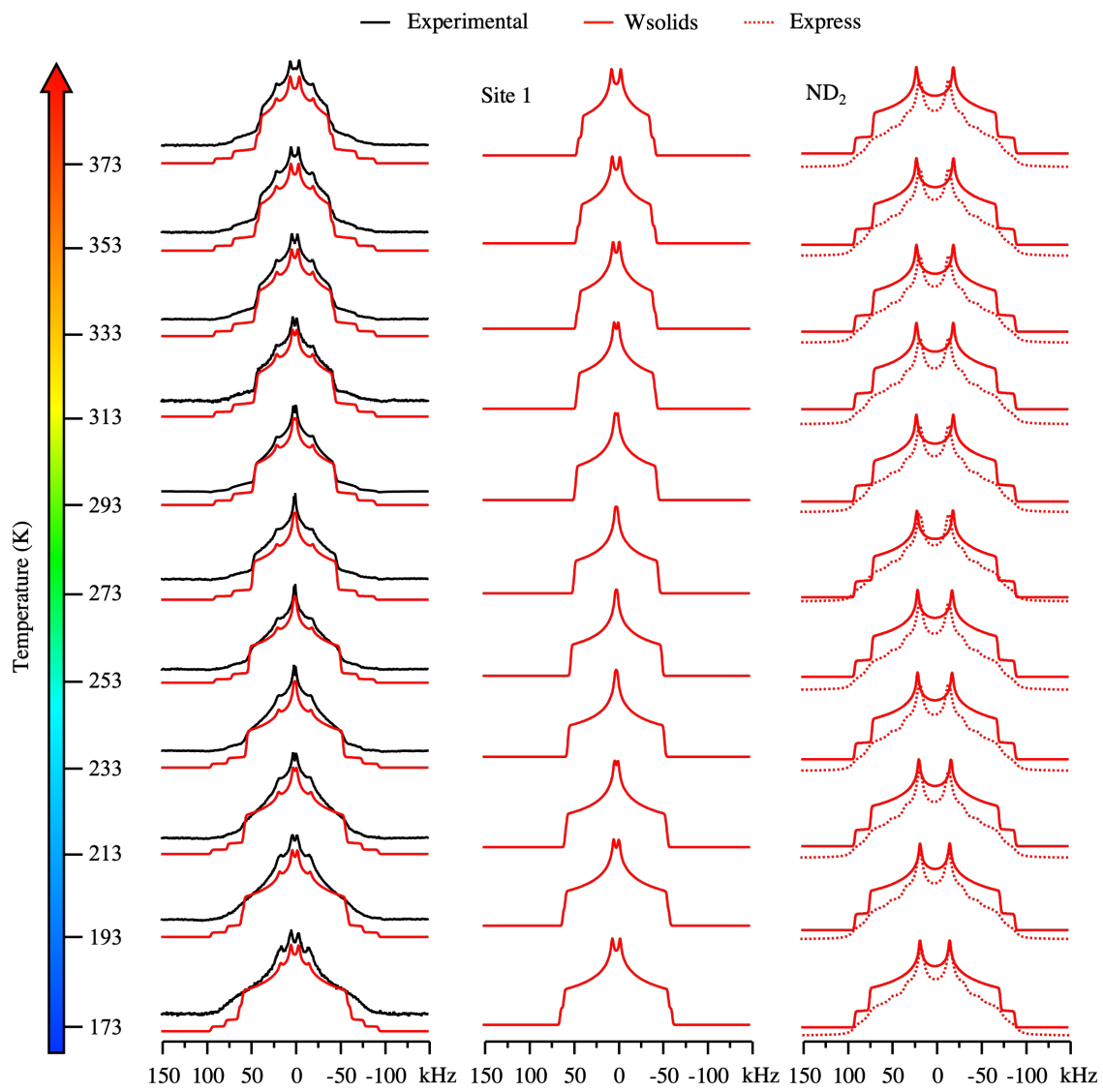


Figure A6.14. Experimental and simulated VT static ^2H NMR spectra of ZnAtzOx co-loaded with 8% D_2O and 0.2 equivalent of CO_2 .

Table A6.1. Bond lengths around the Zn metal centers.

Bond	Length (Å)	Bond	Length (Å)
Zn1–N5	1.98	Zn2–N3	2.00
Zn1–N7	2.03	Zn2–N2	2.02
Zn1–O3	2.03	Zn2–O1	2.05
Zn1–N1	2.08	Zn2–N6	2.10
Zn1–O4	2.10	Zn2–O2	2.18

Table A6.2. Bond angles around the Zn metal centers.

Bond	Angle (°)	Bond	Angle (°)
N5–Zn1–N7	112	N3–Zn2–N2	110
N5–Zn1–O3	117	N3–Zn2–O1	135
N5–Zn1–N1	103	N3–Zn2–N6	95
N5–Zn1–O4	91	N3–Zn2–O2	88
N7–Zn1–O3	128	N2–Zn2–O1	113
N7–Zn1–N1	94	N2–Zn2–N6	104
N7–Zn1–O4	88	N2–Zn2–O2	93
O3–Zn1–N1	87	O1–Zn2–N6	87
O3–Zn1–O4	78	O1–Zn2–O2	78
N1–Zn1–O4	163	N6–Zn2–O2	161

Table A6.3. Details of guest loading in the ZnAtzOx. The molecular formula of ZnAtzOx is $\text{Zn}_2\text{C}_6\text{H}_6\text{N}_8\text{O}_4$, and the molecular weight is 384.9 g mol^{-1} . Moles of CO_2 were estimated by considering the ideal gas law. Density of D_2O is 1.107 g mL^{-1} . ^aThe maximum CO_2 is the maximum theoretical CO_2 capacity based on the mass of the ZnAtzOx samples.

Guest loading	Mass of sample (g)	Max. CO_2^{a} (mmol)	Act. CO_2 (mbar)	Act. CO_2 (mmol)	Volume of D_2O (μL)	Moles of D_2O (mmol)
0.1 eq. $^{13}\text{CO}_2$	0.159(1)	0.72(1)	25(2)	0.04	-	-
0.2 eq. $^{13}\text{CO}_2$	0.135(1)	0.61(1)	42(2)	0.08	-	-
0.5 eq. $^{13}\text{CO}_2$	0.120(1)	0.54(1)	92(2)	0.14	-	-
2% D_2O	0.222(1)	-	-	-	4(1)	0.004(1)
4% D_2O	0.226(1)	-	-	-	9(1)	0.010(1)
8% D_2O	0.175(1)	-	-	-	13(1)	0.014(1)
12% D_2O	0.142(1)	-	-	-	15(1)	0.017(1)
0.1 eq. $^{13}\text{CO}_2$ + 4% D_2O	0.186(1)	0.84(1)	36(2)	0.12	7(1)	0.008(1)
0.1 eq. $^{13}\text{CO}_2$ + 8% D_2O	0.167(1)	0.75(1)	29(2)	0.10	12(1)	0.013(1)
0.2 eq. $^{13}\text{CO}_2$ + 4% D_2O	0.207(1)	0.93(1)	72(2)	0.24	8(1)	0.009(1)
0.2 eq. $^{13}\text{CO}_2$ + 8% D_2O	0.206(1)	0.93(1)	71(2)	0.24	15(1)	0.017(1)
0.5 eq. $^{13}\text{CO}_2$ + 4% D_2O	0.133(1)	0.60(1)	100(2)	0.33	5(1)	0.006(1)
0.5 eq. $^{13}\text{CO}_2$ + 8% D_2O	0.115(1)	0.52(1)	87(2)	0.29	9(1)	0.010(1)

Table A6.4. Experimental ^2H quadrupolar parameters of signal from D_2O adsorbed within ZnAtzOx at a loading level of 2%.

T (K)	Int. (%)	δ_{iso} (ppm)	C_Q (kHz)	η_Q	D-O-D ($^\circ$)	γ ($^\circ$)
D_2O						
373	33	0(5)	85(5)	0.90(2)	54.0(5)	38(2)
353	33	0(5)	85(5)	0.94(2)	54.0(5)	36(2)
333	33	0(5)	90(5)	0.96(2)	54.0(5)	34(2)
313	33	0(5)	90(5)	0.97(2)	54.0(5)	32(2)
293	33	0(5)	95(5)	0.96(2)	54.0(5)	28(2)
273	33	0(5)	100(5)	0.94(2)	54.0(5)	24(2)
253	40	0(5)	105(5)	0.90(2)	53.5(5)	14(2)
233	40	0(5)	110(5)	0.90(2)	53.5(5)	0(2)
213	50	0(5)	110(5)	0.86(2)	53.0(5)	0(2)
193	55	0(5)	110(5)	0.82(2)	53.0(5)	0(2)
173	60	0(5)	110(2)	0.82(1)	53.0(5)	0(2)
ND_2						
373	67	0(5)	120(2)	0.54(1)	-	-
353	67	0(5)	120(2)	0.54(1)	-	-
333	67	0(5)	120(2)	0.54(1)	-	-
313	67	0(5)	120(2)	0.54(1)	-	-
293	67	0(5)	120(2)	0.54(1)	-	-
273	67	0(5)	120(2)	0.55(1)	-	-
253	60	0(5)	120(2)	0.57(1)	-	-
233	60	0(5)	120(2)	0.60(1)	-	-
213	50	0(5)	120(5)	0.60(1)	-	-
193	45	0(5)	120(5)	0.62(2)	-	-
173	40	0(5)	120(5)	0.62(2)	-	-

Table A6.5. Experimental ^2H quadrupolar parameters of signal from D_2O adsorbed within ZnAtzOx at a loading level of 4%.

T (K)	Int. (%)	δ_{iso} (ppm)	C_Q (kHz)	η_Q	D-O-D ($^\circ$)	γ ($^\circ$)
D ₂ O						
373	40	0(5)	80(5)	0.92(2)	54.0(5)	42(2)
353	38	0(5)	80(5)	0.96(2)	54.0(5)	40(2)
333	38	0(5)	85(5)	0.96(2)	54.0(5)	38(2)
313	37	0(5)	85(5)	0.96(2)	54.0(5)	36(2)
293	38	0(5)	90(5)	0.94(2)	54.0(5)	34(2)
273	35	0(5)	90(5)	0.92(2)	54.0(5)	32(2)
253	38	0(5)	95(5)	0.90(2)	54.0(5)	30(2)
233	38	0(5)	95(5)	0.88(2)	53.5(5)	28(2)
213	42	0(5)	95(5)	0.86(2)	53.0(5)	28(2)
193	45	0(5)	95(5)	0.80(2)	53.0(5)	28(2)
173	70	0(5)	96(2)	0.79(1)	53.0(5)	28(2)
ND ₂						
373	60	0(5)	120(2)	0.54(1)	-	-
353	62	0(5)	120(2)	0.54(1)	-	-
333	62	0(5)	120(2)	0.54(1)	-	-
313	63	0(5)	120(2)	0.54(1)	-	-
293	62	0(5)	120(2)	0.54(1)	-	-
273	65	0(5)	120(2)	0.55(1)	-	-
253	62	0(5)	120(2)	0.57(1)	-	-
233	62	0(5)	120(2)	0.60(1)	-	-
213	58	0(5)	120(5)	0.60(1)	-	-
193	55	0(5)	120(5)	0.62(2)	-	-
173	30	0(5)	120(5)	0.62(2)	-	-

Table A6.6. Experimental ^2H quadrupolar parameters of signal from D_2O adsorbed within ZnAtzOx at a loading level of 8%.

T (K)	Int. (%)	δ_{iso} (ppm)	C_Q (kHz)	η_Q	D-O-D ($^\circ$)	γ ($^\circ$)
D ₂ O						
373	60	0(5)	54(2)	0.69(1)	53.0(5)	60(1)
353	60	0(5)	56(2)	0.73(1)	53.0(5)	60(1)
333	60	0(5)	56(2)	0.78(1)	53.5(5)	59(1)
313	63	0(5)	58(2)	0.81(1)	53.5(5)	59(1)
293	63	0(5)	60(2)	0.87(1)	54.0(5)	57(1)
273	63	0(5)	62(2)	0.90(1)	54.0(5)	55(1)
253	63	0(5)	66(2)	0.92(1)	54.0(5)	52(1)
233	70	0(5)	70(2)	0.94(1)	54.0(5)	50(1)
213	65	0(5)	74(2)	0.96(1)	54.0(5)	48(1)
193	65	0(5)	76(2)	0.96(1)	54.0(5)	46(1)
173	60	0(5)	80(2)	0.96(1)	54.0(5)	42(1)
ND ₂						
373	40	0(5)	120(2)	0.54(1)	-	-
353	40	0(5)	120(2)	0.54(1)	-	-
333	40	0(5)	120(2)	0.54(1)	-	-
313	37	0(5)	120(2)	0.54(1)	-	-
293	37	0(5)	120(2)	0.54(1)	-	-
273	37	0(5)	120(2)	0.55(1)	-	-
253	37	0(5)	120(2)	0.57(1)	-	-
233	30	0(5)	120(2)	0.60(1)	-	-
213	35	0(5)	120(5)	0.60(1)	-	-
193	35	0(5)	120(5)	0.62(2)	-	-
173	40	0(5)	120(5)	0.62(2)	-	-

Table A6.7. Experimental ^{13}C CSA parameters of ZnAtzOx loaded with 0.2 equivalent of $^{13}\text{CO}_2$ and 4% D_2O .

Temp. (K)	Int. (%)	δ_{iso} (ppm)	Ω (ppm)	κ	α ($^\circ$)	β ($^\circ$)
373	92	123(1)	268(2)	0.68(1)	13(1)	22(1)
333	95	123(1)	274(2)	0.65(1)	12(1)	22(1)
293	93	123(1)	284(2)	0.76(1)	12(1)	18(1)
253	89	123(1)	286(2)	0.78(1)	9(1)	18(1)
213	87	123(1)	290(2)	0.79(1)	9(1)	18(1)
173	82	123(1)	300(2)	0.83(1)	6(1)	16(1)

Table A6.8. Experimental ^{13}C CSA parameters of ZnAtzOx loaded with 0.2 equivalent of $^{13}\text{CO}_2$ and 8% D_2O .

Temp. (K)	Int. (%)	δ_{iso} (ppm)	Ω (ppm)	κ	α ($^\circ$)	β ($^\circ$)
Site 1						
373	99	125(1)	270(2)	0.73(1)	14(1)	21(1)
333	100	125(1)	274(2)	0.77(1)	15(1)	19(1)
293	100	125(1)	280(2)	0.81(1)	15(1)	16(1)
253	100	125(1)	294(2)	0.86(1)	12(1)	15(1)
213	100	125(1)	300(2)	0.90(1)	11(1)	13(1)
173	100	125(1)	310(2)	0.93(1)	6(1)	12(1)

Table A6.9. Experimental ^{13}C CSA parameters of ZnAtzOx loaded with 0.5 equivalent of $^{13}\text{CO}_2$ and 4% D_2O .

Temp. (K)	Int. (%)	δ_{iso} (ppm)	Ω (ppm)	κ	α ($^\circ$)	β ($^\circ$)
373	78	123(1)	260(2)	0.53(1)	10(1)	26(1)
333	94	123(1)	260(2)	0.52(1)	10(1)	26(1)
293	96	124(1)	262(2)	0.57(1)	13(1)	24(1)
253	98	123(1)	260(2)	0.47(1)	15(1)	25(1)
213	98	123(1)	258(2)	0.45(1)	10(1)	26(1)
173	93	120(1)	258(2)	0.52(1)	10(1)	24(1)

Table A6.10. Experimental ^{13}C CSA parameters of ZnAtzOx loaded with 0.5 equivalent of $^{13}\text{CO}_2$ and 8% D_2O .

Temp. (K)	Int. (%)	δ_{iso} (ppm)	Ω (ppm)	κ	α ($^\circ$)	β ($^\circ$)
Site 1						
373	79	126(2)	270(5)	0.72(2)	13(1)	22(1)
333	77	126(2)	275(5)	0.77(2)	13(1)	22(1)
293	77	126(2)	283(5)	0.81(2)	14(1)	16(1)
253	80	126(1)	290(2)	0.86(1)	12(1)	16(1)
213	82	126(1)	300(2)	0.90(1)	7(1)	15(1)
173	86	126(1)	310(2)	0.92(1)	2(1)	13(1)
Site 2						
373	21	125(5)	35(10)	0.50(5)	50(1)	30(1)
333	23	125(5)	60(10)	0.65(5)	48(1)	29(1)
293	23	125(5)	100(10)	0.70(5)	40(1)	26(1)
253	20	125(5)	140(10)	0.40(5)	33(1)	27(1)
213	18	125(5)	140(10)	0.40(5)	33(1)	27(1)
173	14	125(5)	140(10)	0.40(5)	33(1)	27(1)

Curriculum Vitae

Name:	Vinicius Martins
Post-secondary Education and Degrees:	Universidade Federal Fluminense Niteroi, Rio de Janeiro, Brazil 2010-2015 B.Sc. Chemistry Universidade do Minho Braga, Portugal 2013 Academic Exchange Universidade Federal Fluminense Niteroi, Rio de Janeiro, Brazil 2015-2017 M.Sc. Chemistry University of Western Ontario London, Ontario, Canada 2017-2021 Ph.D. Chemistry
Honours and Awards:	17 th Brazilian Meeting on Inorganic Chemistry Poster presentation award 2014 Universidade Federal Fluminense Laurea Academic Honor for Student of the Year 2016 32 nd MOOT NMR Minisymposium Poster presentation award 2019 6.5 th CEEMWOQ Oral presentation award 2020 University of Western Ontario G. Michael and Joan Bancroft Excellence in Research Award 2020
Related Work Experience	Teaching Assistant Universidade Federal Fluminense

2016

Teaching Assistant
The University of Western Ontario
2017-2021

Member of Graduate Education Council
The University of Western Ontario
2020-2022

Chair of Program Committee
Science Rendezvous, University of Western Ontario
2019-2020

Publications:

1. N. Kumar, S. Mukherjee, N. C. Harvey-Reid, A. A. Bezrukov; K. Tan; V. Martins; M. Vandiche; T. Pham, L. M. van Wyk, K. Oyekan, A. Kumar, K. A. Forrest, K. M. Patil, L. J. Barbour, B. Space, Y. Huang, P. E. Kruger, M. J. Zaworotko. Breaking the trade-off between selectivity and adsorption capacity for gas separation, *Chem*, 2021, 7, 3085-3098.
2. V. Martins, J. Xu, I. Hung, Z. Gan, C. Gervais, C. Bonhomme, and Yining Huang. ^{17}O solid-state NMR at ultrahigh magnetic field of 35.2 T: Resolution of inequivalent oxygen sites in different phases of MOF MIL-53(Al), *Magn. Reson. Chem.* 2021, 59, 940-950.
3. V. Martins, J. Xu, X. Wang, K. Chen, I. Hung, Z. Gan, C. Gervais, C. Bonhomme, S. Jiang, A. Zheng, B. E. G. Lucier, and Y. Huang. Higher Magnetic Fields, Finer MOF Structural Information: ^{17}O Solid-State NMR at 35.2 T, *J. Am. Chem. Soc.* 2020, 142, 35, 14877–14889.
4. Y. T. A. Wong, V. Martins, B. E. G. Lucier, Y. Huang. Solid-State NMR Spectroscopy: A Powerful Technique to Directly Study Small Gas Molecules Adsorbed in Metal–Organic Frameworks. *Chem. Eur. J.* 2019, 25, 1848-1853.
5. V. Martins, V. J. A. L. C. Resende, and C. M. Ronconi. A series of coordination networks constructed from the rigid ligand 4,4'-ethynylenedibenzoate: topological diversity, entanglement, supramolecular interactions and photophysical properties. *CrystEngComm.* 2017, 19, 3103-3116.
6. V. Martins, and C. M. Ronconi. Coordination Networks: Design, Synthesis, Topology and Photophysical Properties. *Rev. Virt. Quim.* 2017, 9, 1318-1341.

Presentations:

1. (Oral) V. Martins. ^{17}O solid-state NMR at 35.2 T: Ultrahigh spectral resolution unlocks ultrafine information on oxygen environments in MOFs. The 2020 Bancroft Award Lecture. University of Western Ontario, 2020.
2. (Oral) V. Martins, B. E. G. Lucier, V. V. Terskikh, and Y. Huang. Evaluating the impact of H_2O on CO_2 capture in an ultra-microporous MOF via solid-state NMR spectroscopy. 6.5th Crystal Engineering and Emerging Materials Workshop of Ontario and Quebec. Online Conference, June 2020.
3. (Oral) V. Martins, X. Wang, I. Hung, Z. Gan, A. Zheng, and Yining Huang. Characterization of Framework Oxygen in MOFs by ^{17}O Solid-state NMR at Ultra-high Magnetic Field of 35.2 T. 102nd Canadian Chemistry Conference and Exhibition. Quebec City, QC, May 2019.
4. (Oral) V. Martins, B. E. G. Lucier, V. V. Terskikh, and Y. Huang. Probing Water Dynamics in an Ultramicroporous Metal-Organic Framework for Water Harvesting via Solid-State NMR Spectroscopy. Centre for Advanced Materials and Biomaterials Research Day. London, ON, April 2019.
5. (Poster) V. Martins, B. E. G. Lucier, V. V. Terskikh, and Y. Huang. Abstract of Papers, Investigating the Effect of Water on the CO_2 Adsorption of an Ultramicroporous Metal-Organic Framework via Solid-State NMR Spectroscopy. 32nd MOOT NMR Minisymposium. Ottawa, ON, November 2019.
6. (Poster) V. Martins, B. E. G. Lucier, V. V. Terskikh, and Y. Huang. Probing Water Dynamics in an Ultramicroporous Metal-Organic Framework for Water Harvesting via Solid-State NMR Spectroscopy. Centre for Advanced Materials and Biomaterials Research Day. London, ON, April 2019.
7. (Poster) V. Martins, B. E. G. Lucier, and Y. Huang. Studying Water Dynamics Inside an Ultra-microporous Metal-Organic Framework. Fallona Interdisciplinary Conference. London, ON, April 2017
8. (Poster) V. Martins, C. M. Ronconi. Influence of the ligand 4,4'-ethynilenedibenzoic acid in the design of new coordination networks based on alkali metals. 5th Annual Meeting of the Chemistry Graduate Program Students. Fluminense Federal University. Niteroi, RJ – Brazil, 2016.
9. (Poster) V. Martins, J. A. L. C. Resende, C. M. Ronconi. Syntheses of two new lanthanide metal-organic frameworks based on a rigid acetylenic ligand. 37th Annual Meeting of the Brazilian Chemical Society. Araxa, MG – Brazil, 2015.

10. (Poster) V. Martins, J. A. L.C. Resende, C. M. Ronconi. The Effect of building blocks on the design and construction of four extended networks based on a rigid acetylenic ligand. 22nd ABCr and 1st LACA. São Paulo, SP – Brazil, 2015.
11. (Poster) V. Martins, J. A. L. C. Resende, C. M. Ronconi. Synthesis and crystal structure of two new rigid coordination polymers of Co(II) and Cd(II). 35th Annual Meeting of the Brazilian Chemical Society. Águas de Lindóia, SP – Brazil, 2014.
12. (Poster) V. Martins, J. A. L. C. Resende, C. M. Ronconi. Ligands obtained by Sonogashira cross-coupling reaction for the construction of rigid metal-organic frameworks. XXIV Vasconcellos Torres Seminar of undergraduate research and Science and Technology, Fluminense Federal University. Niteroi, RJ – Brazil, 2012.